UC Davis

UC Davis Electronic Theses and Dissertations

Title

Shaping the Germline: Molecular and Nutritional Regulation of Male Meiosis

Permalink

https://escholarship.org/uc/item/2rm8881b

ISBN

9798193265337

Author

Esparza, Jasmine Marie

Publication Date

2026-09-08

Peer reviewed|Thesis/dissertation

eScholarship.org Powered by the California Digital Library
University of California

Shaping the Germline: Molecular and Nutritional Regulation of Male Meiosis

By

JASMINE MARIE ESPARZA
DISSERTATION

Submitted in partial satisfaction of the requirements for the degree of

DOCTOR OF PHILOSOPHY

in

Biochemistry, Molecular, Cellular, and Developmental Biology

in the

OFFICE OF GRADUATE STUDIES

of the

UNIVERSITY OF CALIFORNIA

DAVIS

Approved:

_____
Satoshi Namekawa, Chair

_____
Richard Schultz

_____
JoAnne Engebrecht

Committee in Charge

2026

To my fiancé, family, friends, community, and all my ancestors, past & present, who never stopped believing in me.

This degree is dedicated to you.

A mi familia y prometido, con todo mi amor, por apoyar mis sueños y mi educación.

IN MEMORIAM

In loving memory of my cousin, Anthony Angel Gomez, whose unwavering support, even in our final conversation, made this degree possible.

Table of Contents

Abstract ..... *iv*

Acknowledgements ..... *vi*

Introduction *1*

Abstract **2**

Chapter 1: ATF7IP2/MCAF2 directs H3K9 methylation and meiotic gene regulation in the male germline *18*

My contributions **19**

Abstract **20**

Chapter 2: Paternal folate deficiency reveals meiosis as a metabolic sensing window in the male germline *67*

My contribution **68**

Abstract **69**

Concluding remarks *117*

Conclusions **118**

Future Directions **121**

Final Perspective **124**

Abstract

Worldwide, over 15% of couples have difficulty conceiving a child. Long-term fertility in males is governed by spermatogenesis, the developmental program responsible for producing mature sperm. Sperm were once viewed primarily as carriers of paternal DNA, but they also carry epigenetic information that can influence fertilization and early embryonic development. This information is established through the remodeling of chromatin, the combination of DNA and associated proteins, as germ cells develop. However, why and how molecular regulators and environmental conditions shape the epigenome remains incompletely understood.

To address this gap in knowledge, I investigated how intrinsic and environmental factors influence the epigenetic trajectory of the male germline. I approached this biological question using two complementary mouse models: genetic deletion of a chromatin regulator, ATF7IP2/MCAF2, and dietary folate deficiency. By independently assessing each model using a combination of imaging and genome-wide analysis of gene expression and chromatin, I found that disruption of either factor resulted in distinct, but converging cellular and epigenetic changes in spermatogenesis. Genetic deletion of ATF7IP2/MCAF2 revealed an unexpected role in gene regulation and epigenetic reprograming in male meiosis. These findings also refined our understanding of how meiotic checkpoints respond to disrupted chromatin regulation. In the second model, paternal folate deficiency altered germ cell development, meiotic gene expression and various chromatin features in meiosis.

Together, these findings identify meiosis as a period of both epigenetic vulnerability and responsiveness. I propose that meiosis functions as a metabolic sensing window during which nutritional conditions can influence the chromatin landscape as it is being extensively reprogrammed. This conceptual framework helps explain how molecular regulation and

environmental exposures interact to shape sperm development and potentially influence the information transmitted to the next generation.

Acknowledgements

First, I want to thank my advisor, Dr. Satoshi Namekawa, for supporting me throughout my doctoral training. I am thankful to have a brilliant, supportive, and overall outstanding mentor these past six years. The Namekawa lab was a place I could indulge in my scientific curiosity and creativity every day. I learned how to read, write, present, and most importantly, think like a scientist. Satoshi, I will always be indebted for your support and dedication to my mentorship.

My dissertation committee of Dr. Satoshi Namekawa, Dr. Richard Schultz, and Dr. JoAnne Engebrecht, helped *remodel* my dissertation into something I am extremely proud of. Thank you for your constant support and engaging, thought-provoking discussions that improved my project beyond my expectations.

I am thankful to all the members of the Namekawa lab for their extensive scientific discussions, and more importantly, for their friendships. I owe much of my success to my undergraduate mentees who were right there with me every failure and success. I am eternally grateful to Rohan Kumar, Saanvi Jain, and Amr Gebrail for going above and beyond to support my research while balancing their own undergraduate studies. I look forward to when the healthcare system gains three very deserving M.Ds.

I am grateful for the entirety of BMCDB, especially all the graduate students who made my experience full of excitement and community. A huge shoutout to Alyssa Parsons, who was an anchor for my retention these last few years.

I want to thank my undergraduate research advisor, Dr. William Lowry, and the Lowry lab for nurturing my scientific curiosity, confidence, and community that encouraged me to pursue a Ph.D. in the first place.

I am grateful to have found a community dedicated to increasing representation in science through my involvement with the SACNAS national organization. Shoutout to the two UC Davis chapters, Graduate Student & Postdoctoral chapter and the undergraduate UC Davis chapter.

Every day I am thankful for my friends I made along the way. When my research had me at my wit's end, I could always count on my friends to make me laugh away the pain. I hold all these memories close to my heart. From trying new restaurants, discovering new hobbies, bonding over books, exploring new countries, crying from laughter, watching new movie releases, or just venting about research, I will always be grateful for choosing UC Davis because I wouldn't have met my people who I hold so dearly in my heart.

To my mom, my dad, and my sister: You never questioned my decision to pursue graduate school and always pushed me to shoot for the stars. This degree was a sacrifice for all of us, but I dedicate my success to your unwavering support and positivity. The sacrifices you made to ensure I had opportunities like this will never be forgotten.

To my fiancé, Saitiel: I am blessed to have found a thoughtful, hilarious, committed, patient, ambitious, and brilliant partner & best friend who only ever supported my dreams. Although this dream involved moving 400 miles away for 6 years, you never left my corner. You were my rock when I wanted to give up. You believed in me when I didn't believe in myself. I can't wait to be Dr. & Dr. soon.

To my late cousin, Anthony, it hurts me to know that you can't be here to see my success today. Every single conversation we had ended with you saying how proud you were of me and to never give up. I know you are my angel, always watching over me. I dedicate this degree to you.

Introduction[1]

[1] Esparza JM, Namekawa SH. Epigenetic trajectory of male meiosis. Biol Reprod. 2026 Jul 20:ioag148. doi: 10.1093/biolre/ioag148. Epub ahead of print. PMID: 42476517.

Abstract

Male meiosis is the developmental process in which germ cells halve their chromosome number while continuing toward sperm formation. This review focuses on mechanistic studies of male meiosis in mouse and develops an epigenetic framework for this transition, centered on two key concepts. First, the foundation of meiosis is established ahead of meiotic entry. Prior to meiosis, germ-cell genes are poised and chromosomes are organized to support the upcoming meiotic program. Stage-specific signals and transcription factors then act on this prepared state to initiate meiotic gene expression. Second, meiosis reorganizes the germline in preparation for the post-meiotic spermiogenic program. In early prophase, nascent transcription remains low, allowing chromosomes to reorganize for recombination. Later, pachytene spermatocytes undergo an autosomal transcriptomic burst required for meiotic progression and post-meiotic development, while retrotransposon expression is controlled and unsynapsed sex chromosomes are silenced. Together, these concepts frame male meiosis as both the execution of a prepared developmental process and a critical window during which the germline genome is reshaped. This epigenetic trajectory connects gene regulation, chromosome organization, genome defense, and developmental timing to ensure production of functional sperm.

Biology of Reproduction, 2026, 1–15
https://doi.org/10.1093/biolre/ioag148
Review

Epigenetic trajectory of male meiosis

Jasmine M. Esparza and Satoshi H. Namekawa*

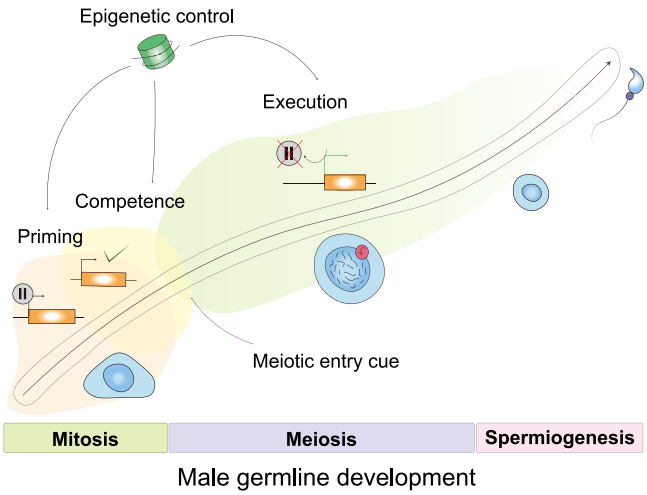
Department of Microbiology and Molecular Genetics, University of California Davis, Davis, California, United States

***Correspondence:** Department of Microbiology and Molecular Genetics, University of California Davis, One Shields Avenue, Davis, California, 95616, United States. E-mail: snamekawa@ucdavis.edu

Abstract

Male meiosis is the developmental process in which germ cells halve their chromosome number while continuing toward sperm formation. This review focuses on mechanistic studies of male meiosis in mouse and develops an epigenetic framework for this transition, centered on two key concepts. First, the foundation of meiosis is established ahead of meiotic entry. Prior to meiosis, germ-cell genes are poised and chromosomes are organized to support the upcoming meiotic program. Stage-specific signals and transcription factors then act on this prepared state to initiate meiotic gene expression. Second, meiosis reorganizes the germline in preparation for the post-meiotic spermiogenic program. In early prophase, nascent transcription remains low, allowing chromosomes to reorganize for recombination. Later, pachytene spermatocytes undergo an autosomal transcriptomic burst required for meiotic progression and post-meiotic development, while retrotransposon expression is controlled and unsynapsed sex chromosomes are silenced. Together, these concepts frame male meiosis as both the execution of a prepared developmental process and a critical window during which the germline genome is reshaped. This epigenetic trajectory connects gene regulation, chromosome organization, genome defense, and developmental timing to ensure production of functional sperm.

Graphical Abstract



Key words: meiosis, epigenetic priming, spermatogenesis, germ cells, spermatocytes, meiotic sex chromosome inactivation.

Introduction

Spermatogenesis is a tightly regulated developmental process that produces male gametes through the coordinated progression of mitotic proliferation, meiotic chromosome reduction, and post-meiotic differentiation. In mouse testis, spermatogenesis occurs within the seminiferous tubules and is organized by the seminiferous epithelial cycle, where germ cells progress through distinct developmental stages in a highly organized spatial and temporal cycle. A key transition during spermatogenesis is entry into meiosis, when differentiating spermatogonia develop into preleptotene spermatocytes. These germ cells initiate premeiotic deoxyribonucleic acid (DNA) replication and proceed into meiotic prophase I. During this transition, germ cells must activate meiotic gene-expression programs, assemble chromosome axes, initiate homologous recombination, and subsequently establish specialized chromatin domains such as the XY body. Thus, male meiosis in mice is not simply a cell-division program; it is a precisely controlled developmental process governed by epigenetic mechanisms that integrate gene regulation, chromosome architecture, genome defense, and germline differentiation.

Received: May 26, 2026. **Revised:** July 7, 2026. **Accepted:** July 9, 2026
© The Author(s) 2026. Published by Oxford University Press on behalf of the Society for the Study of Reproduction. All rights reserved. For commercial re-use, please contact reprints@oup.com for reprints and translation rights for reprints. All other permissions can be obtained through our RightsLink service via the Permissions link on the article page on our site—for further information please contact journals.permissions@oup.com.

Downloaded from academic.oup.com/biolreprod/advance-article/doi/10.1093/biolre/ioag148/8738469 by University of California, Davis - Library user on 24 August 2026

Viewed from this broader perspective, meiosis has long been proposed to function beyond merely reducing chromosome number. In addition to reshuffling genetic information through recombination, meiosis may also contribute to epigenetic reprogramming and cellular rejuvenation across generations [1, 2]. In male mouse germ cells, this process is achieved through a developmental program in which pre-existing regulatory competence is converted into new chromatin, transcriptional, and chromosomal states that support haploid differentiation. Therefore, the epigenetic trajectory of male meiosis in mice is both permissive and restrictive: germ cells must activate meiotic and post-meiotic transcriptional programs while simultaneously extinguishing earlier mitotic programs, thereby preventing inappropriate transcription, suppressing retrotransposon expression, and silencing the sex chromosomes.

Although much of meiotic regulation is conserved between sexes and across species, mouse spermatogenesis provides a distinctive framework in which meiotic entry and subsequent programming can be followed continuously within the seminiferous epithelium. In contrast to male meiosis, female meiosis and fetal germ-cell sex determination involve distinct developmental timing, regulatory inputs, and chromatin states, and are discussed elsewhere [3, 4]. Related reviews have covered mammalian meiotic initiation and gene regulation, germ-cell transcriptomics, meiotic sex chromosome inactivation (MSCI), retrotransposon regulation, and three-dimensional (3D) genome organization [5–13]. Here, we examine how chromatin regulation shapes successful execution of male meiosis during spermatogenesis in mice.

We propose that male meiosis is best understood through two complementary epigenetic principles (Figure 1). First, the meiotic program is prepared before meiotic entry. Throughout fetal and postnatal germ-cell development, chromatin states and genomic architecture are progressively configured for germ cells competent to respond to meiotic cues. Thus, meiotic entry as a response to retinoic acid (RA) is not de novo. Instead, differentiating spermatogonia inherit and refine a preconfigured chromatin landscape that permits timely meiotic initiation. Second, extensive chromatin reorganization occurs during meiosis. Following meiotic entry, early prophase I undergoes low nascent transcription, recombination, and extensive chromosome remodeling. At pachytene, autosomes become transcriptionally active, retrotransposon expression is selectively controlled, and MSCI silences the unsynapsed X and Y chromosomes. Therefore, the male germline is epigenetically primed before meiosis and extensively remodeled during meiosis.

Here, we use the term "epigenetic trajectory" to describe the directional yet dynamic progression of the chromatin landscape as male germ cells prepare for and progress through meiosis. This trajectory begins before meiotic entry, when spermatogonia establish a regulatory foundation that maintains their developmental state while making meiotic genes ready for activation. After meiotic entry, this prepared state is remodeled to support chromosome organization, recombination, and low nascent transcription in early prophase. Later, pachytene spermatocytes activate large-scale but selective autosomal gene expression while controlling retrotransposons and silencing the X and Y chromosomes. In this review, we follow these stepwise changes to show that male meiosis is not triggered by a single switch, but instead develops from a primed germ-cell state that is extensively remodeled to prepare the genome for haploid differentiation.

Before meiotic entry: building a primed regulatory foundation in spermatogonia

In male germ cells, meiotic competence is progressively established before the RA response and subsequent activation of the STRA8–MEIOSIN transcriptional program [13] (Figure 2). In this review, we define competence as the ability of a gene-regulatory state to respond to an activating signal by initiating transcription. This competence can arise through different combinations of priming, licensing, and poising. Early germline DNA methylation reprogramming creates a permissive promoter landscape upon which eventual male germline transcriptional programs are built. Studies of the primordial germ cell-to-prospermatogonia (also known as gonocytes) transition have identified DNA methylation and Polycomb-associated reprogramming as key features of gonadal germline maturation [14–16]. Further, emerging evidence suggests that protection of promoters from de novo DNA methylation, together with early chromatin priming in embryonic male germ cells, creates a promoter landscape with long-term regulatory potential [17]. In parallel, studies of male germ-cell reconstitution and fetal-to-postnatal germ-cell transitions indicate that differentiation programs are established before a spermatogonial stem cell population is fully formed, accompanied by extensive chromatin remodeling and nuclear reorganization [18, 19]. *Hence, meiotic competence in spermatogonia reflects earlier epigenetic priming, rather than being newly established at meiotic entry.*

Epigenetic priming refers to the earlier establishment of chromatin-based regulatory states that predispose a locus to later activation. In spermatogenesis, many promoters used after meiotic entry are already accessible before meiosis, representing a key feature of this primed landscape. Genome-wide profiling of open chromatin during spermatogenesis showed that promoter accessibility is relatively stable, in contrast to stage-specific remodeling of distal regulatory elements [20]. This observation suggests that promoters provide a permissive foundation for future gene activation. Consistent with this idea, in spermatogonia, meiotic and spermatogenic genes often carry accessible promoters, active epigenetic marks such as H3K4me2/3, and paused ribonucleic acid (RNA) polymerase II (Pol II), allowing for later activation through developmentally regulated pause release [21–24]. In this review, we categorize promoters as licensed when they acquire permissive chromatin features, such as increased accessibility, active histone modifications, enhancer engagement, or removal of repressive constraints, but remain transcriptionally inactive or lowly transcribed. Thus, promoter licensing constitutes an early layer of meiotic competence (Figure 2).

To preserve developmental timing and spermatogonial identity, this permissive promoter framework must be balanced by repressive mechanisms. In adult undifferentiated spermatogonia, Polycomb repressive complex 1 (PRC1) directs Polycomb repressive complex 2 (PRC2)-dependent H3K27me3 deposition, thereby preventing spermatogonial stem cell differentiation [25]. To overcome the repression, spermatogonial differentiation is accompanied by widespread reduction and redistribution of H3K27me3, suggesting that Polycomb-mediated repression is remodeled during germ cell differentiation. SCML2, a germline-enriched Polycomb group protein,

Downloaded from academic.oup.com/biolreprod/advance-article/doi/10.1093/biolre/ioag148/8738469 by University of California, Davis - Library user on 24 August 2026

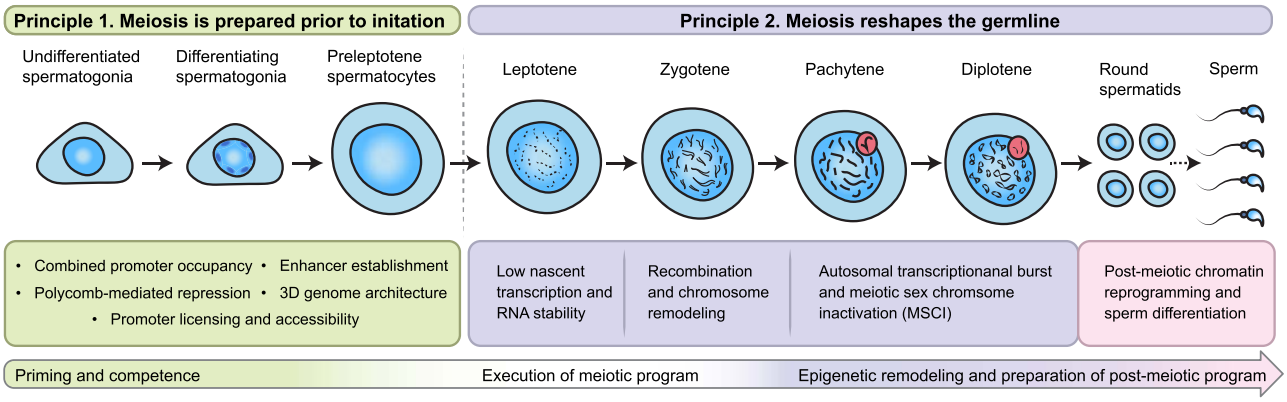


Figure 1. The epigenetic trajectory of mouse male meiosis. Male meiosis is prepared before it begins and remodeled as it proceeds. Before meiotic entry, spermatogonia build a chromatin and gene-regulatory landscape that supports later activation of the meiotic program. During meiotic prophase I, spermatocytes undergo chromosome remodeling, recombination, low nascent transcription in early prophase, autosomal transcriptional activation, retrotransposon control, MSCI, and preparation for post-meiotic differentiation.

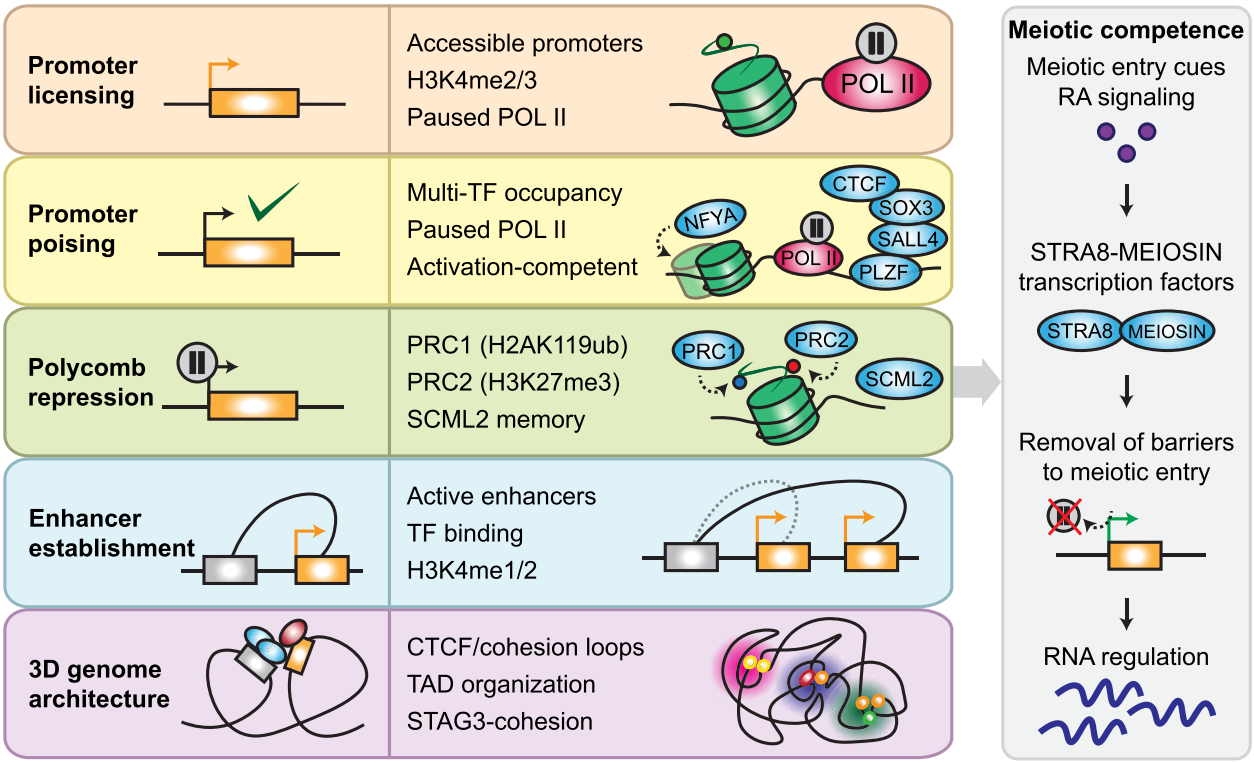


Figure 2. Building a primed regulatory landscape before meiosis. Spermatogonia acquire regulatory competence before meiotic entry. Accessible promoters, active chromatin marks, paused Pol II, Polycomb regulation, promoter-bound transcription factors, enhancers, and 3D genome organization together prepare germ cells for later meiotic activation. Retinoic acid signaling, STRA8–MEIOSIN, chromatin remodeling, and RNA-regulatory pathways then act on this prepared landscape to initiate meiosis.

adds an additional mechanism of precise developmental timing by marking spermatogonial genes that are active in spermatogonia but later repressed during meiosis, illustrating that priming can encode both future activation and repression [26]. Thus, Polycomb regulation couples promoter licensing with developmental restraint, preserving future activation potential while simultaneously bookmarking earlier programs for later repression (Figure 2).

Together, these findings indicate that promoter competence is not established by a single regulatory input, but instead likely emerges from the combined action of multiple promoter-bound factors. Recent profiling of undifferentiated spermatogonia shows that transcription factor ZBTB16/PLZF co-occupies meiotic promoter networks with SALL4, SOX3, CTCF, and Pol II, indicating that multi-factor occupancy poises spermatogonia for differentiation and later meiotic entry [24]. Additionally, recent work on NFYA adds an important mechanistic layer to this model. Expressed in spermatogonia, NFYA helps establish the competence of STRA8–MEIOSIN target promoters and is required for proper meiotic entry, suggesting that promoter licensing before meiosis enables timely activation of the meiotic program [27]. Studies of CTCF and its germline paralog, BORIS/CTCFL demonstrate that coordinated factor binding regulates spermatogenic

Downloaded from academic.oup.com/biolreprod/advance-article/doi/10.1093/biolre/ioag148/8738469 by University of California, Davis - Library user on 24 August 2026

gene expression [28, 29]. Promoter poising refers to a more immediately activation-ready state that includes bound transcription factors, paused Pol II, and in some cases, bivalent chromatin that maintains a gene in a regulated, reversible state until activating cues arrive. Together, these findings support a model whereby multiple promoter-bound factors cooperate to establish meiotic poising in spermatogonia (Figure 2).

Through enhancer activation and higher-order genome architecture, this permissive promoter framework is linked to stage-specific gene activation. Distal regulatory elements are extensively remodeled during germ-cell development and spermatogenic differentiation, indicating that enhancer activation provides an additional layer of developmental competence [20, 30] (Figure 2). Recent work from our group suggests that spermatogonial epigenetic poising may contribute to later RA responsiveness [31]. In this model, the chromatin remodeler SMARCA5 and the transcription factor DMRT1 help establish accessibility at poised enhancers and promoters during the transition from prospermatogonia to undifferentiated spermatogonia, and a subset of these sites are later bound by RA receptors. These findings suggest that pre-established chromatin accessibility may prime germ cells for RA-induced spermatogenic differentiation. Enhancer accessibility established during this transition may therefore represent a pioneer-like priming step that creates regulatory competence for the subsequent activation of meiotic gene-expression programs. Higher-order genome architecture further organizes this regulatory potential: long-range interactions involving meiotic gene loci are already present in spermatogonia and persist into meiosis, whereas long-range interactions associated with mitotic programs decline as germ cells progress through meiosis [32]. Consistent with this observation, STAG3, traditionally viewed as a meiosis-specific cohesin, also functions earlier in spermatogonia to shape cohesin-dependent nucleome organization and support differentiation priming [33]. Spermatogonia, therefore, carry a poised regulatory landscape that preserves mitotic identity while remaining competent for meiotic entry. This poised state must also be coupled with anti-meiotic repression to prevent premature activation of the meiotic program. DMRT1 acts as a transcriptional gatekeeper that maintains the spermatogonial program and suppresses inappropriate meiotic entry, whereas NANOS2, an RNA-binding protein required for male germ-cell fate, represses meiotic programs earlier in male germline development [34, 35].

Collectively, these findings support a model in which meiotic competence is established prior to meiosis through promoter configuration using a combination of chromatin and molecular factors (Figure 2). Despite several factors contributing to meiotic competence in spermatogonia, premeiotic priming is likely permissive rather than fully instructive. It remains unknown if all major factors of meiotic entry, such as RA responsiveness, RNA regulation, and cell-cycle state, are predetermined in spermatogonia.

RA–STRA8–MEIOSIN: executing a preconfigured program

Acting on pre-established chromatin states in responsive germ cells, RA signaling provides a critical stage-dependent cue for spermatogonial differentiation and subsequent meiotic entry in the postnatal testis. In the seminiferous epithelium, somatic Sertoli cells and pachytene spermatocytes supply RA that drives pulsatile signaling to coordinate stage-specific germ-cell differentiation [36–39] (Figure 3). Importantly, a recent study suggests that RA is required for spermatogonial differentiation but may be dispensable for meiotic initiation and progression, reinforcing the idea that RA acts primarily as an upstream differentiation cue rather than a stand-alone meiotic trigger [40].

Retinoic acid signaling promotes STRA8 expression, and STRA8 and MEIOSIN function together as a heterodimeric transcription factor complex to activate the meiotic gene-expression program [41]. STRA8 is expressed in differentiating spermatogonia and preleptotene spermatocytes [42–44], whereas MEIOSIN is expressed in the preleptotene stage, when germ cells undergo premeiotic S phase to prepare for meiotic entry [41]. Premeiotic S phase, STRA8-MEIOSIN activation, and prophase I onset are tightly coordinated but separable steps of the mitosis-to-meiosis transition. Premeiotic S phase is not merely a mitotic-like replication cycle: it is an unusually prolonged phase in which premeiotic replication follows a distinctive program with reduced origin firing, and this replication pattern is linked to the broad-scale organization of recombination in mice and humans [45]. Recent comparative and genetic analyses further refine this model by showing that MEIOSIN can initiate aspects of meiotic entry independently of STRA8, whereas STRA8 reinforces MEIOSIN activity to ensure robust and complete meiotic gene activation [46]. Although both STRA8 and MEIOSIN cooperate in meiotic gene activation [41, 47], their genetic ablation phenotypes are not identical. *Stra8*-deficient spermatocytes can initiate aspects of meiosis but fail to complete the program [44], indicating that STRA8 is important for robust transcriptional activation and stable meiotic progression. By contrast, MEIOSIN functions as a central execution factor for the mitosis-to-meiosis transition, and *Meiosin* loss causes a severe failure of meiotic gene activation and meiotic program progression [41]. Thus, MEIOSIN acts on a primed regulatory landscape to provide core meiotic gene activation, while STRA8 enhances the efficiency to ensure the robust and coordinated execution of the meiotic program.

To support the execution of STRA8-MEIOSIN activation, histone-specific chromatin remodeling marks meiotic genes for targeted activation. ZNHIT1, a subunit of the SRCAP chromatin remodeling complex, promotes deposition of the histone variant H2A.Z and co-occupies promoters with STRA8 to activate meiotic genes, including *Meiosin*. Loss of *Znhit1* arrests male germ cells as differentiating spermatogonia and disrupts meiotic initiation [48]. This arrest indicates that histone variant deposition cooperatively establishes promoter competence for meiotic gene activation.

Meiotic entry requires not only induction of the STRA8–MEIOSIN axis but also release from anti-meiotic repression (Figure 3). DMRT1 is a key transcriptional gatekeeper that maintains the spermatogonial program and suppresses precocious meiotic entry [35, 49]. By contrast, DMRT6 functions in differentiating spermatogonia to promote the mitosis-to-meiosis transition by repressing spermatogonial differentiation genes and activating meiotic genes [50]. Timely Dmrt6 expression is fine-tuned post-transcriptionally through direct targeting by miR-202 [51]. MEIOSIN and other meiotic genes are also restrained before the appropriate developmental window. In mouse embryonic stem (ES) cells, the noncanonical PRC1 subcomplex PRC1.6, which contains transcription

Downloaded from academic.oup.com/biolreprod/advance-article/doi/10.1093/biolre/ioag148/8738469 by University of California, Davis - Library user on 24 August 2026

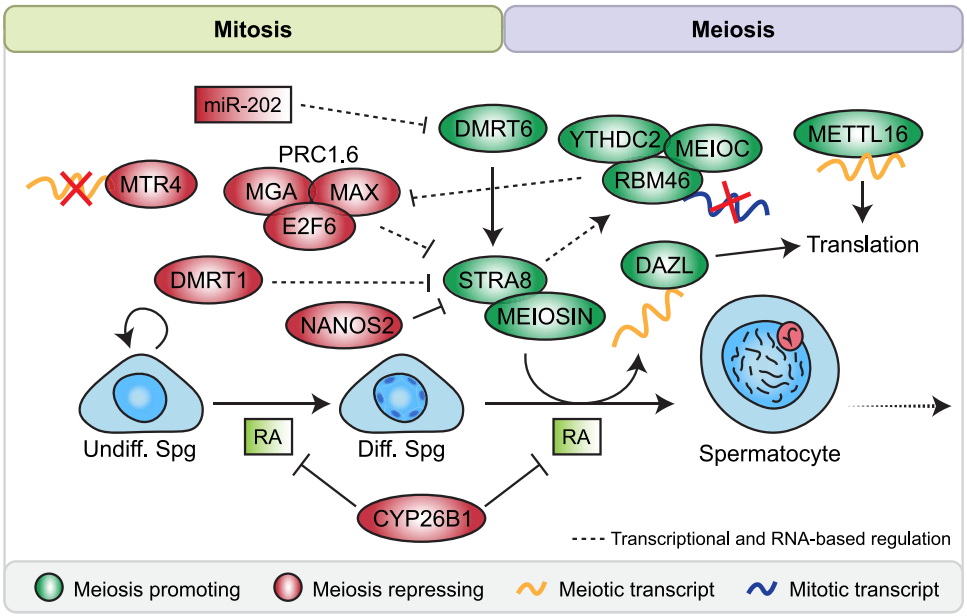


Figure 3. Molecular regulation of meiotic initiation. Meiotic initiation converts a primed spermatogonial state into execution of the meiotic program. Pro- and anti-meiotic factors maintain spermatogonial identity while preventing premature meiotic entry. Retinoic acid signaling induces STRA8 and MEIOSIN, which activate meiotic genes, while RNA-binding and post-transcriptional regulators reinforce the transition by promoting meiotic protein production and limiting mitotic transcripts.

factors such as MGA, MAX, and E2F6, suppresses germline and meiotic gene expression [52–54], although its in vivo role in repressing meiotic genes remains unclear. *Together, these mechanisms support a model in which meiotic initiation depends on both activation of the meiotic program and removal of anti-meiotic repression.*

Post-transcriptional regulation further reinforces this highly orchestrated transition. DAZL links RA-induced meiotic competence by post-transcriptionally enhancing translation of key meiotic transcripts, including genes involved in synapsis and recombination [55–57]. After meiotic initiation, the YTHDC2–MEIOC–RBM46 RNA binding complex stabilizes the mitosis-to-meiosis transition by remodeling the germ-cell transcriptome [58–62]. Loss of YTHDC2, MEIOC, or RBM46 allows partial meiotic initiation but disrupts progression, in part through inappropriate persistence of mitotic cell-cycle regulators such as CCNA2/Cyclin A2 and failure to accumulate meiotic proteins efficiently [59, 60, 62]. Emerging evidence suggests that MEIOC–YTHDC2–RBM46 enhances meiotic competence by promoting turnover of messenger RNAs (mRNAs) encoding transcriptional repressors such as E2F6 and MGA. By promoting post-transcriptional mRNA turnover, germ cells enhance their competence to activate STRA8–MEIOSIN and initiate meiosis in response to RA [63].

Beyond regulating expression, post-transcriptional mechanisms shape timing by modulating which transcripts accumulate. RNA decay is an example of one such mechanism. The nuclear exosome-associated RNA helicase exemplifies this role, limiting premature meiotic transcript accumulation and supporting proper meiotic initiation and early prophase progression [64]. An additional RNA-regulatory layer involves N6-methyladenosine (m6A), an mRNA modification that can influence RNA splicing, stability, and translation [65]. Studies of m6A-associated factors, including METTL16 and METTL3/METTL14, indicate that RNA modification contributes to spermatogenic progression [66, 67]. However, these pathways are best viewed as broader RNA-regulatory mechanisms rather than core components of the STRA8–MEIOSIN meiotic-entry pathway.

Finally, meiotic entry may also be coupled to metabolic remodeling. In cultured spermatogonia, nutrient restriction cooperates with RA to induce meiotic gene expression and SPO11-dependent double-strand break (DSB) formation [68]. In vivo studies further suggest that STRA8 represses nutrient transporter genes and reduces nutrient-sensing pathway activity during meiotic initiation [69]. These findings point to an additional layer in which RA–STRA8 signaling is coordinated with metabolic state, although the physiological role of nutrient restriction as an instructive meiotic cue remains to be fully established.

Collectively, RA–STRA8–MEIOSIN converts premeiotic competence into meiotic execution. RA signaling is a stage-dependent cue, STRA8–MEIOSIN activates the transcriptional program, anti-meiotic repressors prevent premature entry, and RNA regulatory pathways reinforce the transition by limiting mitotic transcripts and supporting meiotic protein accumulation. This transition culminates in premeiotic S phase, followed by meiotic prophase I, a prolonged G2-like interval in which germ cells carry out homolog pairing, recombination, synapsis, and chromosome remodeling before the first meiotic division. *Thus, meiotic entry is best understood as the coordinated execution of a preconfigured program rather than a de novo response to RA alone.*

Early prophase: low nascent transcription and recombination

Following premeiotic DNA replication and meiotic entry, germ cells enter prophase I, a prolonged and non-proliferative stage that lasts approximately 10 days in mouse spermatogenesis and requires the accurate completion of chromosome

Downloaded from academic.oup.com/biolreprod/advance-article/doi/10.1093/biolre/ioag148/8738469 by University of California, Davis - Library user on 24 August 2026

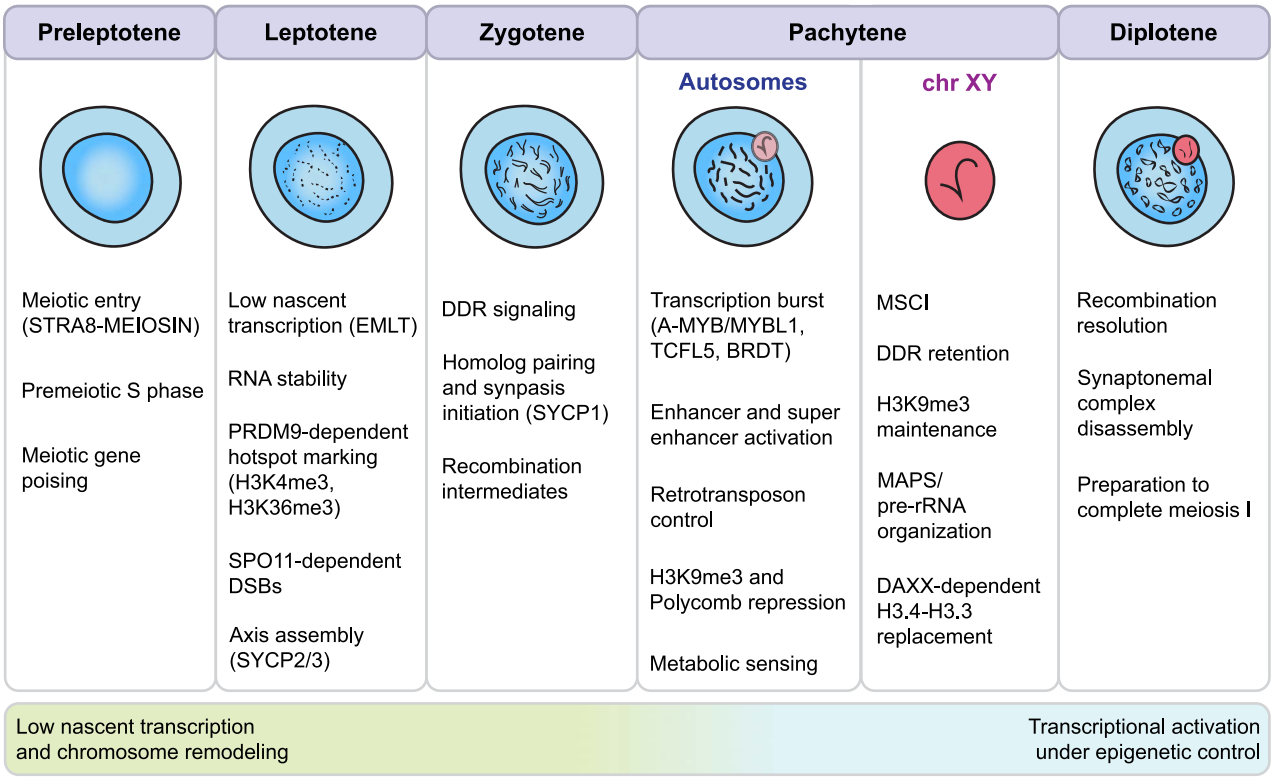


Figure 4. Meiotic prophase I: chromosome remodeling and transcriptional control. Meiotic prophase I coordinates chromosome remodeling with changes in gene regulation. In preleptotene, germ cells enter meiosis and undergo premeiotic S phase. In leptotene and zygotene, low nascent transcription, chromosome-axis formation, DSB formation, homolog pairing, recombination, and synapsis occur. In pachytene, autosomes show large-scale but selective transcriptional activation, while retrotransposons are controlled and the X and Y chromosomes undergo MSCI. In diplotene, synapsis is released, recombination is resolved, and cells prepare for meiotic division.

remodeling before gamete formation (Figure 4). During leptotene and zygotene, chromosomes undergo axis formation, programmed DSB formation, homologous recombination, and synapsis while nascent transcription remains low. This extended duration of prophase I may provide a developmental window for high-fidelity chromosome organization, ensuring that recombination and synapsis are completed with the precision needed to safeguard genetic information transmitted to the next generation. This juxtaposition of reduced nascent transcription and chromosome remodeling makes early prophase a distinct example of epigenetic control in meiosis: chromatin features commonly associated with active genes are repurposed to specify where recombination-initiating DSBs form and how recombination proceeds.

Low nascent transcriptional activity in leptotene and zygotene spermatocytes has long been recognized from classical RNA synthesis studies and later transcriptomic analyses [70–72]. Recent nascent transcription profiling defined this state more precisely as early meiotic low transcription (EMLT), showing that nascent transcription is reduced around meiotic entry and leptotene and recovers toward pachytene [73]. EMLT is accompanied by mRNA stabilization, depends on proper STRA8-mediated timing of meiotic entry, and is not simply caused by DSB formation or recombination repair, providing a mechanistic framework for early prophase transcriptional restraint [73]. *Together, these findings define early prophase as a restrained state in which nascent transcription is reduced, existing RNAs are stabilized, and chromosome remodeling for recombination proceeds.*

Recombination is central to this early-prophase logic because it shows how chromatin features normally associated with transcriptionally active regions can be repurposed to organize chromosome remodeling. Meiotic recombination promotes accurate homolog segregation and reshuffles genetic information between generations [74]. In mammals, meiotic recombination is initiated at discrete genomic regions known as recombination hotspots, whose specification is largely directed by PRDM9, a sequence-specific histone methyltransferase that recognizes DNA motifs through its C2H2 zinc finger domain and deposits H3K4me3 and H3K36me3 through its PR/SET domain [75–79]. These PRDM9-dependent marks are deposited independently of DSB formation and precede recruitment of the DSB machinery, placing chromatin marks upstream of physical break formation [80, 81]. Consistent with this role in DSB formation, altering the PRDM9 DNA-binding domain redirects DSB hotspots and restores synapsis and fertility in otherwise sterile male hybrids [82]. These data indicate that the proper placement of PRDM9-dependent H3K4me3 marks is critical for productive recombination. PRDM9-marked hotspots also show increased chromatin accessibility. This local opening is promoted in part by HELLS, a chromatin remodeler that cooperates with PRDM9 and is required for PRDM9-dependent DSB activity at hotspots [81, 83]. Temporal epigenomic profiling further suggests that hotspot chromatin state can influence not only DSB localization but also recombination outcome, with early-forming, accessible hotspots showing greater competence to

Downloaded from academic.oup.com/biolreprod/advance-article/doi/10.1093/biolre/ioag148/8738469 by University of California, Davis - Library user on 24 August 2026

proceed toward crossover formation [84]. In species lacking PRDM9, recombination preferentially occurs at CpG islands and promoter-associated H3K4me3 sites, reinforcing the idea that conserved chromatin features can guide hotspot localization when PRDM9 is absent [85, 86].

Following hotspot specification, recombination sites are spatially organized through their association with the chromosome axis, where DSB formation occurs. Meiotic chromosomes are structured into loop-axis configurations, with axes composed of cohesin complexes and meiosis-specific axis-associated proteins such as SYCP2, SYCP3, HORMAD1, and HORMAD2. PRDM9-marked hotspots located on chromatin loops are tethered to the axis through DSB factors, including MEI4, REC114, and IHO1, which help connect hotspots with the SPO11 recombination machinery [87–89]. This spatial organization ensures that DSBs form at properly designated sites along meiotic chromosomes.

DSB formation is then tightly controlled to preserve genome integrity. The DNA damage response (DDR) kinases ATM and ATR limit excessive or closely spaced breaks by enforcing feedback mechanisms such as DSB interference and by modulating the stability of axis-associated factors including IHO1 [90–94]. Additional chromatin remodelers also contribute to early prophase progression. CHD8 is required for spermatogonial proliferation and for progression through early meiotic prophase I; loss of CHD8 is associated with defective DSB repair, reduced RAD51 accumulation, persistent γH2AX, and pachytene arrest, highlighting a role for chromatin remodeling in coordinating recombination repair with prophase progression [95]. DSB formation is also temporally restricted: as cells approach pachytene, ZFP541 represses promoters of DSB machinery genes, helping prevent inappropriate DSB formation after the normal recombination window [96]. Thus, early prophase chromatin regulation not only establishes where DSBs form but also helps ensure that this potentially dangerous process is limited in time and space.

The relationship between EMLT and DSB-associated signaling is important for the broader logic of this review. Leptotene and zygotene spermatocytes show broad γH2AX deposition associated with programmed DSBs, which raises the possibility that DNA damage signaling directly causes transcriptional repression. However, Bellutti et al. showed that EMLT is not simply caused by DSB formation, DSB signaling, or recombination repair [73]. Instead, transcriptional restraint and recombination appear to be parallel features of the early prophase program. In this view, early prophase creates a low nascent transcription chromatin environment in which chromosomes can undergo DSB formation, homology search, and synapsis before the later pachytene transcriptional activation state.

Low nascent transcription does not mean lack of regulation. During EMLT, early meiotic spermatocytes preserve transcript availability while new transcription is reduced, with mRNA stabilization inferred from spliced-to-unspliced RNA ratios that reflect preservation of the mature transcript pool [73]. Regulated intron retention in meiotic spermatocytes can also generate stable nuclear transcripts that are stored and later recruited for translation, providing a mechanism for delayed transcript usage during germ-cell differentiation [97]. Alongside RNA decay pathways that remove precocious transcripts, these mechanisms suggest that early meiotic spermatocytes actively manage the transcript pool by preserving needed RNAs, storing transcripts for later use, and clearing RNAs that accumulate at inappropriate stages [64]. *This balance of RNA stabilization, storage, and decay helps synchronize meiotic progression during a window in which nascent transcription is low.*

After DSB formation, hotspot-associated chromatin marks are interpreted by reader proteins to promote repair. By recognizing dual H3K4me3/H3K36me3 signatures deposited by PRDM9, ZCWPW1 efficiently processes recombination intermediates toward proper repair outcomes [98–100]. ZCWPW2 provides a related reader function at PRDM9-marked hotspots, although its role is still emerging [101]. A subset of DSBs is ultimately resolved as crossovers, marked cytologically by MLH1 and MLH3, ensuring proper homolog segregation during the first meiotic division [102, 103].

Together, leptotene and zygotene represent a specialized early-prophase state in which nascent transcription is reduced, transcripts are stabilized, and chromatin is repurposed for recombination. This state connects the STRA8–MEIOSIN-driven entry program to the chromosome-scale events of meiosis. As synapsis and repair progress, DSB formation is curtailed and cells transition toward pachytene, where autosomal transcription is resumed. Thus, recombination-associated chromatin regulation is distinct from promoter/enhancer-based gene regulation, but the two are temporally connected: transcriptional programs produce the chromosome-axis and DSB machinery, while PRDM9-dependent chromatin marking determines where that machinery acts.

Autosomal transcriptional burst in pachytene spermatocytes

In this section, we focus on autosomal transcription in pachytene spermatocytes; regulation of the sex chromosomes is discussed separately below. As germ cells progress from zygotene to pachytene, the low-transcription state of early prophase gives way to a major increase in autosomal transcription. Pachytene and post-meiotic germ cells have long been recognized as stages of widespread transcriptional activity and a generally permissive chromatin state, as revealed by transcriptome and chromatin profiling across spermatogenesis [72, 104–106]. However, pachytene transcription should not be viewed simply as global autosomal activation. Here, we emphasize that the pachytene transcriptional burst is large-scale but selective. Pachytene spermatocytes increase autosomal nascent transcription to activate stage-specific genes and produce transcripts needed for later post-meiotic development. However, this activation does not reflect a uniformly permissive chromatin state: retrotransposons remain controlled, inappropriate mitotic programs are suppressed, and developmental genes remain in a repressed bivalent state. Thus, pachytene represents large-scale autosomal transcription within an epigenetically controlled environment that supports robust gene activation while preserving regulatory specificity and genome defense.

The biological purpose of this activation extends beyond meiotic prophase itself. Pachytene spermatocytes activate genes required for meiotic progression, chromosome remodeling, and preparation for the meiotic divisions, but they also produce transcripts needed later during haploid differentiation. As spermatids undergo chromatin compaction and histone-to-protamine replacement, transcription becomes increasingly constrained; therefore, many transcripts required during round and elongating spermatid development are

Downloaded from academic.oup.com/biolreprod/advance-article/doi/10.1093/biolre/ioag148/8738469 by University of California, Davis - Library user on 24 August 2026

produced earlier and regulated post-transcriptionally [8, 104, 107]. Thus, pachytene transcription functions as a preparatory phase for the post-meiotic program, linking meiotic progression to spermiogenesis.

Transcriptional activation in pachytene spermatocytes is closely linked to enhancer remodeling. Genome-wide chromatin accessibility profiling showed that promoters remain relatively stable across spermatogenesis, whereas distal regulatory elements are extensively reorganized, particularly at the mitosis-to-meiosis transition and during meiotic progression [108–110]. Super-enhancer switching provides a clear example of this principle. Spermatogonia and spermatocytes use distinct sets of high-density regulatory elements, and the pachytene super-enhancer landscape is associated with stage-specific transcriptional activation [30]. Thus, pachytene transcription reflects large-scale rewiring of enhancer usage, transcription factor occupancy, and chromatin accessibility.

A central driver of this pachytene regulatory landscape is the transcription factor A-MYB/MYBL1 [111]. A-MYB is highly expressed in pachytene spermatocytes and activates an expansive network of meiotic and post-meiotic genes required for spermatogenic progression. Genetic and genomic studies have shown that A-MYB controls expression of many pachytene-stage transcripts, including protein-coding genes and pachytene PIWI-interacting RNA (piRNA) loci, and that loss of A-MYB disrupts the spermatocyte transcriptional program [30, 111, 112]. Beyond promoter-proximal regulation, A-MYB contributes to enhancer reprogramming by helping establish H3K27ac-enriched regulatory regions that support stage-specific gene activation [30, 113]. This acetylated enhancer landscape provides a platform for BRDT, a testis-specific BET-family bromodomain protein that recognizes acetylated chromatin and promotes spermatogenic gene activation [114–116]. The transcription factor TCFL5 reinforces this network. A-MYB and TCFL5 form a regulatory circuit that supports pachytene gene expression and activation of pachytene piRNA loci, which are marked by active chromatin features including H3K4me3 and Pol II occupancy [112, 117, 118]. BRDT adds another layer by promoting productive transcriptional elongation and release of paused Pol II, enabling high-level transcriptional output during this stage [115, 119, 120]. Together, enhancer rewiring, A-MYB-dependent establishment of H3K27ac-enriched regulatory regions, TCFL5-mediated reinforcement, BRDT recognition of acetylated chromatin, and Pol II pause release help convert the restrained early-prophase state into a robust pachytene transcriptional activation program.

Pachytene piRNA production is closely linked to this transcriptional wave. Pachytene piRNA loci are among the most highly transcribed regions in the male germline and generate abundant small RNAs implicated in post-transcriptional regulation during spermatogenesis. Because pachytene piRNA biogenesis and function have been reviewed extensively elsewhere [121–125], we do not discuss the pathway in detail here. The key point for this review is that pachytene transcriptional activation includes not only protein-coding genes but also highly transcribed piRNA precursor loci, although the functions of many non-transposon-derived pachytene piRNAs remain incompletely understood.

Retrotransposon-derived sequences are an important component of the regulatory landscape in pachytene spermatocytes. Although potentially active endogenous retroviruses (ERVs) and other transposable elements must be repressed to protect genome integrity, some retrotransposon-derived loci show regulated transcription or chromatin accessibility in germ cells, suggesting that these sequences can function as regulatory elements. Over evolutionary time, ERV insertions can also be co-opted as promoter and enhancer elements that shape germline gene regulation during meiotic and post-meiotic stages [113, 126]. Because many ERV insertions are species- or lineage-specific, their co-option may contribute to species-specific spermatogenic transcriptomes. KRAB zinc-finger proteins are a rapidly evolving family of DNA-binding proteins that recognize and regulate ERV-associated sequences, and studies of these factors support a model in which retrotransposons are balanced between repression and regulatory use during spermatogenesis [127, 128]. *Thus, the pachytene transcriptional burst is large-scale but selective, shaped not only by regulatory element remodeling and transcription factor activity, but also by retrotransposon control and chromatin-context-dependent regulation.*

Autosomal chromatin and epigenetic control in pachytene spermatocytes

The pachytene transcriptional burst occurs within a chromatin environment that is permissive but not unrestricted. Histone modifications in pachytene must therefore be interpreted in their chromatin context. Active marks such as H3K4me3 and repressive marks such as H3K27me3 or H3K9me3 do not have fixed biological roles across spermatogenesis; their regulatory consequences depend on genomic position, developmental stage, depositing enzyme, histone variant composition, and the surrounding chromatin environment. This context dependence is especially important in pachytene, where transcriptional activation coincides with repression of selected developmental programs and retrotransposons. *Thus, the epigenetic trajectory of pachytene is not defined by individual histone marks alone, but by how activating and repressive chromatin states are combined and deployed.*

The interpretation of histone modifications must also account for histone variant composition. H3K4me3 and H3K27me3 are often discussed as modifications on histone H3, but spermatogenesis involves extensive replacement and specialization of H3 variants. The testis-specific H3 variant H3T/H3.4 is required for early spermatogenesis [129], and recent work demonstrated that DAXX directs H3.4-to-H3.3 replacement during male meiosis [130]. On autosomes, this replacement is coupled to transcriptional activity, indicating that histone variant exchange is integrated with the pachytene transcriptional program rather than serving merely as a passive change in histone substrate. Thus, the meaning of a given histone mark depends not only on where it is deposited, but also on which histone variant carries it.

Polycomb-associated bivalency provides another example of context-dependent chromatin meaning. In pachytene spermatocytes, broad bivalent domains marked by H3K4me3 and H3K27me3 emerge at developmental gene loci, preserving repression while maintaining future regulatory potential [22, 131, 132]. Earlier work identified poised chromatin and bivalent domains during the mitosis-to-meiosis transition, and spermatogonial H3K4me2-marked promoters have been linked to subsequent transcriptional activation in pachytene spermatocytes [22, 30, 32]. SCML2 was later shown to promote PRC2-dependent H3K27me3 at H3K4me2/3-rich,

Downloaded from academic.oup.com/biolreprod/advance-article/doi/10.1093/biolre/ioag148/8738469 by University of California, Davis - Library user on 24 August 2026

hypomethylated promoters in the male germline [20, 22]. H3K9 methylation provides an additional layer of repressive control during meiosis. ATF7IP2/MCAF2, a germline-enriched partner of the H3K9 methyltransferase SETDB1, directs H3K9 methylation and meiotic gene regulation in the male germline, supporting the idea that pachytene autosomes are regulated by both activation and repression [133, 134]. Together with recent work on Polycomb and DNA methylation remodeling during spermatogenesis [135, 136], these findings suggest that pachytene chromatin is not simply permissive; it is organized into domains that balance activation, repression, and future developmental potential.

Metabolic inputs may further tune this pachytene and post-meiotic chromatin landscape. One-carbon metabolism supplies methyl donors for nucleotide synthesis and chromatin modification, and recent work on paternal folate deficiency suggests that meiotic and post-meiotic development can be sensitive to nutritional state, with effects on chromatin accessibility and histone modification landscapes [137, 138]. Although this area is still emerging, these studies support the idea that meiotic prophase and its aftermath form a metabolically sensitive window of epigenomic remodeling.

Three-dimensional genome organization is also remodeled during meiotic and post-meiotic development, but we discuss this topic only briefly here because it has been reviewed in detail elsewhere [12]. Hi-C studies in mouse spermatogenesis have consistently shown that topologically associating domains (TADs) are attenuated or absent in pachytene spermatocytes, revealing a global reprogramming of 3D chromatin architecture [32, 110, 139–145]. For a broader discussion of germ-cell 3D genome remodeling and its relationship to meiotic chromosome dynamics, see our recent review [12]. The key point here is that pachytene transcriptional activation occurs within a reorganized spatial genome environment, not through promoter and enhancer activation alone.

Together, pachytene spermatocytes exhibit a highly active but tightly regulated transcriptional state. Transcription factors, enhancer switching, Pol II pause release, and active chromatin states promote robust autosomal gene expression, while repressive chromatin mechanisms, retrotransposon control, histone-variant dynamics, metabolic inputs, and genome architecture constrain where and how this activation occurs. This balance prepares germ cells for haploid differentiation while preserving genome integrity and regulatory specificity. Pachytene therefore marks the point at which the primed meiotic program is not only expressed but extensively remodeled into the transcriptional and chromatin state required for post-meiotic development.

Chromosome-wide silencing of the X and Y chromosomes in pachytene spermatocytes

Pachytene creates divergent chromosome fates. Autosomes resolve most DDR signaling and enter a transcriptionally activated state, whereas the largely unsynapsed X and Y chromosomes accumulate DDR signaling, undergo MSCI, and form the XY body, a specialized silencing compartment. The core mechanisms of MSCI, including BRCA1-regulated ATR signaling [146–149], MDC1-dependent γH2AX spreading [150], and XY-body formation, are reviewed in detail elsewhere [151–158] (Figure 5A), including our earlier review proposing a phase-separation model for MSCI and XY-body organization [10]. Here, we focus on recent updates that refine this model, especially how sex chromosome silencing is established, maintained, and coordinated with the transcriptionally active autosomal environment of pachytene spermatocytes.

A key update is that MSCI is more dynamic and reversible than previously appreciated. ATR-dependent DDR signaling constitutes the central pathway for initiating and maintaining sex-chromosome silencing. Inhibition of ATR disrupts the γH2AX domain, permits Pol II loading and nascent transcription on the sex chromosomes, and thereby reverses MSCI [159]. Upon removal of ATR inhibition, γH2AX accumulation and Pol II exclusion are restored on XY chromatin. These findings demonstrate that MSCI requires ongoing ATR-dependent DDR signaling, rather than being a passively maintained silent chromatin state. Thus, ATR-dependent DDR signaling provides the core regulatory framework for MSCI, while H3K9me3 deposition, histone-variant exchange, RNA-associated mechanisms, and chromosome-scale compartmentalization function as interconnected components that reinforce and organize sex-chromosome silencing (Figure 5B). SETDB1 links meiotic DDR signaling to H3K9me3 deposition on the sex chromosomes [160], and the SETDB1-associated factor ATF7IP2/MCAF2 accumulates on XY chromatin and supports H3K9 methylation and MSCI maintenance [134]. In this view, H3K9me3 is not the initiating signal for MSCI, but part of a chromosome-scale repression system that reinforces and helps organize silencing across the sex chromosomes.

Recent work also refines the physical model of the XY body. The phase-separation model proposed that DDR-dependent MSCI involves condensate-like organization of sex-chromosome chromatin [10]. Subsequent studies support this idea from complementary angles. MAPS, a male pachynema-specific protein, drives phase separation in vitro and regulates sex body formation and chromatin behavior in vivo [161]. In parallel, pre-ribosomal RNA localizes to the XY body and reorganizes DNA repair factors around programmed DSB sites during meiotic prophase, suggesting that RNA can contribute to the spatial organization of DDR signaling [162]. These studies suggest that MSCI is embedded in a higher-order nuclear environment shaped by DDR signaling, chromatin proteins, and RNA (Figure 5B).

Recent work further shifts attention from histone modifications to the nucleosome substrate on which those modifications are written. The XY body is enriched for the replication-independent histone variant H3.3 [163], and new evidence indicates that this enrichment is generated through DAXX-dependent replacement of the testis-specific H3 variant H3T/H3.4 with H3.3 during male meiosis [130]. This finding suggests that sex-chromosome silencing involves not only deposition of repressive marks on pre-existing nucleosomes, but also active remodeling of nucleosome composition across XY chromatin (Figure 5B).

Together, these updates refine the XY body as an actively maintained chromatin compartment in which ATR-dependent DDR signaling provides the core regulatory framework, while H3K9me3-associated pathways, protein- and RNA-mediated organization, and DAXX-dependent histone-variant exchange act together to reinforce and organize sex-chromosome silencing.

Conclusion: principles of the epigenetic trajectory

The epigenetic trajectory of mouse male meiosis is best understood as a developmental continuum rather than a single switch at meiotic entry. Meiosis is prepared before it begins:

Downloaded from academic.oup.com/biolreprod/advance-article/doi/10.1093/biolre/ioag148/8738469 by University of California, Davis - Library user on 24 August 2026

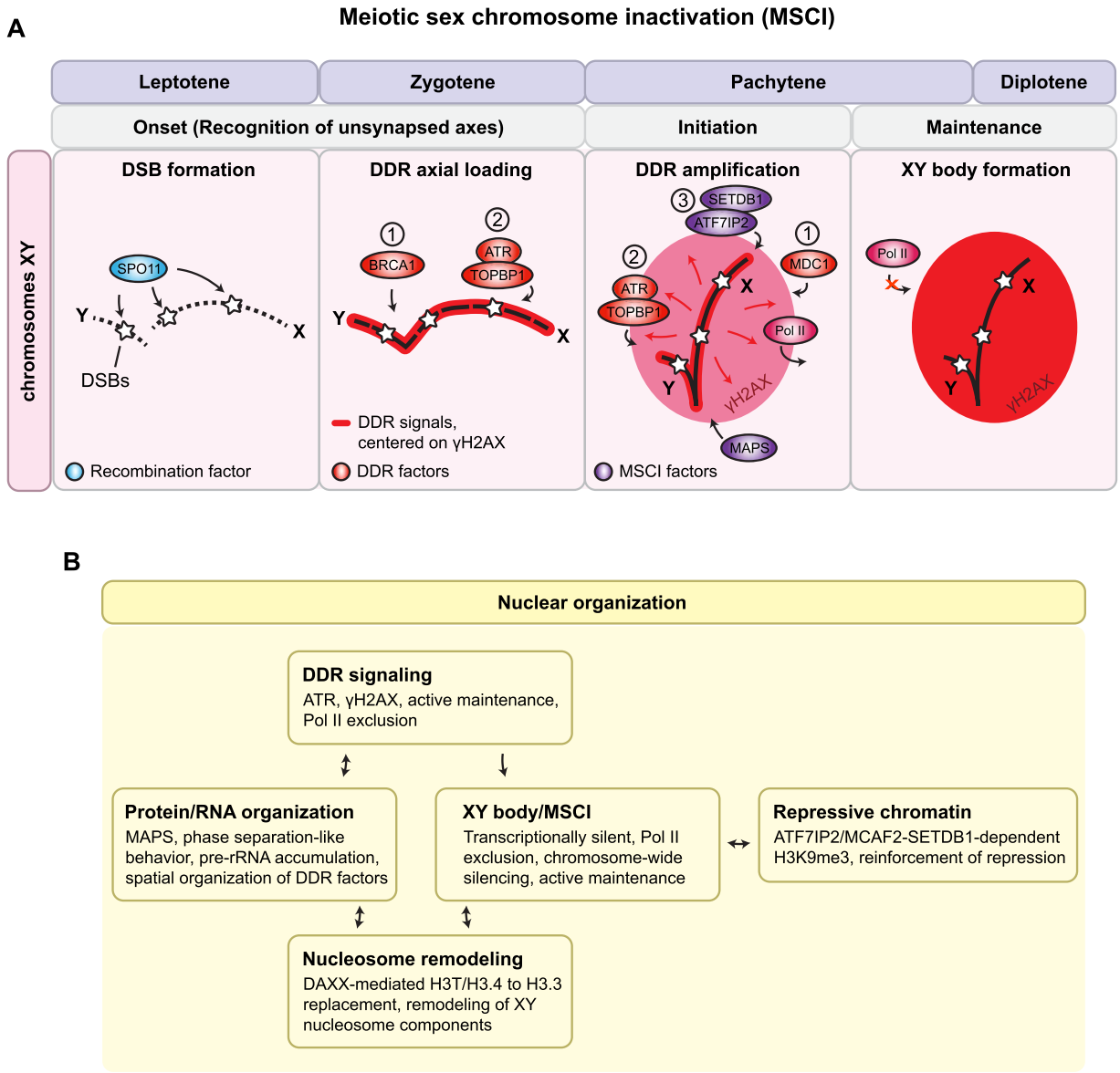


Figure 5. Model for MSCI and XY-body organization. The XY body is a specialized chromatin compartment formed during male meiosis. (A) SPO11-induced DSBs on unsynapsed X and Y chromosomes recruit BRCA1 and DDR signaling. ATR and MDC1 amplify the γH2AX domain, helping maintain MSCI and Pol II exclusion. (B) MSCI is accompanied by nuclear reorganization. Protein- and RNA-based mechanisms help organize the XY body, while histone-variant exchange replaces H3T/H3.4 with H3.3 on XY chromatin.

spermatogonia carry a regulatory landscape shaped by promoter licensing, Polycomb-mediated restraint, combinatorial promoter occupancy, enhancer establishment, and 3D genome architecture (Figure 1). This premeiotic organization allows germ cells to preserve spermatogonial identity while acquiring competence to respond to meiotic cues. In this framework, RA and STRA8–MEIOSIN do not build the meiotic program from scratch; they execute a program whose regulatory potential has already been established and constrained (Figure 2).

Yet meiosis is not merely the release of a pre-existing transcriptional program. Entry into meiotic prophase creates a new chromatin environment in which gene regulation becomes coordinated with chromosome-scale processes. In early prophase, low nascent transcription, RNA stability, recombination-associated chromatin marking, and chromosome-axis organization allow histone modifications and chromatin accessibility to be redeployed from conventional gene-regulatory contexts toward recombination hotspot specification, DSB formation, and homolog engagement. As cells progress to pachytene, autosomal transcription is strongly activated to support meiotic progression and prepare the post-meiotic program, but this activation remains embedded within a regulated chromatin landscape. Thus, meiotic chromatin is used not only to control transcription, but also to organize chromosome remodeling, ensuring that pachytene represents robust transcriptional activation under epigenetic constraint (Figure 4).

These observations reconcile two views of spermatogenesis. On one hand, the male germline remembers: regulatory competence is established before meiotic entry and carried forward into differentiating spermatogonia. On the other hand, the male germline is rebuilt: meiotic prophase reorganizes transcription, chromatin state, recombination landscapes, retrotransposon control, and chromosome architecture. The

Downloaded from academic.oup.com/biolreprod/advance-article/doi/10.1093/biolre/ioag148/8738469 by University of California, Davis - Library user on 24 August 2026

same epigenetic systems that license future gene expression also impose developmental timing, genome defense, and chromosome-specific regulation.

An important frontier is to understand how this meiotic chromatin state is resolved as cells exit prophase I. The transition from pachytene and diplotene into the meiotic divisions and post-meiotic differentiation is not simply the endpoint of earlier remodeling, but likely requires its own regulatory trajectory framework. Work on the ZFP541–KCTD19 complex suggests that meiotic prophase completion involves active repression and reconstruction of transcriptional and chromatin networks, thereby linking late prophase progression to the onset of post-meiotic development [164].

A central principle emerges from this dual trajectory: activation and repression are not opposing endpoints, but coordinated modes of germline control. Competence must be paired with restraint, transcription must be coordinated with chromosome behavior, and epigenetic marks must be interpreted within their genomic, developmental, and histone-variant contexts. Mouse male meiosis therefore provides a powerful model for understanding how a germ cell converts inherited regulatory potential into a new epigenetic state capable of supporting chromosome reduction, genome integrity, and the formation of the next generation.

Acknowledgment

We regret that, owing to the breadth of the topic and the journal's space limitations, we were unable to cite many important contributions from our colleagues. We thank Richard Schultz, Megan Motley, and members of the Namekawa lab for critical reading of the manuscript and stimulating discussions. This work was supported by the NIGMS T32 predoctoral training program in Molecular and Cellular Biology (MCB) at UC Davis (T32GM007377) and a National Academies Ford Foundation Fellowship to J.M.E.; R35GM141085 to S.H.N.; and a supplement to R35GM141085 to J.M.E. and S.H.N.

Conflict of Interest: Satoshi Namekawa holds the position of Board of Reviewing Editors for Biology of Reproduction and has not peer reviewed or made any editorial decisions for this paper.

Data availability

No new data were generated or analyzed in support of this review.

References

1. Holliday R. The biological significance of meiosis. *Symp Soc Exp Biol* 1984; **38**:381–394.
2. Berger F. Meiosis as a mechanism for epigenetic reprogramming and cellular rejuvenation. *Development* 2024; **151**:dev203046.
3. Shirane K, Lorincz M. Epigenetic mechanisms governing female and male germline development in mammals. *Sex Dev* 2022; **16**: 365–387.
4. Shimada R, Ishiguro KI. Female-specific mechanisms of meiotic initiation and progression in mammalian oocyte development. *Genes Cells* 2024; **29**:797–807.
5. Gao J, Qin Y, Schimenti JC. Gene regulation during meiosis. *Trends Genet* 2024; **40**:326–336.
6. Ishiguro KI. Mechanisms of meiosis initiation and meiotic prophase progression during spermatogenesis. *Mol Aspects Med* 2024; **97**:101282.
7. Feng C-W, Bowles J, Koopman P. Control of mammalian germ cell entry into meiosis. *Mol Cell Endocrinol* 2014; **382**:488–497.
8. Geisinger A, Rodríguez-Casuriaga R, Benavente R. Transcriptomics of meiosis in the male mouse. *Front Cell Dev Biol* 2021; **9**:626020.
9. Kaltsas A, Kyrgiafini MA, Mamuris Z, Chrisofos M, Sofikitis N. Spermatogenesis beyond DNA: integrated RNA control of the epitranscriptome and three-dimensional genome architecture. *Curr Issues Mol Biol* 2026; **48**:123.
10. Alavattam KG, Maezawa S, Andreassen PR, Namekawa SH. Meiotic sex chromosome inactivation and the XY body: a phase separation hypothesis. *Cell Mol Life Sci* 2021; **79**:18.
11. Zhou S, Sakashita A, Yuan S, Namekawa SH. Retrotransposons in the mammalian male germline. *Sex Dev* 2022; **16**:404–422.
12. Kitamura Y, Namekawa SH. The 3D genome during germline development and meiosis. *Trends Genet* 2026; **42**:255–267.
13. Kitamura Y, Namekawa SH. Epigenetic priming in the male germline. *Curr Opin Genet Dev* 2024; **86**:102190.
14. Hargan-Calvopina J, Taylor S, Cook H, Hu Z, Lee SA, Yen MR, Chiang YS, Chen PY, Clark AT. Stage-specific demethylation in primordial germ cells safeguards against precocious differentiation. *Dev Cell* 2016; **39**:75–86.
15. Hill PWS, Leitch HG, Requena CE, Sun Z, Amouroux R, Roman-Trufero M, Borkowska M, Terragni J, Vaisvila R, Linnett S, Bagci H, Dharmalingham G, *et al.* Epigenetic reprogramming enables the transition from primordial germ cell to gonocyte. *Nature* 2018; **555**:392–396.
16. Huang T-C, Wang Y-F, Vazquez-Ferrer E, Theofel I, Requena CE, Hanna CW, Kelsey G, Hajkova P. Sex-specific chromatin remodelling safeguards transcription in germ cells. *Nature* 2021; **600**:737–742.
17. Li P, Fujisawa T, Narita H, Uneme Y, Seki M, Hu M, Narumi R, Namekawa SH, Khan SS, Davie JR, Suzuki Y, Adachi J, *et al.* Priming epigenetic landscape at gene promoters through transcriptional activation in mammalian germ cells. *bioRxiv* 2024; 2024.11.24.625111.
18. Ishikura Y, Ohta H, Sato T, Murase Y, Yabuta Y, Kojima Y, Yamashiro C, Nakamura T, Yamamoto T, Ogawa T, Saitou M. In vitro reconstitution of the whole male germ-cell development from mouse pluripotent stem cells. *Cell Stem Cell* 2021; **28**:2167–2179.e2169.
19. Nagano M, Saitou M. Dynamic three-dimensional epigenomic reorganization for the development of undifferentiated spermatogonia in mice. *Curr Opin Genet Dev* 2025; **94**:102383.
20. Maezawa S, Yukawa M, Alavattam KG, Barski A, Namekawa SH. Dynamic reorganization of open chromatin underlies diverse transcriptomes during spermatogenesis. *Nucleic Acids Res* 2018; **46**:593–608.
21. Hammoud SS, Low DH, Yi C, Carrell DT, Guccione E, Cairns BR. Chromatin and transcription transitions of mammalian adult germline stem cells and spermatogenesis. *Cell Stem Cell* 2014; **15**: 239–253.
22. Sin HS, Kartashov AV, Hasegawa K, Barski A, Namekawa SH. Poised chromatin and bivalent domains facilitate the mitosis-to-meiosis transition in the male germline. *BMC Biol* 2015; **13**:53.
23. Kaye EG, Basavaraju K, Nelson GM, Zomer HD, Roy D, Joseph II, Rajabi-Toustani R, Qiao H, Adelman K, Reddi PP. RNA polymerase II pausing is essential during spermatogenesis for appropriate gene expression and completion of meiosis. *Nat Commun* 2024; **15**:848.
24. Yi C, Kitamura Y, Maezawa S, Namekawa SH, Cairns BR. ZBTB16/PLZF regulates juvenile spermatogonial stem cell development through an extensive transcription factor poising network. *Nat Struct Mol Biol* 2025; **32**:1213–1226.
25. Hu M, Yeh YH, Maezawa S, Nakagawa T, Yoshida S, Namekawa SH. PRC1 directs PRC2-H3K27me3 deposition to shield adult spermatogonial stem cells from differentiation. *Nucleic Acids Res* 2024; **52**:2306–2322.
26. Hasegawa K, Sin HS, Maezawa S, Broering TJ, Kartashov AV, Alavattam KG, Ichijima Y, Zhang F, Bacon WC, Greis KD,

Downloaded from academic.oup.com/biolreprod/advance-article/doi/10.1093/biolre/ioag148/8738469 by University of California, Davis - Library user on 24 August 2026

Andreassen PR, Barski A, *et al.* SCML2 establishes the male germline epigenome through regulation of histone H2A ubiquitination. *Dev Cell* 2015; **32**:574–588.
27. Säflund M, Askari M, Eghbali A, Abdi MM, Er DD, Östlund Farrants AK, Yu T, Özata DM. Transcription factor NFYA directs male meiotic entry by regulating accessible chromatin at meiotic promoters in mice. *EMBO J* 2026; **45**:2523–2560.
28. Rivero-Hinojosa S, Kang S, Lobanenkov VV, Zentner GE. Testis-specific transcriptional regulators selectively occupy BORIS-bound CTCF target regions in mouse male germ cells. *Sci Rep* 2017; **7**:41279.
29. Rivero-Hinojosa S, Pugacheva EM, Kang S, Méndez-Catalá CF, Kovalchuk AL, Strunnikov AV, Loukinov D, Lee JT, Lobanenkov VV. The combined action of CTCF and its testis-specific paralog BORIS is essential for spermatogenesis. *Nat Commun* 2021; **12**:3846.
30. Maezawa S, Sakashita A, Yukawa M, Chen X, Takahashi K, Alavattam KG, Nakata I, Weirauch MT, Barski A, Namekawa SH. Super-enhancer switching drives a burst in gene expression at the mitosis-to-meiosis transition. *Nat Struct Mol Biol* 2020; **27**:978–988.
31. Kitamura Y, Munakata Y, Abe H, Hu M, Oya S, Murugesan S, Rizwan M, Katz SP, Picketts DJ, Schultz RM, Namekawa SH. The SMARCA5–DMRT1 Pioneer complex establishes epigenetic priming to direct male germline development. *bioRxiv* 2025; 2025.07.29.667536.
32. Kitamura Y, Takahashi K, Maezawa S, Munakata Y, Sakashita A, Katz SP, Kaplan N, Namekawa SH. CTCF-mediated 3D chromatin sets up the gene expression program in the male germline. *Nat Struct Mol Biol* 2025; **32**:1227–1240.
33. Nagano M, Hu B, Ogata K, Umemura F, Ishikura Y, Suzuki S, Katsifis CC, Yoshinaga M, Litos G, Nagasaka K, Tang W, Nosaka Y, *et al.* The mitotic STAG3-cohesin complex shapes male germline nucleome. *Nat Struct Mol Biol* 2025; **32**:2203–2218.
34. Suzuki A, Saga Y. Nanos2 suppresses meiosis and promotes male germ cell differentiation. *Genes Dev* 2008; **22**:430–435.
35. Matson CK, Murphy MW, Griswold MD, Yoshida S, Bardwell VJ, Zarkower D. The mammalian doublesex homolog DMRT1 is a transcriptional gatekeeper that controls the mitosis versus meiosis decision in male germ cells. *Dev Cell* 2010; **19**:612–624.
36. Sugimoto R, Nabeshima Y, Yoshida S. Retinoic acid metabolism links the periodical differentiation of germ cells with the cycle of Sertoli cells in mouse seminiferous epithelium. *Mech Dev* 2012; **128**:610–624.
37. Gely-Pernot A, Raverdeau M, Célébi C, Dennefeld C, Feret B, Klopfenstein M, Yoshida S, Ghyselinck NB, Mark M. Spermatogonia differentiation requires retinoic acid receptor γ. *Endocrinology* 2012; **153**:438–449.
38. Endo T, Romer KA, Anderson EL, Baltus AE, de Rooij DG, Page DC. Periodic retinoic acid-STRA8 signaling intersects with periodic germ-cell competencies to regulate spermatogenesis. *Proc Natl Acad Sci U S A* 2015; **112**:E2347–E2356.
39. Griswold MD. Spermatogenesis: the commitment to meiosis. *Physiol Rev* 2016; **96**:1–17.
40. Kirsanov O, Johnson TA, Niedenberger BA, Malachowski TN, Hale BJ, Chen Q, Lackford B, Wang J, Singh A, Schindler K, Hermann BP, Hu G, *et al.* Retinoic acid is dispensable for meiotic initiation but required for spermiogenesis in the mammalian testis. *Development* 2023; 150:dev201638.
41. Ishiguro KI, Matsuura K, Tani N, Takeda N, Usuki S, Yamane M, Sugimoto M, Fujimura S, Hosokawa M, Chuma S, Ko MSH, Araki K, *et al.* MEIOSIN directs the switch from mitosis to meiosis in mammalian germ cells. *Dev Cell* 2020; **52**:e410.
42. Baltus AE, Menke DB, Hu YC, Goodheart ML, Carpenter AE, de Rooij DG, Page DC. In germ cells of mouse embryonic ovaries, the decision to enter meiosis precedes premeiotic DNA replication. *Nat Genet* 2006; **38**:1430–1434.
43. Anderson EL, Baltus AE, Roepers-Gajadien HL, Hassold TJ, de Rooij DG, van Pelt AMM, Page DC. Stra8 and its inducer, retinoic acid, regulate meiotic initiation in both spermatogenesis and oogenesis in mice. *Proc Natl Acad Sci* 2008; **105**:14976–14980.
44. Mark M, Jacobs H, Oulad-Abdelghani M, Dennefeld C, Féret B, Ng V, Codreanu C-A, Chambon P, Ghyselinck NB. STRA8-deficient spermatocytes initiate, but fail to complete, meiosis and undergo premature chromosome condensation. *J Cell Sci* 2008; **121**:3233–3242.
45. Pratto F, Brick K, Cheng G, Lam KG, Cloutier JM, Dahiya D, Wellard SR, Jordan PW, Camerini-Otero RD. Meiotic recombination mirrors patterns of germline replication in mice and humans. *Cell* 2021; **184**:e4220.
46. Shimada R, Imai Y, Araki K, Kawasaki T, Iisaka S, Usuki S, Yasunaga K-ı, Fujimura S, Tani N, Niwa H, Kuraku S, Sakai N, *et al.* MEIOSIN retains an intrinsic STRA8-independent activity that drives meiotic entry across vertebrate evolution. *bioRxiv* 2026; 2026.03.04.709545.
47. Kojima ML, de Rooij DG, Page DC. Amplification of a broad transcriptional program by a common factor triggers the meiotic cell cycle in mice. *eLife* 2019; **8**:e43738.
48. Sun S, Jiang Y, Zhang Q, Pan H, Li X, Yang L, Huang M, Wei W, Wang X, Qiu M, Cao L, He H, *et al.* Znhit1 controls meiotic initiation in male germ cells by coordinating with Stra8 to activate meiotic gene expression. *Dev Cell* 2022; **57**:901–913.e904.
49. Krentz AD, Murphy MW, Sarver AL, Griswold MD, Bardwell VJ, Zarkower D. DMRT1 promotes oogenesis by transcriptional activation of Stra8 in the mammalian fetal ovary. *Dev Biol* 2011; **356**:63–70.
50. Zhang T, Murphy MW, Gearhart MD, Bardwell VJ, Zarkower D. The mammalian Doublesex homolog DMRT6 coordinates the transition between mitotic and meiotic developmental programs during spermatogenesis. *Development* 2014; **141**:3662–3671.
51. Chen J, Gao C, Lin X, Ning Y, He W, Zheng C, Zhang D, Yan L, Jiang B, Zhao Y, Hossen MA, Han C. The microRNA miR-202 prevents precocious spermatogonial differentiation and meiotic initiation during mouse spermatogenesis. *Development* 2021; **148**:dev199799.
52. Kitamura Y, Uranishi K, Hirasaki M, Nishimoto M, Suzuki A, Okuda A. Identification of germ cell-specific Mga variant mRNA that promotes meiosis via impediment of a non-canonical PRC1. *Sci Rep* 2021; **11**:9737.
53. Uranishi K, Hirasaki M, Kitamura Y, Mizuno Y, Nishimoto M, Suzuki A, Okuda A. Two DNA binding domains of MGA act in combination to suppress ectopic activation of meiosis-related genes in mouse embryonic stem cells. *Stem Cells* 2021; **39**:1435–1446.
54. Urli T, Greenberg MVC. Epigenetic relay: Polycomb-directed DNA methylation in mammalian development. *PLoS Genet* 2025; **21**:e1011854.
55. Lin Y, Gill ME, Koubova J, Page DC. Germ cell-intrinsic and -extrinsic factors govern meiotic initiation in mouse embryos. *Science* 2008; **322**:1685–1687.
56. Gill ME, Hu YC, Lin Y, Page DC. Licensing of gametogenesis, dependent on RNA binding protein DAZL, as a gateway to sexual differentiation of fetal germ cells. *Proc Natl Acad Sci U S A* 2011; **108**:7443–7448.
57. Zagore LL, Sweet TJ, Hannigan MM, Weyn-Vanhentenryck SM, Jobava R, Hatzoglou M, Zhang C, Licatalosi DD. DAZL regulates germ cell survival through a network of PolyA-proximal mRNA interactions. *Cell Rep* 2018; **25**:e1226.
58. Abby E, Tourpin S, Ribeiro J, Daniel K, Messiaen S, Moison D, Guerquin J, Gaillard JC, Armengaud J, Langa F, Toth A, Martini E, *et al.* Implementation of meiosis prophase I programme requires a conserved retinoid-independent stabilizer of meiotic transcripts. *Nat Commun* 2016; **7**:10324.
59. Soh YQS, Mikedis MM, Kojima M, Godfrey AK, de Rooij DG, Page DC. Meioc maintains an extended meiotic prophase I in mice. *PLoS Genet* 2017; **13**:e1006704.

Downloaded from academic.oup.com/biolreprod/advance-article/doi/10.1093/biolre/ioag148/8738469 by University of California, Davis - Library user on 24 August 2026

60. Wojtas MN, Pandey RR, Mendel M, Homolka D, Sachidanandam R, Pillai RS. Regulation of m(6)a transcripts by the 3′–>5′ RNA helicase YTHDC2 is essential for a successful meiotic program in the mammalian germline. *Mol Cell* 2017; **68**:e312.
61. Bailey AS, Batista PJ, Gold RS, Chen YG, de Rooij DG, Chang HY, Fuller MT. The conserved RNA helicase YTHDC2 regulates the transition from proliferation to differentiation in the germline. *eLife* 2017; **6**:e26116.
62. Jain D, Puno MR, Meydan C, Lailler N, Mason CE, Lima CD, Anderson KV, Keeney S. Ketu mutant mice uncover an essential meiotic function for the ancient RNA helicase YTHDC2. *elife* 2018; **7**:e30919.
63. Pfaltzgraff NG, Liu B, de Rooij DG, Page DC, Mikedis MM. Destabilization of mRNAs enhances competence to initiate meiosis in mouse spermatogenic cells. *Development* 2024; **151**:dev202740.
64. Zhang L, Wang J, Tang Z, Lin Z, Su R, Hu N, Tang Y, Ge G, Fan J, Tong MH, Xue Y, Zhou Y, *et al.* The nuclear exosome cofactor MTR4 shapes the transcriptome for meiotic initiation. *Nat Commun* 2025; **16**:2605.
65. Zhong D, Chen M, Zhang L, Chen H, Shi D, Liu Q, Li H. Aberrant regulation of RNA methylation during spermatogenesis. *Reprod Domest Anim* 2021; **56**:3–11.
66. Ma Q, Gui Y, Ma X, Zhang B, Xiong W, Yang S, Cao C, Mo S, Shu G, Ye J, Liu K, Wang X, *et al.* N6-methyladenosine writer METTL16-mediated alternative splicing and translation control are essential for murine spermatogenesis. *Genome Biol* 2024; **25**:193.
67. Lin Z, Hsu PJ, Xing X, Fang J, Lu Z, Zou Q, Zhang K-J, Zhang X, Zhou Y, Zhang T, Zhang Y, Song W, *et al.* Mettl3−/Mettl14-mediated mRNA N6-methyladenosine modulates murine spermatogenesis. *Cell Res* 2017; **27**:1216–1230.
68. Zhang X, Gunewardena S, Wang N. Nutrient restriction synergizes with retinoic acid to induce mammalian meiotic initiation in vitro. *Nat Commun* 2021; **12**:1758.
69. Zhang X, Liu Y, Sosa F, Gunewardena S, Crawford PA, Zielen AC, Orwig KE, Wang N. Transcriptional metabolic reprogramming implements meiotic fate decision in mouse testicular germ cells. *Cell Rep* 2023; **42**:112749.
70. Monesi V. Ribonucleic acid synthesis during mitosis and meiosis in the mouse testis. *J Cell Biol* 1964; **22**:521–532.
71. Kierszenbaum AL, Tres LL. Nucleolar and perichromosomal RNA synthesis during meiotic prophase in the mouse testis. *J Cell Biol* 1974; **60**:39–53.
72. Ernst C, Eling N, Martinez-Jimenez CP, Marioni JC, Odom DT. Staged developmental mapping and X chromosome transcriptional dynamics during mouse spermatogenesis. *Nat Commun* 2019; **10**:1251.
73. Bellutti L, Chan Sock Peng E, Cluzet V, Guerquin MJ, Rolland A, Messiaen S, Llano E, Dereli I, Martini E, Toth A, Pendas AM, Chalmel F, *et al.* Genome-wide transcriptional silencing and mRNA stabilization allow the coordinated expression of the meiotic program in mice. *Nucleic Acids Res* 2025; **53**: gkaf146.
74. Hunter N. Meiotic recombination: the essence of heredity. *Cold Spring Harb Perspect Biol* 2015; **7**:a016618.
75. Baudat F, Buard J, Grey C, Fledel-Alon A, Ober C, Przeworski M, Coop G, de Massy B. PRDM9 is a major determinant of meiotic recombination hotspots in humans and mice. *Science* 2010; **327**: 836–840.
76. Myers S, Bowden R, Tumian A, Bontrop RE, Freeman C, MacFie TS, McVean G, Donnelly P. Drive against hotspot motifs in primates implicates the PRDM9 gene in meiotic recombination. *Science* 2010; **327**:876–879.
77. Parvanov ED, Petkov PM, Paigen K. Prdm9 controls activation of mammalian recombination hotspots. *Science* 2010; **327**:835.
78. Eram MS, Bustos SP, Lima-Fernandes E, Siarheyeva A, Senisterra G, Hajian T, Chau I, Duan S, Wu H, Dombrovski L, Schapira M, Arrowsmith CH, *et al.* Trimethylation of histone H3 lysine 36 by human methyltransferase PRDM9 protein. *J Biol Chem* 2014; **289**:12177–12188.
79. Wu H, Mathioudakis N, Diagouraga B, Dong A, Dombrovski L, Baudat F, Cusack S, de Massy B, Kadlec J. Molecular basis for the regulation of the H3K4 methyltransferase activity of PRDM9. *Cell Rep* 2013; **5**:13–20.
80. Grey C, Clément JAJ, Buard J, Leblanc B, Gut I, Gut M, Duret L, De Massy B. In vivo binding of PRDM9 reveals interactions with noncanonical genomic sites. *Genome Res* 2017; **27**:580–590.
81. Spruce C, Dlamini S, Ananda G, Bronkema N, Tian H, Paigen K, Carter GW, Baker CL. HELLS and PRDM9 form a pioneer complex to open chromatin at meiotic recombination hot spots. *Genes Dev* 2020; **34**:398–412.
82. Davies B, Hatton E, Altemose N, Hussin JG, Pratto F, Zhang G, Hinch AG, Moralli D, Biggs D, Diaz R, Preece C, Li R, *et al.* Re-engineering the zinc fingers of PRDM9 reverses hybrid sterility in mice. *Nature* 2016; **530**:171–176.
83. Imai Y, Biot M, Clément JAJ, Teragaki M, Urbach S, Robert T, Baudat F, Grey C, de Massy B. PRDM9 activity depends on HELLS and promotes local 5-hydroxymethylcytosine enrichment. *eLife* 2020; **9**:e57117.
84. Chen Y, Lyu R, Rong B, Zheng Y, Lin Z, Dai R, Zhang X, Xie N, Wang S, Tang F, Lan F, Tong MH. Refined spatial temporal epigenomic profiling reveals intrinsic connection between PRDM9-mediated H3K4me3 and the fate of double-stranded breaks. *Cell Res* 2020; **30**:256–268.
85. Lichten M, de Massy B. The impressionistic landscape of meiotic recombination. *Cell* 2011; **147**:267–270.
86. Hoge C, de Manuel M, Mahgoub M, Okami N, Fuller Z, Banerjee S, Baker Z, McNulty M, Andolfatto P, Macfarlan TS, Schumer M, Tzika AC, *et al.* Patterns of recombination in snakes reveal a tug-of-war between PRDM9 and promoter-like features. *Science* 2024; **383**:eadj7026.
87. Keeney S. Mechanism and control of meiotic recombination initiation. *Curr Top Dev Biol* 2001; **52**:1–53.
88. Grey C, de Massy B. Chromosome Organization in Early Meiotic Prophase. *Front Cell Dev Biol* 2021; **9**:688878.
89. Biot M, Toth A, Brun C, Guichard L, de Massy B, Grey C. Principles of chromosome organization for meiotic recombination. *Mol Cell* 2024; **84**:1826–1841.e1825.
90. Garcia V, Gray S, Allison RM, Cooper TJ, Neale MJ. Tel1(ATM)-mediated interference suppresses clustered meiotic double-strand-break formation. *Nature* 2015; **520**:114–118.
91. Lange J, Pan J, Cole F, Thelen MP, Jasin M, Keeney S. ATM controls meiotic double-strand-break formation. *Nature* 2011; **479**:237–240.
92. Cooper TJ, Wardell K, Garcia V, Neale MJ. Homeostatic regulation of meiotic DSB formation by ATM/ATR. *Exp Cell Res* 2014; **329**:124–131.
93. Dereli I, Stanzione M, Olmeda F, Papanikos F, Baumann M, Demir S, Carofiglio F, Lange J, De Massy B, Baarends WM, Turner J, Rulands S, *et al.* Four-pronged negative feedback of DSB machinery in meiotic DNA-break control in mice. *Nucleic Acids Res* 2021; **49**:2609–2628.
94. Lukaszewicz A, Lange J, Keeney S, Jasin M. De novo deletions and duplications at recombination hotspots in mouse germlines. *Cell* 2021; **184**:5970–5984.e5918.
95. Nitahara K, Kawamura A, Kitamura Y, Kato K, Namekawa SH, Nishiyama M. Chromatin remodeler CHD8 is required for spermatogonial proliferation and early meiotic progression. *Nucleic Acids Res* 2024; **52**:2995–3010.
96. Xu J, Gao J, Liu J, Huang X, Zhang H, Ma A, Ye J, Zhang X, Li Y, Yang G, Yin H, Khan R, *et al.* ZFP541 maintains the repression of pre-pachytene transcriptional programs and promotes male meiosis progression. *Cell Rep* 2022; **38**:110540.
97. Naro C, Jolly A, Di Persio S, Bielli P, Setterblad N, Alberdi AJ, Vicini E, Geremia R, De la Grange P, Sette C. An orchestrated intron retention program in meiosis controls timely usage of transcripts during germ cell differentiation. *Dev Cell* 2017; **41**:e84.

Downloaded from academic.oup.com/biolreprod/advance-article/doi/10.1093/biolre/ioag148/8738469 by University of California, Davis - Library user on 24 August 2026

98. Huang T, Yuan S, Gao L, Li M, Yu X, Zhan J, Yin Y, Liu C, Zhang C, Lu G, Li W, Liu J, *et al.* The histone modification reader ZCWPW1 links histone methylation to PRDM9-induced double-strand break repair. *eLife* 2020; **9**:e53459.
99. Mahgoub M, Paiano J, Bruno M, Wu W, Pathuri S, Zhang X, Ralls S, Cheng X, Nussenzweig A, Macfarlan TS. Dual histone methyl reader ZCWPW1 facilitates repair of meiotic double strand breaks in male mice. *eLife* 2020; **9**:e53360.
100. Wells D, Bitoun E, Moralli D, Zhang G, Hinch A, Jankowska J, Donnelly P, Green C, Myers SR. ZCWPW1 is recruited to recombination hotspots by PRDM9 and is essential for meiotic double strand break repair. *eLife* 2020; **9**:e53392.
101. Ruan T, Ma J, Shen G, Wang X, Yang Y, Zhuo L, Jiang C, Zhao G, Tian Y, Zhao S, Zhou R, Liu M, *et al.* A novel dual histone mark reader ZCWPW2 regulates meiotic recombination through lactylation and transcriptional regulation in humans and mice. *Nucleic Acids Res* 2026; **54**:gkag049.
102. Zakharyevich K, Tang S, Ma Y, Hunter N. Delineation of joint molecule resolution pathways in meiosis identifies a crossover-specific resolvase. *Cell* 2012; **149**:334–347.
103. Toledo M, Sun X, Brieño-Enríquez MA, Raghavan V, Gray S, Pea J, Milano CR, Venkatesh A, Patel L, Borst PL, Alani E, Cohen PE. A mutation in the endonuclease domain of mouse MLH3 reveals novel roles for mutlγ during crossover formation in meiotic prophase I. *PLoS Genet* 2019; **15**:e1008177.
104. Soumillon M, Necsulea A, Weier M, Brawand D, Zhang X, Gu H, Barthès P, Kokkinaki M, Nef S, Gnirke A, Dym M, de Massy B, *et al.* Cellular source and mechanisms of high transcriptome complexity in the mammalian testis. *Cell Rep* 2013; **3**:2179–2190.
105. Green CD, Ma Q, Manske GL, Shami AN, Zheng X, Marini S, Moritz L, Sultan C, Gurczynski SJ, Moore BB, Tallquist MD, Li JZ, *et al.* A comprehensive roadmap of murine spermatogenesis defined by single-cell RNA-Seq. *Dev Cell* 2018; **46**:e610.
106. Chen Y, Zheng Y, Gao Y, Lin Z, Yang S, Wang T, Wang Q, Xie N, Hua R, Liu M, Sha J, Griswold MD, *et al.* Single-cell RNA-seq uncovers dynamic processes and critical regulators in mouse spermatogenesis. *Cell Res* 2018; **28**:879–896.
107. Kleene KC. Connecting cis-elements and trans-factors with mechanisms of developmental regulation of mRNA translation in meiotic and haploid mammalian spermatogenic cells. *Reproduction* 2013; **146**:R1–R19.
108. Maezawa S, Hasegawa K, Yukawa M, Kubo N, Sakashita A, Alavattam KG, Sin HS, Kartashov AV, Sasaki H, Barski A, Namekawa SH. Polycomb protein SCML2 facilitates H3K27me3 to establish bivalent domains in the male germline. *Proc Natl Acad Sci U S A* 2018; **115**:4957–4962.
109. Jung M, Wells D, Rusch J, Ahmad S, Marchini J, Myers SR, Conrad DF. Unified single-cell analysis of testis gene regulation and pathology in five mouse strains. *Elife* 2019; **8**:e43966.
110. Wang Y, Wang H, Zhang Y, Du Z, Si W, Fan S, Qin D, Wang M, Duan Y, Li L, Jiao Y, Li Y, *et al.* Reprogramming of meiotic chromatin architecture during spermatogenesis. *Mol Cell* 2019; **73**:e546.
111. Bolcun-Filas E, Bannister LA, Barash A, Schimenti KJ, Hartford SA, Eppig JJ, Handel MA, Shen L, Schimenti JC. A-MYB (MYBL1) transcription factor is a master regulator of male meiosis. *Development* 2011; **138**:3319–3330.
112. Li XZ, Roy CK, Dong X, Bolcun-Filas E, Wang J, Han BW, Xu J, Moore MJ, Schimenti JC, Weng Z, Zamore PD. An ancient transcription factor initiates the burst of piRNA production during early meiosis in mouse testes. *Mol Cell* 2013; **50**:67–81.
113. Sakashita A, Maezawa S, Takahashi K, Alavattam KG, Yukawa M, Hu YC, Kojima S, Parrish NF, Barski A, Pavlicev M, Namekawa SH. Endogenous retroviruses drive species-specific germline transcriptomes in mammals. *Nat Struct Mol Biol* 2020; **27**:967–977.
114. Matzuk MM, McKeown MR, Filippakopoulos P, Li Q, Ma L, Agno JE, Lemieux ME, Picaud S, Yu RN, Qi J, Knapp S, Bradner JE. Small-molecule inhibition of BRDT for male contraception. *Cell* 2012; **150**:673–684.
115. Gaucher J, Boussouar F, Montellier E, Curtet S, Buchou T, Bertrand S, Hery P, Jounier S, Depaux A, Vitte AL, Guardiola P, Pernet K, *et al.* Bromodomain-dependent stage-specific male genome programming by Brdt. *EMBO J* 2012; **31**:3809–3820.
116. Her YR, Wang L, Chepelev I, Manterola M, Berkovits B, Cui K, Zhao K, Wolgemuth DJ. Genome-wide chromatin occupancy of BRDT and gene expression analysis suggest transcriptional partners and specific epigenetic landscapes that regulate gene expression during spermatogenesis. *Mol Reprod Dev* 2021; **88**:141–157.
117. Gan H, Cai T, Lin X, Wu Y, Wang X, Yang F, Han C. Integrative proteomic and transcriptomic analyses reveal multiple post-transcriptional regulatory mechanisms of mouse spermatogenesis. *Mol Cell Proteomics* 2013; **12**:1144–1157.
118. Yu T, Biasini A, Cecchini K, Saflund M, Mou H, Arif A, Eghbali A, de Rooij DG, Weng Z, Zamore PD, Ozata DM. A-MYB/TCFL5 regulatory architecture ensures the production of pachytene piRNAs in placental mammals. *RNA* 2022; **29**:30–43.
119. Berkovits BD, Wolgemuth DJ. The role of the double bromodomain-containing BET genes during mammalian spermatogenesis. *Curr Top Dev Biol* 2013; **102**:293–326.
120. Alexander AK, Rice EJ, Lujic J, Simon LE, Tanis S, Barshad G, Zhu L, Lama J, Cohen PE, Danko CG. A-MYB and BRDT-dependent RNA polymerase II pause release orchestrates transcriptional regulation in mammalian meiosis. *Nat Commun* 2023; **14**:1753.
121. Ozata DM, Gainetdinov I, Zoch A, O'Carroll D, Zamore PD. PIWI-interacting RNAs: small RNAs with big functions. *Nat Rev Genet* 2019; **20**:89–108.
122. Fu Q, Wang PJ. Mammalian piRNAs: biogenesis, function, and mysteries. *Spermatogenesis* 2014; **4**:e27889.
123. Sun YH, Lee B, Li XZ. The birth of piRNAs: how mammalian piRNAs are produced, originated, and evolved. *Mamm Genome* 2022; **33**:293–311.
124. Haase AD, Ketting RF, Lai EC, van Rij RP, Siomi M, Svoboda P, van Wolfswinkel JC, Wu P-H. PIWI-interacting RNAs: who, what, when, where, why, and how. *EMBO J* 2024; **43**:5335–5339.
125. Xu MM, Li XZ. Enigmatic pachytene PIWI-interacting RNAs. *Genome Biol Evol* 2024; **16**:evae162.
126. Davis MP, Carrieri C, Saini HK, van Dongen S, Leonardi T, Bussotti G, Monahan JM, Auchynnikava T, Bitetti A, Rappsilber J, Allshire RC, Shkumatava A, *et al.* Transposon-driven transcription is a conserved feature of vertebrate spermatogenesis and transcript evolution. *EMBO Rep* 2017; **18**:1231–1247.
127. Imbeault M, Helleboid PY, Trono D. KRAB zinc-finger proteins contribute to the evolution of gene regulatory networks. *Nature* 2017; **543**:550–554.
128. Otsuka K, Sakashita A, Maezawa S, Schultz RM, Namekawa SH. KRAB zinc-finger proteins regulate endogenous retroviruses to sculpt germline transcriptomes and genome evolution. *Genome Res* 2025; **35**:417–431.
129. Ueda J, Harada A, Urahama T, Machida S, Maehara K, Hada M, Makino Y, Nogami J, Horikoshi N, Osakabe A, Taguchi H, Tanaka H, *et al.* Testis-specific histone variant H3t gene is essential for entry into spermatogenesis. *Cell Rep* 2017; **18**:593–600.
130. Yeh YH, Hu M, Otsuka K, Alger BM, Nene SS, Wang H, Maezawa S, Namekawa SH. DAXX directs dual modes of H3.4-to-H3.3 histone replacement in the male germline. *Genes Dev* 2026; **40**:796–804.
131. Lesch BJ, Dokshin GA, Young RA, McCarrey JR, Page DC. A set of genes critical to development is epigenetically poised in mouse germ cells from fetal stages through completion of meiosis. *Proc Natl Acad Sci U S A* 2013; **110**:16061–16066.

Downloaded from academic.oup.com/biolreprod/advance-article/doi/10.1093/biolre/ioag148/8738469 by University of California, Davis - Library user on 24 August 2026

132. Lesch BJ, Silber SJ, McCarrey JR, Page DC. Parallel evolution of male germline epigenetic poising and somatic development in animals. *Nat Genet* 2016; **48**:888–894.
133. Shao Q, Zhang Y, Liu Y, Shang Y, Li S, Liu L, Wang G, Zhou X, Wang P, Gao J, Zhou J, Zhang L, *et al.* ATF7IP2, a meiosis-specific partner of SETDB1, is required for proper chromosome remodeling and crossover formation during spermatogenesis. *Cell Rep* 2023; **42**:112953.
134. Alavattam KG, Esparza JM, Hu M, Shimada R, Kohrs AR, Abe H, Munakata Y, Otsuka K, Yoshimura S, Kitamura Y, Yeh YH, Hu YC, *et al.* ATF7IP2/MCAF2 directs H3K9 methylation and meiotic gene regulation in the male germline. *Genes Dev* 2024; **38**:115–130.
135. Bocker MT, Fanourgakis G, Wetzel K, Komarov PA, Royo H, Rohmer A, Chun S, Liang CY, Kohler H, Chen T, Mao X, Labow MA, *et al.* The histone H3 lysine 36 demethylase KDM2A/FBXL11 controls Polycomb-mediated gene repression and germ cell development in male mice. *Nat Commun* 2025; **16**:6803.
136. Maezawa S, Yukawa M, Sakashita A, Barski A. Namekawa SH. Site-specific DNA demethylation during spermatogenesis presets the sites of nucleosome retention in mouse sperm. *eLife* 2025; 105926.1.
137. Esparza JM, Kumar RV, Hu M, Munakata Y, Jain S, Sakashita A, Maezawa S, Schultz RM, Namekawa SH. Paternal folate deficiency reveals meiosis as a metabolic sensing window in the male germline. *bioRxiv* 2026; 2026.04.22.720272.
138. Ikuyo A, Fuse N, Mori M, Hirayama A, Yamada Y, Nakamura T, Sagi T, Otsuka K, Namekawa SH, Soga T, Hayashi Y, Maezawa S. Folate-dependent one-carbon metabolism controls meiotic and post-meiotic epigenome remodeling in the male germline. *bioRxiv* 2026; 2026.04.23.720283.
139. Alavattam KG, Maezawa S, Sakashita A, Khoury H, Barski A, Kaplan N, Namekawa SH. Attenuated chromatin compartmentalization in meiosis and its maturation in sperm development. *Nat Struct Mol Biol* 2019; **26**:175–184.
140. Patel L, Kang R, Rosenberg SC, Qiu Y, Raviram R, Chee S, Hu R, Ren B, Cole F, Corbett KD. Dynamic reorganization of the genome shapes the recombination landscape in meiotic prophase. *Nat Struct Mol Biol* 2019; **26**:164–174.
141. Vara C, Paytuví-Gallart A, Cuartero Y, Le Dily F, Garcia F, Salvà-Castro J, Gómez HL, Julià E, Moutinho C, Aiese Cigliano R, Sanseverino W, Fornas O, *et al.* Three-dimensional genomic structure and cohesin occupancy correlate with transcriptional activity during spermatogenesis. *Cell Rep* 2019; **28**:352–367.e359.
142. Luo Z, Wang X, Jiang H, Wang R, Chen J, Chen Y, Xu Q, Cao J, Gong X, Wu J, Yang Y, Li W, *et al.* Reorganized 3D genome structures support transcriptional regulation in mouse spermatogenesis. *iScience* 2020; **23**:101034.
143. Zuo W, Chen G, Gao Z, Li S, Chen Y, Huang C, Chen J, Chen Z, Lei M, Bian Q. Stage-resolved hi-C analyses reveal meiotic chromosome organizational features influencing homolog alignment. *Nat Commun* 2021; **12**:5827.
144. He J, Yan A, Chen B, Huang J, Kee K. 3D genome remodeling and homologous pairing during meiotic prophase of mouse oogenesis and spermatogenesis. *Dev Cell* 2023; **58**:3009–3027.e3006.
145. Cheng G, Li X, Brick K, Alleva B, Huang M, Lam KWG, Pratto F, Camerini-Otero RD. High-resolution chromatin mapping reveals that CTCF anchors meiotic loops to the chromosome axis. *Nat Commun* 2026; **17**:7550.
146. Broering TJ, Alavattam KG, Sadreyev RI, Ichijima Y, Kato Y, Hasegawa K, Camerini-Otero RD, Lee JT, Andreassen PR, Namekawa SH. BRCA1 establishes DNA damage signaling and pericentric heterochromatin of the X chromosome in male meiosis. *J Cell Biol* 2014; **205**:663–675.
147. Perera D, Perez-Hidalgo L, Moens PB, Reini K, Lakin N, Syvaoja JE, San-Segundo PA, Freire R. TopBP1 and ATR colocalization at meiotic chromosomes: role of TopBP1/Cut5 in the meiotic recombination checkpoint. *Mol Biol Cell* 2004; **15**:1568–1579.
148. Royo H, Prosser H, Ruzankina Y, Mahadevaiah SK, Cloutier JM, Baumann M, Fukuda T, Hoog C, Toth A, de Rooij DG, Bradley A, Brown EJ, *et al.* ATR acts stage specifically to regulate multiple aspects of mammalian meiotic silencing. *Genes Dev* 2013; **27**:1484–1494.
149. ElInati E, Russell HR, Ojarikre OA, Sangrithi M, Hirota T, de Rooij DG, McKinnon PJ, Turner JMA. DNA damage response protein TOPBP1 regulates X chromosome silencing in the mammalian germ line. *Proc Natl Acad Sci U S A* 2017; **114**:12536–12541.
150. Ichijima Y, Ichijima M, Lou Z, Nussenzweig A, Camerini-Otero RD, Chen J, Andreassen PR, Namekawa SH. MDC1 directs chromosome-wide silencing of the sex chromosomes in male germ cells. *Genes Dev* 2011; **25**:959–971.
151. Solari AJ. The behavior of the XY pair in mammals. *Int Rev Cytol* 1974; **38**:273–317.
152. McKee BD, Handel MA. Sex chromosomes, recombination, and chromatin conformation. *Chromosoma* 1993; **102**:71–80.
153. Hoyer-Fender S. Molecular aspects of XY body formation. *Cytogenet Genome Res* 2003; **103**:245–255.
154. Turner JM. Meiotic sex chromosome inactivation. *Development* 2007; **134**:1823–1831.
155. Handel MA. The XY body: a specialized meiotic chromatin domain. *Exp Cell Res* 2004; **296**:57–63.
156. Yan W, McCarrey JR. Sex chromosome inactivation in the male. *Epigenetics* 2009; **4**:452–456.
157. Ichijima Y, Sin HS, Namekawa SH. Sex chromosome inactivation in germ cells: emerging roles of DNA damage response pathways. *Cell Mol Life Sci* 2012; **69**:2559–2572.
158. Turner JM. Meiotic silencing in mammals. *Annu Rev Genet* 2015; **49**:395–412.
159. Abe H, Yeh YH, Munakata Y, Ishiguro KI, Andreassen PR, Namekawa SH. Active DNA damage response signaling initiates and maintains meiotic sex chromosome inactivation. *Nat Commun* 2022; **13**:7212.
160. Hirota T, Blakeley P, Sangrithi MN, Mahadevaiah SK, Encheva V, Snijders AP, ElInati E, Ojarikre OA, de Rooij DG, Niakan KK, Turner JMA. SETDB1 links the meiotic DNA damage response to sex chromosome silencing in mice. *Dev Cell* 2018; **47**:645–659.e6.
161. Lin Z, Li D, Zheng J, Yao C, Liu D, Zhang H, Feng H, Chen C, Li P, Zhang Y, Jiang B, Hu Z, *et al.* The male pachynema-specific protein MAPS drives phase separation in vitro and regulates sex body formation and chromatin behaviors in vivo. *Cell Rep* 2024; **43**:113651.
162. Gai X, Xin D, Wu D, Wang X, Chen L, Wang Y, Ma K, Li Q, Li P, Yu X. Pre-ribosomal RNA reorganizes DNA damage repair factors in nucleus during meiotic prophase and DNA damage response. *Cell Res* 2022; **32**:254–268.
163. van der Heijden GW, Derijck AA, Pósfai E, Giele M, Pelczar P, Ramos L, Wansink DG, van der Vlag J, Peters AH, de Boer P. Chromosome-wide nucleosome replacement and H3.3 incorporation during mammalian meiotic sex chromosome inactivation. *Nat Genet* 2007; **39**:251–258.
164. Horisawa-Takada Y, Kodera C, Takemoto K, Sakashita A, Horisawa K, Maeda R, Shimada R, Usuki S, Fujimura S, Tani N, Matsuura K, Akiyama T, *et al.* Meiosis-specific ZFP541 repressor complex promotes developmental progression of meiotic prophase towards completion during mouse spermatogenesis. *Nat Commun* 2021; **12**:3184.

Downloaded from academic.oup.com/biolreprod/advance-article/doi/10.1093/biolre/ioag148/8738469 by University of California, Davis - Library user on 24 August 2026

© The Author(s) 2026. Published by Oxford University Press on behalf of the Society for the Study of Reproduction. All rights reserved. For commercial re-use, please contact reprints@oup.com for reprints and translation rights for reprints. All other permissions can be obtained through our RightsLink service via the Permissions link on the article page on our site—for further information please contact journals.permissions@oup.com.
Biology of Reproduction, 2026, 1–15
https://doi.org/10.1093/biolre/ioag148
Review

Chapter 1: **ATF7IP2/MCAF2 directs H3K9 methylation and meiotic gene regulation in the male germline**[2]

[2] Alavattam KG, Esparza JM, Hu M, Shimada R, Kohrs AR, Abe H, Munakata Y, Otsuka K, Yoshimura S, Kitamura Y, Yeh YH, Hu YC, Kim J, Andreassen PR, Ishiguro KI, Namekawa SH. ATF7IP2/MCAF2 directs H3K9 methylation and meiotic gene regulation in the male germline. Genes Dev. 2024 Mar 22;38(3-4):115-130. doi: 10.1101/gad.351569.124. PMID: 38383062; PMCID: PMC10982687.

My contributions

I began this project during my first year as a graduate student. I learned crucial skills and techniques that I used in my dissertation project. In this 2024 publication, I performed several of the careful image quantification (Fig. 3E-F, 4A-E, Supplemental Fig. S4, Supplemental Fig. S6, Supplemental Fig. S7C-G, Supplemental Fig. S8) that led to the refinement of the model proposed (Fig. 4I). I supported the optimization and first FACS-based collection of ATF7IP2/MCAF2-knockout spermatocytes, a task that was unexpectedly difficult and complicated, but fruitful. With these isolated cell populations, we performed ATF7IP2/MCAF2 CUT&Tag to identify where our protein of interests binds throughout the genome. I performed several of the downstream CUT&Tag analyses, including Fig. 6A, C-D. I also learned how to analyze RNA-seq data for the first time, which led to my contribution of Fig. 7A and Supplemental Fig. S12.

Revisions for this manuscript were plentiful, but they greatly improved the logic and overall strength of the paper. Most importantly, I experienced the entire process of assembling, writing, figure-making, submitting, and revising a large scientific paper. This first-hand experience proved to be invaluable for writing my self-first author paper (Chapter 2).

Abstract

H3K9 trimethylation (H3K9me3) plays emerging roles in gene regulation, beyond its accumulation on pericentric constitutive heterochromatin. It remains a mystery why and how H3K9me3 undergoes dynamic regulation in male meiosis. Here, we identify a novel, critical regulator of H3K9 methylation and spermatogenic heterochromatin organization: the germline-specific protein ATF7IP2 (MCAF2). We show that in male meiosis, ATF7IP2 amasses on autosomal and X-pericentric heterochromatin, spreads through the entirety of the sex chromosomes, and accumulates on thousands of autosomal promoters and retrotransposon loci. On the sex chromosomes, which undergo meiotic sex chromosome inactivation (MSCI), the DNA damage response pathway recruits ATF7IP2 to X-pericentric heterochromatin, where it facilitates the recruitment of SETDB1, a histone methyltransferase that catalyzes H3K9me3. In the absence of ATF7IP2, male germ cells are arrested in meiotic prophase I. Analyses of ATF7IP2-deficient meiosis reveal the protein's essential roles in the maintenance of MSCI, suppression of retrotransposons, and global up-regulation of autosomal genes. We propose that ATF7IP2 is a downstream effector of the DDR pathway in meiosis that coordinates the organization of heterochromatin and gene regulation through the spatial regulation of SETDB1-mediated H3K9me3 deposition.

ATF7IP2/MCAF2 directs H3K9 methylation and meiotic gene regulation in the male germline

Kris G. Alavattam,[1,2,8] Jasmine M. Esparza,[3,8] Mengwen Hu,[1,3,8] Ryuki Shimada,[4,8] Anna R. Kohrs,[1] Hironori Abe,[1,3,4] Yasuhisa Munakata,[1,3] Kai Otsuka,[3] Saori Yoshimura,[4] Yuka Kitamura,[3] Yu-Han Yeh,[1,3] Yueh-Chiang Hu,[1,5] Jihye Kim,[6] Paul R. Andreassen,[5,7] Kei-ichiro Ishiguro,[4] and Satoshi H. Namekawa[1,3,5]

[1]Reproductive Sciences Center, Division of Developmental Biology, Cincinnati Children's Hospital Medical Center, Cincinnati, Ohio 45229, USA; [2]Basic Sciences Division, Fred Hutchinson Cancer Center, Seattle, Washington 98109, USA; [3]Department of Microbiology and Molecular Genetics, University of California, Davis, Davis, California 95616, USA; [4]Department of Chromosome Biology, Institute of Molecular Embryology and Genetics (IMEG), Kumamoto University, Kumamoto 860-0811, Japan; [5]Department of Pediatrics, University of Cincinnati College of Medicine, Cincinnati, Ohio 49229, USA; [6]Laboratory of Chromosome Dynamics, Institute of Molecular and Cellular Biosciences, University of Tokyo, Tokyo 113-0032, Japan; [7]Division of Experimental Hematology and Cancer Biology, Cincinnati Children's Hospital Medical Center, Cincinnati, Ohio 45229, USA

H3K9 trimethylation (H3K9me3) plays emerging roles in gene regulation, beyond its accumulation on pericentric constitutive heterochromatin. It remains a mystery why and how H3K9me3 undergoes dynamic regulation in male meiosis. Here, we identify a novel, critical regulator of H3K9 methylation and spermatogenic heterochromatin organization: the germline-specific protein ATF7IP2 (MCAF2). We show that in male meiosis, ATF7IP2 amasses on autosomal and X-pericentric heterochromatin, spreads through the entirety of the sex chromosomes, and accumulates on thousands of autosomal promoters and retrotransposon loci. On the sex chromosomes, which undergo meiotic sex chromosome inactivation (MSCI), the DNA damage response pathway recruits ATF7IP2 to X-pericentric heterochromatin, where it facilitates the recruitment of SETDB1, a histone methyltransferase that catalyzes H3K9me3. In the absence of ATF7IP2, male germ cells are arrested in meiotic prophase I. Analyses of ATF7IP2-deficient meiosis reveal the protein's essential roles in the maintenance of MSCI, suppression of retrotransposons, and global up-regulation of autosomal genes. We propose that ATF7IP2 is a downstream effector of the DDR pathway in meiosis that coordinates the organization of heterochromatin and gene regulation through the spatial regulation of SETDB1-mediated H3K9me3 deposition.

[*Keywords*: meiosis; constitutive heterochromatin; H3K9me3; meiotic sex chromosome inactivation; gene activation; ATF7IP2/MCAF2]

Supplemental material is available for this article.

Received September 30, 2023; revised version accepted January 31, 2024.

Constitutive heterochromatin forms mainly at pericentromeres and is maintained to ensure genome stability. A hallmark of constitutive heterochromatin is histone H3K9 trimethylation (H3K9me3) (Saksouk et al. 2015). It was initially considered a static histone mark due to its stable accumulation on tandem satellite repeats at pericentric heterochromatin (PCH); however, a growing literature reveals that H3K9me3—particularly H3K9me3 mediated by the histone methyltransferase SETDB1—has broad, dynamic roles in suppressing developmental regulator genes and endogenous retroviruses in embryonic stem cells (Bilodeau et al. 2009; Matsui et al. 2010), thereby defining cellular identities in somatic development (Becker et al. 2016; Nicetto and Zaret 2019).

An essential factor in the germline, SETDB1 is required for gene regulation, the suppression of transposable elements (TEs), and the control of meiotic chromosome behavior (Liu et al. 2014; Hirota et al. 2018; Mochizuki et al. 2018; Cheng et al. 2021). The redundant H3K9me3 methyltransferases SUV39H1 and SUV39H2 are also required for male meiosis (Peters et al. 2001). Thus, the

[8]**These authors contributed equally to this work.**
Corresponding authors: snamekawa@ucdavis.edu, ishiguro@kumamoto-u.ac.jp
Article published online ahead of print. Article and publication date are online at http://www.genesdev.org/cgi/doi/10.1101/gad.351569.124.

© 2024 Alavattam et al. This article is distributed exclusively by Cold Spring Harbor Laboratory Press for the first six months after the full-issue publication date (see http://genesdev.cshlp.org/site/misc/terms.xhtml). After six months, it is available under a Creative Commons License (Attribution-NonCommercial 4.0 International), as described at http://creativecommons.org/licenses/by-nc/4.0/.

regulation of H3K9me3 is critical in male meiosis, where constitutive heterochromatin is remodeled to undergo synapsis and meiotic recombination on homologous chromosomes (Scherthan et al. 2014; Berrios 2017; Maezawa et al. 2018a). However, it remains a mystery why and how H3K9me3 undergoes dynamic regulation in male meiosis.

In addition to its roles at PCH, H3K9me3 is subject to dynamic temporal and spatial regulation on the male sex chromosomes as they undergo meiotic sex chromosome inactivation (MSCI) (Turner 2015; Alavattam et al. 2022). An essential event in the male germline, MSCI is initiated and maintained by a DNA damage response (DDR) pathway (Ichijima et al. 2011; Royo et al. 2013; Abe et al. 2022). Downstream from the DDR, SETDB1 establishes H3K9me3 on the sex chromosome and regulates MSCI (Hirota et al. 2018). SETDB1 is expressed in a broad range of cells, but there is a major knowledge gap as to how SETDB1 and H3K9me3 function in meiosis.

Here, we identify activating transcription factor 7-interacting protein 2 (ATF7IP2), also known as MBD1-containing chromatin-associated factor 2 (MCAF2), as a novel, critical regulator of SETDB1's spatiotemporal activity, H3K9 methylation, and global spermatogenic gene regulation. We identified ATF7IP2 based on its gene expression in the germline. In the midst of our investigation, an IP-mass spectrometry analysis identified ATF7IP2 as a SETDB1-binding protein (Hirota et al. 2018), lending the factor further contextual significance. In mitotically cycling cells, its homolog, ATF7IP (MCAF1), regulates SETDB1 for H3K9me3 establishment and transcriptional silencing (Ichimura et al. 2005; Timms et al. 2016; Tsusaka et al. 2019, 2020). We show that ATF7IP2 is a counterpart to ATF7IP that is highly expressed in the germline and is essential in male meiosis, revealing roles for ATF7IP2 in MSCI, global meiotic gene regulation, and the fine-tuning of retrotransposon-derived loci such as endogenous retroviruses. By uncovering ATF7IP2's germline functions, our study clarifies the regulatory logic for dynamic H3K9me3 deposition—and thus heterochromatin—in the male germline.

Results

ATF7IP2 is highly expressed in male meiosis and accumulates on heterochromatin

To understand the meiosis-specific regulation of H3K9me3, we focused on *Atf7ip2* (*Mcaf2*), a gene that is highly expressed in male meiosis, as evidenced in RNA-seq data sets for germ cell development and spermatogenesis (Fig. 1A; Seisenberger et al. 2012; Hasegawa et al. 2015; Maezawa et al. 2018b). *Atf7ip2* expression is low in male germ cells until the stage of meiosis, at which point it is highly up-regulated in meiotic pachytene spermatocytes (Fig. 1A). On the other hand, its homolog, *Atf7ip* (*Mcaf1*), which functions in mitotically dividing/somatic cells (Ichimura et al. 2005; Timms et al. 2016), is highly expressed in primordial germ cells and spermatogonia but is down-regulated in pachytene spermatocytes. Among various tissues, *Atf7ip2* is highly expressed in testes (Supplemental Fig. S1A). Furthermore, mouse ATF7IP2 has high homology with human ATF7IP2 (Supplemental Fig. S1B), except for its long N-terminal amino acid tail, and ATF7IP2 is highly expressed in the meiotic spermatocytes of human testes (Supplemental Fig. S1C). These results raise the possibility that ATF7IP2 is an evolutionarily conserved counterpart to ATF7IP that is highly expressed in late stages of spermatogenesis.

To understand the regulatory mechanism for *Atf7ip2* expression, we examined the genomic distribution of MEIOSIN and STRA8, both transcription factors that heterodimerize to initiate meiosis-specific transcription (Kojima et al. 2019; Ishiguro et al. 2020). We observed MEIOSIN and STRA8 peaks at the *Atf7ip2* transcription start site (TSS) in preleptotene-enriched testes (the preleptotene stage is a liminal stage for germ cells transitioning from mitosis to meiotic prophase I) (Fig. 1B, which is a reanalysis of data from Ishiguro et al. 2020). These peaks coincide with the accumulation of RNA polymerase II (POLII) and cap analysis of gene expression (CAGE) signals in postnatal day 10.5 (P10.5) testes, which are enriched for preleptotene spermatocytes (Fig. 1B, which is a reanalysis of data from Li et al. 2013). In support of a role for MEIOSIN and STRA8 in *Atf7ip2* expression, *Atf7ip2* was down-regulated in *Stra8*$^{-/-}$ and *Meiosin*$^{-/-}$ testes at P21 (Fig. 1C). In mouse testes, the first wave of meiosis occurs semisynchronously, and *Atf7ip2* expression is at its highest in P18 testes, when late stages of meiotic prophase I spermatocytes first appear (Fig. 1C). Taken together, these results demonstrate that the expression of *Atf7ip2* is up-regulated by MEIOSIN and STRA8, occurring amid a broad range of meiotic transcription (Kojima et al. 2019; Ishiguro et al. 2020).

To better understand the potential function of ATF7IP2, we investigated ATF7IP2 protein localization during stages of mouse male meiosis by performing immunofluorescence microscopy with chromosome spreads (Fig. 1D,E). In the leptotene stage of meiotic prophase I, when meiotic chromosome axes begin to condense, ATF7IP2 localizes on DAPI-discernible heterochromatin. ATF7IP2 continues to localize on all DAPI-discernible PCH through the zygotene stage, when homologs undergo synapsis; the pachytene stage, when homologs have completed synapsis; and the diplotene stage, when homologs begin desynapsis (Fig. 1E). Meiotic nuclei were staged through observations of chromosome axes as identified by SYCP3 (Alavattam et al. 2016, 2018), a component of meiotic axes, and the presence of the testis-specific histone variant H1T, which appears in mid-pachytene nuclei and persists into haploid spermatids (Inselman et al. 2003). At the onset of the pachytene stage, the unsynapsed sex chromosomes undergo MSCI, and the most intense ATF7IP2 signals were observed on X-chromosome PCH (X-PCH) at that time (Fig. 1E,F). In the early and mid-pachytene stages, ATF7IP2 localizes primarily on X-PCH; from the late pachytene stage onward, ATF7IP2 gradually spreads across the entirety of the sex chromosome domain (also referred to as the "XY domain" or "XY chromatin"). Thus, ATF7IP2 exhibits two distinct

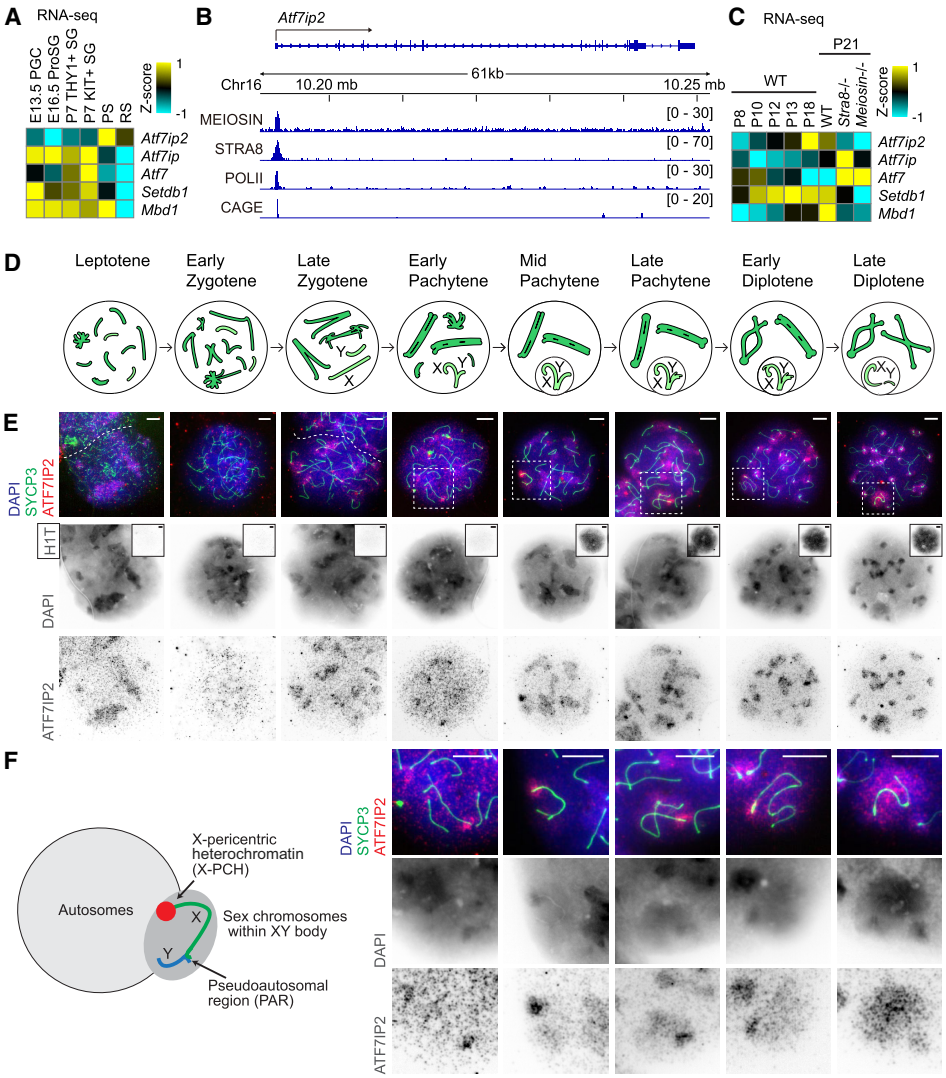


Figure 1. ATF7IP2 is highly expressed in male meiosis and accumulates on heterochromatin. (*A*,*C*) Heat maps showing bulk RNA-seq gene expression levels across a male germline time course for *Atf7ip2* and related genes. (PGC) Primordial germ cells, (ProSG) prospermatogonia, (SG) spermatogonia, (PS) pachytene spermatocytes, (RS) round spermatids. Original data for *A* are from Seisenberger et al. (2012), Hasegawa et al. (2015), and Maezawa et al. (2018b), and original data for *C* are from Ishiguro et al. (2020). (*B*) Track views for MEIOSIN (preleptotene-enriched testes), STRA8 (preleptotene-enriched testes), and RNA polymerase II (POLII; postnatal day 10.5 [P10.5] testes) ChIP-seq data and for CAGE (P10.5 testes). Numbers in brackets indicate ranges of normalized coverage. (*D*) Schematic of chromosome behavior in meiotic prophase I of male *Mus musculus*. (Darker green) Autosomes, (lighter green) sex chromosomes. (*E*) Meiotic chromosome spreads stained with DAPI and antibodies raised against ATF7IP2, SYCP3, and H1T; spreads represent stages of meiotic prophase I. (*Insets*) H1T immunostaining; H1T is a nuclear marker that appears in mid-pachytene nuclei and persists into haploid spermatids. SYCP3 is a marker of meiotic chromosome axes. Dashed squares are magnified in *F*. Scale bars, 5 µm. (*F*, *left*) Schematic of sex chromosome configuration in male meiosis. (*Right*) Magnified images of sex chromosomes from *E*. Scale bars, 5 µm.

localization patterns in meiotic prophase I: One is on the PCH of all chromosomes, and the other is intense accumulation on X-PCH that proceeds to spread through the entirety of the XY chromatin.

ATF7IP2 is required for male meiosis

To test the function of ATF7IP2, we performed CRISPR-mediated genome editing to generate *Atf7ip2* knockout mice. We targeted a guide RNA to a site within exon 4 (Fig. 2A), which encodes a portion of the SETDB1-binding domain (SETDB1-BD) that is conserved between ATF7IP2 and ATF7IP (Fig. 2B). We obtained three alleles with deletion lengths of 17, 31, and 169 bp. All caused *Atf7ip2* frameshift mutations, and all three homozygous *Atf7ip2* mutants displayed consistent and obvious testicular defects. For subsequent analyses, we selected the 17-bp deletion allele as a representative; hereafter, the homozygous 17-bp allele model is denoted as *Atf7ip2*$^{-/-}$. *Atf7ip2*$^{-/-}$ male mice were viable but infertile and had much smaller

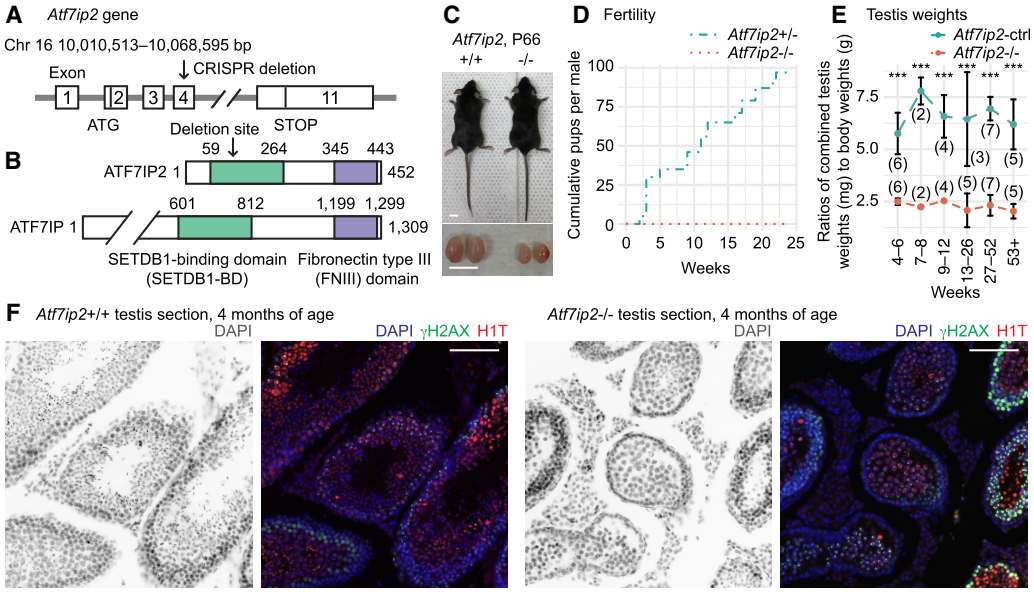


Figure 2. ATF7IP2 is required for male fertility. (*A*) Schematic of the mouse *Atf7ip2* gene and the location of the CRISPR-mediated deletion. (*B*) Schematic of mouse ATF7IP2 and ATF7IP proteins and their functional domains. (*C*) *Atf7ip2*$^{+/+}$ and *Atf7ip2*$^{-/-}$ males and their testes at postnatal day 66 (P66). Scale bars, 10 mm. (*D*) Cumulative numbers of pups sired by *Atf7ip2*$^{+/-}$ and *Atf7ip2*$^{-/-}$ males. (*E*) Testis weights for *Atf7ip2*$^{-/-}$ males and littermate controls (*Atf7ip2*-ctrl: *Atf7ip2*$^{+/+}$ and *Atf7ip2*$^{+/-}$). Numbers of independent mice analyzed are shown in parentheses. (***) $P < 0.001$, from pairwise *t*-tests adjusted with Benjamini–Hochberg post-hoc tests. Data are presented as mean ± SD. (*F*) Testis sections from *Atf7ip2*$^{+/+}$ and *Atf7ip2*$^{-/-}$ mice at 4 mo of age stained with DAPI and antibodies raised against ATF7IP2, γH2AX (a marker of the DNA damage response), and H1T (a marker of germ cells in mid-pachytene and subsequent stages). Scale bars, 100 μm.

testes compared with littermate controls (Fig. 2C–E). We confirmed the depletion of ATF7IP2 proteins in *Atf7ip2*$^{-/-}$ spermatocytes via immunofluorescence microscopy (Supplemental Fig. S2). Analyses of testicular tissue sections showed that *Atf7ip2*$^{-/-}$ testes were devoid of haploid spermatids, and seminiferous tubules were smaller than in control testes (Fig. 2F). However, *Atf7ip2*$^{-/-}$ spermatocytes reached the stage when H1T is enriched, the mid-pachytene stage, indicating that *Atf7ip2*$^{-/-}$ spermatocytes are arrested and eliminated in meiotic prophase I. Unlike *Atf7ip2*$^{-/-}$ males, *Atf7ip2*$^{-/-}$ female mice were fertile and, when crossed with *Atf7ip2*$^{+/-}$ males, gave birth at Mendelian ratios (Supplemental Fig. S3). These results suggest that the *Atf7ip2*$^{-/-}$ phenotype is caused by an essential, male-specific event in the germline that has become defective.

Meiotic phenotypes in male Atf7ip2$^{-/-}$ *mice*

To determine the function of ATF7IP2, we characterized the meiotic phenotype of *Atf7ip2*$^{-/-}$ male mice in detail. We performed immunostaining to analyze chromosome spreads from *Atf7ip2*$^{-/-}$ testes for a specific marker of the DDR: phosphorylated serine 139 of the histone variant H2AX (γH2AX). In the leptotene and zygotene stages, the DDR/checkpoint kinase ataxia telangiectasia mutated (ATM) triggers the formation of γH2AX domains throughout nuclei in response to programmed double-stranded breaks (DSBs; induced by the topoisomerase-related enzyme SPO11); with the completion of DNA repair and concomitant autosomal synapsis, γH2AX disappears from autosomes (Mahadevaiah et al. 2001; Bellani et al. 2005). In the latter steps of this process, ataxia telangiectasia and Rad3-related (ATR), another DDR/checkpoint kinase, mediates γH2AX formation on unsynapsed chromatin; in normal pachytene nuclei, this results in the confinement of γH2AX to the unsynapsed XY chromosomes, an essential event in the initiation of MSCI (Royo et al. 2013). Thus, γH2AX staining, together with SYCP3 staining, provides key insights into general meiotic phenotypes (Abe et al. 2018; Alavattam et al. 2018). In *Atf7ip2*$^{-/-}$ spermatocytes, pan-nuclear γH2AX formation occurs normally in the early/mid-zygotene stage (Fig. 3A), and relative populations of zygotene spermatocytes are comparable between *Atf7ip2*$^{-/-}$ testes and littermate controls (Fig. 3B). In the *Atf7ip2*$^{-/-}$ pachytene spermatocytes, γH2AX formation on the XY chromosomes takes place (Fig. 3A); however, we noted an increase in the relative population of early/mid-pachytene spermatocytes, whereas late pachytene and diplotene spermatocytes were rare and largely depleted from *Atf7ip2*$^{-/-}$ testes (Fig. 3B). These analyses suggest that ATF7IP2 has a critical function as spermatocytes transition from the pachytene to diplotene stages.

Following our established criteria for SYCP3- and γH2AX-based meiotic staging (Abe et al. 2018; Alavattam et al. 2018), we analyzed γH2AX staining patterns in more detail. In *Atf7ip2*$^{-/-}$ early/mid-pachytene spermatocytes, the removal of γH2AX from autosomes was disrupted in comparison with controls (Fig. 3C). In normal meiosis,

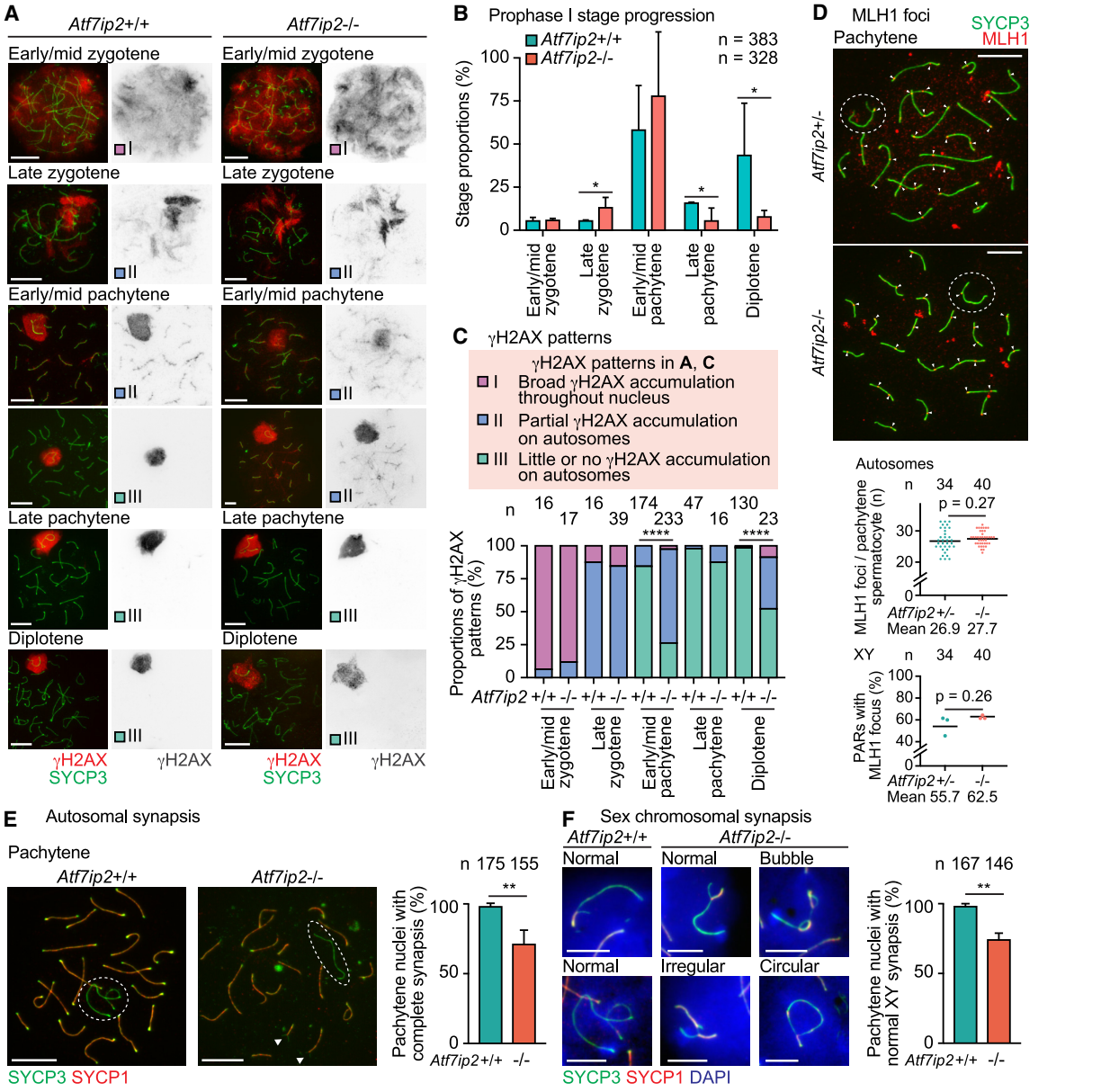


Figure 3. DDR and chromosome synapsis are mildly impaired in *Atf7ip2*$^{-/-}$ spermatocytes. (*A*) *Atf7ip2*$^{+/+}$ and *Atf7ip2*$^{-/-}$ spermatocyte chromosome spreads stained with antibodies raised against SYCP3 and γH2AX. γH2AX accumulation patterns are one of three classifications described in *C*. Scale bars, 10 µm. (*B*) Meiotic prophase I stage populations quantified as mean ± SD. Numbers of analyzed nuclei are indicated. Data are from three independent littermate pairs at P44, P66, and P69. (*) $P < 0.05$, from unpaired two-tailed *t*-tests. (*C*) Stage-wise proportions of γH2AX accumulation patterns for three independent littermate pairs and are quantified as mean ± SD. Patterns are classified with three criteria (see *top*). (****) $P < 0.0001$, from Fisher's exact tests. (*D*) Chromosome spreads stained with antibodies raised against SYCP3 and MLH1. Arrowheads indicate MLH1 foci. The *top* dot plot shows distributions of MLH1 counts. The *bottom* dot plot shows proportions of MLH1 focus-associated XY pseudoautosomal regions (PARS). Numbers of analyzed nuclei are indicated. Data are from three independent littermate pairs at P108, P115, and P122. Bars represent means. *P*-values are from unpaired *t*-tests. (*E*,*F*) Chromosome spreads stained with antibodies raised against SYCP3 (a marker of all chromosome axes) and SYCP1 (a marker of only synapsed axes). Scale bars: *E*, 10 µm; *F*, 5 µm. Bar plots show proportions of pachytene nuclei with normal synapsis of autosomes (*E*) and sex chromosomes (*F*). Data are from three independent littermate pairs at P44, P66, and P69 and are presented as mean ± SD. Numbers of analyzed nuclei are indicated. (**) $P < 0.01$, from unpaired *t*-tests.

γH2AX accumulates through the whole of leptotene and early zygotene nuclei (pattern I) (Fig. 3A,C). As spermatocytes progress into the late zygotene stage, γH2AX accumulation transitions from a pan-nuclear diffuse signal to concentrated accumulation on the chromatin associated with unsynapsed chromosome axes, albeit with partial signals remaining along synapsed autosomes (pattern II). By the mid and late pachytene stages, γH2AX is confined

to XY chromatin, having largely disappeared from autosomes (pattern III). In *Atf7ip2*$^{-/-}$ early/mid-pachytene spermatocytes, γH2AX remains on autosomes in comparison with littermate controls (Fig. 3C), suggesting that in the absence of ATF7IP2, autosomal DDR signaling is affected.

Following on this, we investigated the outcome of meiotic recombination by scoring the numbers of MLH1 foci (which illuminate crossover sites) on chromosome axes. Numbers of MLH1 foci on autosomes were comparable between *Atf7ip2*$^{+/-}$ and *Atf7ip2*$^{-/-}$ H1T-positive mid/late pachytene spermatocytes (Fig. 3D). Although a recent study of a separate *Atf7ip2*$^{-/-}$ mouse line reported reduced numbers of XY pseudoautosomal regions (PARs) with MLH1 foci (Shao et al. 2023), our observations showed no significant difference in the proportions of MLH1-associated PARs in *Atf7ip2*$^{+/-}$ and *Atf7ip2*$^{-/-}$ models (Fig. 3D). Next, we analyzed chromosome synapsis by immunostaining for SYCP3 (a marker of both unsynapsed and synapsed axes) and SYCP1 (a marker of only synapsed axes). We observed occasional but significant autosomal asynapsis in *Atf7ip2*$^{-/-}$ pachytene spermatocytes; ∼67% of *Atf7ip2*$^{-/-}$ pachytene nuclei evidenced complete synapsis, while nearly all *Atf7ip2*$^{+/+}$ spermatocytes showed complete synapsis (Fig. 3E). On occasion, the shapes of sex chromosome axes exhibited abnormal configurations, including apparent looped synapsis ("bubbles"), synapsis with large portions of itself ("irregular"), and synapsis at ends ("circular") (Fig. 3F); ∼26% of *Atf7ip2*$^{-/-}$ pachytene nuclei demonstrated abnormal sex chromosome synapsis (Fig. 3F). These results suggest that although ATF7IP2 may not play an outsized role in meiotic recombination, both DDR signaling and chromosome synapsis are impaired to some extent in *Atf7ip2*$^{-/-}$ spermatocytes.

ATF7IP2 directs SETDB1 and H3K9 methylation in male meiosis

Because ATF7IP binds SETDB1 to regulate H3K9me3 in somatic cells (Ichimura et al. 2005), we suspected that ATF7IP2 regulates H3K9me3 during meiosis. In meiotic prophase I, H3K9me3 accumulates on autosomal PCH and the sex chromosomes, where it is subject to dynamic regulation as XY undergoes MSCI (van der Heijden et al. 2007); H3K9me3 on the sex chromosomes is established by the methyltransferase SETDB1 (Hirota et al. 2018; Abe et al. 2022). Consistent with this, we observed normal H3K9me3 accumulation on autosomal PCH and XY chromatin in wild-type pachytene nuclei (Fig. 4A). Through careful examination, we noted multiple H3K9me3 accumulation patterns on the sex chromosome in the early pachytene stage of wild-type spermatocytes and recognized four general patterns: class I, covering the entirety of XY; class II, covering the entirety of Y and X-PCH; class III, covering X-PCH only; and class IV, in which H3K9me3 is absent from XY (i.e., no signal) (Fig. 4A,B; Supplemental Fig. S4A). We evaluated the proportions of patterns and found that H3K9me3 enrichment on the XY domain was impaired in the early pachytene stage of *Atf7ip2*$^{-/-}$ spermatocytes; 21% of nuclei showed essentially no signal anywhere on the XY chromosomes (class IV), a pattern that was not observed in any *Atf7ip2*$^{+/+}$ early pachytene nuclei (Fig. 4A,B). In normal mid and late pachytene stages, H3K9me3 is retained on X-PCH as it disappears from the remainder of XY chromatin (Fig. 4A), presumably due to histone replacement and the incorporation of histone variant H3.3 (van der Heijden et al. 2007). Next, in the normal diplotene stage, H3K9me3 signals promulgate through the XY chromatin in a likely reflection of H3K9me3's de novo deposition on H3.3 (Fig. 4A). However, in *Atf7ip2*$^{-/-}$ mid and late pachytene spermatocytes, H3K9me3 on X-PCH decreased, and re-establishment through the entirety of XY did not take place in the diplotene stage (Fig. 4A,C). Alongside the diplotene re-establishment of H3K9me3, H3K9me2 also accumulates on XY chromatin; however, in *Atf7ip2*$^{-/-}$ diplotene spermatocytes, we noted a clear loss of H3K9me2 (Fig. 4D,E). Concomitant with these changes, in *Atf7ip2*$^{-/-}$ spermatocytes, we observed the strong accumulation of H3K9 acetylation (H3K9ac), which counteracts H3K9 methylation, on X-PCH (Supplemental Fig. S4B). On the other hand, proportions of H3K9me1 accumulation patterns were unchanged between control and *Atf7ip2*$^{-/-}$ spermatocytes (Supplemental Fig. S4C,D), highlighting a specific role for ATF7IP2 in the regulation of H3K9me2/3 and H3K9ac. Together, these results indicate that ATF7IP2 regulates the establishment of H3K9me2/3 on diplotene XY chromatin, consistent with the concurrent, dynamic localization of ATF7IP2 from X-PCH through XY chromatin.

Given this, we hypothesized that ATF7IP2 regulates the spatiotemporal recruitment of SETDB1 (which mediates H3K9me3) to the sex chromosomes. In wild-type early and mid-pachytene nuclei, SETDB1 localizes on the XY chromosomes and is notably enriched on the X-PCH. In corresponding *Atf7ip2*$^{-/-}$ spermatocytes, SETDB1 was not enriched on X-PCH, localizing instead to sex chromosome-adjacent nucleoli (Fig. 4F). Consistent with this, *Atf7ip2*$^{-/-}$ X-PCH was less DAPI-intense compared with controls (Supplemental Fig. S5), suggesting a defect in heterochromatin formation. We also noticed that the pachytene accumulation of SETDB1 on autosomal PCH was disrupted in corresponding *Atf7ip2*$^{-/-}$ spermatocytes. In contrast to the constrained, intense SETDB1 signals of wild-type samples, we observed diffuse SETDB1 signals through the whole of mutant nuclei (Fig. 4F). We also observed that in *Setdb1* conditionally deleted mutants driven by the germline-specific *Ddx4*-Cre (*Setdb1*-cKO) (Abe et al. 2022), the accumulation of ATF7IP2 on X-PCH was significantly reduced (Supplemental Fig. S6A). Taken together, these results indicate a pan-nuclear role for ATF7IP2 in the spatiotemporal regulation of SETDB1; furthermore, at X-PCH, ATF7IP2 and SETDB1 likely operate in tandem, possibly as a protein complex.

A hallmark of normal MSCI is the sex chromosome-wide accumulation of γH2AX, and γH2AX domain formation is tightly associated with the initiation and maintenance of MSCI (Fernandez-Capetillo et al. 2003; Abe et al. 2022). γH2AX domain formation is directed by MDC1, a γH2AX-binding protein and central mediator

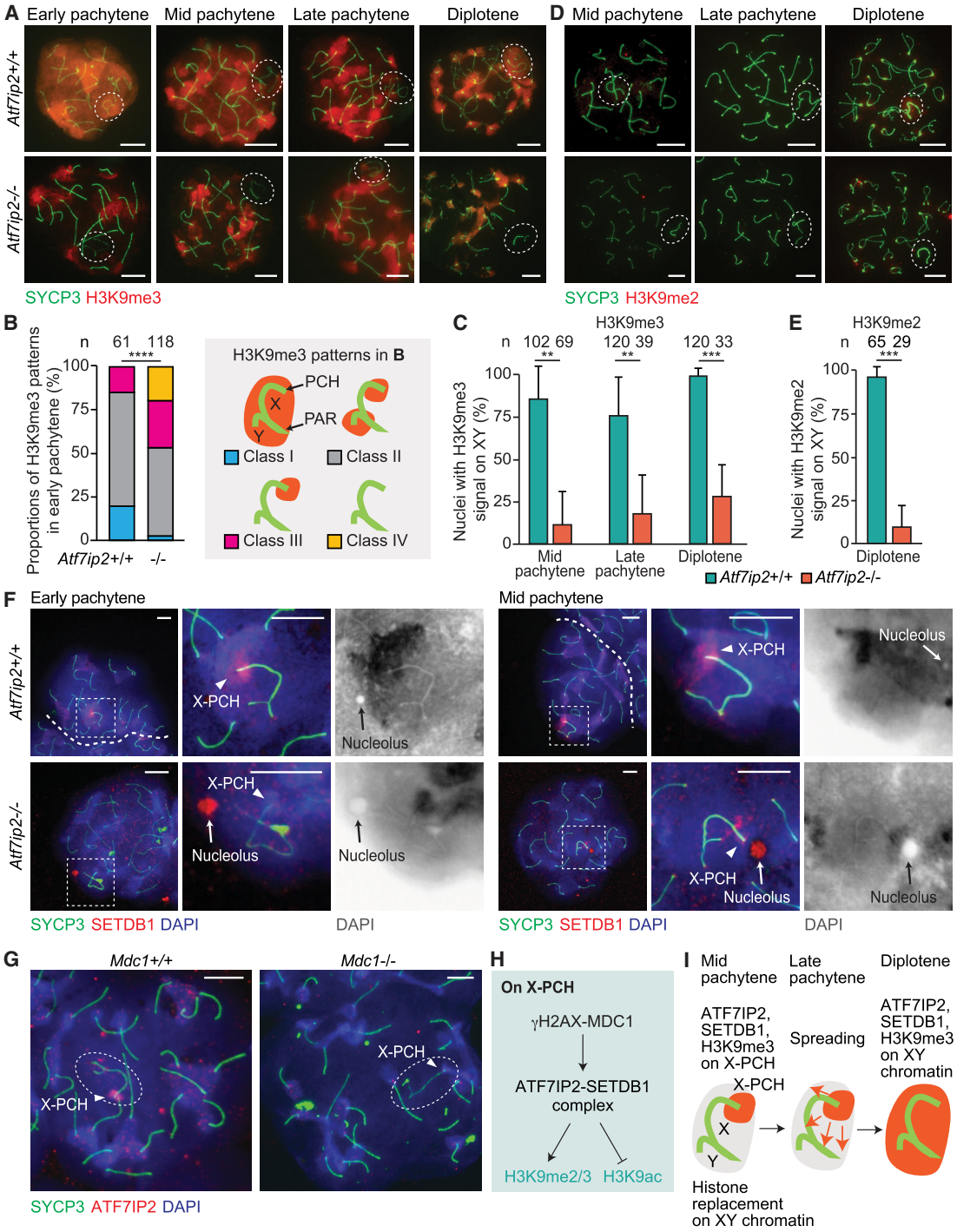


Figure 4. ATF7IP2 is required for H3K9 methylation on the sex chromosomes during male meiosis. (*A*) *Atf7ip2*$^{+/+}$ and *Atf7ip2*$^{-/-}$ spermatocyte chromosome spreads stained with antibodies raised against H3K9me3 and SYCP3 (a marker of chromosome axes, both synapsed and unsynapsed). Dashed circles indicate the sex chromosomes. Scale bars, 10 µm. (*B*) H3K9me3 accumulation patterns on the sex chromosomes of *Atf7ip2*$^{+/+}$ and *Atf7ip2*$^{-/-}$ early pachytene spermatocytes. Patterns are classified with four criteria (shown at the *right*). Data are from five independent littermate pairs and are quantified as mean ± SD. Numbers of analyzed nuclei are indicated. (****) $P < 0.0001$, from a Fisher's exact test. (*C*) Quantification of mid-pachytene, late pachytene, and diplotene spermatocytes with H3K9me3 signals on the sex chromosomes. Data are from four, six, and four independent littermate pairs, respectively, and are quantified as mean ± SD. Numbers of analyzed nuclei are indicated. (**) $P < 0.01$, (***) $P < 0.001$, from unpaired *t*-tests. (*D*) *Atf7ip2*$^{+/+}$ and *Atf7ip2*$^{-/-}$ chromosome spreads stained with antibodies raised against H3K9me2 and SYCP3. Scale bars, 10 µm. (*E*) Quantification of diplotene spermatocytes with H3K9me2 signals on the sex chromosomes for four independent experiments quantified as mean ± SD. Numbers of analyzed nuclei are indicated. (***) $P < 0.001$, from unpaired *t*-tests. (*F*) *Atf7ip2*$^{+/+}$ and *Atf7ip2*$^{-/-}$ chromosome spreads stained with antibodies raised against SETDB1 and SYCP3. Dashed squares are magnified in the panels at the *right*. Scale bars, 5 µm. (*G*) *Mdc1*$^{+/+}$ and *Mdc1*$^{-/-}$ spermatocyte chromosome spreads stained with antibodies raised against ATF7IP2 and SYCP3. Scale bars, 10 µm. (*H*) Summary of the γH2AX/MDC1–ATF7IP2–SETDB1 pathway on X-PCH. (*I*) Schematic showing the establishment of H3K9me3 on the sex chromosomes in normal mid-pachytene to diplotene spermatocytes.

of the DDR, through a feed-forward mechanism (Ichijima et al. 2011). We hypothesized that the accumulation of ATF7IP2 on XY chromatin occurs downstream from MDC1. To test this, we stained for ATF7IP2 in *Mdc1*$^{-/-}$ spermatocytes and found that in the absence of MDC1, ATF7IP2 failed to concentrate on X-PCH (Fig. 4G). Similarly, the accumulation of SETDB1 on X-PCH depended on MDC1 (Supplemental Fig. S6B). These results suggest that the MDC1-dependent DDR pathway regulates ATF7IP2 and SETDB1 localization on the sex chromosomes. We infer that, in pachytene spermatocytes, the MDC1-dependent DDR pathway recruits ATF7IP2 (presumably forming a complex with SETDB1) to X-PCH; in the subsequent diplotene stage, both factors spread through the XY chromatin, and as this occurs, SETDB1 deposits pan-XY H3K9me2/3 (Fig. 4H,I). Corroborating this model, we found that MDC1 accumulation on XY chromatin occurred independently of ATF7IP2 or SETDB1 (Supplemental Fig. S6C,D).

To parse mechanisms related to ATF7IP2, we tested the localization of related factors. A previous study suggested a role for the SETDB1-interacting protein TRIM28 as a linker between the DDR pathway and SETDB1 (Hirota et al. 2018). However, we found that TRIM28 does not localize on the sex chromosomes in wild-type meiosis (Supplemental Fig. S7A), which raises the possibility that ATF7IP2 works independently of TRIM28 to link the DDR pathway and SETDB1. In line with this possibility, TRIM28 is dispensable for male meiotic progression (Tan et al. 2020). Downstream from the DDR pathway, the chromatin remodeler CHD4 is recruited to X-PCH (Broering et al. 2014); in *Atf7ip2*$^{-/-}$ spermatocytes, CHD4 accumulation on X-PCH was unchanged from controls (Supplemental Fig. S7B). The germline-specific Polycomb protein SCML2 also accumulates in pachytene and diplotene nuclei; in *Atf7ip2*$^{-/-}$ spermatocytes, SCML2 localization did not differ from controls (Supplemental Fig. S7C,D). These results suggest that the disfunction of ATF7IP2 is not related to the localization of TRIM28, CHD4, and SCML2.

We also examined the localization of ATF7IP in *Atf7ip2*$^{-/-}$ spermatogenesis. In wild-type tissue sections, ATF7IP was predominantly found in the nuclei of primary spermatocytes (Supplemental Fig. S7E); more specifically, it localized to the X-PCH in wild-type pachytene spermatocytes (Supplemental Fig. S7F,G). Contrastingly, in *Atf7ip2*$^{-/-}$ pachytene spermatocytes, ATF7IP was absent from the X-PCH and instead localized to the XY PAR. These results demonstrate that ATF7IP2 is essential for directing ATF7IP and SETDB1 to X-PCH in pachytene spermatocytes.

ATF7IP2 is required for meiotic gene regulation

Having established its meiotic phenotype and essential role in H3K9 methylation, we sought to investigate the function of ATF7IP2 in meiotic gene regulation. To this end, we performed single-cell RNA sequencing (scRNA-seq) analyses of whole testicular cells from *Atf7ip2*$^{-/-}$ mice and their *Atf7ip2*$^{+/+}$ littermates at P15. The cellular composition of the testis changes as development progresses, leading us to confirm that in P15 testes, the first wave of spermatogenesis exhibited a similar cellular composition between *Atf7ip2*$^{+/+}$ and *Atf7ip2*$^{-/-}$ mice. Indeed, we observed this was the case until the mid to late pachytene stages, when defects appeared based on immunostaining against major markers of spermatogenesis, including ZBTB16/PLZF, STRA8, SYCP3, γH2AX, and H1T (Supplemental Fig. S8).

Using the scRNA-seq data, we endeavored to determine when ATF7IP2 functions in wild-type spermatogenesis. Since ATF7IP2 expression was restricted to germ cells, scRNA-seq data derived from germ cell populations (spermatogonia and spermatocytes) were analyzed apart from those of testicular somatic cells (Sertoli cells, Leydig cells, peritubular myoid cells, endothelial cells, and hemocytes) (Fig. 5A; Supplemental Fig. S9A,B). Using the UMAP of scRNA-seq data from *Atf7ip2*$^{+/+}$ and *Atf7ip2*$^{-/-}$ germ cell populations, we identified 13 cell type clusters; the cluster numbers are based on the numbers of cells comprising each cluster; cluster 0 is the largest, and cluster 12 is the smallest (Fig. 5B,C; Supplemental Fig. S9C,D). Assessing the expression of key marker genes for spermatogenesis with respect to the UMAP, we inferred the developmental trajectory of P15 spermatogenesis (Fig. 5D). As suggested by the high expression of *Gfra1*, cluster 8 represented a population of undifferentiated spermatogonia, including spermatogonial stem cells. Cluster 1 represented a population of differentiating spermatogonia, as indicated by the initial up-regulation of *Stra8*. Clusters 6 and 7 represented cells at the initiation of meiosis, consistent with the up-regulation of *Meiosin* and *Stra8*. Cluster 11 represented a population of spermatocytes in early meiotic prophase, as denoted by the up-regulation of *Prdm9*. Based on the expression of marker genes with respect to the UMAP, we inferred that spermatogenesis progressed along the trajectory from cluster 8 to cluster 12. Although *Atf7ip2* was expressed in a broad range of spermatogenic stages, its expression level was higher in clusters 7, 6, 11, and 5, all of which correspond to meiotic prophase (Fig. 5E). Given that *Atf7ip2* is bound by MEIOSIN and STRA8 (Fig. 1B), it is possible that the expression of *Atf7ip2* is boosted, rather than initiated, at the entry to meiosis. In contrast, *Atf7ip* is constitutively expressed in spermatogenesis (Fig. 5E).

Next, we sought to understand when cell death takes place in *Atf7ip2*$^{-/-}$ spermatocytes. Starting from cluster 8 through to cluster 5, the gene expression profiles for *Atf7ip2*$^{+/+}$ and *Atf7ip2*$^{-/-}$ germ cell populations overlapped one another to a high degree (Fig. 5A,B), indicating that *Atf7ip2*$^{-/-}$ spermatogenesis progressed until the stage of spermatogenesis that corresponds to cluster 5. However, we noticed certain subpopulations—clusters 10, 0, 2, and 3, representing B spermatogonia through to preleptotene cells—were more numerous in *Atf7ip2*$^{-/-}$ germ cells (Fig. 5C); the increased cluster sizes suggest that in the absence of ATF7IP2, the entry into meiosis is hampered. Furthermore, the subpopulation represented by cluster 12 was present in *Atf7ip2*$^{+/+}$ germ cells but missing amid *Atf7ip2*$^{-/-}$ germ cells (Fig. 5B,C).

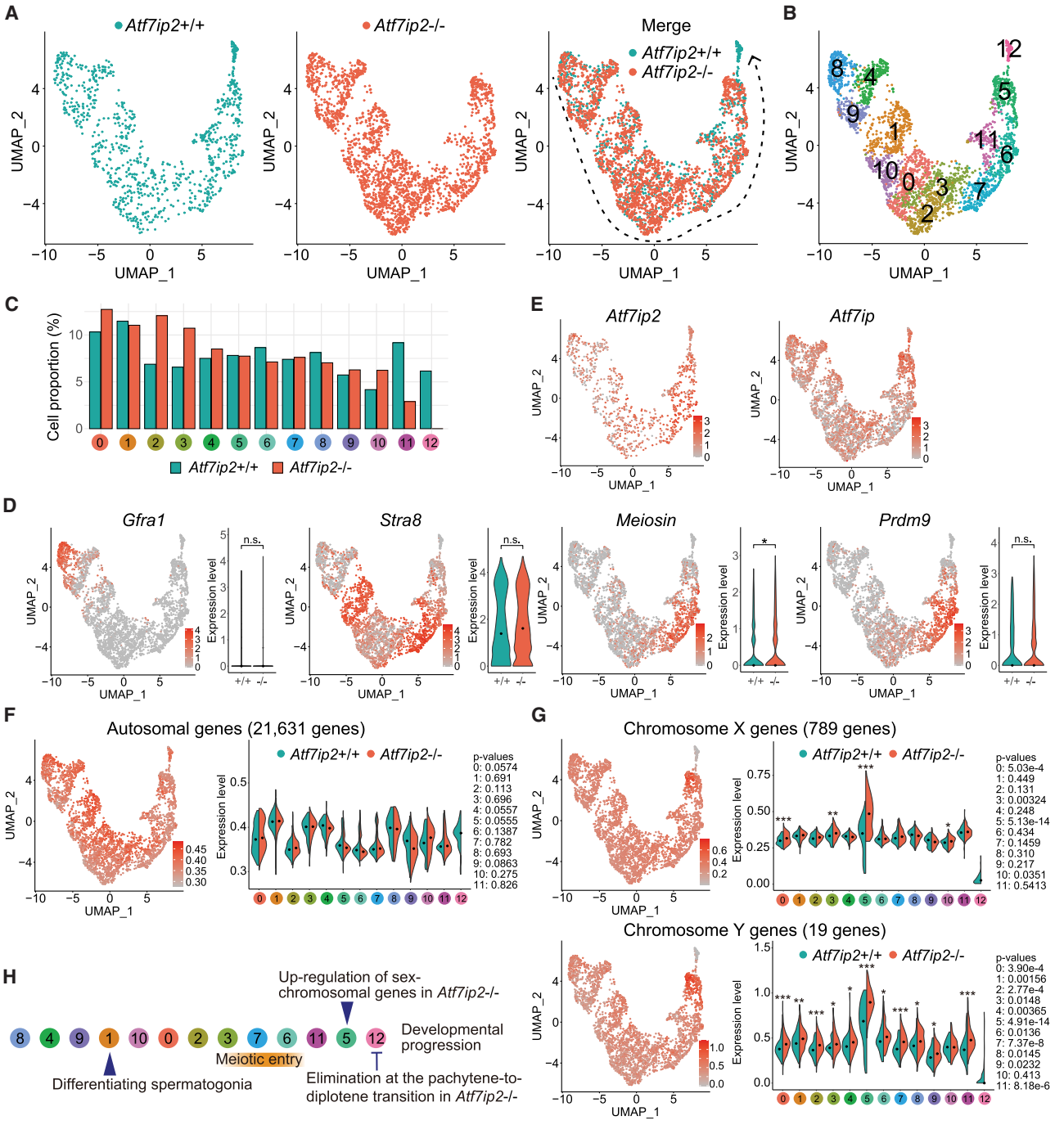


Figure 5. scRNA-seq analyses of *Atf7ip2*$^{+/+}$ and *Atf7ip2*$^{-/-}$ spermatogenic germ cells. (*A*) UMAP representations of scRNA-seq transcriptome profiles for germ cells from *Atf7ip2*$^{+/+}$ testes (*left*, P15), *Atf7ip2*$^{-/-}$ testes (*middle*, P15), and both *Atf7ip2*$^{+/+}$ and *Atf7ip2*$^{-/-}$ testes (*right*). (Gray arrow) Inferred developmental trajectory. (*B*) Clustering of UMAP-projected scRNA-seq transcriptome profiles for *Atf7ip2*$^{+/+}$ and *Atf7ip2*$^{-/-}$ germ cells based on gene expression patterns. (*C*) Bar graph showing the proportions of *Atf7ip2*$^{+/+}$ and *Atf7ip2*$^{-/-}$ germ cells among the clusters. (*D*) UMAP representations showing expression patterns for key developmental marker genes in spermatogenic cells. Genes shown include *Gfra1*, which represents undifferentiated spermatogonia; *Stra8*, which represents differentiating spermatogonia; *Meiosin*, which represents preleptotene spermatocytes; and *Prdm9*, which represents early meiotic prophase spermatocytes. (n.s.) Not significant, (*) $P < 0.05$, from Wilcoxon rank sum tests. (*E*) Expression patterns for *Atf7ip2* and *Atf7ip* upon the UMAP. (*F*) Expression levels for autosomal genes. (*G*) Expression levels for X-chromosomal genes (*top*) and Y-chromosomal genes (*bottom*) are shown. (*) $P < 0.05$, (**) $P < 0.01$, (***) $P < 0.001$, from Wilcoxon rank sum tests. (*H*) Summary of *Atf7ip2*$^{-/-}$ phenotypes in spermatogenic germ cells. Subtype clusters are ordered by inferred developmental progression. Key cell types and events in *Atf7ip2*$^{+/+}$ and *Atf7ip2*$^{-/-}$ spermatogenesis are shown.

Furthermore, in *Atf7ip2*$^{+/+}$ germ cells, expression levels of sex-linked genes were abruptly down-regulated in the transition from cluster 5 to cluster 12 compared with that of autosomal genes (Fig. 5F,G). Intriguingly, in *Atf7ip2*$^{-/-}$ cells, cluster 5 was associated with a strong, abrupt up-regulation of sex-linked gene expression (Fig. 5G), suggesting that MSCI failure began in the cluster 5 subpopulation of *Atf7ip2*$^{-/-}$ cells. Thus, the loss of the cluster 12 subpopulation in *Atf7ip2*$^{-/-}$ testes was preceded by an ectopic up-regulation of X- and Y-chromosomal genes in cluster 5 (Fig. 5G), indicating that clusters 5 and 12 represent pachytene spermatocytes.

Remarkably, gene enrichment analysis revealed that genes related to late spermatogenesis (e.g., *Clgn*, *Hspa2*, *Piwil1*, and *Ldhc*) were highly expressed in the cluster 12 subpopulation of spermatocytes (Supplemental Fig. S9C; Supplemental Table S1). Because those genes are known to be expressed in the late pachytene stage onward, we inferred that cluster 12 corresponds to cytologically defined late pachytene spermatocytes (and/or diplotene spermatocytes). It is important to note that aligning exact substages between cytology-defined and gene expression-based criteria can be challenging. However, the single-cell RNA sequencing (scRNA-seq) results aligned well with cytological observations, indicating that *Atf7ip2*$^{-/-}$ spermatocytes progress through early meiotic prophase but are predominantly eliminated via cell death during the transition from the late pachytene to diplotene stages (Fig. 3B). Thus, ATF7IP2 is required for spermatocytes to progress beyond the pachytene-to-diplotene transition (Fig. 5H).

ATF7IP2 binds broadly to the sex chromosomes and autosomal gene promoters

To determine where ATF7IP2 binds the genome of wild-type pachytene spermatocytes, we performed CUT&Tag for ATF7IP2 in two biological replicates. We observed the specific enrichment of ATF7IP2 CUT&Tag signals relative to IgG CUT&Tag signals (Supplemental Fig. S10A). Given the high correlation between replicates (Supplemental Fig. S10B), we combined them for subsequent analyses. Analyses of ATF7IP2 coverage revealed 61,839 genome-wide regions of enriched ATF7IP2 binding; i.e., "ATF7IP2 peaks" (Fig. 6A). We observed ATF7IP2 peaks on TSSs (26.73%), gene bodies (27.74%), TESs (0.1%), and intergenic regions (45.43%). TSS peaks were enriched on autosomes, whereas intergenic peaks were enriched on the sex chromosomes (Fig. 6A), suggesting distinct functions for ATF7IP2 on the autosomes and sex chromosomes. In our continued investigation of wild-type pachytene spermatocytes, we conducted a clustering analysis incorporating ATF7IP2 peaks, regions of H3K9me3 coverage (data newly generated for this study, shown in Supplemental Fig. S10C), and regions of coverage for the active promoter mark H3K4me3 (data from our previous study, as shown in Maezawa et al. 2018b); this analysis resulted in three distinct clusters (Fig. 6B). Cluster I regions (6632) are associated with H3K4me3 deposition (Fig. 6B) on autosomes and at TSSs (Fig. 6C,D). Cluster II regions (22,579) are associated with broad H3K9me3 enrichment (Fig. 6B); 70% of these regions are on the sex chromosomes (Fig. 6C), mostly at intergenic regions and gene bodies (Fig. 6D), which is in line with the role of ATF7IP2 in the regulation of H3K9me3 on the sex chromosomes. Cluster III regions (32,628) largely represent autosomal intergenic regions and gene bodies (Fig. 6C,D).

Based on the enrichment of ATF7IP2 at TSSs, we sought to identify ATF7IP2 target genes in pachytene spermatocytes. Our analyses revealed 4917 autosomal genes and 270 sex chromosomal genes (Supplemental Table S2). ATF7IP2 binds the promoters of a broad range of genes required for meiotic prophase and spermiogenesis, including *Hormad1* and *Sycp3*, both autosomal genes, as well

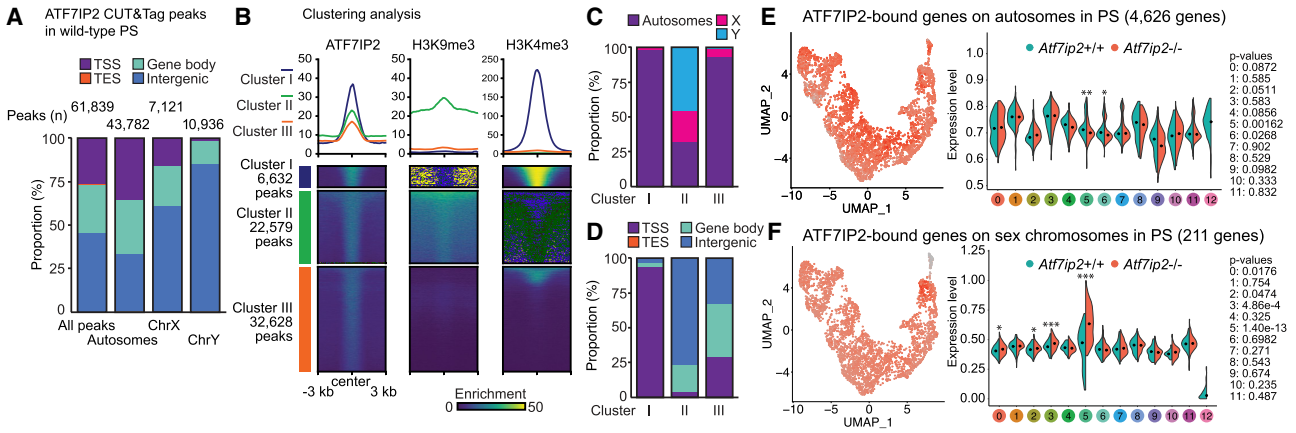


Figure 6. ATF7IP2-binding sites in pachytene spermatocytes. (*A*) Numbers and genomic distribution of ATF7IP2 CUT&Tag peaks in wild-type pachytene spermatocytes. (*B*) Clustering analysis of ATF7IP2 CUT&Tag peaks and H3K9me3- and H3K4me3-enriched regions. Average tag density profiles (*top*) and heat maps (*bottom*) for each cluster are shown. (*C*) Chromosomal distribution of ATF7IP2 peak clusters. (*D*) Genomic distribution of ATF7IP2 peak clusters. (*E*) Expression levels of ATF7IP2-bound autosomal genes in scRNA-seq. (*) $P < 0.05$, (**) $P < 0.01$, from Wilcoxon rank sum tests. (*F*) Expression levels for ATF7IP2-bound sex chromosomal genes in scRNA-seq. (*) $P < 0.05$, (***) $P < 0.001$, from Wilcoxon rank sum tests.

as Y-linked *Zfy1*. These promoter peaks are associated with the active histone modifications H3K4me3 and H3K27ac (Supplemental Fig. S10D). Next, using our scRNA-seq data set for *Atf7ip2*$^{+/+}$ and *Atf7ip2*$^{-/-}$ spermatogenic germ cells, we sought to understand the regulation of ATF7IP2 target genes. We detected the expression of 4626 ATF7IP2 target genes on autosomes and 211 ATF7IP2 target genes on the sex chromosomes. The autosomal genes were down-regulated in *Atf7ip2*$^{-/-}$ pachytene spermatocytes (Fig. 6E, clusters 6 to 5, representing the early to mid-pachytene stages). Because wild-type autosomal promoter peaks are associated with H3K4me3, these results indicate that ATF7IP2 binds to and positively regulates the expression of these genes. On the other hand, in *Atf7ip2*$^{-/-}$ pachytene spermatocytes, the 211 sex chromosomal genes are highly up-regulated in cluster 5 (Fig. 6F, mid-pachytene spermatocytes), indicating that ATF7IP2 binds to and negatively regulates the expression of these genes. These results reveal two separate functions for ATF7IP2 in pachytene spermatocytes: one for autosomal gene expression and, contrastingly, another for sex chromosomal gene repression.

ATF7IP2 directs meiotic gene regulation

To elucidate gene regulatory mechanisms associated with ATF7IP2, we isolated pachytene spermatocytes from both *Atf7ip2*$^{+/+}$ and *Atf7ip2*$^{-/-}$ testes and, after confirming their purity, conducted bulk RNA sequencing with ERCC spike-in controls across three biological replicates. The transcription data derived from this process were then analyzed (Supplemental Fig. S10E,F; Supplemental Table S3). While isolating the cells, we were surprised to observe that *Atf7ip2*$^{-/-}$ spermatocytes were smaller than their *Atf7ip2*$^{+/+}$ counterparts (Supplemental Fig. S10E). This gross decrease in size suggests that in *Atf7ip2*$^{-/-}$ spermatocytes, the pachytene transcriptional burst (Maezawa et al. 2020) is compromised, a possibility consistent with the global down-regulation of ATF7IP2-bound autosomal genes detected with scRNA-seq.

Comparing the spike-in-normalized mutant and control RNA-seq data, we identified 9446 autosomal differentially expressed genes (DEGs)—218 up-regulated and 9228 down-regulated (Fig. 7A). To understand how autosomal DEGs are expressed during normal spermatogenesis, we reanalyzed separate RNA-seq data taken from cell types sampled across wild-type spermatogenesis (Maezawa et al. 2018b). The 218 up-regulated genes displayed high expression levels in wild-type spermatogonia but were suppressed in wild-type pachytene spermatocytes (Supplemental Fig. S11A). Thus, their up-regulation in *Atf7ip2*$^{-/-}$ pachytene spermatocytes suggests an ectopic expression of normally repressed premeiotic genes. The top gene ontology (GO) (Ashburner et al. 2000) enrichment terms for these genes are related to immune system functions (Supplemental Fig. S11B), suggesting that ATF7IP2 suppresses the expression of immune genes in pachytene spermatocytes. In contrast, many of the 9228 down-regulated genes were highly expressed in wild-type pachytene spermatocytes (Supplemental Fig. S11A), and the associated GO enrichment terms were related to spermatogenesis (Supplemental Fig. S11B). These findings indicate that many spermatogenesis-related genes fail to activate in *Atf7ip2*$^{-/-}$ pachytene spermatocytes. Furthermore, in *Atf7ip2*$^{-/-}$ spermatocytes, *Atf7ip* expression was decreased (Supplemental Fig. S11C). Shifting focus to the sex chromosomes, we detected 539 DEGs associated with the *Atf7ip2*$^{-/-}$ pachytene X chromosome; 533 were up-regulated in mutants relative to controls, whereas six were down-regulated (Fig. 7A). On the Y chromosome, 12 DEGs were up-regulated, and we detected no down-regulated DEGs (Fig. 7A). These results are largely consistent with bulk RNA-seq analyses of P14 juvenile testes (Supplemental Fig. S12), together indicating that MSCI is disrupted in *Atf7ip2*$^{-/-}$ pachytene spermatocytes.

We next examined the regulation of ATF7IP2 target genes in *Atf7ip2*$^{-/-}$ pachytene spermatocytes. A significant overlap exists between these target genes and DEGs in *Atf7ip2*$^{-/-}$ spermatocytes (Supplemental Fig. S11D). Notably, there is a considerable intersection between down-regulated autosomal DEGs and ATF7IP2 autosome targets, with an enrichment in key processes such as mRNA and DNA metabolism, as well as translation (Supplemental Fig. S11D). This indicates a direct regulatory role for ATF7IP2 in vital cellular functions. Furthermore, there is a significant overlap between XY up-regulated DEGs and ATF7IP2 XY targets (Supplemental Fig. S11E), reinforcing our conclusion that ATF7IP2 is involved in suppressing gene expression to preserve MSCI.

MSCI is initiated by the DDR pathway and maintained through active DDR signaling (Ichijima et al. 2011; Abe et al. 2022). On the *Atf7ip2*$^{-/-}$ XY domain, γH2AX signals were observed (Fig. 2), but H3K9me2/3 deposition was not established as the pachytene stage progressed into the diplotene stage (Fig. 4). Indeed, in place of H3K9me2/3, we observed signals for the active transcriptional mark H3K9ac (Supplemental Fig. S4B). Thus, we suspect that MSCI is initiated but not maintained in *Atf7ip2*$^{-/-}$ spermatocytes. To test this, we stained for POLII in *Atf7ip2*$^{-/-}$ pachytene spermatocytes. In normal mid-pachytene spermatocytes, we observed the exclusion of POLII from XY domains in 100% of observed nuclei ($n = 65$) (Supplemental Fig. S11F), confirming the accurate detection of MSCI through POLII immunostaining. However, in *Atf7ip2*$^{-/-}$ mid-pachytene spermatocytes, we observed the exclusion of POLII from XY chromatin in only 73.3% of nuclei ($n = 105$) (Supplemental Fig. S11G); 26.7% of *Atf7ip2*$^{-/-}$ nuclei included POLII in XY domains (Supplemental Fig. S11H), which is evidence for defective MSCI. These results suggest that in the absence of ATF7IP2, the initiation of MSCI occurs, but MSCI fails to be maintained.

To understand the mechanism through which ATF7IP2 regulates H3K9me3 deposition, we produced and analyzed H3K9me3 CUT&RUN data from *Atf7ip2*$^{+/+}$ and *Atf7ip2*$^{-/-}$ pachytene spermatocytes (Supplemental Fig. S10G). We found that H3K9me3 is largely dependent on ATF7IP2, especially at the sites of cluster II ATF7IP2-bound peaks (Fig. 7C; cluster II peaks are defined in Fig. 6B). ATF7IP2 and H3K9me3 signals frequently overlapped, with many regions of H3K9me3 deposition

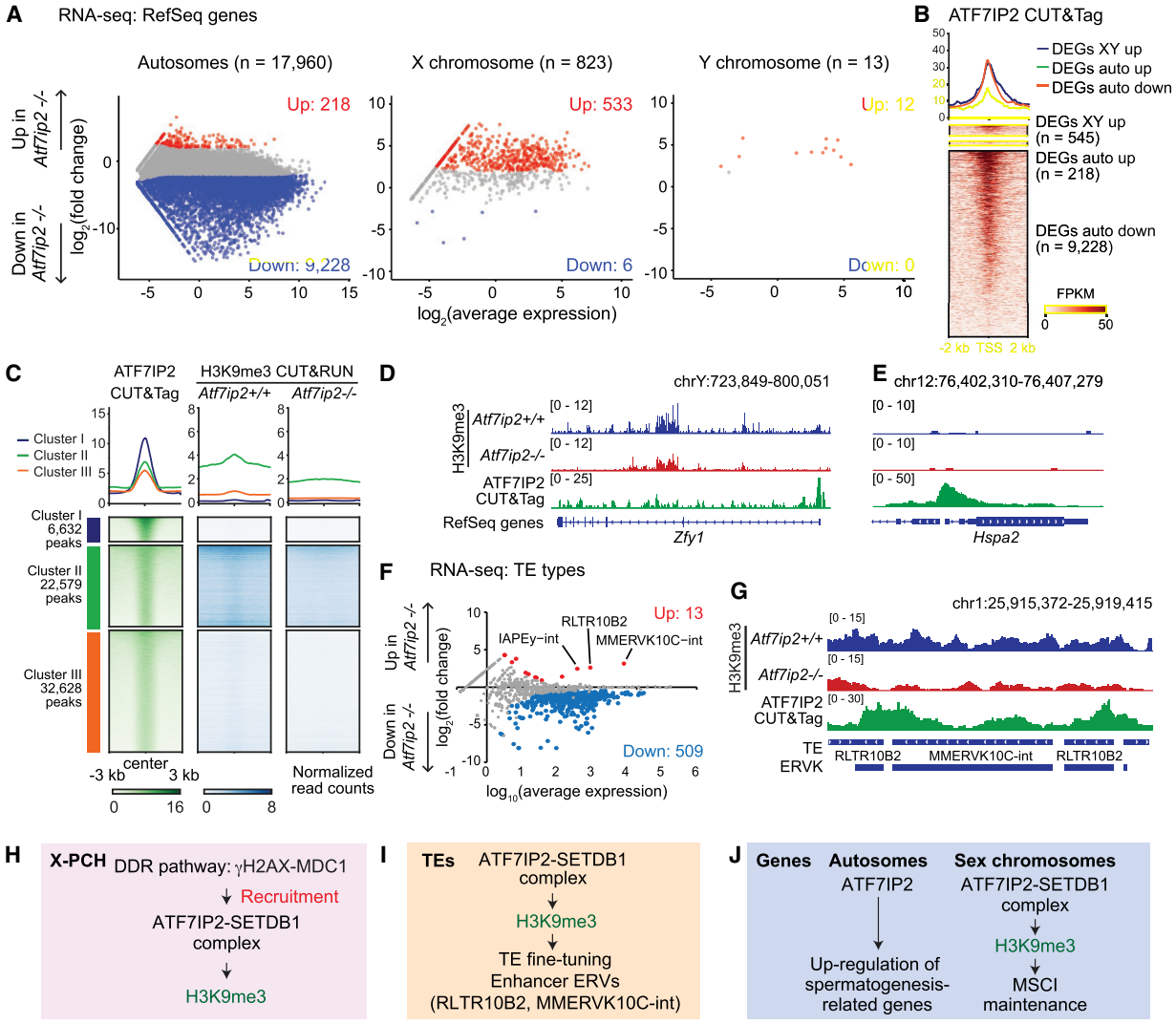


Figure 7. ATF7IP2 directs meiotic gene regulation and regulates TEs. (*A*) Comparison of *Atf7ip2*$^{+/+}$ and *Atf7ip2*$^{-/-}$ pachytene spermatocyte transcriptomes. Autosomal, X, and Y genes were analyzed separately. Three independent biological replicates were examined. All genes with adjusted *P*-values (Benjamini–Hochberg method) are plotted. Differentially expressed genes (DEGs; $\log_2$ fold change > 2, adjusted *P*-value < 0.05) are indicated by color ([red] up-regulated in *Atf7ip2*$^{-/-}$, [blue] down-regulated in *Atf7ip2*$^{-/-}$), and numbers are shown. (*B*) ATF7IP2 CUT&Tag enrichment at DEG TSSs ± 2 kb in wild-type pachytene spermatocytes. Average tag density profiles (*top*) and heat maps (*bottom*) for each cluster are shown. (*C*) ATF7IP2 CUT&Tag and H3K9me3 CUT&RUN enrichment in clusters I–III (defined in Fig. 6B). Average tag density profiles (*top*) and heat maps (*bottom*) for each cluster are shown. (*D*,*E*) Track views of the *Zfy1* locus (an up-regulated Y-linked locus) and the *Hspa2* locus (a down-regulated autosomal locus). (*F*) Comparison of *Atf7ip2*$^{+/+}$ and *Atf7ip2*$^{-/-}$ pachytene spermatocyte transposable element (TE) expression. All TE types are plotted. Differentially expressed TE types (DEGs; $\log_2$ fold change > 2, adjusted *P*-value < 0.05) are indicated by color ([red] up-regulated in *Atf7ip2*$^{-/-}$, [blue] down-regulated in *Atf7ip2*$^{-/-}$), and numbers are shown. (*G*) Track view of the ATF7IP2 targeted TEs RLTR10B2 and MMERVK10C-int. (*H*) Summary and model of the function of ATF7IP2 on X-PCH. (*I*) Summary and model of the function of ATF7IP2 in TE regulation. (*J*) Summary and model of the function of ATF7IP2 in gene expression regulation.

centered on ATF7IP2 peaks (Fig. 7C). Notably, H3K9me3 deposition was completely absent or strongly diminished in the *Atf7ip2*$^{-/-}$ model, indicating that H3K9me3 enrichment is dependent on ATF7IP2 (Fig. 7C). As shown in a track view of the Y-linked *Zfy1* locus, ATF7IP2-binding sites frequently align with, or are immediately adjacent to, locations of ATF7IP2-dependent H3K9me3 (Fig. 7D). Conversely, there was no observed H3K9me3 enrichment on ATF7IP2-dependent autosomal genes, as evidenced by loci such as *Hspa2* (Fig. 7E). We conclude that ATF7IP2 directs H3K9me3 deposition while simultaneously orchestrating meiotic gene activation on autosomes, much of which is independent of H3K9me3. Furthermore, by categorizing H3K9me3 peaks in wild-type pachytene spermatocytes based on their ATF7IP2 binding status, we revealed a reduction in H3K9me3 enrichment in both ATF7IP2-bound and unbound regions in *Atf7ip2*$^{-/-}$ spermatocytes (Supplemental Fig. S10H). This finding

supports a model in which ATF7IP2 potentially governs H3K9me3 levels by regulating the nuclear localization of SETDB1.

ATF7IP2 fine-tunes the expression of transposable elements

SETDB1-mediated H3K9me3 is a well-known suppressor of transposable elements (TEs) (Matsui et al. 2010; Rowe et al. 2013). Therefore, we sought to examine TE expression using our RNA-seq data in combination with a "best-match" TE annotation set (Sakashita et al. 2020), which enabled the detection of alignments uniquely mapped to TEs that are not exon-derived (mRNA-derived). This strategy eliminated detection of TEs that are parts of mRNA, preventing the conflation of mRNA and TE expression. In *Atf7ip2*$^{-/-}$ pachytene spermatocytes, we observed an up-regulation of 13 TE types, including IAPEy-int, RLTR10B2, and MMERVK10C-int, whereas 509 types were down-regulated (Fig. 7F; Supplemental Table S4). This up-regulation, particularly of IAPEy-int, RLTR10B2, and MMERVK10C-int, was further confirmed by scRNA-seq analysis (Supplemental Fig. S13). ATF7IP2 was found to bind these up-regulated TEs, with the H3K9me3 enrichment at these loci being dependent on ATF7IP2 (Fig. 7G). In wild-type spermatogenesis, TE expression undergoes dynamic changes at the mitosis-to-meiosis transition, and a subset of TEs—specifically, endogenous retrovirus K (ERV) families that are also known as long-terminal repeats (LTRs)—are activated as enhancers in meiosis (Sakashita et al. 2020). Notably, these meiotic enhancer ERVs (RLTR10B2) are among the up-regulated TEs (Fig. 7F). The meiotic enhancer ERVs are active in wild-type pachytene spermatocytes and are further up-regulated in *Atf7ip2*$^{-/-}$ cells. Thus, ATF7IP2 may fine-tune the activity of these TEs. In contrast, various TE types, particularly those enriched with LTRs and active in the pachytene stage, are down-regulated in *Atf7ip2*$^{-/-}$ spermatocytes. In all, our study identified distinct functions for ATF7IP2 in regulating protein-coding genes on autosomes and sex chromosomes, as well as in the regulation of TEs (Fig. 7H–J).

Discussion

Our study identified ATF7IP2 as a counterpart to ATF7IP that is highly expressed in the male germline and directs SETDB1-mediated H3K9 methylation—a conclusion supported by two major observations. First, in wild-type meiosis, ATF7IP2, SETDB1, and H3K9me3 accumulate on autosomal PCH; in pachytene spermatocytes, all are enriched on the X-PCH, the site from which they spread through the diplotene XY domain. Second, in *Atf7ip2*$^{-/-}$ pachytene spermatocytes, SETDB1 was grossly delocalized, and H3K9me2/3 was largely absent on the XY chromatin in the late pachytene to diplotene stages. As might be expected, the *Atf7ip2*$^{-/-}$ meiotic phenotype overlaps to some extent the meiotic phenotype of *Setdb1*-cKO mice. Thus, our study revealed the molecular logic for the management of SETDB1 and H3K9me3 in meiosis, demonstrating the unique nature of meiotic heterochromatin and its distinct regulation with respect to autosomes and the sex chromosomes.

However, in the early pachytene stage, there is a phenotypic difference between *Atf7ip2*$^{-/-}$ and *Setdb1*-cKO mice with regard to H3K9me3 localization: H3K9me3, a SETDB1-dependent marker of XY chromatin (Hirota et al. 2018; Abe et al. 2022), is affected by but not completely absent from XY chromatin in *Atf7ip2*$^{-/-}$ mice. Thus, there may be an alternate regulator of SETDB1 in early pachytene spermatocytes. In support of this possibility, *Setdb1*-cKO spermatocytes evidenced more severe chromosome synapsis defects (Hirota et al. 2018; Cheng et al. 2021; Abe et al. 2022) than *Atf7ip2*$^{-/-}$ spermatocytes. Nevertheless, the meiotic arrest phenotype indicates that the ATF7IP2-dependent regulation of SETDB1 (likely through an ATF7IP2–SETDB1 complex) and H3K9me3 becomes essential in the pachytene-to-diplotene transition. Curiously, we found that ATF7IP2 regulates ATF7IP localization in meiosis, highlighting the critical role of ATF7IP2 in meiosis. Although *Atf7ip* expression was reduced in the *Atf7ip2*$^{-/-}$ spermatocytes, in our ATF7IP2 CUT&Tag analysis, ATF7IP2 did not appear to bind to the *Atf7ip* gene promoter. We infer that the observed effects could be attributed to an indirect influence.

Our study also revealed novel aspects of the meiotic sex chromosomes. We propose that, through the recruitment of SETDB1, ATF7IP2 functions as an effector that links DDR signaling and SETDB1-mediated H3K9me3. The γH2AX-binding partner MDC1 is necessary for the recruitment of ATF7IP2 to X-PCH (Fig. 4G). A previous study proposed that TRIM28 (KAP1), a SETDB1 partner in ERV suppression, links the DDR and SETDB1 on the meiotic sex chromosomes (Hirota et al. 2018). However, we did not observe TRIM28 enrichment on XY, and so we question TRIM28's status as a linker. Furthermore, it was reported that young *Trim28* mutant mice are initially fertile and only become sterile with age (Tan et al. 2020), indicating that TRIM28 is not essential for MSCI.

We found that the enrichment of H3K9me2/3 on diplotene XY chromatin is largely ATF7IP2-dependent. Given the extensive histone replacement that occurs in MSCI (H3.1/H3.2 to H3.3) (van der Heijden et al. 2007), H3K9me2/3 deposition is likely to take place on "fresh" H3.3. In the latter stages of spermatogenesis, H3K9me2/3 is a persistent mark on the sex chromosomes, from MSCI to postmitotic silencing (Namekawa et al. 2007); thus, the ATF7IP2-dependent mechanisms described here could be driving heritable epigenetic states through meiotic divisions.

Unexpectedly, our study demonstrates that ATF7IP2 is required for global gene regulation in pachytene spermatocytes. In mid-pachytene spermatocytes, a burst of gene activation takes place that is driven by the transcription factor A-MYB (MYBL1) through the activation of meiotic enhancers (Bolcun-Filas et al. 2011; Maezawa et al. 2020). Thus, there is an intriguing possibility that such meiosis-specific transcription requires ATF7IP2. Importantly, ATF7IP2 is present at thousands of autosomal promoters,

where H3K9me3 is notably absent. Thus, ATF7IP2 could regulate transcriptional mechanisms independent of H3K9me3. Intriguingly, ATF7, an ATF7IP2-interacting protein, also accumulates on a wide range of autosomal promoters in testicular germ cells, mediating epigenetic inheritance through the regulation of H3K9me2 (Yoshida et al. 2020). In future studies, a key goal will be to determine the mechanistic relationship between ATF7IP2 and ATF7 in the context of meiotic gene regulation. While ATF7IP2's localization on the sex chromosomes requires MDC1, it is unknown what regulates its recruitment to autosomes, although one possibility is ATM-dependent DDR signaling. Furthermore, it is unknown what coordinates ATF7IP2's distinct autosomal and XY functions.

Finally, we show that ATF7IP2 fine-tunes the expression of retrotransposon-derived loci in male germ cells, a function that coincides with SETDB1's role in TE silencing. In *Atf7ip2*$^{-/-}$ spermatocytes, we observed the up-regulated expression of immune genes, a phenomenon akin to SETDB1-mediated immune escape in tumorigenesis (Griffin et al. 2021). In tumor cells, the depletion of SETDB1 facilitates the expression of immune genes, thereby driving the intrinsic immunogenicity of tumors. Also in tumor cells, SETDB1 works together with the HUSH complex—itself functionally linked to ATF7IP (Timms et al. 2016)—to suppress large domains of the genome enriched for rapidly evolved TEs (Griffin et al. 2021). Notably, a large number of the germline genes activated in pachytene spermatocytes are rapidly evolved (Soumillon et al. 2013), as are the meiotic ERV enhancer loci that drive germline gene expression (Sakashita et al. 2020). In wild-type spermatocytes, these loci are associated with broad domains of H3K9me3. Furthermore, like many tumor cells, testicular germ cells are immunoprivileged, found beyond the blood–testis barrier. Given the similarities between germ and tumor cells, it is possible that ATF7IP2-directed SETDB1 mechanisms, which regulate MSCI and TEs, drive the quick-paced evolution of the germline genome. It may be that this work establishes a foundation to understand the mechanisms behind germline evolution in mammals.

A recent study reported another *Atf7ip2* mutant mouse line (Shao et al. 2023), and although the mouse phenotypes detailed in the two studies were largely consistent, we did not observe the reported difference in XY obligatory crossover (Shao et al. 2023). This could be due to an *Atf7ip2* mutational difference in the mouse lines. Further investigations are warranted to clarify the role of ATF7IP2 in male meiosis.

Materials and methods

Animals

All mice were handled according to the guidelines of the Institutional Animal Care and Use Committee (IACUC; protocol nos. IACUC2018-0040 and 21931) at Cincinnati Children's Hospital Medical Center and the University of California, Davis.

Generation of Atf7ip2$^{-/-}$ *mice*

Atf7ip2$^{-/-}$ mice were generated using an sgRNA (target sequence TTCATGTCTACTCTTGCACT) that was selected according to location and the on-target and off-target scores from the web tool CRISPOR (Haeussler et al. 2016).

Preparation of meiotic chromosome spreads

Meiotic chromosome spread preparation, immunostaining, and data analysis were performed as described previously (Alavattam et al. 2018). Histology and immunostaining were performed as described previously (Abe et al. 2022).

Isolation of pachytene spermatocytes

Isolation of pachytene spermatocytes using fluorescence-activated cell sorting (FACS) was performed using an SH800S Cell Sorter (Sony), with Vybrant DyeCycle Violet (DCV)-stained (Invitrogen V35003) testicular single-cell suspensions prepared as described previously (Yeh et al. 2021).

Next-generation sequencing analysis

Library generation and data analyses for bulk RNA-seq, CUT&Tag, CUT&RUN, and scRNA-seq are described in the Supplemental Material.

Other detailed experimental procedures are described in the Supplemental Material.

Data availability

RNA-seq data and CUT&RUN/Tag data sets were deposited in the Gene Expression Omnibus (accession no. GSE244088). Bulk RNA-seq data for testes were deposited in the Gene Expression Omnibus (accession no. GSE223742). Single-cell RNA-seq data are available at the DNA Databank of Japan (DDBJ) Sequence Read Archive (DRA) under BioProject accession number PRJDB16643.

Competing interest statement

The authors declare no competing interests.

Acknowledgments

We thank Yoshinori Watanabe, Hiroki Shibuya, Akihiro Morimoto, and Shohei Yamamoto for their contributions to the early stage of this investigation; members of the Namekawa laboratory for discussion and helpful comments regarding this manuscript; So Maezawa and Masashi Yukawa for the initial RNA-seq analysis; Neil Hunter and Richard M. Schultz for discussion; Yasuhiro Fujiwara and Yuki Okada for aiding in the transfer of the anti-ATF7IP2 antibody; the Transgenic Animal and Genome Editing Core at Cincinnati Children's Hospital Medical Center for generation of the *Atf7ip2*$^{-/-}$ mouse model; Yoichi

Shinkai for providing the *Setdb1* floxed mouse line; Junjie Chen for providing the *Mdc1*-KO mice; and Mary Ann Handel for providing the anti-H1T antibody. Funding was received from National Institutes of Health (NIH) Training Program in Molecular and Cellular Biology grant T32GM007377 and a Ford Foundation Predoctoral Fellowship to J.M.E.; R01 GM134731 to P.R.A.; Grants-in-Aid for Scientific Research (KAKENHI) grants 19H05743 and 23H00379, Japan Agency for Medical Research and Development (AMED), Precursory Research for Innovative Medical Care (PRIME) grant 23gm6310021h0003, and the program of the Research for High Depth Omics, Institute of Molecular Embryology and Genetics Kumamoto University to K.-I.I.; and a University of California, Davis, startup fund and NIH R01 GM098605, R35 GM141085, and GM141085 diversity supplements to S.H.N.

Author contributions: K.G.A., J.M.E., M.H., R.S., K.-I.I., and S.H.N. designed the study. K.G.A., J.M.E., M.H., A.R.K., H.A., Y.K., Y.-H.Y., and J.K. performed experiments. K.G.A., J.M.E., M.H., A.R.K., H.A., and Y.K. analyzed the mouse phenotypes. J.M.E. and M.H. isolated germ cells and performed scRNA-seq experiments. M.H. performed bulk RNA-seq, CUT&Tag, and CUT&RUN experiments. R.S. analyzed the scRNA-seq data. K.G.A., J.M.E., M.H., R.S., Y.M., K.O., S.Y., K.-I.I., and S.H.N. designed and interpreted the computational analyses. Y.-C.H. generated the *Atf7ip2*$^{-/-}$ mouse line. K.G.A., J.M.E., M.H., R.S., P.R.A., K.-I.I., and S.H.N. interpreted the results and wrote the manuscript with critical feedback from all other authors. S.H.N. supervised the project.

References

Abe H, Alavattam KG, Kato Y, Castrillon DH, Pang Q, Andreassen PR, Namekawa SH. 2018. CHEK1 coordinates DNA damage signaling and meiotic progression in the male germline of mice. *Hum Mol Genet* **27:** 1136–1149. doi:10.1093/hmg/ddy022

Abe H, Yeh YH, Munakata Y, Ishiguro KI, Andreassen PR, Namekawa SH. 2022. Active DNA damage response signaling initiates and maintains meiotic sex chromosome inactivation. *Nat Commun* **13:** 7212. doi:10.1038/s41467-022-34295-5

Alavattam KG, Kato Y, Sin HS, Maezawa S, Kowalski IJ, Zhang F, Pang Q, Andreassen PR, Namekawa SH. 2016. Elucidation of the Fanconi anemia protein network in meiosis and its function in the regulation of histone modifications. *Cell Rep* **17:** 1141–1157. doi:10.1016/j.celrep.2016.09.073

Alavattam KG, Abe H, Sakashita A, Namekawa SH. 2018. Chromosome spread analyses of meiotic sex chromosome inactivation. *Methods Mol Biol* **1861:** 113–129. doi:10.1007/978-1-4939-8766-5_10

Alavattam KG, Maezawa S, Andreassen PR, Namekawa SH. 2022. Meiotic sex chromosome inactivation and the XY body: a phase separation hypothesis. *Cell Mol Life Sci* **79:** 18. doi:10.1007/s00018-021-04075-3

Ashburner M, Ball CA, Blake JA, Botstein D, Butler H, Cherry JM, Davis AP, Dolinski K, Dwight SS, Eppig JT, et al. 2000. Gene ontology: tool for the unification of biology. The gene ontology consortium. *Nat Genet* **25:** 25–29. doi:10.1038/75556

Becker JS, Nicetto D, Zaret KS. 2016. H3K9me3-dependent heterochromatin: barrier to cell fate changes. *Trends Genet* **32:** 29–41. doi:10.1016/j.tig.2015.11.001

Bellani MA, Romanienko PJ, Cairatti DA, Camerini-Otero RD. 2005. SPO11 is required for sex-body formation, and Spo11 heterozygosity rescues the prophase arrest of *Atm*$^{-/-}$ spermatocytes. *J Cell Sci* **118:** 3233–3245. doi:10.1242/jcs.02466

Berrios S. 2017. Nuclear architecture of mouse spermatocytes: chromosome topology, heterochromatin, and nucleolus. *Cytogenet Genome Res* **151:** 61–71. doi:10.1159/000460811

Bilodeau S, Kagey MH, Frampton GM, Rahl PB, Young RA. 2009. SetDB1 contributes to repression of genes encoding developmental regulators and maintenance of ES cell state. *Genes Dev* **23:** 2484–2489. doi:10.1101/gad.1837309

Bolcun-Filas E, Bannister LA, Barash A, Schimenti KJ, Hartford SA, Eppig JJ, Handel MA, Shen L, Schimenti JC. 2011. A-MYB (MYBL1) transcription factor is a master regulator of male meiosis. *Development* **138:** 3319–3330. doi:10.1242/dev.067645

Broering TJ, Alavattam KG, Sadreyev RI, Ichijima Y, Kato Y, Hasegawa K, Camerini-Otero RD, Lee JT, Andreassen PR, Namekawa SH. 2014. BRCA1 establishes DNA damage signaling and pericentric heterochromatin of the X chromosome in male meiosis. *J Cell Biol* **205:** 663–675. doi:10.1083/jcb.201311050

Cheng EC, Hsieh CL, Liu N, Wang J, Zhong M, Chen T, Li E, Lin H. 2021. The essential function of SETDB1 in homologous chromosome pairing and synapsis during meiosis. *Cell Rep* **34:** 108575. doi:10.1016/j.celrep.2020.108575

Fernandez-Capetillo O, Mahadevaiah SK, Celeste A, Romanienko PJ, Camerini-Otero RD, Bonner WM, Manova K, Burgoyne P, Nussenzweig A. 2003. H2AX is required for chromatin remodeling and inactivation of sex chromosomes in male mouse meiosis. *Dev Cell* **4:** 497–508. doi:10.1016/S1534-5807(03)00093-5

Griffin GK, Wu J, Iracheta-Vellve A, Patti JC, Hsu J, Davis T, Dele-Oni D, Du PP, Halawi AG, Ishizuka JJ, et al. 2021. Epigenetic silencing by SETDB1 suppresses tumour intrinsic immunogenicity. *Nature* **595:** 309–314. doi:10.1038/s41586-021-03520-4

Haeussler M, Schönig K, Eckert H, Eschstruth A, Mianné J, Renaud JB, Schneider-Maunoury S, Shkumatava A, Teboul L, Kent J, et al. 2016. Evaluation of off-target and on-target scoring algorithms and integration into the guide RNA selection tool CRISPOR. *Genome Biol* **17:** 148. doi:10.1186/s13059-016-1012-2

Hasegawa K, Sin HS, Maezawa S, Broering TJ, Kartashov AV, Alavattam KG, Ichijima Y, Zhang F, Bacon WC, Greis KD, et al. 2015. SCML2 establishes the male germline epigenome through regulation of histone H2A ubiquitination. *Dev Cell* **32:** 574–588. doi:10.1016/j.devcel.2015.01.014

Hirota T, Blakeley P, Sangrithi MN, Mahadevaiah SK, Encheva V, Snijders AP, ElInati E, Ojarikre OA, de Rooij DG, Niakan KK, et al. 2018. SETDB1 links the meiotic DNA damage response to sex chromosome silencing in mice. *Dev Cell* **47:** 645–659.e6. doi:10.1016/j.devcel.2018.10.004

Ichimura T, Watanabe S, Sakamoto Y, Aoto T, Fujita N, Nakao M. 2005. Transcriptional repression and heterochromatin formation by MBD1 and MCAF/AM family proteins. *J Biol Chem* **280:** 13928–13935. doi:10.1074/jbc.M413654200

Ichijima Y, Ichijima M, Lou Z, Nussenzweig A, Camerini-Otero RD, Chen J, Andreassen PR, Namekawa SH. 2011. MDC1 directs chromosome-wide silencing of the sex chromosomes in male germ cells. *Genes Dev* **25:** 959–971. doi:10.1101/gad.2030811

Inselman A, Eaker S, Handel MA. 2003. Temporal expression of cell cycle-related proteins during spermatogenesis: establishing a timeline for onset of the meiotic divisions. *Cytogenet Genome Res* **103:** 277–284. doi:10.1159/000076813

Ishiguro KI, Matsuura K, Tani N, Takeda N, Usuki S, Yamane M, Sugimoto M, Fujimura S, Hosokawa M, Chuma S, et al. 2020. MEIOSIN directs the switch from mitosis to meiosis in mammalian germ cells. *Dev Cell* **52:** 429–445.e10. doi:10.1016/j.devcel.2020.01.010

Kojima ML, de Rooij DG, Page DC. 2019. Amplification of a broad transcriptional program by a common factor triggers the meiotic cell cycle in mice. *Elife* **8:** e43738. doi:10.7554/eLife.43738

Li XZ, Roy CK, Dong X, Bolcun-Filas E, Wang J, Han BW, Xu J, Moore MJ, Schimenti JC, Weng Z, et al. 2013. An ancient transcription factor initiates the burst of piRNA production during early meiosis in mouse testes. *Mol Cell* **50:** 67–81. doi:10.1016/j.molcel.2013.02.016

Liu S, Brind'Amour J, Karimi MM, Shirane K, Bogutz A, Lefebvre L, Sasaki H, Shinkai Y, Lorincz MC. 2014. *Setdb1* is required for germline development and silencing of H3K9me3-marked endogenous retroviruses in primordial germ cells. *Genes Dev* **28:** 2041–2055. doi:10.1101/gad.244848.114

Maezawa S, Hasegawa K, Alavattam KG, Funakoshi M, Sato T, Barski A, Namekawa SH. 2018a. SCML2 promotes heterochromatin organization in late spermatogenesis. *J Cell Sci* **131:** jcs217125. doi:10.1242/jcs.217125

Maezawa S, Hasegawa K, Yukawa M, Kubo N, Sakashita A, Alavattam KG, Sin HS, Kartashov AV, Sasaki H, Barski A, et al. 2018b. Polycomb protein SCML2 facilitates H3K27me3 to establish bivalent domains in the male germline. *Proc Natl Acad Sci* **115:** 4957–4962. doi:10.1073/pnas.1804512115

Maezawa S, Sakashita A, Yukawa M, Chen X, Takahashi K, Alavattam KG, Nakata I, Weirauch MT, Barski A, Namekawa SH. 2020. Super-enhancer switching drives a burst in gene expression at the mitosis-to-meiosis transition. *Nat Struct Mol Biol* **27:** 978–988. doi:10.1038/s41594-020-0488-3

Mahadevaiah SK, Turner JM, Baudat F, Rogakou EP, de Boer P, Blanco-Rodríguez J, Jasin M, Keeney S, Bonner WM, Burgoyne PS. 2001. Recombinational DNA double-strand breaks in mice precede synapsis. *Nat Genet* **27:** 271–276. doi:10.1038/85830

Matsui T, Leung D, Miyashita H, Maksakova IA, Miyachi H, Kimura H, Tachibana M, Lorincz MC, Shinkai Y. 2010. Proviral silencing in embryonic stem cells requires the histone methyltransferase ESET. *Nature* **464:** 927–931. doi:10.1038/nature08858

Mochizuki K, Tando Y, Sekinaka T, Otsuka K, Hayashi Y, Kobayashi H, Kamio A, Ito-Matsuoka Y, Takehara A, Kono T, et al. 2018. SETDB1 is essential for mouse primordial germ cell fate determination by ensuring BMP signaling. *Development* **145:** dev164160. doi:10.1242/dev.164160

Namekawa SH, VandeBerg JL, McCarrey JR, Lee JT. 2007. Sex chromosome silencing in the marsupial male germ line. *Proc Natl Acad Sci* **104:** 9730–9735. doi:10.1073/pnas.0700323104

Nicetto D, Zaret KS. 2019. Role of H3K9me3 heterochromatin in cell identity establishment and maintenance. *Curr Opin Genet Dev* **55:** 1–10. doi:10.1016/j.gde.2019.04.013

Peters AH, O'Carroll D, Scherthan H, Mechtler K, Sauer S, Schöfer C, Weipoltshammer K, Pagani M, Lachner M, Kohlmaier A, et al. 2001. Loss of the Suv39h histone methyltransferases impairs mammalian heterochromatin and genome stability. *Cell* **107:** 323–337. doi:10.1016/S0092-8674(01)00542-6

Rowe HM, Friedli M, Offner S, Verp S, Mesnard D, Marquis J, Aktas T, Trono D. 2013. De novo DNA methylation of endogenous retroviruses is shaped by KRAB-ZFPs/KAP1 and ESET. *Development* **140:** 519–529. doi:10.1242/dev.087585

Royo H, Prosser H, Ruzankina Y, Mahadevaiah SK, Cloutier JM, Baumann M, Fukuda T, Höög C, Tóth A, de Rooij DG, et al. 2013. ATR acts stage specifically to regulate multiple aspects of mammalian meiotic silencing. *Genes Dev* **27:** 1484–1494. doi:10.1101/gad.219477.113

Sakashita A, Maezawa S, Takahashi K, Alavattam KG, Yukawa M, Hu YC, Kojima S, Parrish NF, Barski A, Pavlicev M, et al. 2020. Endogenous retroviruses drive species-specific germline transcriptomes in mammals. *Nat Struct Mol Biol* **27:** 967–977. doi:10.1038/s41594-020-0487-4

Saksouk N, Simboeck E, Déjardin J. 2015. Constitutive heterochromatin formation and transcription in mammals. *Epigenetics Chromatin* **8:** 3. doi:10.1186/1756-8935-8-3

Scherthan H, Schöfisch K, Dell T, Illner D. 2014. Contrasting behavior of heterochromatic and euchromatic chromosome portions and pericentric genome separation in pre-bouquet spermatocytes of hybrid mice. *Chromosoma* **123:** 609–624. doi:10.1007/s00412-014-0479-4

Seisenberger S, Andrews S, Krueger F, Arand J, Walter J, Santos F, Popp C, Thienpont B, Dean W, Reik W. 2012. The dynamics of genome-wide DNA methylation reprogramming in mouse primordial germ cells. *Mol Cell* **48:** 849–862. doi:10.1016/j.molcel.2012.11.001

Shao Q, Zhang Y, Liu Y, Shang Y, Li S, Liu L, Wang G, Zhou X, Wang P, Gao J, et al. 2023. ATF7IP2, a meiosis-specific partner of SETDB1, is required for proper chromosome remodeling and crossover formation during spermatogenesis. *Cell Rep* **42:** 112953. doi:10.1016/j.celrep.2023.112953

Soumillon M, Necsulea A, Weier M, Brawand D, Zhang X, Gu H, Barthès P, Kokkinaki M, Nef S, Gnirke A, et al. 2013. Cellular source and mechanisms of high transcriptome complexity in the mammalian testis. *Cell Rep* **3:** 2179–2190. doi:10.1016/j.celrep.2013.05.031

Tan JHL, Wollmann H, van Pelt AMM, Kaldis P, Messerschmidt DM. 2020. Infertility-causing haploinsufficiency reveals TRIM28/KAP1 requirement in spermatogonia. *Stem Cell Reports* **14:** 818–827. doi:10.1016/j.stemcr.2020.03.013

Timms RT, Tchasovnikarova IA, Antrobus R, Dougan G, Lehner PJ. 2016. ATF7IP-mediated stabilization of the histone methyltransferase SETDB1 is essential for heterochromatin formation by the HUSH complex. *Cell Rep* **17:** 653–659. doi:10.1016/j.celrep.2016.09.050

Tsusaka T, Shimura C, Shinkai Y. 2019. ATF7IP regulates SETDB1 nuclear localization and increases its ubiquitination. *EMBO Rep* **20:** e48297. doi:10.15252/embr.201948297

Tsusaka T, Fukuda K, Shimura C, Kato M, Shinkai Y. 2020. The fibronectin type-III (FNIII) domain of ATF7IP contributes to efficient transcriptional silencing mediated by the SETDB1 complex. *Epigenetics Chromatin* **13:** 52. doi:10.1186/s13072-020-00374-4

Turner JM. 2015. Meiotic silencing in mammals. *Annu Rev Genet* **49:** 395–412. doi:10.1146/annurev-genet-112414-055145

van der Heijden GW, Derijck AA, Pósfai E, Giele M, Pelczar P, Ramos L, Wansink DG, van der Vlag J, Peters AH, de Boer P. 2007. Chromosome-wide nucleosome replacement and H3.3 incorporation during mammalian meiotic sex chromosome inactivation. *Nat Genet* **39:** 251–258. doi:10.1038/ng1949

Yeh YH, Hu M, Nakagawa T, Sakashita A, Yoshida S, Maezawa S, Namekawa SH. 2021. Isolation of murine spermatogenic cells using a violet-excited cell-permeable DNA binding dye. *J Vis Exp* **2021:** e61666. doi:10.3791/61666

Yoshida K, Maekawa T, Ly NH, Fujita SI, Muratani M, Ando M, Katou Y, Araki H, Miura F, Shirahige K, et al. 2020. ATF7-dependent epigenetic changes are required for the intergenerational effect of a paternal low-protein diet. *Mol Cell* **78:** 445–458.e6. doi:10.1016/j.molcel.2020.02.028

Supplemental Material

Methods

Animals

Mice were maintained on a 12:12 light:dark cycle in a temperature- and humidity-controlled vivarium (22 ± 2 °C; 40–50% humidity) with free access to food and water in a pathogen-free animal care facility. All mice were handled according to the guidelines of the Institutional Animal Care and Use Committee (IACUC: protocol no. IACUC2018-0040 and 21931) at Cincinnati Children's Hospital Medical Center and the University of California, Davis. At least three independent littermate pairs were used as biological replicates for all experiments with the exception of the scRNA-seq, P14 whole-testis bulk RNA-seq, and CUT&Tag next-generation sequencing experiments, which were performed using two independent biological replicates. C57BL/6 (hereafter described as B6) mice were used for all experiments involving *Atf7ip2*$^{-/-}$ mice and littermate controls. To generate *Setdb1*-cKO (*Setdb1*$^{flox/flox}$: *Ddx4-Cre*$^{Tg/+}$) mice, a male carrying the *Setdb1*$^{flox/+}$: *Ddx4-Cre*$^{Tg/+}$ alleles was crossed with a female carrying the *Setdb1*$^{flox/flox}$ allele as described in our previous report (Abe et al. 2022). Males carrying the *Setdb1*$^{flox/+}$; *Ddx4-Cre*$^{Tg/+}$ alleles obtained from the same litter were used as littermate controls. The control and *Setdb1*cKO mice greater than three weeks of age were harvested and analyzed. The *Mdc1* knockout (*Mdc1*$^{-/-}$) mice used in this study are described in our previous report (Ichijima et al. 2011). In this study, the definition of postnatal days is the same as days postpartum.

Generation of *Atf7ip2*$^{-/-}$ mice

Atf7ip2$^{-/-}$ mice were generated using a sgRNA (target sequence: TTCATGTCTACTCTTGCACT) that was selected according to location and the on- and off-target scores from the web tool CRISPOR (Haeussler et al. 2016). The sgRNA was *in vitro* synthesized using a MEGAshorscript T7 kit (Thermo Fisher) and purified using a MEGAclear Kit (Thermo Fisher), according to the manufacturer's instructions. The sgRNA (100 ng/μL) and Cas9 protein (200 ng/μL, Thermo Fischer) were mixed at 37 °C for 15 min to form the ribonucleoprotein complex, then injected into the cytoplasm of one cell-stage embryos in the C57BL/6N genetic background by piezo-driven microinjection (Scott and Hu 2019). Injected embryos were immediately transferred into the oviductal ampulla of pseudopregnant CD-1 females. Live-born pups were genotyped by PCR and Sanger sequencing (data not shown).

Preparation of meiotic chromosome spreads

Meiotic chromosome spreads from testes were prepared essentially as described (Alavattam et al. 2018). Testes were excised, detunicated, and placed in 1× phosphate-buffered saline (PBS). Seminiferous tubules were dissociated from whole testes. Seminiferous tubules were transferred to one well of a four-well dish (Thermo Fisher Nunc, 055047) containing 1 mL of cold PBS kept on ice. Seminiferous tubules were then gently unraveled into small clumps with fine-point tweezers; care was taken not to tear or mince the tubules. The clumps of seminiferous tubules were subsequently transferred to the second and third wells of 1 mL PBS for additional unraveling before transfer to the fourth well, which contained 1 mL hypotonic extraction buffer [HEB: 30 mM Tris base, 17 mM trisodium citrate, 5 mM ethylenediaminetetraacetic acid (EDTA), 50 mM sucrose, 5 mM dithiothreitol (DTT), and 1× cOmplete Protease Inhibitor

Cocktail (Sigma, 11836145001), pH. 8.2]. Once there, fine-point tweezers were used to carefully expose the surface area of tubules to HEB. The seminiferous tubules were incubated in HEB on ice for 30 min with gentle stirring every 10 min. After incubation, seminiferous tubules were mashed using a disposable surgical blade in 60 μL of 100 mM sucrose on a plain, uncharged microscope slide (Gold Seal: Thermo Fisher Scientific, 3010–002). After approximately 15–25 mashes, a semi-translucent cell suspension was formed. An additional 120 μL of sucrose (100 mM) was added to the suspension, and the suspension was mixed via gentle pipetting up and down several times. The diluted cell suspension was applied to positively charged slides (Probe On Plus: Thermo Fisher Scientific, 22-230-900) in volumes of 30 μL; before application of the suspension, the slides had been incubated in chilled fixation solution (2% paraformaldehyde, 0.1% Triton X-100, and 0.02% sodium monododecyl sulfate, adjusted to pH 9.2 with sodium borate buffer) for a minimum of 2 min. After applying the cell suspension/sucrose mixture, the slide was slowly and gently tilted up and down at slight angles (<10°) to mix the cell suspension/sucrose mixture with the remaining fixation solution. The slides were placed in "humid chambers" (closed pipet tip boxes filled to approximately two-thirds volume with water) at RT for a minimum of 1 h (maximum overnight). Then, the slides were washed in a low-concentration surfactant, 0.4% Photo-Flo 200 (Kodak, 146– 4510), at RT two times, 2 min per wash. Slides were dried completely at RT (~30 min) before staining or storage in slide boxes at −80 °C.

Immunostaining of meiotic chromosome spreads

For immunostaining experiments, chromosome spreads were incubated in 1× PBS containing 0.1% Tween 20 (PBST) for 5–30 min before blocking in antibody dilution buffer (PBST containing 0.15% BSA) for an additional 30–60 min. Primary and secondary antibodies (described below) were diluted in an antibody dilution buffer. Then, chromosome spreads were coated with 100 μL of the antibody/antibody dilution buffer solution, gently covered with Parafilm (Parafilm M All-Purpose Laboratory Film, Bemis Company, Inc.), and stored in humid chambers at 4 °C for a minimum of 6 h to a maximum of overnight (~15 h). This study made use of the following primary antibodies at the following dilutions [format: host anti-protein (source or company with product/catalog number if applicable), dilution]: rabbit anti-ATF7IP2 (generated for this study and recognizing amino acids 201–452 of mouse ATF7IP2), 1/500; mouse anti-SYCP3 (Abcam, ab97672), 1/5,000; rabbit anti-SYCP3 (Novus, NB300–232), 1/500; rabbit anti-SYCP1 (Abcam, ab15090), 1/500; rabbit anti-H3K9me3 (Abcam, ab8898), 1/500; rabbit anti-H3K9me3 (Millipore, 07-442), 1/200; mouse anti-H3K9me2 (Abcam, ab1220), 1/500; rabbit anti-H3K9me1 (Millipore, 04-450), 1/500; rabbit anti-H3K9me1 (Millipore, 07-450), 1/500; rabbit anti-H3K9Ac (Millipore, 06-942), 1/500; mouse anti-SYCP3 conjugated with Alexa-488 (Abcam, ab205846), ½,000; rabbit anti-SCML2 (generated in the Namekawa Lab (Hasegawa et al. 2015)), 1/500; rabbit anti-SETDB1 (Proteintech, 11231-1-AP), 1/200; guinea pig anti-H1T (a gift from Dr. Mary Ann Handel (Inselman et al. 2003)), 1/500; rabbit anti-MLH1 (Santa Cruz, sc-11442), 1/200; mouse anti-TRIM28 (Active Motif, 61173), 1/250; rabbit anti-CHD4 (Active Motif, 39290), 1/100; mouse anti-H2AX-pS139 (γH2AX: Millipore, 05-636-1), 1/5,000; mouse anti-H2AX-pS139 conjugated Alexa 647 (γH2AX: Millipore, 05-636-AF647), 1/5,000; rabbit anti-ATF7IP (Abcam, ab84497), 1/500; and sheep anti-MDC1 (ABD Sertec, AHP799), 1/500. After incubation with primary antibodies, slides were washed three times in PBST, 5 min per wash. Then, the slides were incubated with the appropriate secondary antibodies conjugated to Alexa 488, 555, or 647 fluorophores (Thermo Fisher Scientific). All

secondary antibodies were diluted 1/500 in antibody dilution buffer. Slides were coated with 100 µL of the antibody/antibody dilution buffer solution; then, they were gently covered with Parafilm for 1 h incubation at RT in humid chambers in darkness. After slides were washed three times in PBST in darkness, 5 min per wash, they were counterstained with the DNA-binding chemical 4′,6-diamidino-2-phenylindole (DAPI; Sigma, D9542–5MG) diluted to 1 µg/mL concentration in PBS. Finally, slides were mounted using 20 µL undiluted ProLong Gold Antifade Mountant (Thermo Fisher Scientific, P36930). Slides were either imaged immediately or stored at 4 °C in darkness for later imaging. Images were obtained with an ECLIPSE Ti-2 microscope (Nikon) equipped with an ORCA-Fusion sCMOS camera (Hamamatsu) and a 60× CFI Apochromat TIRF oil immersion objective NA 1.4 (Nikon), and were processed using NIS-Elements Basic Research (Nikon), Photoshop (Adobe), and Illustrator (Adobe) software.

Judgement of pachytene substages

Histone variant H1T is expressed starting in the mid-pachytene stage of male mouse meiosis (Drabent et al. 1996), and the duration of the pachytene stage is approximately 160 h (7 days) in mouse spermatogenesis (van der Heijden et al. 2007). H1T-negative early pachytene spermatocytes and H1T-positive mid-late pachytene spermatocytes were separately analyzed based on H1T staining. In addition to assessing H1T, pachytene substages were determined by examining the morphology of chromosome axes stained with the anti-SYCP3 antibody as previously described (Alavattam et al. 2016; Alavattam et al. 2018).

Histology and immunostaining

For the preparation of testis paraffin blocks, testes were fixed with 4% paraformaldehyde and 0.1% Triton X-100 in PBS at 4 °C overnight. Testes were dehydrated and embedded in paraffin. For histological analyses, 6 µm-thick paraffin sections were deparaffinized and stained with hematoxylin and eosin. For immunostaining, sections were autoclaved in Target Retrieval Solution, Citrate pH 6.1 (DAKO, S-1700) at 121 °C and 100 kPa (15 psi) for 10 min. The sections were blocked with Blocking One Histo (Nacalai USA, 06349–64) at RT for 30 min; the sections were then incubated with primary antibodies diluted in PBST at 4 °C overnight. The following antibodies were used at the following dilutions [format: host anti-protein (source or company with product/catalog number), dilution]: mouse anti-H2AX-pS139 (γH2AX: Millipore, 05-636), 1/5000; guinea pig anti-H1T (a gift from Dr. Mary Ann Handel (Inselman et al. 2003)), 1/500; rabbit anti-ATF7IP (Abcam, ab84497), 1/500; rabbit anti-STRA8 (Abcam, ab49602), 1/500; goat anti-ZBTB16/PLZF (R&D Systems, AF2944); 1/500; goat anti-CD117/c-KIT (R&D Systems, AF1356), 1/500; mouse anti-H2AX-pS139 (γH2AX: Millipore, 05-636), 1/5000; and mouse anti-H2AX-pS139 conjugated to Alexa 647 (γH2AX: Millipore, 05-636-AF647), 1/5,000. The resulting signals were detected with secondary antibodies conjugated to Alexa 488 or 555 (Thermo Fisher Scientific), diluted 1/1,000 in PBST, and incubated at RT for 1 h. Sections were counterstained with DAPI as described above. Images were obtained with a Zeiss LSM800 confocal microscope equipped with an Axiocam 506 monochrome camera (Zeiss) and a C-Apochromat 40×/1.2 water lens (Zeiss), and were processed using Fiji (NIH) (Schindelin et al. 2012), Photoshop (Adobe), and Illustrator (Adobe) software.

Isolation of pachytene spermatocytes

Isolation of pachytene spermatocytes using fluorescence-activated cell sorting (FACS) was performed using a SONY SH800S instrument, with Vybrant DyeCycle Violet Stain (DCV)

(Invitrogen, V35003) stained testicular single-cell suspensions prepared as described previously (Yeh et al. 2021). For H3K9me3 CUT&RUN experiments and bulk RNA-seq experiments, early-to-mid pachytene spermatocytes were isolated from P15 *Atf7ip2*$^{+/+}$ mice, when germ cells reach early-mid pachynema in the first wave of spermatogenesis. As spermatocytes are arrested at mid-pachynema in *Atf7ip2*$^{-/-}$ mice, >P15 mice were used for isolating arrested pachytene spermatocytes from *Atf7ip2*$^{-/-}$ mice. For ATF7IP2 CUT&Tag experiments and H3K9me3 CUT&RUN experiments using wild-type pachytene spermatocytes, adult C57BL/6J mice were used for isolation of pachytene spermatocytes.

In brief, to prepare single cells suspensions for cell sorting, detangled seminiferous tubules from adult mouse testes were first washed with 1× Hanks' Balanced Salt Solution (HBSS, Gibco, 14175095) 3 times and then incubated with 1 mg/mL collagenage type 1 (Worthington, CLS1) for 20 min at 35 °C to remove interstitial cells. Then, the tubules were digested in Dulbecco's Modified Eagle Medium (DMEM, Gibco, 11885076) containing 2% Fetal Bovine Serum (FBS, Gibco, 16000044), 2 mg/mL collagenase type 1, 0.25 mg/mL DNase I (Sigma, D5025), 1.5 mg/mL hyaluronidase (Sigma, H3506) and 700 U/ml recombinant collagenase (FUJIFILM Wako Pure Chemical Corporation, 036-23141) at 35 ℃ for 20–30 min with vigorous pipetting for cell dissociation. The resulting cell suspension was plated in lectin from *Datura stramonium* (Sigma L2766)-coated plates for 20 min in DMEM/F-12 medium (Gibco, 11330107) supplemented with 10% fetal bovine serum (FBS), which promoted the adhesion of the remaining somatic cells. The floating germ cell-enriched cell suspension was then collected from plates and washed with 10 mL FACS buffer (PBS containing 2% FBS) 3 times by centrifugation at 300 × g for 5 min and filtered through a 70 μm nylon cell strainer (Falcon, 352350). The resultant single cells were stained with DCV. After 30 min incubation at 35 ℃, cells were filtered into a 5 mL FACS tube through a 35 μm nylon mesh cap (Falcon, 352235). Samples were kept on ice until sorting.

Single-cell RNA-seq library generation

Testes were collected from two P15 *Atf7ip2*$^{+/+}$ and three P15 *Atf7ip2*$^{-/-}$ mice. In brief, to prepare a testicular single-cell suspension, detangled seminiferous tubules from adult mouse testes were first washed with 1× HBSS three times and then incubated in DMEM containing 2% FBS, 2 mg/mL collagenase type 1, 0.25 mg/mL DNase I, 1.5 mg/mL hyaluronidase, and 700 U/mL recombinant collagenase at 35 °C for 20 min. Then, the tubules were dissociated using vigorous pipetting before being incubated at 35 ℃ for another 10 min. The single cell suspension was then washed with 10 mL FACS buffer (PBS containing 2% FBS) three times by centrifugation at 300 × g for 5 min prior to being filtered into a 5 mL FACS tube through a 35 μm nylon mesh cap (Falcon, 352235). 7-AAD Viability Staining Solution (Invitrogen, 00-6993-50) was added to cell suspension for the exclusion of dead cells. Cells were collected using a SONY Cell Sorter SH800 after removing 7-AAD-positive dead cells.

Collected cells were resuspended in PBS containing 2% BSA and submitted to the DNA Technologies & Expression Analysis Core of the University of California, Davis, for library preparation. Briefly, suspensions of approximately 10,000 single cells were loaded on the Chromium Controller (10X Genomics Inc.). Single-cell RNA-seq libraries were generated using Chromium Single Cell 3' Reagent Kits (v3) following the manufacturer's instructions and sequenced on an Element Biosciences AVITI system with 75-bp paired-end reads.

Bulk RNA-seq library generation with ERCC RNA spike-in for isolated pachytene spermatocytes

RNA-seq libraries were prepared from *Atf7ip2*$^{+/+}$ and *Atf7ip2*$^{-/-}$ pachytene spermatocytes using the Smart-Seq2 method (Picelli et al. 2014). For each of the two independent biological replicates, approximately 10,000 cells were used. Prior to RNA extraction, the External RNA Controls Consortium (ERCC) RNA Spike-In Mix (Invitrogen, 4456740) was added to the cell lysis. This mix was first diluted 1,000-fold with nuclease-free water, and then 1 µL of this dilution was added to each suspension of 10,000 cells.

Total RNA was extracted using an RNeasy Plus Micro Kit (QIAGEN, 74034) according to the manufacturer's instructions. Libraries were constructed using a NEBNext Single Cell/Low Input RNA Library Prep Kit for Illumina (NEB, E6420S) according to the manufacturer's instructions. Prepared RNA-seq libraries were sequenced on a HiSeq 4000 system (Illumina) with 150-bp paired-end reads.

Bulk RNA-seq library generation for juvenile testes samples

For whole-testis bulk RNA-seq library preparation, total RNA was purified from *Atf7ip2*$^{+/+}$ or *Atf7ip2*$^{-/-}$ testes using an RNeasy Plus Micro Kit (QIAGEN, 74034) according the manufacturer's instructions. Two independent biological replicates were used for the RNA-seq library generation. RNA quality and quantity were checked using, respectively, a Bioanalyzer (Agilent) and Qubit (Life Technologies). Library construction was performed by the CCHMC DNA Sequencing and Genotyping Core (Cincinnati, Ohio, USA) using the TruSeq stranded mRNA Kit (Illumina) after polyA enrichment. Prepared RNA-seq libraries were sequenced on a Novaseq 6000 system (Illumina) with 100-bp paired-end reads.

CUT&RUN/Tag library generation

Atf7ip2$^{+/+}$ or *Atf7ip2*$^{-/-}$ pachytene-spermatocyte H3K9me3 CUT&RUN library preparation was conducted as previously described (Skene et al. 2018). A step-by-step protocol is available from protocols.io: https://www.protocols.io/view/cut-amp-run-targeted-in-situ-genome-wide-profiling-14egnr4ql5dy/v3. For each of the two independent biological replicates, approximately 10,000 cells were used. The antibody used was rabbit anti-H3K9me3 (Abcam, ab8898) at 1/100 dilution. Homemade Protein A/G-MNase was provided by the laboratory of Dr. Artem Barski. Quantitative spike-in with *E. coli* DNA (0.4 ng/10,000 cells) was included in each reaction. The libraries, constructed using NEBNext Ultra II DNA Library Prep Kit for Illumina (NEB, E7645S), were sequenced on a HiSeq 4000 system with 150-bp paired-end reads.

Wild-type pachytene-spermatocyte ATF7IP2 CUT&Tag library preparation with rabbit anti-ATF7IP2 (generated for this study) at 1/100 and IgG control (Rabbit mAb IgG; CST, 66362) was prepared using CUTANA pAG-Tn5 (Epicypher, 15-1017), as previously described (Kaya-Okur et al. 2019; Kaya-Okur et al. 2020). A step-by-step protocol is available from protocols.io: https://www.protocols.io/view/bench-top-cut-amp-tag-kqdg34qdpl25/v3. CUT&Tag libraries were constructed and sequenced as described in the preceding paragraph.

scRNA-seq data processing

FASTQ files were processed and aligned to the mouse mm10 transcriptome (GENCODE vM23/Ensembl 98) using the 10X Genomics Cell Ranger pipeline (version 7.0.0). Further analyses were conducted using R (version 3.6.2) via RStudio (version 1.2.1335). Quality assessment of scRNA-seq data and primary analyses were conducted using the package Seurat (version 3.2.2) (Butler et al. 2018)(Stuart et al. 2019). To exclude the effects of low-quality cells, only those cells that expressed more than 200 genes were used for further analyses. The scRNA-seq data were merged and normalized using the Seurat function SCTransform. Dimension reduction analyses and visualization of clusters were conducted using the Seurat function RunUMAP. The clustering of cells was conducted using Seurat functions FindNeighbors and FindClusters with default settings. The determination of differentially expressed genes (DEGs) was performed using the Seurat function FindAllMarkers with the following options: only.pos = TRUE, min.pict = 0.25, and logfc.threshold = 0.25; this was performed to identify marker genes for each cluster. The Seurat function FindMarker was called with default settings to characterize arbitrary groups of cells. To extract the germ cell population, cell populations expressing the germ-cell marker *Ddx4* were selected. Selected cell populations were then re-plotted on the UMAP. Cell populations exhibiting the expression of somatic-cell marker genes and the enrichment of mitochondrial genes were removed; the remaining cells were used as germ-cell populations. RNA velocity analysis was conducted using the RNA velocyto package (La Manno et al. 2018) for Python (Python 3.7.3) and R with default settings. They were visualized on UMAP plots via Seurat.

Gene enrichment analyses were performed using Metascape (Zhou et al. 2019) with default settings, and the results were visualized using R and Prism 9 (GraphPad). To characterize features of each cluster, the top 100 representative genes in each cluster were used. The genes located on autosomes and sex chromosomes were obtained from an mm10 GTF file. Average expression values of genes on autosomes and sex chromosomes were calculated using normalized values for each gene.

Bulk RNA-seq with ERCC spike-in data processing

Trim Galore (version 0.6.6) was used to trim raw RNA-seq reads with the --paired parameter prior to alignment to the mouse genome (GRCm38/mm10) using STAR (version 2.5.4b) (Dobin et al. 2013). Raw read-count files were generated using featureCounts (version 2.0.1) (Liao et al. 2014), incorporating UCSC mouse RefGene and ERCC annotated sequences. For ERCC spike-in normalization and analysis, the edgeR (Robinson et al. 2010) and Limma (Ritchie et al. 2015) packages were employed. Normalization factors were calculated from reads mapped to ERCC annotated sequences, followed by the filtering of raw reads such that there were a minimum of two counts in at least one sample. The filtered reads were assessed for library size using normalization factors prior to voom transformation. The topTable function was used to identify differentially expressed genes (DEGs) through the following criteria: Benjamini-Hochberg-adjusted p-value < 0.05 and Log2FoldChange > 2. For GO analyses of DEGs, we utilized Metascape (Zhou et al. 2019). Heatmaps of expression profiles were generated using Morpheus (https://software.broadinstitute.org/morpheus).

Testis bulk RNA-seq data processing

Raw RNA-seq reads were trimmed and filtered using trimmomatic (version 0.39) (Bolger et al. 2014) prior to alignment to the mouse genome (GRCm38/mm10) using STAR (version 2.5.4b)

(Dobin et al. 2013). To exclude >1 multi-mapping alignments, STAR was invoked with the parameter --outFilterMultimapNmax 1. For analyses, the sequencing data were uploaded to the Galaxy web platform (Afgan et al. 2016). To identify DEGs between *Atf7ip2*$^{+/+}$ or the *Atf7ip2*$^{-/-}$ conditions, raw read-count files were generated using featureCounts (version 2.0.1) (Liao et al. 2014) with respect to the UCSC mouse RefGene annotation. After quantification, a read-count file was input to DESeq2 (version. 1.38.2) (Love et al. 2014) for differential gene expression analyses. DEGs were identified through the following criteria: Benjamini-Hochberg-adjusted p-value ≤ 0.05 and fold change ≥ 1.5 among expressed genes, which were defined as having TPM values >1 in either *Atf7ip2*$^{+/+}$ or *Atf7ip2*$^{-/-}$.

P-values for autosome and sex-chromosome comparisons were obtained from hypergeometric tests. Average fold changes for autosomes and sex chromosomes were calculated from the per-chromosome TPM averages for *Atf7ip2*$^{+/+}$ or *Atf7ip2*$^{-/-}$. Genes with TPM > 1 in *Atf7ip2*$^{+/+}$ or *Atf7ip2*$^{-/-}$ were defined as expressed and were used in subsequent analyses. Plots of differentially expressed genes for autosomes and sex chromosomes were produced using ggplot2 (3.4.0). For Gene Ontology (GO) analyses, the Database for Annotation, Visualization and Integrated Discovery (DAVID) (version 2022q3) was used to identify terms (Huang da et al. 2009; Sherman et al. 2022). Heatmaps of expression profiles were produced using Morpheus (https://software.broadinstitute.org/morpheus).

CUT&RUN/Tag data processing

For CUT&RUN/Tag data processing, the following step-by-step protocol available from protocols.io was employed: https://protocols.io/view/cut-amp-tag-data-processing-and-analysis-tutorial-bjk2kkye.html. Briefly, raw paired-end reads were trimmed with Trim Galore (version 0.6.6) prior to alignment to the mouse genome (GRCm38/mm10) using Bowtie 2 (version 2.4.2) (Langmead and Salzberg 2012) with the following options: --end-to-end --very-sensitive --no-mixed --no-discordant --phred33 -I 10 -X 700. For the alignment of *E.coli* spike-in reads, we also the Bowtie 2 options --no-overlap --no-dovetail were invoked to avoid cross-mapping. PCR duplicates were removed using the Picard (version 2.23.8) MarkDuplicates command . To compare replicates, Pearson correlation coefficients were calculated and plotted with the following deepTools (version 3.5.0) (Ramirez et al. 2016) commands: multiBamSummary bins and plotCorrelation. Spike-in normalization was implemented using the exogenous scaling factor computed from the *E.coli* mapping files; for CUT&RUN, scale factors = 1,000,000/spike-in reads.

SEACR (Meers et al. 2019) was used to identify regions of enrichment—i.e., "peaks"—for H3K9me3 CUT&RUN and ATF7IP2 CUT&Tag data. For peak annotation, HOMER (version 4.11) (Heinz et al. 2010) was utilized. To intersect H3K9me3 and ATF7IP2 peaks, the bedtools (version 2.29.2) (Quinlan and Hall 2010) function intersect was used. Genes with ATF7IP2 peaks in the promoter region were classified as ATF7IP2 target genes. On the sex chromosomes, genes with ATF7IP2 peaks associated with gene-body regions were also considered targets of ATF7IP2.

To visualize H3K9me3 genome coverage in *Atf7ip2*$^{+/+}$ and *Atf7ip2*$^{-/-}$ pachytene spermatocytes, the Integrative Genomics Viewer (version 2.5.3) (Robinson et al. 2011) was used. Genome coverage tracks were generated with the bedtools (version 2.29.2) function genomecov,

applying the -bg -scale "${scale_factor}" parameter for spike-in normalization. Additionally, deepTools (Ramirez et al. 2016) was used for the creation of tag density plots and heatmaps illustrating enrichment.

Analysis of TE expression

For the evaluation of TE expression, RNA-seq reads were aligned to the mouse genome (GRCm38/mm10) using STAR (version 2.5.4b) (Dobin et al. 2013), allowing only uniquely mapped reads. Raw read-count files were generated with featureCounts (version 2.0.1) (Liao et al. 2014) with respect to a "best-match TE annotation" (Sakashita et al. 2020), thereby enabling the counting of reads uniquely mapped to non-exon-derived TEs. This approach excludes the counting of TEs that intersect with genes, thus mitigating the potential for erroneously counting intron-derived reads as TEs. Alignments with >2 counts in at least one sample were analyzed with DEseq2 (Love et al. 2014) to determine differential expression; the following criteria were used: Benjamini-Hochberg adjusted p-value < 0.05 and Log2FoldChange > 2. For ERCC normalization, the DESeq2 function estimateSizeFactor was employed with the controlGenes option.

Quantification and statistical analysis

No data were excluded from analyses. The experiments were not randomized. For non-next-generation sequencing experiments and outcome assessments reported in the study's main figures, investigators were blinded to allocation. Where appropriate, the mean is reported as a measurement of central tendency, and the standard deviation (SD) is used as a measure of precision. Statistical significance is threshold at $\alpha = 0.05$; where appropriate, Benjamini-Hochberg-adjusted p-values < α are considered significant; otherwise, unadjusted p-values < α are considered significant. Details for statistical analyses performed in this study are described in relevant portions of the Results section and figure legends, as are sample sizes used for analyses. In predetermining sample sizes, we sought to analyze a minimum of three independent replicates composed of knockout and wild-type or heterzygotic littermate controls; the only exception is P14 whole-testis bulk RNA-seq, CUT&RUN, and CUT&Tag analyses, which are composed of two independent samples. Measurements were recorded in Excel (Microsoft) or Sheets (Google).

Code availability

Source code for analyses performed by K.G.A. are available at the following GitHub repository: https://github.com/kalavattam/2023_Atf7ip2.
Source code for all software and tools used in this study with documentation, examples, and additional information, is available at the URLs listed below:

trimmomatic [http://www.usadellab.org/cms/?page=trimmomatic]
Trim Galore [https://github.com/FelixKrueger/TrimGalore]
STAR [https://github.com/alexdobin/STAR]
Bowtie 2 [https://github.com/BenLangmead/bowtie2]
bedtools[https://github.com/arq5x/bedtools2]
featureCounts [http://subread.sourceforge.net]
DESeq2 [https://bioconductor.org/packages/release/bioc/html/DESeq2.html]
ggplot2 [https://github.com/tidyverse/ggplot2]
deepTools [https://deeptools.readthedocs.io/en/develop/index.html]

Morpheus [https://software.broadinstitute.org/morpheus]
DAVID [https://david.ncifcrf.gov]
Galaxy [https://usegalaxy.org]
Hypergeometric p-value calculator [https://systems.crump.ucla.edu/hypergeometric/]
Picard tools [https://broadinstitute.github.io/picard/]
SEACR [https://seacr.fredhutch.org/]
Metascape [http://metascape.org]

References

Abe H, Yeh YH, Munakata Y, Ishiguro KI, Andreassen PR, Namekawa SH. 2022. Active DNA damage response signaling initiates and maintains meiotic sex chromosome inactivation. *Nat Commun* **13**: 7212.

Afgan E, Baker D, van den Beek M, Blankenberg D, Bouvier D, Čech M, Chilton J, Clements D, Coraor N, Eberhard C et al. 2016. The Galaxy platform for accessible, reproducible and collaborative biomedical analyses: 2016 update. *Nucleic Acids Res* **44**: W3-w10.

Alavattam KG, Abe H, Sakashita A, Namekawa SH. 2018. Chromosome Spread Analyses of Meiotic Sex Chromosome Inactivation. *Methods Mol Biol* **1861**: 113-129.

Alavattam KG, Kato Y, Sin HS, Maezawa S, Kowalski IJ, Zhang F, Pang Q, Andreassen PR, Namekawa SH. 2016. Elucidation of the Fanconi Anemia Protein Network in Meiosis and Its Function in the Regulation of Histone Modifications. *Cell Rep* **17**: 1141-1157.

Bolger AM, Lohse M, Usadel B. 2014. Trimmomatic: a flexible trimmer for Illumina sequence data. *Bioinformatics* **30**: 2114-2120.

Butler A, Hoffman P, Smibert P, Papalexi E, Satija R. 2018. Integrating single-cell transcriptomic data across different conditions, technologies, and species. *Nat Biotechnol* **36**: 411-420.

Dobin A, Davis CA, Schlesinger F, Drenkow J, Zaleski C, Jha S, Batut P, Chaisson M, Gingeras TR. 2013. STAR: ultrafast universal RNA-seq aligner. *Bioinformatics* **29**: 15-21.

Drabent B, Bode C, Bramlage B, Doenecke D. 1996. Expression of the mouse testicular histone gene H1t during spermatogenesis. *Histochem Cell Biol* **106**: 247-251.

Haeussler M, Schönig K, Eckert H, Eschstruth A, Mianné J, Renaud JB, Schneider-Maunoury S, Shkumatava A, Teboul L, Kent J et al. 2016. Evaluation of off-target and on-target scoring algorithms and integration into the guide RNA selection tool CRISPOR. *Genome Biol* **17**: 148.

Hasegawa K, Sin HS, Maezawa S, Broering TJ, Kartashov AV, Alavattam KG, Ichijima Y, Zhang F, Bacon WC, Greis KD et al. 2015. SCML2 establishes the male germline epigenome through regulation of histone H2A ubiquitination. *Dev Cell* **32**: 574-588.

Heinz S, Benner C, Spann N, Bertolino E, Lin YC, Laslo P, Cheng JX, Murre C, Singh H, Glass CK. 2010. Simple combinations of lineage-determining transcription factors prime cis-regulatory elements required for macrophage and B cell identities. *Mol Cell* **38**: 576-589.

Huang da W, Sherman BT, Lempicki RA. 2009. Systematic and integrative analysis of large gene lists using DAVID bioinformatics resources. *Nat Protoc* **4**: 44-57.

Ichijima Y, Ichijima M, Lou Z, Nussenzweig A, Camerini-Otero RD, Chen J, Andreassen PR, Namekawa SH. 2011. MDC1 directs chromosome-wide silencing of the sex chromosomes in male germ cells. *Genes Dev* **25**: 959-971.

Inselman A, Eaker S, Handel MA. 2003. Temporal expression of cell cycle-related proteins during spermatogenesis: establishing a timeline for onset of the meiotic divisions. *Cytogenet Genome Res* **103**: 277-284.

Kaya-Okur HS, Janssens DH, Henikoff JG, Ahmad K, Henikoff S. 2020. Efficient low-cost chromatin profiling with CUT&Tag. *Nat Protoc* **15**: 3264-3283.

Kaya-Okur HS, Wu SJ, Codomo CA, Pledger ES, Bryson TD, Henikoff JG, Ahmad K, Henikoff S. 2019. CUT&Tag for efficient epigenomic profiling of small samples and single cells. *Nat Commun* **10**: 1930.

La Manno G, Soldatov R, Zeisel A, Braun E, Hochgerner H, Petukhov V, Lidschreiber K, Kastriti ME, Lonnerberg P, Furlan A et al. 2018. RNA velocity of single cells. *Nature* **560**: 494-498.
Langmead B, Salzberg SL. 2012. Fast gapped-read alignment with Bowtie 2. *Nat Methods* **9**: 357-359.
Liao Y, Smyth GK, Shi W. 2014. featureCounts: an efficient general purpose program for assigning sequence reads to genomic features. *Bioinformatics* **30**: 923-930.
Love MI, Huber W, Anders S. 2014. Moderated estimation of fold change and dispersion for RNA-seq data with DESeq2. *Genome Biol* **15**: 550.
Meers MP, Tenenbaum D, Henikoff S. 2019. Peak calling by Sparse Enrichment Analysis for CUT&RUN chromatin profiling. *Epigenetics Chromatin* **12**: 42.
Picelli S, Faridani OR, Björklund AK, Winberg G, Sagasser S, Sandberg R. 2014. Full-length RNA-seq from single cells using Smart-seq2. *Nat Protoc* **9**: 171-181.
Quinlan AR, Hall IM. 2010. BEDTools: a flexible suite of utilities for comparing genomic features. *Bioinformatics* **26**: 841-842.
Ramirez F, Ryan DP, Gruning B, Bhardwaj V, Kilpert F, Richter AS, Heyne S, Dundar F, Manke T. 2016. deepTools2: a next generation web server for deep-sequencing data analysis. *Nucleic Acids Res* **44**: W160-165.
Ritchie ME, Phipson B, Wu D, Hu Y, Law CW, Shi W, Smyth GK. 2015. limma powers differential expression analyses for RNA-sequencing and microarray studies. *Nucleic Acids Res* **43**: e47.
Robinson JT, Thorvaldsdottir H, Winckler W, Guttman M, Lander ES, Getz G, Mesirov JP. 2011. Integrative genomics viewer. *Nat Biotechnol* **29**: 24-26.
Robinson MD, McCarthy DJ, Smyth GK. 2010. edgeR: a Bioconductor package for differential expression analysis of digital gene expression data. *Bioinformatics* **26**: 139-140.
Sakashita A, Maezawa S, Takahashi K, Alavattam KG, Yukawa M, Hu YC, Kojima S, Parrish NF, Barski A, Pavlicev M et al. 2020. Endogenous retroviruses drive species-specific germline transcriptomes in mammals. *Nat Struct Mol Biol* **27**: 967-977.
Schindelin J, Arganda-Carreras I, Frise E, Kaynig V, Longair M, Pietzsch T, Preibisch S, Rueden C, Saalfeld S, Schmid B et al. 2012. Fiji: an open-source platform for biological-image analysis. *Nat Methods* **9**: 676-682.
Scott MA, Hu YC. 2019. Generation of CRISPR-Edited Rodents Using a Piezo-Driven Zygote Injection Technique. *Methods Mol Biol* **1874**: 169-178.
Sherman BT, Hao M, Qiu J, Jiao X, Baseler MW, Lane HC, Imamichi T, Chang W. 2022. DAVID: a web server for functional enrichment analysis and functional annotation of gene lists (2021 update). *Nucleic Acids Res* **50**: W216-221.
Skene PJ, Henikoff JG, Henikoff S. 2018. Targeted in situ genome-wide profiling with high efficiency for low cell numbers. *Nat Protoc* **13**: 1006-1019.
Stuart T, Butler A, Hoffman P, Hafemeister C, Papalexi E, Mauck WM, 3rd, Hao Y, Stoeckius M, Smibert P, Satija R. 2019. Comprehensive Integration of Single-Cell Data. *Cell* **177**: 1888-1902 e1821.
van der Heijden GW, Derijck AA, Pósfai E, Giele M, Pelczar P, Ramos L, Wansink DG, van der Vlag J, Peters AH, de Boer P. 2007. Chromosome-wide nucleosome replacement and H3.3 incorporation during mammalian meiotic sex chromosome inactivation. *Nat Genet* **39**: 251-258.

Yeh YH, Hu M, Nakagawa T, Sakashita A, Yoshida S, Maezawa S, Namekawa SH. 2021. Isolation of Murine Spermatogenic Cells using a Violet-Excited Cell-Permeable DNA Binding Dye. *J Vis Exp*.

Zhou Y, Zhou B, Pache L, Chang M, Khodabakhshi AH, Tanaseichuk O, Benner C, Chanda SK. 2019. Metascape provides a biologist-oriented resource for the analysis of systems-level datasets. *Nat Commun* **10**: 1523.

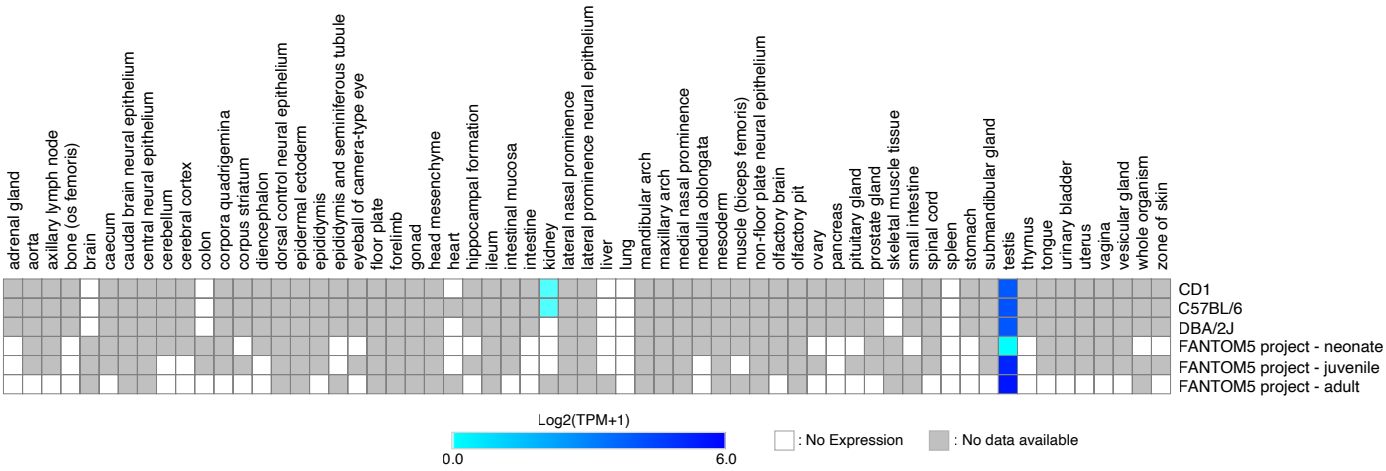
Table S1 scRNA-seq analysis.
Top 100 differentially expressed genes for each cluster, and results of gene enrichment analyses for each cluster.

Table S2 ATF7IP2-binding target genes as determined by ATF7IP2 CUT&Tag analyses.
Lists of (a) autosomal ATF7IP2-binding target genes for which ATF7IP2 binds promoters., (b) XY-linked ATF7IP2-binding target genes for which ATF7IP2 binds promoters, and (c) XY-linked ATF7IP2-binding target genes for which ATF7IP2 binds gene bodies.

Table S3 Differentially expressed genes in *Atf7ip2*$^{+/+}$ versus *Atf7ip2*$^{-/-}$ pachytene spermatocytes.
List of differentially expressed genes (DEGs) following ERCC spike-in normalization.

Table S4 Differentially expressed TEs in *Atf7ip2*$^{+/+}$ versus *Atf7ip2*$^{-/-}$ pachytene spermatocytes.
List of differentially expressed TEs following ERCC spike-in normalization.

A Expresson of *Atf7ip2* in mouse tissues



B Amino acid sequences of human ATF7IP2 (682 aa) and mouse ATF7IP2 (452 aa)

```
Human       MASPDRSKRKILKAKKTMPLSCRKQVEMLNKSRNVEALKTAIGSNVPSGNQSFSPSVITR      60
Mouse       ------------------------------------------------------------

Human       TTEITKCSPSENGASSLDSNKNSISEKSKVFSQNCIKPVEEIVHSETKLEQVVCSYQKPS      120
Mouse       ------------------------------------------------------------      0

Human       RTTESPSRVFTEEAKDSLNTSENDSEHQTNVTRSLFEHEGACSLKSSCCPPSVLSGVVQM      180
Mouse       ------------------------------------------------------------      0

Human       PESTVTSTVGDKKTDQMVFHLETNSNSESHDKRQSDNILCSEDSGFVPVEKTPNLVNSVT      240
Mouse       -------------------------MESPDRKR-QKVLKAKK--TMPTS----------      21
                                     ** *::: :::* ::.   :*..

Human       SNNCADDILKTDECSRTSISNCESADSTWQSSLDTNNNSHYQKKRMFSENEENVKRMKTS      300
Mouse       -YQKQLEILNK-------STNVEAPKTT-----VGTNIPNGHNQKMFSKNKENVKVMKVS      68
              :   :**:.        :* *: .:*       .*  : ::::***:*:**** **.*

Human       EQINENICVSLERQTAFLEQVRHLIQQEIYSINYELFDKKLKELNQRIGKTECRNKHEGI      360
Mouse       EQINENACGALERHTALLEQVKHWIRQEICMINCNLFDKKLNELNERIGKTQCKSRHEAI      128
            ****** * :***:**:****:* *:***  ** :******:***:*****:*:.:**.*

Human       ADKLLAKIAKLQRRIKTVLLFQRNCLKPNMLSSNGASKVANSEAMILDKNLESVNSPI-E      419
Mouse       AGELFVKIRRLQKRIKTVLSSQRNCLEPNTLPSNTVCKVTDSEAMNLNVTQKSVKSRSKR      188
            *.:*:.** :**:******  *****:** * ** ..**::**** *: . :**:*   .

Human       KSSVNYEPSNPSEKGSKKINLSSDQNKSVSESNNDDVMLISVESPNLTTPITSNPTDTRK      479
Mouse       ISSVNHTPLNSSEKAGRKTNLPSTCVEFASESNTDDVMLISVKNSNLTTSITSEQTEIRK      248
             ****: * * ***..:* ** *   : .****.********:. **** ***: *: **

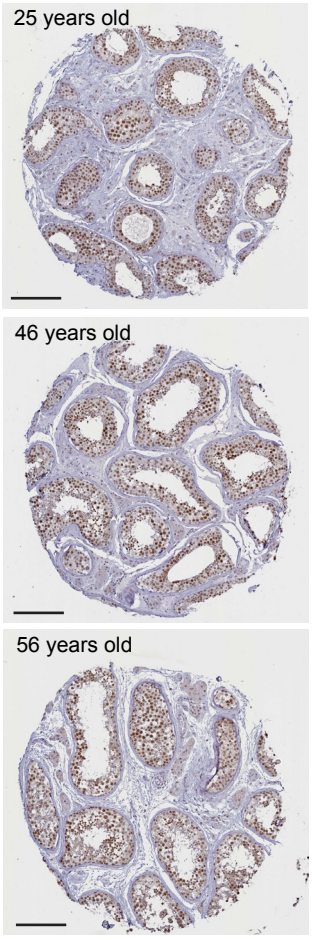
Human       ITSGNSSNSPNAE--VMAVQKKLDSIIDLTKEGLSNCNTESPVSPLESHSKAASNSKETT      537
Mouse       NTSRNLSNSPNSMIKVGPVEKKFDFVIDLTREGPSNYSIESPSFTLKSTSKAVLRSKEII      308
             ** * *****:   *  *:**:* :****:** ** . ***   *:* ***. .***

Human       PLAQNAVQVPESFEHLPPLPEPPAPLPELVDKTRDTLPPQKPELKVKRVFRPNGIALTWN      597
Mouse       PVAENGNEGFGSFEHLPPLPEPPAPLPEMADKIKDTLPPQKPELKVKWVLRPTSIALTWN      368
            *:*:*. :   ******************:.** :************* *:**..******

Human       ITKINPKCAPVESYHLFLCHENSNNKLIWKKIGEIKALPLPMACTLSQFLASNRYYFTVQ      657
Mouse       IPKVNPNCAPVESYHLFLYYENS-DHLTWKKIAEIKALPLPMACTLSQNLASTKYYFAVQ      427
            * *:**:*********** :*** ::* ****.*************** ***.:***:**

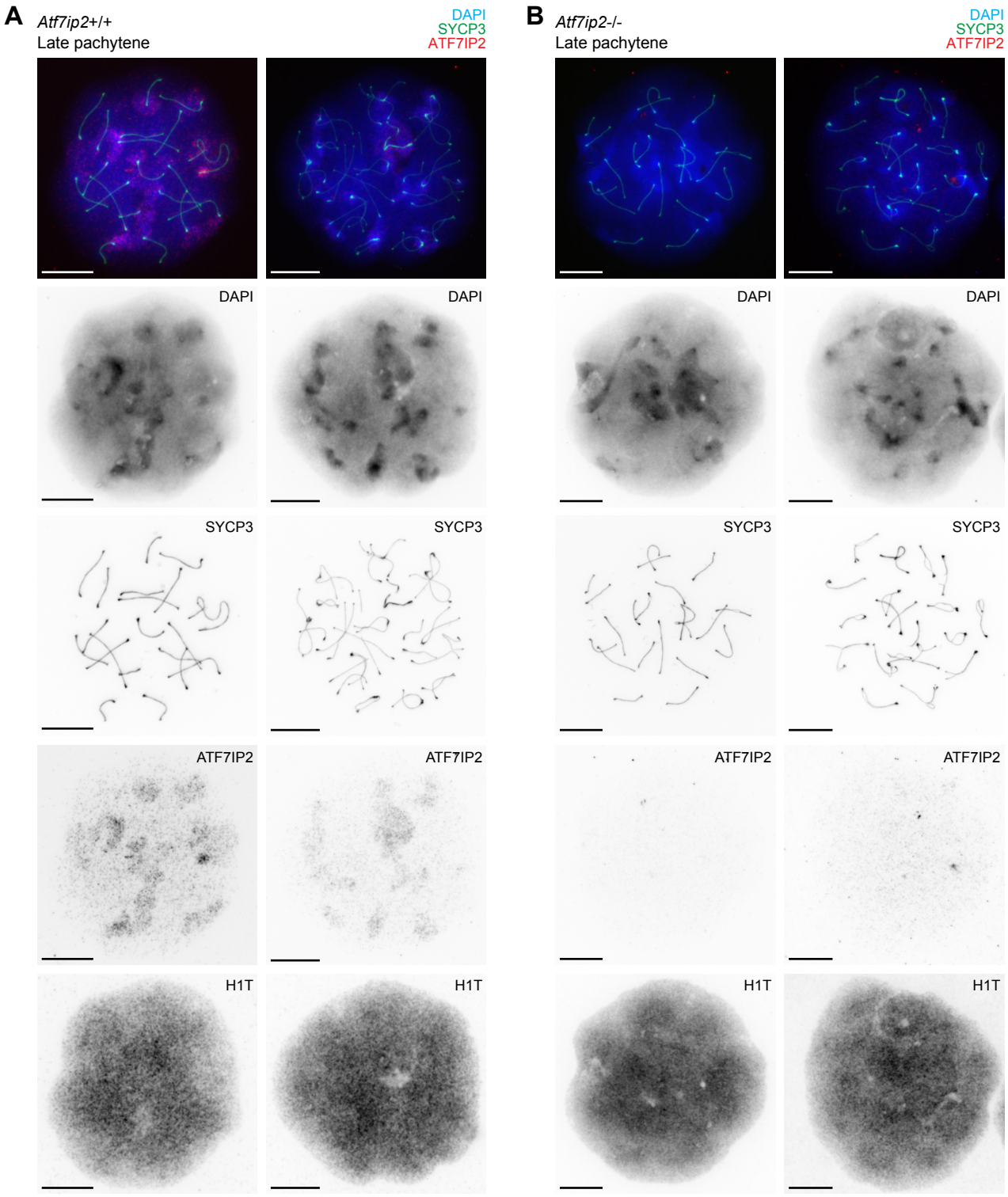
Human       SKDIFGRYGPFCDIKSIPGFSENLT       682
Mouse       SKDIFGRYGPFCNIKSIPRFSENLT       452
```

C Human testicular sections

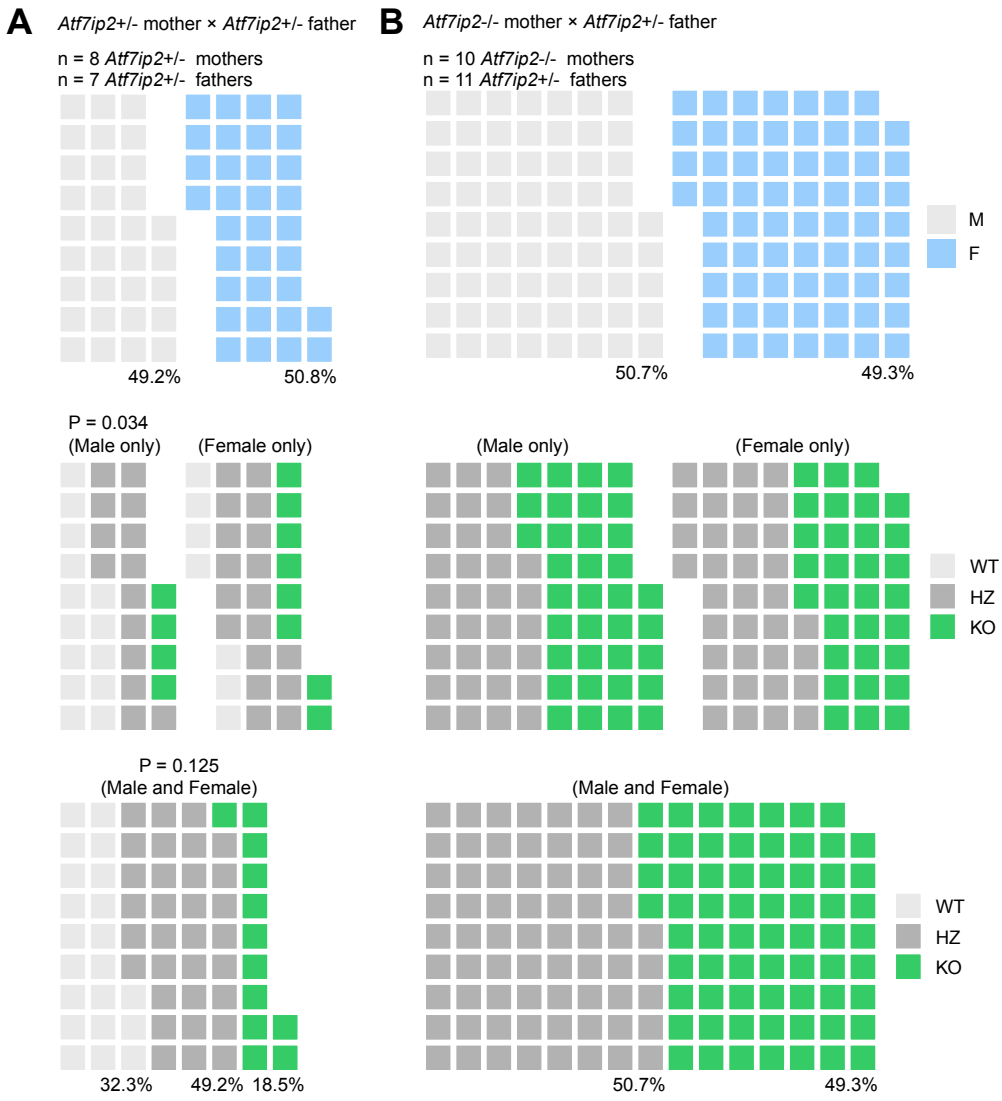


ATF7IP2: DAB staining

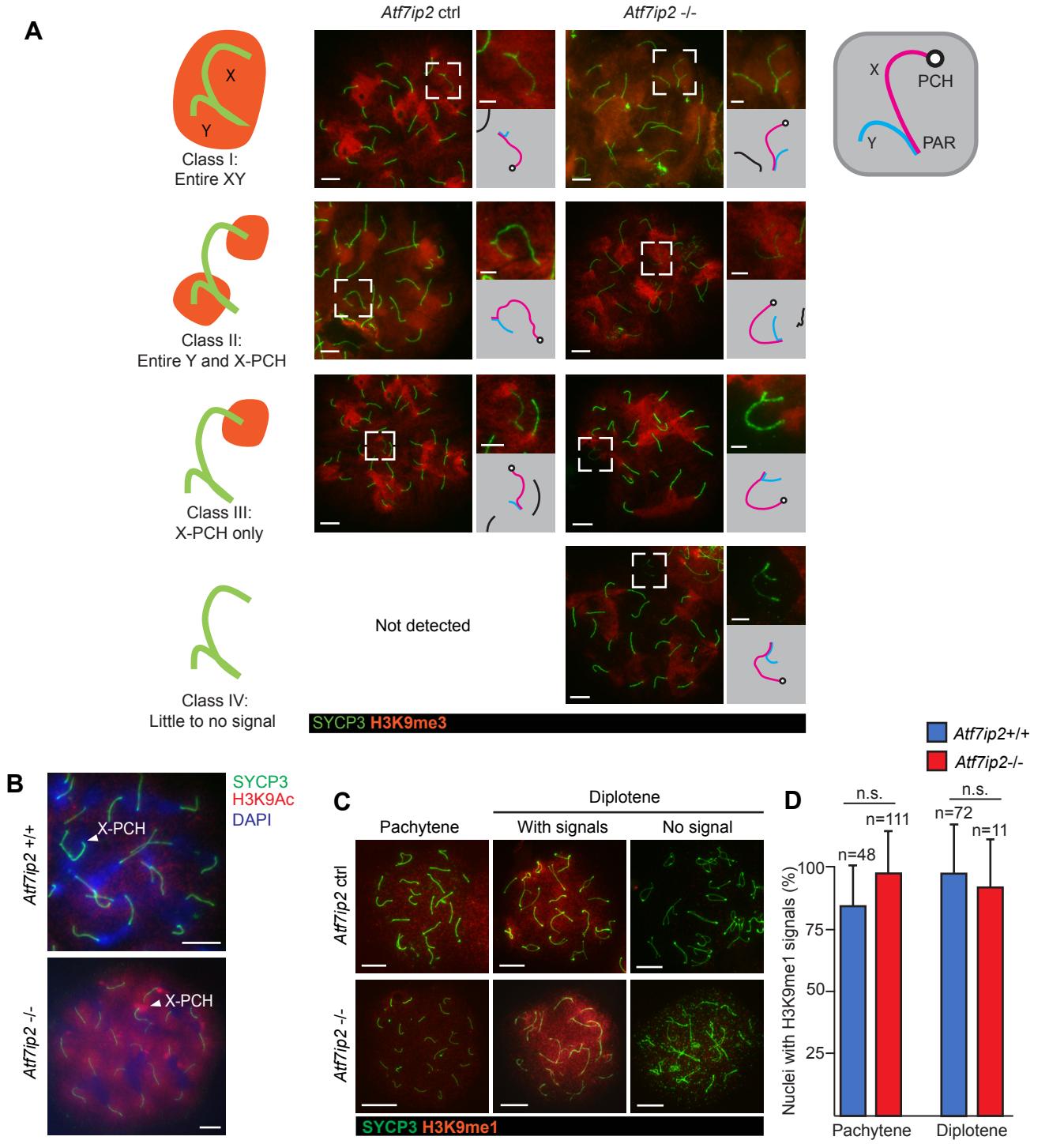
Supplemental Figure S1. ATF7IP2 expression patterns in mouse tissues and human testes.
(A) *Atf7ip2* expression levels in mouse tissues. Data were sourced and adapted from the Expression Atlas (https://www.ebi.ac.uk/gxa/home).
(B) Human and mouse ATF7IP2 amino acid sequences via Clustal Omega alignment.
(C) Representative testis sections from humans at 25, 46, and 56 years of age immunohistochemically stained with an antibody raised against ATF7IP2 (brown) and counterstained with hematoxylin. Images of human testis sections were sourced and adapted from the Human Protein Atlas (https://www.proteinatlas.org/). Scale bars: 200 µm.



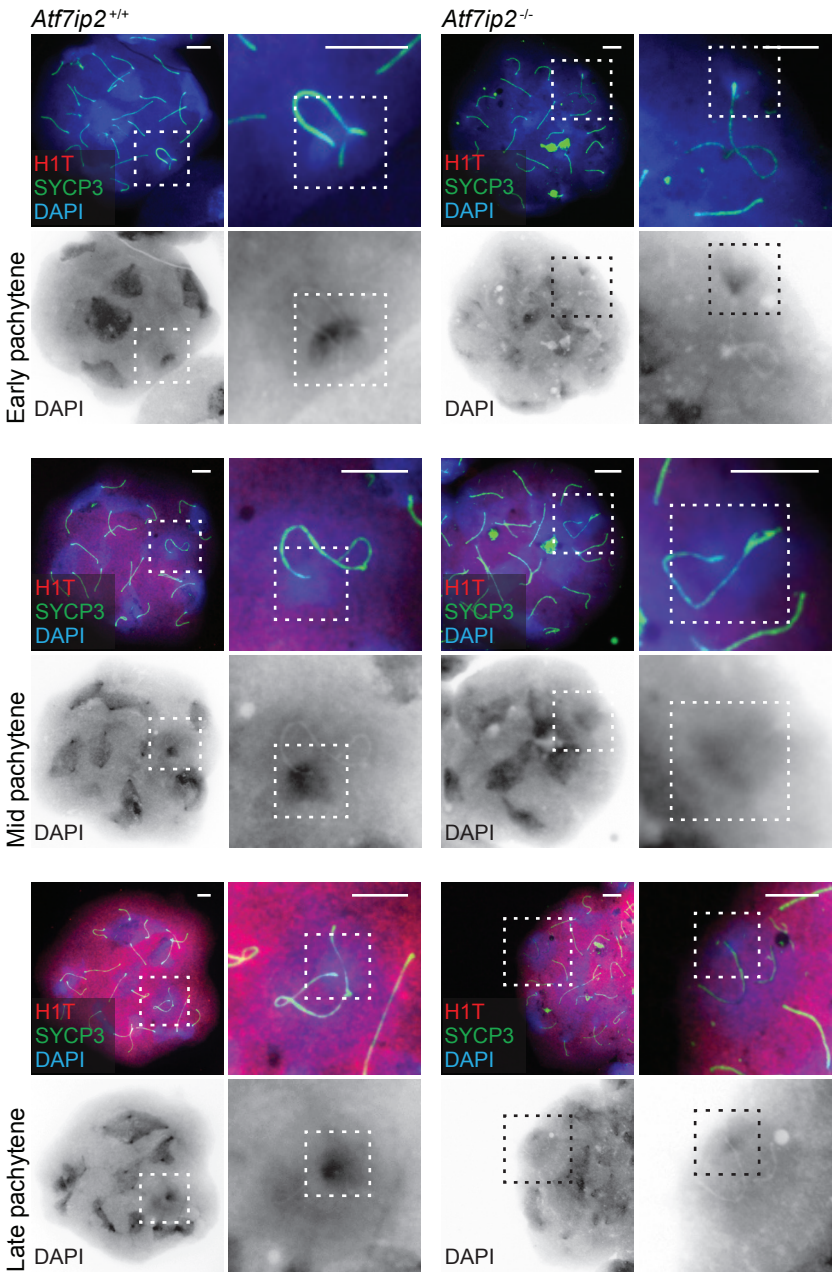
Supplemental Figure S2. ATF7IP2 protein is absent from *Atf7ip2*$^{-/-}$ spermatocytes.
(A, B) Chromosome spreads of *Atf7ip2*$^{+/+}$ **(A)** and *Atf7ip2*$^{-/-}$ **(B)** spermatocytes stained with DAPI and antibodies raised against SYCP3 (a marker of chromosome axes), ATF7IP2, and H1T (a marker of germ cells in mid pachytene and subsequent stages). Scale bars: 10 μm.



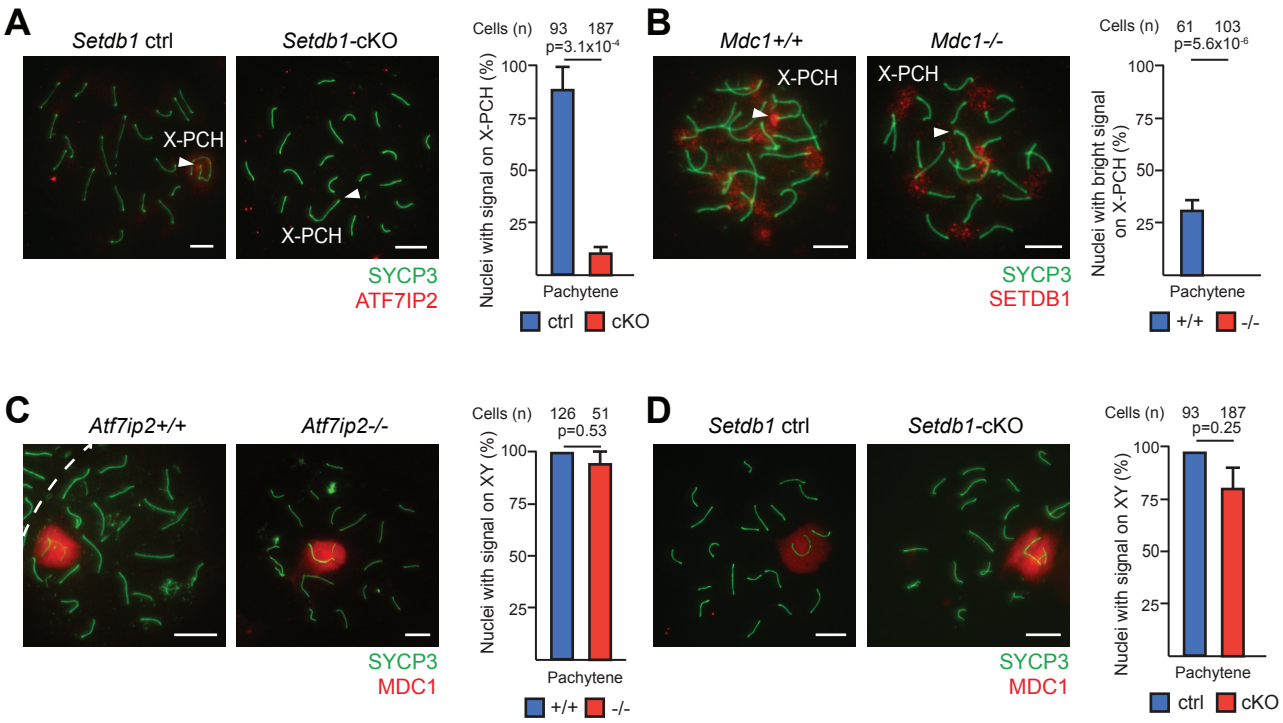
Supplemental Figure S3. Breeding summary of *Atf7ip2* knockout mice.
(A, B) Breeding summary of *Atf7ip2*$^{+/-}$ mothers and *Atf7ip2*$^{+/-}$ fathers **(A)**, and *Atf7ip2*$^{+/-}$ mothers and *Atf7ip2*$^{+/-}$ fathers **(B)**. Each square represents an individual offspring. Numbers of mice used for breeding are shown. P-values are from chi-squared tests.



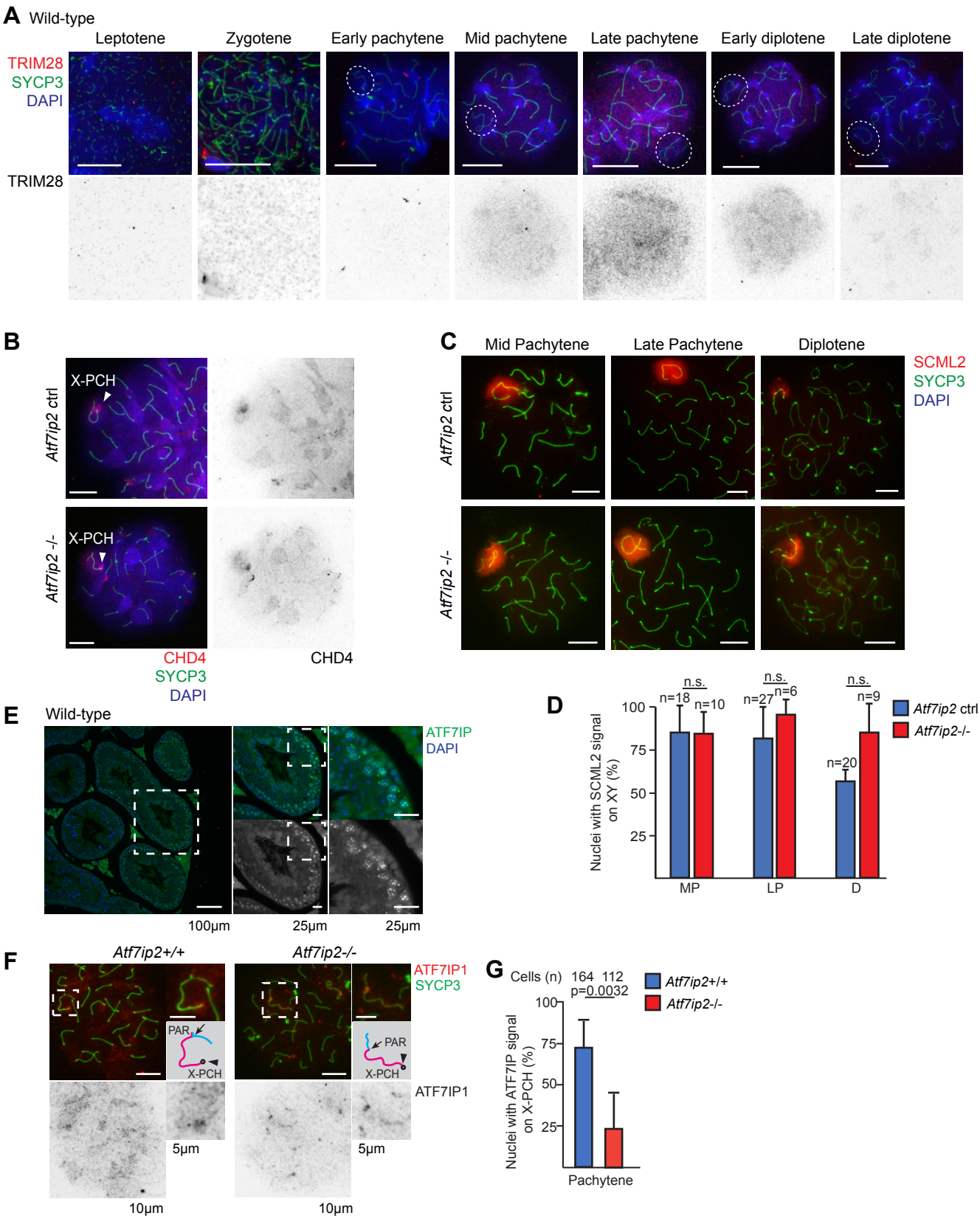
Supplemental Figure S4. H3K9me3, H3K9ac, and H3K9me1 localization in *Atf7ip2*$^{-/-}$ spermatocytes.
(A) H3K9me3 accumulation patterns on the sex chromosomes in early pachytene spermatocytes. H3K9me3 distribution patterns are categorized into four classes. The four classes are organized in order of decreasing H3K9me3 enrichment on the XY domain. Class I: broad, uninterrupted H3K9me3 accumulation on the XY chromosomes; Class II: enrichment of H3K9me3 on X pericentric heterochromatin (PCH) and chromosome Y; Class III: H3K9me3 enrichment on X-PCH only. Class IV: little-to-no H3K9me3 accumulation on XY. Chromosome spreads of *Atf7ip2* control (*Atf7ip2* ctrl: *Atf7ip2*$^{+/+}$ and *Atf7ip2*$^{+/-}$) and *Atf7ip2*$^{-/-}$ spermatocytes stained with antibodies raised against H3K9me3 and SYCP3 (a marker of chromosome axes). Dashed squares are magnified in the panels to the upper right, and XY schema are shown in the lower right. Scale bars: 10 μm for whole nuclei, 5 μm for XY.
(B) *Atf7ip2* Ctrl and *Atf7ip2*$^{-/-}$ spermatocyte chromosome spreads stained with antibodies raised against H3K9ac and SYCP3. Scale bars: 10 μm.
(C) *Atf7ip2* Ctrl and *Atf7ip2*$^{-/-}$ spermatocyte chromosome spreads stained with antibodies raised against H3K9me1 and SYCP3. Representative photos for nuclei with and without H3K9me1 signal are shown for diplotene spermatocytes. Scale bars: 10 μm.
(D) Quantification of pachytene and diplotene spermatocytes with H3K9me1 signals on the sex chromosomes. Three independent experiments. P-values are from Fisher's exact tests: n.s. (not significant).



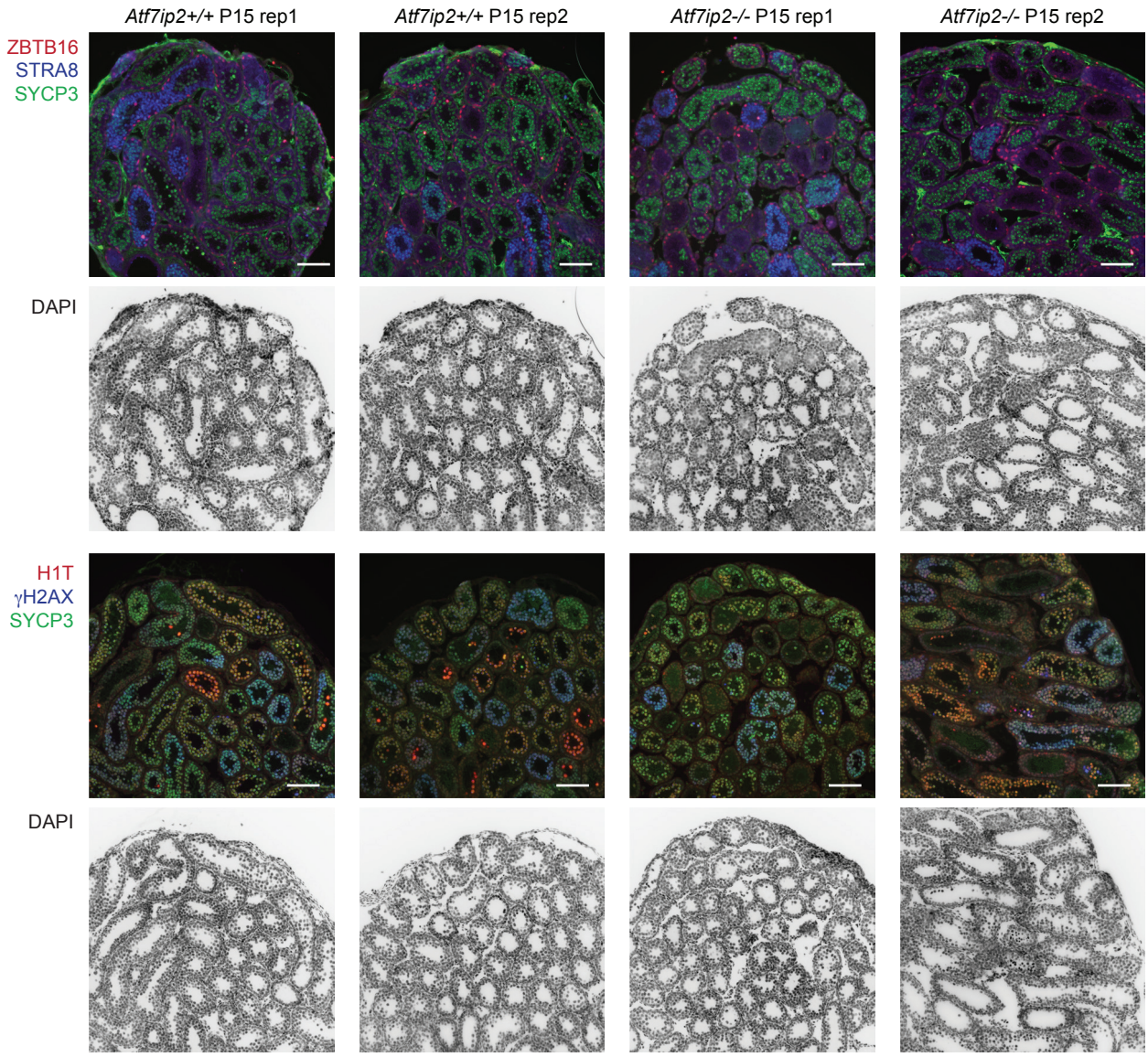
Supplemental Figure S5. X-PCH defects in *Atf7ip2*$^{-/-}$ spermatocytes.
Chromosome spreads of *Atf7ip2*$^{+/+}$ and *Atf7ip2*$^{-/-}$ spermatocytes stained with DAPI and antibodies raised against SYCP3 and H1T. Scale bars: 10 µm. Dashed squares are magnified in the panels to the right. In comparison to controls, *Atf7ip2*$^{-/-}$ X-PCH DAPI intensity is decreased.



Supplemental Figure S6. Evaluation of *Setdb1*-cKO, *Mdc1*$^{-/-}$, and *Atf7ip2*$^{-/-}$ spermatocytes
(A, D) *Setdb1* ctrl and Setdb1-cKO spermatocyte chromosome spreads stained with DAPI and antibodies raised against SYCP3 and ATF7IP2 (A) and MDC1 (D).
(B) *Mdc1*$^{+/+}$ and *Mdc1*$^{-/-}$ spermatocyte chromosome spreads stained with DAPI and antibodies raised against SYCP3 and SETDB1.
(C) *Atf7ip2*$^{+/+}$ and *Atf7ip2*$^{-/-}$ spermatocyte chromosome spreads stained with DAPI and antibodies raised against SYCP3 and MDC1.
Scale bars: 10 µm.


A
Wild-type
Leptotene
Zygotene
Early pachytene
Mid pachytene
Late pachytene
Early diplotene
Late diplotene
TRIM28
SYCP3
DAPI
TRIM28
B
Atf7ip2 ctrl
Atf7ip2 -/-
X-PCH
X-PCH
CHD4
SYCP3
DAPI
CHD4
C
Mid Pachytene
Late Pachytene
Diplotene
Atf7ip2 ctrl
Atf7ip2 -/-
SCML2
SYCP3
DAPI
D
Nuclei with SCML2 signal on XY (%)
100
75
50
25
n=18
n=10
n=27
n=6
n=20
n=9
n.s.
n.s.
n.s.
MP
LP
D
Atf7ip2 ctrl
Atf7ip2-/-
E
Wild-type
ATF7IP
DAPI
100µm
25µm
25µm
F
Atf7ip2+/+
Atf7ip2-/-
ATF7IP1
SYCP3
PAR
X-PCH
PAR
X-PCH
ATF7IP1
5µm
5µm
10µm
10µm
G
Cells (n) 164 112
p=0.0032
Atf7ip2+/+
Atf7ip2-/-
Nuclei with ATF7IP signal on X-PCH (%)
100
75
50
25
Pachytene

Supplemental Figure S7. TRIM28, CHD4, SCML2, and ATF7IP localization in chromosome spreads.
(A) Wild-type spermatocyte chromosome spreads stained with antibodies raised against SYCP3 and TRIM28. Scale bars: 10 μm.
(B) *Atf7ip2* ctrl and *Atf7ip2*$^{-/-}$ spermatocyte chromosome spreads stained with antibodies raised against SYCP3 and CHD4. Scale bars: 10 μm.
(C) *Atf7ip2* ctrl and *Atf7ip2*$^{-/-}$ spermatocyte chromosome spreads stained with antibodies raised against SYCP3 and SCML2. Scale bars: 10 μm.
(D) Quantification of spermatocytes with SCML2 signals on the sex chromosomes. Three independent experiments. P-values are from Fisher's exact tests: n.s.: not significant.
(E) Wild-type testis sections from mice at 4 months of age stained with DAPI and antibodies raised against ATF7IP. Dashed squares are magnified in the panels to the right. Scale bars: 100 μm (left panel) and 25 μm (magnified panels).
(F) *Atf7ip2*$^{+/+}$ and *Atf7ip2*$^{-/-}$ spermatocyte chromosome spreads stained with antibodies raised against SYCP3 and ATF7IP. Scale bars: 10 μm.
(G) Quantification of spermatocytes with X-PCH ATF7IP signals. Three independent experiments. P-value is from Fisher's exact tests.

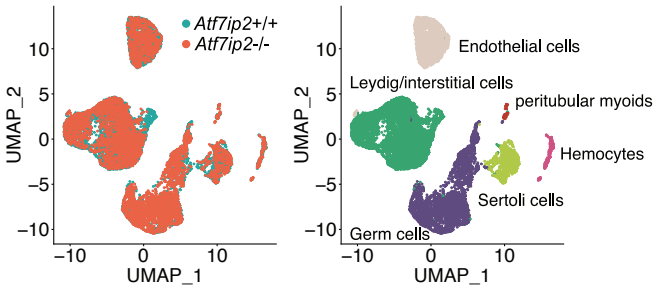


Supplemental Figure S8. Testis sections from *Atf7ip2*$^{+/+}$ and *Atf7ip2*$^{-/-}$ mice at P15.
Testis sections from *Atf7ip2*$^{+/+}$ and *Atf7ip2*$^{-/-}$ mice at P15 (used for scRNA-seq) stained with DAPI and antibodies raised against ZBTB16, STRA8, SYCP3, H1T, and γH2AX. Scale bars: 100 μm.

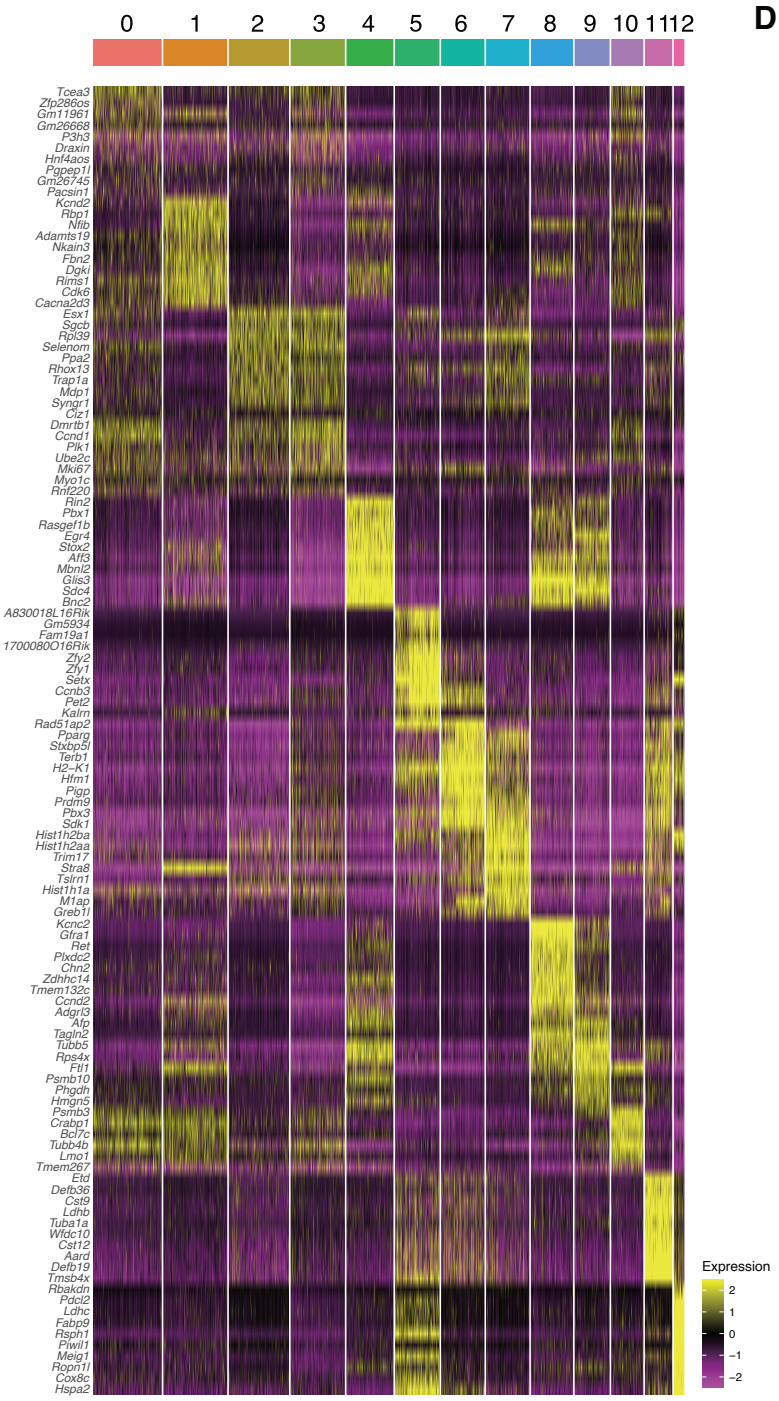
A

Platform: Chromium (10x Genomics)		
Genotype:	*Atf7ip2*+/+	*Atf7ip2*-/-
Sampling stage:	P15	
Cell type:	Whole testicular cells	
Number of used indivisuals:	2	3
Total number of genes detected:	26,168	26,415
Sequencing Saturation:	51.5%	49.5%
Mean reads / cell:	58,206	63,564
Median genes / cell:	4,174	4,566
Median UMI counts / cell:	14,666	16,156
Total number of cells:	9,113	9,015
Number of analyzed testicular germ cells:	959 (10.5%)	2,246 (24.9%)

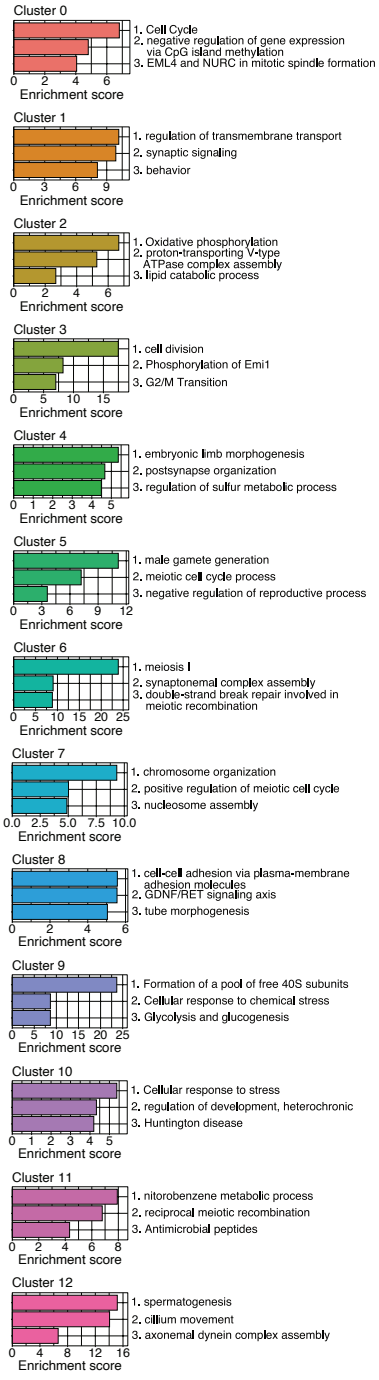
B



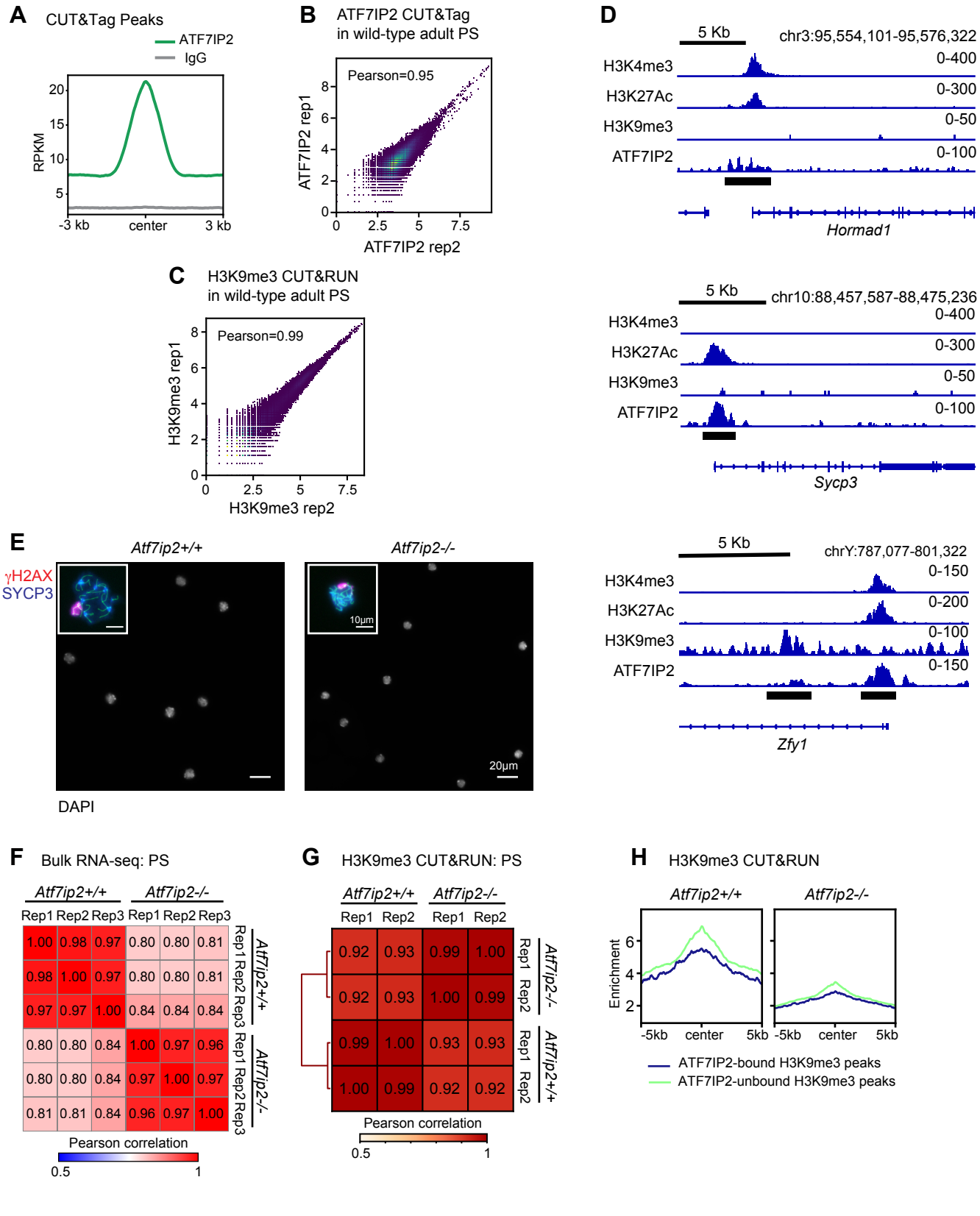
C



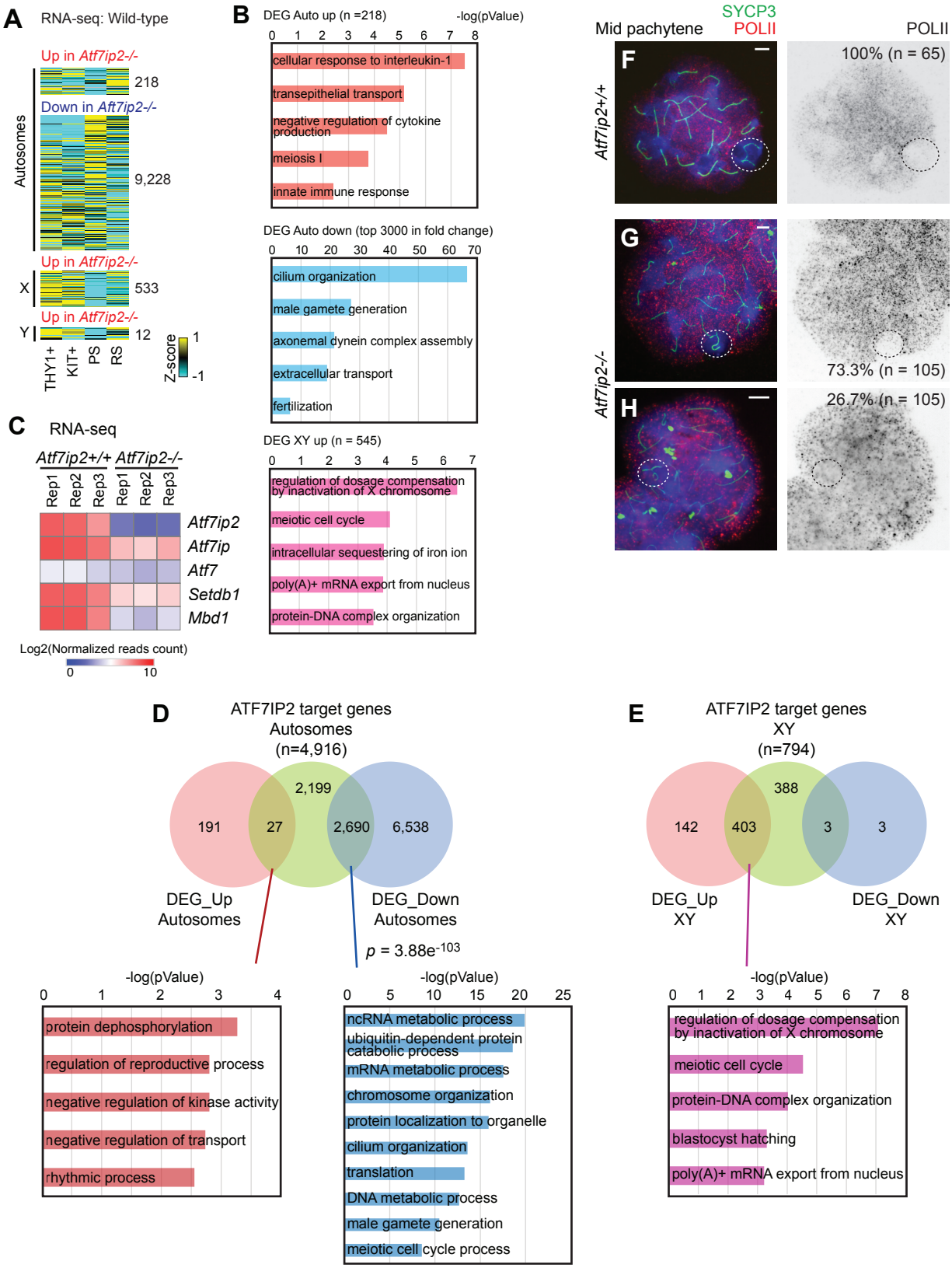
D



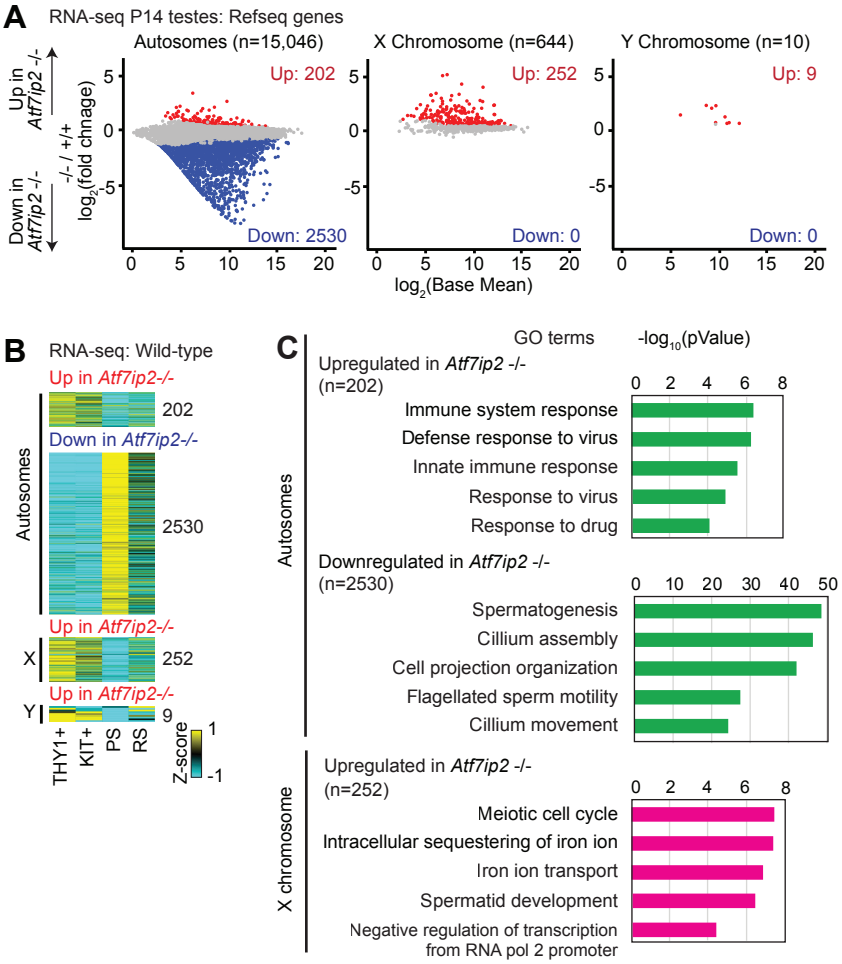
Supplemental Figure S9. Clustering analysis of scRNA-seq data of *Atf7ip2*$^{+/+}$ and *Atf7ip2*$^{-/-}$ spermatogenic germ cells
(A) Table of 10X Genomics Chromium metrics for scRNA-seq analyses of *Atf7ip2*$^{+/+}$ and *Atf7ip2*$^{-/-}$ testicular germ cells. For the *Atf7ip2*$^{+/+}$ sample, two *Atf7ip2*$^{+/+}$ testes from two individuals (P15) were merged. For the *Atf7ip2*$^{-/-}$ sample, three testes from three *Atf7ip2*$^{-/-}$ individuals (P15) were merged. We show the total numbers of testicular germ cells subjected to scRNA-seq analyses and separated from other testicular somatic cells. We also show percentages of extracted testicular germ cells per total single cells subjected to scRNA-seq analyses.
(B) UMAP representation of scRNA-seq transcriptome profiles for whole testicular cells from *Atf7ip2*$^{+/+}$ and *Atf7ip2*$^{-/-}$ testes.
(C) Hierarchically clustered heatmap for the top 10 representative genes for each cluster. Relative expression levels are indicated with the color code: yellow, up two positive standard deviations; black, mean; purple, up to two negative standard deviations.
(D) Gene enrichment analysis for genes in the cell clusters.


A
CUT&Tag Peaks
ATF7IP2
IgG
RPKM
-3 kb
center
3 kb
B
ATF7IP2 CUT&Tag
in wild-type adult PS
Pearson=0.95
ATF7IP2 rep1
ATF7IP2 rep2
C
H3K9me3 CUT&RUN
in wild-type adult PS
Pearson=0.99
H3K9me3 rep1
H3K9me3 rep2
D
5 Kb
chr3:95,554,101-95,576,322
H3K4me3
H3K27Ac
H3K9me3
ATF7IP2
0-400
0-300
0-50
0-100
Hormad1
5 Kb
chr10:88,457,587-88,475,236
Sycp3
5 Kb
chrY:787,077-801,322
0-150
0-200
Zfy1
E
Atf7ip2+/+
Atf7ip2-/-
γH2AX
SYCP3
10μm
20μm
DAPI
F
Bulk RNA-seq: PS
Rep1 Rep2 Rep3 Rep1 Rep2 Rep3
1.00 0.98 0.97 0.80 0.80 0.81
0.98 1.00 0.97 0.80 0.80 0.81
0.97 0.97 1.00 0.84 0.84 0.84
0.80 0.80 0.84 1.00 0.97 0.96
0.80 0.80 0.84 0.97 1.00 0.97
0.81 0.81 0.84 0.96 0.97 1.00
Pearson correlation
0.5
1
G
H3K9me3 CUT&RUN: PS
Rep1 Rep2 Rep1 Rep2
0.92 0.93 0.99 1.00
0.92 0.93 1.00 0.99
0.99 1.00 0.93 0.93
1.00 0.99 0.92 0.92
Pearson correlation
0.5
1
H
H3K9me3 CUT&RUN
Enrichment
-5kb
center
5kb
ATF7IP2-bound H3K9me3 peaks
ATF7IP2-unbound H3K9me3 peaks

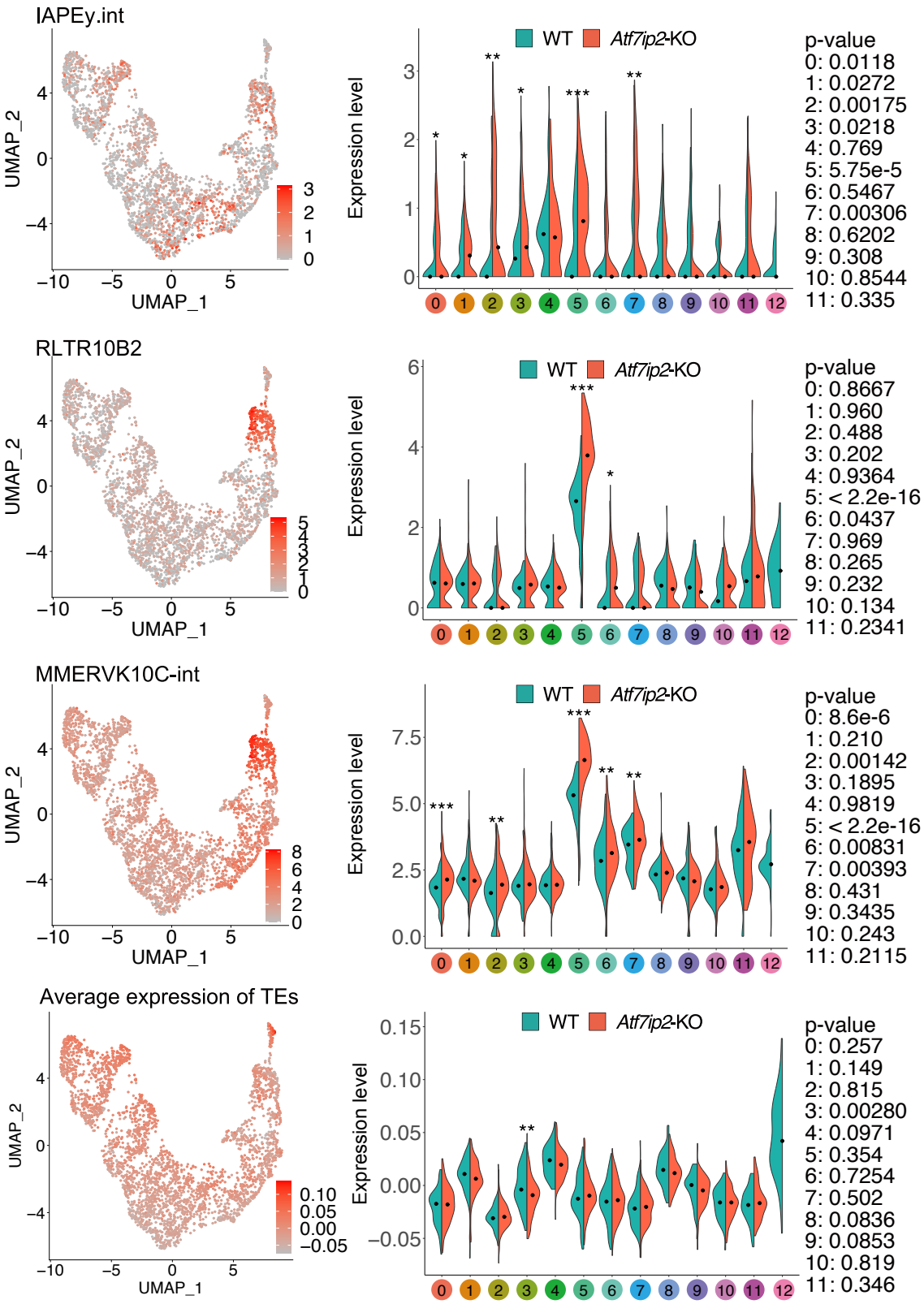
Supplemental Figure S10. ATF7IP2 CUT&Tag, H3K9me3 CUT&RUN, and bulk RNA-seq analyses in pachytene spermatocytes.
(A) Average tag density prots showing enrichment of ATF7IP2 and IgG CUT&Tag reads at ATF7IP2 CUT&Tag peaks ± 3kb.
(B) Scatter plots showing Pearson correlations between biological replicates for ATF7IP2 CUT&Tag data from wild-type adult pachytene spermatocytes.
(C) Scatter plots showing Pearson correlations between biological replicates for H3K9me3 CUT&RUN data from wild-type adult pachytene spermatocytes.
(D) Representative track views of ATF7IP2 peaks at autosomal *Hormad1* and *Sycp3* gene loci, and the Y-linked *Zfy1* gene locus. Solid bars: locations of detected peaks.
(E) Representative photos of isolated pachytene spermatocytes stained with DAPI; scale bars: 20 μm. Insets: Representative photos of isolated pachytene spermatocytes stained with antibodies raised against γH2AX and SYCP3; scale bars: 10 μm.
(F) Heatmap of Pearson correlations demonstrating the reproducibility of RNA-seq biological replicates.
(G) Heatmap of Pearson correlations demonstrating the reproducibility of H3K9me3 CUT&RUN biological replicates.
(H) Average tag density prots showing enrichment of ATF7IP2 CUT&Tag reads at ATF7IP2-bound and ATF7IP2-unbound H3K9me3 peaks ± 3kb.


A
RNA-seq: Wild-type
Up in Atf7ip2-/-
218
Down in Aft7ip2-/-
Autosomes
9,228
Up in Atf7ip2-/-
X
533
Up in Atf7ip2-/-
Y
12
THY1+
KIT+
PS
RS
Z-score
1
-1
B
DEG Auto up (n =218)
-log(pValue)
cellular response to interleukin-1
transepithelial transport
negative regulation of cytokine production
meiosis I
innate immune response
DEG Auto down (top 3000 in fold change)
cilium organization
male gamete generation
axonemal dynein complex assembly
extracellular transport
fertilization
DEG XY up (n = 545)
regulation of dosage compensation by inactivation of X chromosome
meiotic cell cycle
intracellular sequestering of iron ion
poly(A)+ mRNA export from nucleus
protein-DNA complex organization
C
RNA-seq
Atf7ip2+/+
Atf7ip2-/-
Rep1
Rep2
Rep3
Atf7ip2
Atf7ip
Atf7
Setdb1
Mbd1
Log2(Normalized reads count)
F
G
H
Mid pachytene
SYCP3
POLII
POLII
100% (n = 65)
73.3% (n = 105)
26.7% (n = 105)
Atf7ip2+/+
Atf7ip2-/-
D
ATF7IP2 target genes
Autosomes
(n=4,916)
191
27
2,199
2,690
6,538
DEG_Up
Autosomes
DEG_Down
Autosomes
p = 3.88e-103
protein dephosphorylation
regulation of reproductive process
negative regulation of kinase activity
negative regulation of transport
rhythmic process
ncRNA metabolic process
ubiquitin-dependent protein catabolic process
mRNA metabolic process
chromosome organization
protein localization to organelle
cilium organization
translation
DNA metabolic process
male gamete generation
meiotic cell cycle process
E
ATF7IP2 target genes
XY
(n=794)
142
403
388
3
3
DEG_Up
XY
DEG_Down
XY
regulation of dosage compensation by inactivation of X chromosome
meiotic cell cycle
protein-DNA complex organization
blastocyst hatching
poly(A)+ mRNA export from nucleus

Supplemental Figure S11. The roles of ATF7IP2 and SETDB1 in meiotic gene regulation
(A) Heatmaps showing normalized expression of DEGs in *Atf7ip2*$^{+/+}$ and *Atf7ip2*$^{-/-}$ wild-type pachytene spermatocytes: THY1^{+}, undifferentiated spermatogonia; KIT^{+}, differentiating spermatogonia; PS, pachytene spermatocytes; RS, round spermatids.
(B) The top five Gene Ontology enrichment terms for autosomal up- and downregulated genes and XY-linked upregulated genes from differential expression analyses of *Atf7ip2*$^{-/-}$ and *Atf7ip2*$^{+/+}$ pachytene spermatocyte RNA-seq.
(C) Heatmaps showing RNA-seq expression levels of indidated genes.
(D, E) Overlaps among ATF7IP2 target genes detected by ATF7IP2 CUT&Tag and DEGs in *Atf7ip2*-/- pachytene spermatocytes on ausotomes (D) and sex chromosomes (E). Representative Gene Ontology enrichment terms are shown. The P value in panel D: when considering the ratio of ATF7IP2 autosome targets to all autosome genes in the Refseq (4,916 genes divided by all 22,361 autosome genes in the Refseq annotation), this association (2,690 genes divided by 9,228 genes) is statistically significant (p = 3.88e^{-103}, two-sided hypergeometric test).
(F, G, H) *Atf7ip2*$^{+/+}$ and *Atf7ip2*$^{-/-}$ spermatocyte chromosome spreads stained with antibodies raised against SYCP3 (a marker of chromosome axes) and RNA polymerase II (POLII). Three independent littermate pairs were examined. Numbers of analyzed nuclei are shown. Scale bars: 10 μm. Dashed circles indicate the sex chromosomes.



Supplemental Figure S12. RNA-seq analysis of *Atf7ip2*$^{+/+}$ and *Atf7ip2*$^{-/-}$ testes at P14.
(A) Comparison of transcriptomes in P14 *Atf7ip2*$^{+/+}$ and *Atf7ip2*$^{-/-}$ testes. Autosomal, X, and Y genes were separately analyzed. Two independent biological replicates were examined. All genes with adjusted p-values (Benjamini-Hochsberg method) are plotted. Differentially expressed genes (DEGs: fold change ≥ 1.5, adjusted p-value ≤ 0.05) are colored (red: upregulated in *Atf7ip2*$^{-/-}$ testes; blue: downregulated in *Atf7ip2*$^{-/-}$ testes), and numbers are shown.
(B) Heatmaps showing normalized expression of DEGs between *Atf7ip2*$^{+/+}$ and *Atf7ip2*$^{-/-}$ testes in wild-type spermatogenesis: THY1^{+}, undifferentiated spermatogonia; KIT^{+}, differentiating spermatogonia; PS, pachytene spermatocytes; RS, round spermatids.
(C) The top five Gene Ontology enrichment terms for autosomal up- and downregulated genes and X-linked upregulated genes from differential expression analyses of *Atf7ip2*$^{-/-}$ and *Atf7ip2*$^{+/+}$ P14 testis RNA-seq.



Supplemental Figure S13. Expresson of transposable elements (TEs) in scRNA-seq data of *Atf7ip2*$^{+/+}$ and *Atf7ip2*$^{-/-}$ testes at P15.

UMAP representations showing expression patterns for IAPEy-int, RLTR10B2, MMERVK10C-int, and average expression of all TEs in spermatogenic cells. P-values are from Wilcoxon rank sum tests: * < 0.05, ** < 0.01, *** < 0.001.

Chapter 2: **Paternal folate deficiency reveals meiosis as a metabolic sensing window in the male germline**[3]

[3] Esparza JM, Kumar RV, Hu M, Munakata Y, Jain S, Sakashita A, Maezawa S, Schultz RM, Namekawa SH. Paternal folate deficiency reveals meiosis as a metabolic sensing window in the male germline. bioRxiv [Preprint]. 2026 Apr 26:2026.04.22.720272. doi: 10.64898/2026.04.22.720272. PMID: 42079217; PMCID: PMC13131588.

My contribution

This project was a true labor of love. After my initial dissertation project resulted in a complete failure, Satoshi and I came together to quickly build a new dissertation project with only a few weeks away from my qualifying exam. Under Satoshi's guidance, I conceptualized, planned, and executed this entire project (and the revisions) as an independent scientist. This project would not have been possible without the support of two of my undergraduate students, Rohan Kumar and Saanvi Jain.

Abstract

Folate-dependent one-carbon metabolism supplies methyl donors required for chromatin modification, yet how metabolic conditions shape epigenome establishment in the male germline remains poorly understood. Here, using a folate-deficient mouse model, we identify meiotic prophase I as a metabolically sensitive window in the male germline. By integrating in vivo germline analysis with bulk and single-cell transcriptomic and epigenomic profiling, we show that folate deficiency disturbs the transcriptome in pachytene spermatocytes and preferentially perturbs CpG island (CGI)-associated promoters, which are characterized by bivalent H3K4me3 and H3K27me3 during meiosis. Consistent with this selective vulnerability, active chromatin marks, including H3K4me3 and H3K27ac, are markedly reduced at CGI-associated promoters under folate-deficient conditions. Notably, loci that later exhibit altered H3K4me3 enrichment in mature sperm show earlier chromatin perturbations during meiosis, suggesting that these sperm epigenomic alterations may originate during meiotic development. Together, these findings establish a mechanistic link between paternal folate deficiency and dynamic epigenomic remodeling of CGI-associated chromatin in the male germline.

Paternal folate deficiency reveals meiosis as a metabolic sensing window in the male germline

Jasmine M. Esparza[1], Rohan V. Kumar[1], Mengwen Hu[1, 4], Yasuhisa Munakata[1, 5], Saanvi Jain[1], Akihiko Sakashita[2], So Maezawa[3], Richard M. Schultz[1], Satoshi H. Namekawa[1*]

[1] Department of Microbiology and Molecular Genetics, University of California, Davis, Davis, CA, USA.

[2] Laboratory for Developmental Genome Plasticity, RIKEN BioResource Research Center, Ibaraki, 305-0074, Japan

[3] Faculty of Science and Technology, Department of Applied Biological Science, Tokyo University of Science, Noda, Chiba, 281-8510, Japan

[4] Present address: Guangzhou Key Laboratory of Metabolic Diseases and Reproductive Health, Guangdong-Hong Kong Metabolism & Reproduction Joint Laboratory, Reproductive Medicine Center, The Affiliated Guangdong Second Provincial General Hospital of Jinan University, Guangzhou 510317, China.

[5] Present address: Department of Cell Science, Institute of Biomedical Sciences, School of Medicine, Fukushima Medical University, Fukushima, 960-1295 Japan.

*Corresponding author: Email: snamekawa@ucdavis.edu

Running title: Meiosis as a metabolic sensing window

Abstract

Folate-dependent one-carbon metabolism supplies methyl donors required for chromatin modification, yet how metabolic conditions shape epigenome establishment in the male germline remains poorly understood. Here, using a folate-deficient mouse model, we identify meiotic prophase I as a metabolically sensitive window in the male germline. By integrating in vivo germline analysis with bulk and single-cell transcriptomic and epigenomic profiling, we show that folate deficiency disturbs the transcriptome in pachytene spermatocytes and preferentially perturbs CpG island (CGI)-associated promoters, which are characterized by bivalent H3K4me3 and H3K27me3 during meiosis. Consistent with this selective vulnerability, active chromatin marks, including H3K4me3 and H3K27ac, are markedly reduced at CGI-associated promoters under folate-deficient conditions. Notably, loci that later exhibit altered H3K4me3 enrichment in epididymal sperm show earlier chromatin perturbations during meiosis, suggesting that these sperm epigenomic alterations originate during meiotic development. Together, these findings establish a mechanistic link between paternal folate deficiency and dynamic epigenomic remodeling of CGI-associated chromatin in the male germline.

Introduction

The importance of paternal health in shaping offspring outcomes has gained increasing attention in recent years (Rando & Simmons, 2015; Rotimi & Singh, 2024). In humans, poor diet, lifestyle factors, and environmental exposures can negatively affect sperm parameters such as sperm count, motility, and morphology, as well as fertility (Eisenberg *et al*, 2014; Ferramosca & Zara, 2022; Gaskins *et al*, 2012; Giahi *et al*, 2016; Rotimi & Singh, 2024). Beyond their role as carriers of genetic information, sperm convey epigenetic information linked to gene expression during early embryonic development that can influence offspring health (Kimmins & Sassone-Corsi, 2005; Lambrot *et al*, 2013; Lismer *et al*, 2021; Siklenka *et al*, 2015). Nutritional status can shape the epigenome by modulating the availability of metabolites required for chromatin-modifying reactions (Van den Veyver, 2002), providing a mechanistic link between paternal diet and germline epigenetic regulation. However, the developmental origins of diet-induced epigenomic information carried by sperm remain a critical gap in our understanding. Although germline epigenetic reprogramming during fetal development is a well-established window of vulnerability (Hayashi *et al*, 2012; Hill *et al*, 2018; Seisenberger *et al*, 2012), accumulating evidence indicates that environmental exposures and lifestyle factors in adult males also shape sperm epigenetic states and offspring phenotypes (Carone *et al*, 2010; Lambrot *et al.*, 2013; Siklenka *et al.*, 2015; Watkins *et al*, 2018).

Spermatogenesis entails extensive chromatin remodeling and epigenomic reprogramming to establish germ cell-specific transcriptomes required for male fertility (Alavattam *et al*, 2024; Hasegawa *et al*, 2015; Hu *et al*, 2024; Kitamura *et al*, 2025a; Kitamura & Namekawa, 2024, 2025; Kitamura *et al*, 2025b; Lin *et al*, 2025; Maezawa *et al*, 2020; Maezawa *et al*, 2018b; Maezawa *et al*, 2023; Rabbani *et al*, 2022; Sin *et al*, 2015). These processes require tight coordination of cellular metabolism, differentiation, and chromatin regulation. As germ cells enter meiosis, their metabolic requirements shift from direct glucose utilization toward reliance on lactate supplied by Sertoli cells (Rotimi *et al*, 2024). Meiotic prophase is accompanied by extensive chromatin reorganization and robust transcriptional activity in pachytene spermatocytes (Bolcun-Filas *et al*, 2011; Maezawa *et al.*, 2020; Soumillon *et al*, 2013), raising the possibility that this developmental window may be particularly sensitive to perturbations in the metabolic inputs required for epigenetic regulation. Nevertheless, whether meiotic prophase translates nutritional status into germline epigenomic states remains unclear.

One-carbon metabolism, supported by dietary folate (vitamin B9) intake, supplies methyl donors such as S-adenosylmethionine (SAM) for DNA and histone methylation reactions underlying epigenomic regulation, thereby linking nutritional status to chromatin regulation (Petrova *et al*, 2023). Folate, obtained from the diet as naturally occurring folates or as synthetic folic acid from fortified foods and supplements, must be acquired exogenously (Berry *et al*, 2010; Crider *et al*, 2022). Meiotic and postmeiotic germ cells reside within the adluminal compartment of the seminiferous epithelium, where nutrient access is regulated by Sertoli cells and the blood–testis barrier. Although folate transport machinery is expressed in the testis, how folate is delivered to these germ cells remains incompletely understood (Eisenga *et al*, 1992; Fice & Robaire, 2023; Hinken *et al*, 2011). Thus, changes in systemic folate availability could alter the metabolic environment experienced by adluminal germ cells. Perturbations in folate availability may in turn reduce the fidelity of germline epigenetic programming during spermatogenesis. Although the benefits of maternal folate supplementation are

well established (Jankovic-Karasoulos *et al*, 2021; Liu *et al*, 2020; van Uitert & Steegers-Theunissen, 2013; Yang *et al*, 2022), the role of paternal folate status in shaping the germ cell epigenome and offspring health has received comparatively less attention, despite evidence linking paternal folate deficiency to adverse reproductive and developmental outcomes (Hoek *et al*, 2020; Lambrot *et al.*, 2013; Lismer *et al.*, 2021; Ly *et al*, 2017). Paternal folate deficiency alters histone H3 lysine 4 trimethylation (H3K4me3) patterns in epididymal sperm and is associated with offspring phenotypes (Lismer *et al.*, 2021). Whether these epigenomic alterations are established during spermatogenesis, including meiotic prophase, or arise later during postmeiotic germ cell maturation remains unknown.

Here, we integrate histological, bulk and single-cell transcriptomic, and epigenomic analyses to define the developmental timing and chromatin contexts in which paternal folate deficiency perturbs spermatogenesis. We identify meiotic pachytene spermatocytes as a particularly vulnerable stage in which folate deficiency perturbs epigenomic regulation, preceding altered epigenetic states previously observed in epididymal sperm. Together, these findings establish meiotic prophase as a metabolic sensing window in the male germline and link paternal nutrition to stage-specific germline epigenomic reprogramming.

Results

Folate deficiency impairs the germ cell population beginning at meiosis.

To examine how paternal nutrition influences stage-specific epigenetic regulation during spermatogenesis, we used a paternal folate–deficient (FD) mouse model previously established for folate-induced epigenetic inheritance (Lismer *et al.*, 2021) (Fig. 1A). Male littermates were maintained on a folate-sufficient (FS) diet until weaning at 3 weeks of age and then randomly assigned to FS or FD diets until 14 weeks of age (Fig. 1B). Because spermatogenesis from spermatogonia to spermatozoa requires approximately 35 days in mice, the 11-week dietary exposure encompassed multiple complete cycles of spermatogenesis (Lismer *et al.*, 2021) (Fig. 1C, D). Previous work demonstrated reduced intratesticular folate levels under this FD regimen (Lismer *et al.*, 2021). Further supporting reduced methyl-donor availability, immunofluorescence analysis revealed reduced SAM abundance in FD testes compared with FS testes, as measured by fluorescence intensity normalized to DAPI (Fig. EV1A). Consistent with a prior report (Lambrot *et al.*, 2013), testis-to-body weight ratios were comparable between FD and FS mice, although body weight—but not testis weight—was slightly increased in FD mice (Fig. EV1B–D). Weekly food consumption was comparable between groups, indicating that the body-weight difference was not explained by food intake (Fig. EV1E). Notably, several human studies have also reported associations between folate deficiency and increased body mass index or body weight (Jafari *et al*, 2023; Mlodzik-Czyzewska *et al*, 2020; Pereira *et al*, 2019).

To assess the impact of folate deficiency on spermatogenesis, we quantified representative germ cell populations in testicular sections from FS and FD mice. ZBTB16 $(PLZF)^{+}$ undifferentiated spermatogonia and KIT^{+} differentiating spermatogonia were maintained at similar cell densities in FS and FD testes (Fig. EV1F, G), suggesting preservation of mitotically dividing spermatogonia under folate deficiency.

Once germ cells enter meiosis and complete autosomal synapsis, pachytene spermatocytes (PSs) exhibit unsynapsed sex chromosomes marked by γH2AX, reflecting activation of the DNA damage response pathway required for meiotic sex chromosome inactivation (MSCI) and XY-body formation (Abe *et al*, 2022; Alavattam *et al*, 2021). FD testes displayed a reduced cell density of PSs exhibiting $\gamma H2AX^+$ XY bodies (Fig. 1E, F), and relative γH2AX intensity within XY bodies was also decreased (Fig. EV1H). We independently assessed this phenotype using chromosome spreads and found reduced XY-body γH2AX intensity in FD early-, mid-, and late-pachytene spermatocytes and diplotene spermatocytes (Fig. EV1I). Together, these findings suggest that folate deficiency attenuates DDR signaling on the sex chromosomes. The densities of mid PSs and more advanced $H1T^+$ germ cells were also reduced in FD testes (Fig. 1E, G), whereas $SOX9^+$ Sertoli cell densities were comparable between groups (Fig. EV1J). Seminiferous epithelial stage distributions were similar between FS and FD testes (Fig. EV1K), indicating that these differences were not attributable to unequal tubule-stage representation. Together, these data suggest that spermatogenesis is particularly sensitive to folate deficiency at the pachytene stage.

Folate deficiency alters the transcriptome in pachytene spermatocytes.

To determine whether folate deficiency perturbs the transcriptome during meiosis, we performed bulk RNA sequencing (RNA-seq) on fluorescence-activated cell sorting (FACS)-purified PSs from FS and FD testes (Fig. 1D). Consistent with prior studies (Alavattam *et al.*, 2024; Yeh *et al*, 2021; Yeh *et al*, 2026), FACS isolation yielded highly purified PS populations (Fig. EV2A). RNA-seq biological replicates showed high concordance based on Pearson correlation analysis (Fig. EV2B). Relative to FS controls, FD PSs exhibited 625 upregulated and 545 downregulated differentially expressed genes (DEGs) (Fig. 1H, Dataset EV1). Of the 625 upregulated DEGs, 68 were located on the sex chromosomes (63 on the X chromosome and 5 on the Y chromosome), including *Rhox11*, *Cypt1*, and *Pgrmc1*, consistent with altered sex-chromosome regulation (Fig. 1I). Gene ontology (GO) analysis revealed enrichment of spermiogenic pathways, including flagellated sperm motility and spermatid differentiation (Fig. EV3A). These upregulated DEGs are normally highly expressed in wild-type round spermatids (RSs) (Fig. 1J; Data ref: Hasegawa et al., 2015; Maezawa et al., 2018), suggesting increased abundance of transcripts normally enriched at postmeiotic stages in FD PSs.

In contrast, 99% of downregulated DEGs were encoded on autosomes (Fig. 1I) and included multiple epigenetic regulators and methyltransferases, such as *Dot1l*, *Mbd3*, *Mettl14*, *Prdm2*, and *Kmt2b*. GO analysis revealed enrichment in chromatin- and RNA-regulatory processes, including mRNA stability and DNA methylation-dependent constitutive heterochromatin formation (Fig. EV3B). More than half of the downregulated DEGs are normally highly expressed during wild-type meiosis (Fig. 1J), indicating perturbation of the meiotic transcriptome.

As a more stringent assessment, we also analyzed differential expression using an adjusted *P* value (*P-adj*) < 0.05. This analysis identified 115 DEGs in FD PSs, including 75 upregulated and 40 downregulated genes (Fig. EV3C). Despite the reduced number of DEGs, the major developmental expression pattern was preserved: nearly all downregulated DEGs were normally highly expressed in wild-type PSs, whereas nearly all upregulated DEGs were normally highly expressed in wild-type RSs (Fig. EV3D). All 115 DEGs meeting the P-adj < 0.05 criterion were autosomal (Fig. EV3E), indicating

that the sex-chromosome expression changes identified using the original DEG criteria did not remain significant under the more stringent criterion.

In mammals, a large proportion of gene promoters contain CpG islands (CGIs; hereafter referred to as CGI promoters), which are typically maintained in a hypomethylated state (Deaton & Bird, 2011). During spermatogenesis, these hypomethylated CGI promoters are bound by the germline-specific Polycomb protein SCML2, which establishes bivalent chromatin marked by repressive H3K27me3 and active H3K4me3 on thousands of genes in PSs (Maezawa *et al*, 2018a). In contrast, promoters with low CG content are preferentially activated later in haploid RSs (Hammoud *et al*, 2014). Consistent with this regulatory hierarchy, 90% of genes downregulated in folate-deficient PSs were CGI-associated (Fig. 1I), indicating that actively transcribed CGI-associated genes during meiosis are particularly sensitive to folate deficiency. Conversely, 17% of upregulated genes were CGI-associated, consistent with increased abundance of transcripts normally enriched at postmeiotic stages (Fig. 1I). This relationship was also preserved among DEGs meeting the $P\text{-}adj < 0.05$ criterion, with 88% of downregulated DEGs and 15% of upregulated DEGs associated with CGI promoters (Fig. EV3E). Together, these data indicate that folate deficiency preferentially affects CGI-associated meiotic gene regulation and is associated with altered expression of postmeiotic transcripts during meiosis.

Folate deficiency results in loss of active epigenetic modifications in pachytene spermatocytes.

Because folate deficiency caused transcriptomic dysregulation during meiosis, we next examined whether it alters underlying epigenetic states in meiotic cells. Accordingly, we assessed chromatin accessibility—reflecting regulatory chromatin regions—using the assay for transposase-accessible chromatin with sequencing (ATAC-seq). Across five biological replicates of PSs, although minor variability among replicates was observed, samples from the FS and FD groups consistently segregated (Fig. EV2C). This pattern indicates a reproducible effect of folate deficiency despite minor variability among biological replicates.

Combined analysis of ATAC-seq data across biological replicates identified 1,832 differentially accessible regions (DARs) in FD PSs, including 768 regions with increased accessibility and 1,064 regions with decreased accessibility (Fig. 2A). The majority of DARs are located in intergenic regions or within gene bodies, whereas only a small fraction overlapped transcription start sites (TSSs), suggesting that folate deficiency predominantly affects putative regulatory regions outside of promoters in PSs (Fig. 2B). Notably, gained DARs in FD PSs were enriched on the sex chromosomes, consistent with altered regulation of the sex chromosomes, whereas most lost DARs were located on autosomes (Fig. 2B).

To further examine epigenetic alterations associated with folate deficiency, we analyzed histone modifications using cleavage under targets and tagmentation (CUT&Tag) for the active promoter mark histone H3 lysine 4 trimethylation (H3K4me3), the active promoter/enhancer mark histone H3 lysine 27 acetylation (H3K27ac), and the repressive mark histone H3 lysine 27 trimethylation (H3K27me3). We performed CUT&Tag with spike-in controls and cell-number normalization to quantitatively evaluate changes in response to folate deficiency. Because H3K4me3 and H3K27me3 are methylation-based modifications requiring SAM, whereas H3K27ac is acetylation-based, this approach allowed us to

assess whether methyl-donor limitation selectively disturbs methylation-based marks or more broadly alters histone modifications. For all three assays, samples from three biological replicates in both FS and FD groups consistently segregated by diet (Fig. EV2D). Consistent with the widespread loss of chromatin accessibility, enrichment of the active histone modifications H3K4me3 and H3K27ac was markedly reduced at many loci in FD PSs (Fig. 2C–F). Genomic regions surrounding the *Ddx4* and *Prdm2* loci are shown as representative examples (Fig. EV3F, G). Among differentially enriched regions (DERs) for H3K4me3 and H3K27ac, ~99% showed decreased enrichment in FD PSs (Fig. 2C, E). In contrast, a modest gain of H3K27me3 DERs was observed in FD PSs (Fig. 2G). Thus, while active chromatin marks were broadly decreased, regions of H3K27me3 enrichment were comparatively less affected, indicating that folate deficiency does not uniformly alter methylation-based histone modifications.

Unlike DARs, which were predominantly located in intergenic regions and gene bodies away from TSSs, a substantial fraction of DERs for all three histone modifications overlapped TSSs (Fig. 2D, F, and H). Notably, most DERs were located on autosomes, indicating a preferential impact of folate deficiency on autosomal histone modifications compared with sex chromosomes. Together, these data demonstrate that folate deficiency distinctly alters chromatin accessibility and histone modification landscapes during meiosis, with pronounced losses of active histone marks at autosomal promoters.

Folate deficiency results in loss of active epigenetic modifications at CpG island-associated promoters.
Because we found that CGI-associated genes expressed during meiosis are particularly sensitive to folate deficiency, we next examined how CGI genes are regulated in FD PSs. Active histone modifications, H3K4me3 and H3K27ac, were strongly enriched at CGI gene promoters, which are characterized by hypomethylated DNA (Data ref: Maezawa et al., 2025), but were markedly reduced at CGI genes in FD PSs (Fig. 3A). In contrast, enrichment of the repressive mark H3K27me3 was increased at CGI genes in FD PSs (Fig. 3A). These results indicate that CGI genes are primary targets of folate deficiency and that loss of folate is associated with reduced H3K4me3 and H3K27ac accompanied by increased H3K27me3. Consistent with this interpretation, 1,181 and 806 of genes containing lost H3K4me3 and H3K27ac DERs (within the TSS, gene body, or TES) in FD PSs were CGI genes (Fig. 3B), whereas all genes containing ATAC-seq DARs were non-CGI genes. Together, these findings demonstrate that folate deficiency preferentially disrupts histone modifications at CGI genes, whereas alterations in chromatin accessibility predominantly occur at non-CGI genes.

At CGI gene promoters, H3K4me3 and H3K27me3 often coexist to form bivalent promoters, a hallmark of PSs thought to prime chromatin states for spermiogenesis and subsequent embryogenesis (Lesch *et al*, 2016; Maezawa *et al.*, 2018a; Sin *et al.*, 2015). CGI gene promoters (n = 25,775) were classified into four states: H3K4me3 only, H3K27me3 only, both H3K4me3 and H3K27me3 positive, or lacking either modification. When comparing FS and FD conditions, the overall distribution of these states was largely similar; however, the number of CGI gene promoters marked with both H3K4me3 and H3K27me3 increased from 5,752 to 6,500 in FD PSs, arising from promoters previously marked by either H3K4me3 or H3K27me3 alone (Fig. 3C). In contrast, CGI promoters lacking both modifications remained relatively stable between

conditions (Fig. 3C). These data further demonstrate that histone modifications at CGI gene promoters are altered in response to folate deficiency.

CGI genes are subject to epigenomic change in round spermatids in response to folate deficiency.
To examine the effects of folate deficiency during postmeiotic haploid stages, we performed bulk RNA-seq on highly purified FACS-isolated RSs from FS and FD testes (Fig. 4A, Fig. EV2A). RS RNA-seq showed strong concordance among biological replicates (Fig. EV2*B*). Relative to FS, FD RS transcriptomes showed minimal changes, with only 21 DEGs—17 upregulated and 4 downregulated—identified (Fig. 4A), indicating that RS transcriptomes are less sensitive to folate deficiency than those of PSs. Notably, all RS DEGs were autosomal, and the majority of upregulated DEGs were classified as CGI genes (Fig. 4B). Despite these modest transcriptomic changes, FD RSs exhibited widespread alterations in chromatin accessibility, predominantly on autosomes (Fig. 4C, D). In contrast to PSs, where ATAC DARs were enriched at non-CGI genes, ATAC DARs in RSs were preferentially enriched at CGI genes (Fig. 4E), suggesting that CGI genes are particularly susceptible to alterations in chromatin accessibility in RSs in response to folate deficiency.

Consistent with these findings, FD RSs displayed reduced H3K4me3 intensity at CGI promoters (Fig. 4F) and an overall loss of H3K4me3-enriched regions; 93% of H3K4me3 DERs (274/294) were lost in FD RSs, many of which were located at TSSs (Fig. 4G, H). Notably, 99% of H3K27ac DERs (17,101/17,113) were lost in FD RSs, and the majority of these regions are located in intergenic or gene body regions. In contrast, H3K27ac intensity increased at CGI promoters, suggesting a redistribution of H3K27ac from distal regulatory regions to promoters (Fig. 4F, I, and J). Conversely, H3K27me3 intensity, which counteracts H3K27ac, decreased at CGI promoters without substantial changes in the overall number of H3K27me3 DERs (Fig. 4F, K). Together, these results demonstrate that CGI genes continue to exhibit epigenomic alterations in RSs under folate deficiency, but that these chromatin states are reconfigured during the transition from PSs to RSs.

Single-cell transcriptome analysis reveals stage-specific effects of folate deficiency on spermatogenesis.
Having established epigenomic alterations at the bulk-cell level in response to folate deficiency, we next sought to determine how folate deficiency affects the transcriptome at the single-cell level throughout spermatogenesis. To this end, single-cell RNA sequencing (scRNA-seq) was performed on FACS-sorted live testicular cells from two biological replicates of FS and FD mice. The overall cellular composition of the testes was comparable between FS and FD mice (Fig. 5A–C; *Fig.* EV4A). With more than 10,000 reads per cell and a 98.7% mapping rate, the scRNA-seq dataset showed high sequencing quality and detected a total of 17,879 genes (Fig. EV4A, B).

After filtering out low-quality cells and clusters with a high proportion of doublets, uniform manifold approximation and projection (UMAP) analysis identified 19 major cell clusters, and developmental trajectories were inferred based on the expression of key marker genes (Fig. 5D, E; Fig. EV4C–G). Cluster 1 corresponded to spermatogonia, as indicated by high expression of *Kit* (Fig. EV4C). Cluster 4 represented meiotic spermatocytes, consistent with elevated expression of *Pou5f2* (Fig. EV4D). High expression of *Prm1* marked downstream clusters as spermatids (Fig. EV4E). Somatic cells

clustered near mitotically dividing spermatogonia and were represented by Cluster 0, as indicated by high expression of *Vim* (Fig. EV4F).

Notably, a germ cell population corresponding to early meiotic spermatocytes (Cluster 4) was markedly reduced in FD testes compared to FS controls (Fig. 5F). In FD testes, reductions in germ cell proportions were also observed in postmeiotic spermatid stages corresponding to Clusters 10–13, representing early to mid postmeiotic spermatids (Fig. 5E, F). Meiotic spermatocytes represented by Clusters 4 and 5 exhibited a higher number of DEGs compared to spermatids in later clusters, whereas fewer DEGs were identified in spermatid clusters (Clusters 10–13) than in spermatocyte clusters (Fig. 5G, Dataset EV2).

Interestingly, expression of the germ cell marker *Ddx4*, which encodes an essential RNA helicase, was markedly reduced in FD testes (Fig. EV5A, B), consistent with reduced enrichment of active histone marks at the *Ddx4* locus (Fig. EV3F). *Ddx4* belongs to a class of germline reprogramming–responsive genes that undergo promoter DNA demethylation in primordial germ cells and play important roles in gametogenesis and meiosis (Hill *et al.*, 2018). Reduced expression of additional germline reprogramming–responsive genes, including *Adad1*, *Sycp1*, *Sycp2*, and *Tdrd1*, was also observed in FD testes (Fig. EV5C–F). Gene Ontology analysis further indicated perturbation of pathways related to spermatogenesis (Fig. EV4H–K), supporting molecular alterations in FD germ cells despite the modest reduction in germ cell density observed in FD testes (Fig. 1E–G).

Because the whole-testis analysis indicated a particularly strong transcriptomic effect within meiotic spermatocytes, we reclustered the spermatocyte populations to obtain greater resolution of meiotic progression (Fig. 5H, I). This analysis resolved ten spermatocyte subclusters spanning leptotene through the meiotic division transition based on stage-specific marker-gene expression (Fig. 5H). The reclustered populations formed a main developmental trajectory and an alternative trajectory terminating in Cluster 7 (Fig. 5H). Cluster 7 was enriched for FD spermatocytes, whereas Cluster 8 contained comparable proportions of FS and FD cells (Fig. 5I, J), raising the possibility that a subset of FD spermatocytes fails to progress along the main trajectory, although the ultimate fate of these cells remains unresolved. Gene set enrichment analysis showed enrichment of meiotic and chromosome-associated pathways in Cluster 8 relative to Cluster 7 (Fig. EV5G). Stress-response scoring showed no enrichment across spermatocyte clusters (Fig. EV5H), suggesting that the FD-enriched state is not explained by a generalized cellular stress response.

We next examined CGI-promoter association among scRNA-seq DEGs across individual clusters. Downregulated DEGs showed consistently high CGI overlap across clusters containing DEGs, with approximately 50–80% of downregulated genes associated with CGI promoters (Fig. EV5I). In contrast, CGI association among upregulated DEGs was more variable across clusters (Fig. EV5I). This preferential CGI association among downregulated genes was consistent with the pattern observed by bulk RNA-seq in purified PSs, further supporting selective disruption of CGI-associated gene regulation under folate deficiency. We further integrated cluster-specific scRNA-seq DEGs with bulk transcriptomic and

epigenomic profiles from purified PSs, revealing promoter-centered chromatin features across multiple DEG sets (Appendix Fig. S1).

Sperm H3K4me3 alterations are preceded by meiotic chromatin remodeling at CpG-rich regions

Paternal folate deficiency alters H3K4me3 enrichment at developmental loci in epididymal sperm, and these altered regions are associated with embryonic abnormalities (Lismer *et al.*, 2021). We therefore asked whether these sperm epigenomic alterations could be traced to earlier stages of spermatogenesis. Using the published sperm H3K4me3 dataset (Data ref: Lismer et al., 2021), we examined whether regions exhibiting altered H3K4me3 in FD sperm also showed epigenetic changes in FD PSs and RSs. Strikingly, loci that later became enriched for H3K4me3 in FD sperm first exhibited marked depletion of the active chromatin marks H3K4me3 and H3K27ac in FD PSs relative to FS controls (Fig. 6A). In FD RSs, H3K4me3 remained reduced at these loci, whereas H3K27ac increased (Fig. 6C). H3K27me3 showed the opposite developmental pattern, increasing in FD PSs but decreasing in FD RSs (Fig. 6A, C). These stage-specific changes indicate dynamic chromatin remodeling preceding altered H3K4me3 enrichment in sperm.

Notably, 71% of sperm regions showing increased H3K4me3 overlapped CGI genes (Fig. 6E). In contrast, regions exhibiting decreased H3K4me3 in FD sperm showed minimal epigenomic disruption in PSs or RSs (Fig. 6B, D), and only 11% overlapped CGI genes (Fig. 6E). These findings indicate that H3K4me3 gains and losses in FD sperm arise from distinct genomic contexts, with CGI-associated regions showing greater developmental responsiveness to folate deficiency.

The preferential association with CGI-containing genes prompted us to examine whether CGI distribution could explain the broader genomic landscape of folate-sensitive molecular changes in FD PSs. We divided the mouse genome into 5-Mb bins and integrated downregulated PS genes with regions showing reduced H3K4me3 and H3K27ac into a multi-mark loss score (Fig. 6F). Regions with high multi-mark loss scores closely coincided with CGI-rich genomic regions (Fig. 6F, G), and CGI density showed a strong positive correlation with the multi-mark loss score (Spearman $\rho = 0.815$, $P = 1.18 \times 10^{-133}$; Fig. 6H). Thus, genomic regions with greater CGI density were substantially more likely to exhibit coordinated loss of gene expression, H3K4me3, and H3K27ac under folate deficiency.

Together with the preferential CGI association among downregulated genes observed in both bulk and single-cell transcriptomic analyses, these findings identify CGI density as a strong genomic correlate of susceptibility to folate-sensitive epigenomic disruption. We therefore propose that CpG-rich genomic architecture may contribute to the selective vulnerability of meiotic chromatin to folate deficiency, resulting in coordinated disruption of active histone modifications and gene expression in pachytene spermatocytes and subsequent remodeling across later stages of spermatogenesis (Fig. 6I).

Discussion

Epigenetic programming during spermatogenesis is essential for proper sperm formation and for supporting normal offspring development. Although paternal nutrition has emerged as an important determinant of offspring health, how metabolic perturbations influence epigenetic regulation across spermatogenic stages has remained unclear. Previous studies showed that folate deficiency alters H3K4me3 patterns in epididymal sperm, suggesting sensitivity of the sperm epigenome to methyl-donor availability. Here, we demonstrate that paternal folate deficiency alters spermatogenesis beginning at meiotic prophase I, affecting both the transcriptome and chromatin organization. Consistent with impaired one-carbon metabolism, SAM abundance was reduced in FD testes, providing evidence that dietary folate deficiency alters the availability of a major cellular methyl donor within the testis. Importantly**,** transcriptomic perturbations were most pronounced in pachytene spermatocytes and were greatly attenuated by the round spermatid stage, whereas chromatin alterations persisted but were reconfigured during postmeiotic development.

In 1984, Robin Holliday proposed that meiosis functions not only to generate haploid gametes and promote genetic recombination but also to reset epigenetic information for the next generation (Berger, 2024; Holliday, 1984). Although this concept has long been neglected, recent studies have revealed that spermatogenesis is accompanied by extensive chromatin reorganization during the transition from mitotically dividing spermatogonia to meiotic spermatocytes, including large-scale transcriptional activation, histone modification remodeling, and chromatin structural reconfiguration (Alavattam *et al.*, 2024; Hasegawa *et al.*, 2015; Kitamura *et al.*, 2025a; Kitamura & Namekawa, 2024, 2025; Kitamura *et al.*, 2025b; Lin *et al.*, 2025; Maezawa *et al.*, 2020; Maezawa *et al.*, 2018b; Maezawa *et al.*, 2023; Rabbani *et al.*, 2022; Sin *et al.*, 2015). Our findings extend this concept by suggesting that meiotic prophase I may operate as a metabolic sensing window in the male germline, during which nutritional conditions can influence the epigenomic landscape undergoing reprogramming.

A previous paternal folate-deficiency model showed that adult testis histology and sperm counts were largely preserved despite reduced pregnancy rates and adverse reproductive outcomes (Lambrot et al., 2013). In contrast, our study detected reduced densities of pachytene spermatocytes and H1T-positive germ cells under folate deficiency, whereas undifferentiated and differentiating spermatogonia and Sertoli cell densities were largely maintained. Differences between the two models may reflect the timing and duration of folate deficiency, as the previous study initiated dietary exposure during fetal development and continued it throughout life, whereas our exposure began after weaning.

Spermatogenesis is a lifelong developmental process sustained by a spermatogonial stem cell population. In our study, spermatogonia were largely preserved under folate deficiency, whereas transcriptomic and epigenomic alterations were more pronounced during meiosis. These observations raise the possibility that meiotic prophase is more responsive to metabolic perturbation than the mitotic germ cell compartment. In this framework, meiotic prophase I may serve as a developmental buffering stage that balances environmental responsiveness with germline stability. This model offers a potential framework for understanding how adult paternal exposures can influence sperm epigenomic states while preserving the spermatogonial stem cell pool that sustains long-term spermatogenesis.

Single-cell analyses further suggest that folate deficiency alters the developmental trajectory of meiotic germ cells rather than producing a uniform transcriptomic response across spermatogenesis. Reclustering of spermatocytes resolved meiotic progression from leptotene through diplotene and identified an alternative trajectory terminating in an FD-enriched mid/late pachytene population. In contrast, the main trajectory progressed through a mid-pachytene population characterized by expression of canonical spermatocyte genes. Although the ultimate fate of these cells remains unresolved, these findings raise the possibility that folate deficiency shifts a subset of spermatocytes toward an alternative transcriptomic trajectory during pachynema. This altered trajectory is consistent with the pachytene-stage sensitivity observed in the histological and bulk molecular analyses.

The epigenomic response to folate deficiency was not uniform across spermatogenesis. Active chromatin marks, including H3K4me3 and H3K27ac, were reduced at CGI promoters in FD PSs, whereas the repressive mark H3K27me3 was increased at these promoters (Fig. 3). Because both H3K4me3 and H3K27me3 depend on SAM as a methyl donor, their opposing responses despite reduced testicular SAM suggest that methyl-donor limitation does not simply produce a uniform decrease in histone methylation. Instead, folate deficiency may alter the recruitment, deposition, turnover, or stability of specific chromatin states. The accompanying loss of H3K27ac, which is not dependent on SAM, further indicates a broader disruption of active chromatin regulation rather than an effect restricted to methylation reactions. These observations suggest that active chromatin states are particularly sensitive to folate deficiency, whereas repressive chromatin marks are comparatively preserved during meiosis.

Our analyses further identify CGI genes as primary epigenomic sites of vulnerability under folate deficiency. CGI promoters are typically hypomethylated and enriched for bivalent chromatin in PSs, a configuration thought to poise developmental regulators for precise activation or repression during spermatogenesis and early embryogenesis (Lesch *et al.*, 2016; Maezawa *et al.*, 2018a; Sin *et al.*, 2015). Under folate deficiency, we observed widespread depletion of active histone marks at CGI genes accompanied by redistribution toward increased bivalency or relative H3K27me3 dominance. Notably, CGI loci that ultimately acquire strong H3K4me3 enrichment in epididymal sperm exhibited marked depletion during meiosis, indicating that folate-dependent chromatin remodeling at these promoters is dynamic and developmentally progressive. Our analysis integrates previously published sperm epigenomic datasets with stage-resolved profiling of germ cells to infer the developmental origin of sperm chromatin alterations. This vulnerability extended beyond individual CGI loci, as coordinated loss of PS gene expression, H3K4me3, and H3K27ac was concentrated in CGI-rich genomic regions (Fig. 6F–H). Together, these findings suggest that CGI-rich genomic architecture may define regions particularly susceptible to folate deficiency and support a model in which methyl-donor limitation perturbs chromatin regulation during meiosis, potentially predisposing specific loci to altered epigenetic states in sperm.

Beyond these locus- and region-level chromatin changes, folate-dependent remodeling during meiosis may intersect with additional layers of chromatin regulation. Recent work has shown that histone variant exchange mediated by the chaperone DAXX promotes replacement of testis-specific histone H3 variants with H3.3 during meiotic prophase I (Yeh *et al.*, 2026). Because H3.3 preferentially marks retained nucleosomes in epididymal sperm and bivalent chromatin

domains are implicated in paternal epigenetic inheritance (Erkek *et al*, 2013; Sakashita *et al*, 2023), our findings raise the possibility that folate-dependent chromatin regulation intersects with histone variant dynamics. This perspective suggests that metabolic perturbation may influence multiple layers of germline chromatin organization beyond individual histone modifications, contributing to broader epigenomic consequences during germ cell development.

The sensitivity of CGI genes to folate deficiency further raises the possibility that maintenance of DNA hypomethylated states may become destabilized under methyl-donor limitation. Although genome-wide DNA methylation remains largely stable during spermatogenesis, our recent study has revealed locus-specific methylation changes (Maezawa *et al*, 2025). Whether CGI promoters maintain methylation fidelity under conditions of limited methyl-donor availability remains unresolved. Future studies integrating histone modification, histone variant dynamics, chromatin accessibility, and DNA methylation will be necessary to define how metabolic stress reshapes multilayered epigenetic regulation in the germline and how these changes influence paternal epigenetic inheritance.

Together, our findings identify meiotic prophase I as a metabolically sensitive stage that integrates paternal nutritional status into the germline epigenome. Rather than passively reflecting environmental stress, the meiotic program appears positioned to selectively encode metabolic information during a developmental window characterized by extensive chromatin remodeling and transcriptional reorganization. This stage-specific responsiveness provides a conceptual framework for how adult environmental exposures can influence the sperm epigenome while largely preserving the spermatogonial stem cell pool. More broadly, these results support a model in which meiosis functions as an adaptive interface between environment and heredity, translating transient metabolic conditions into epigenetic states that persist into sperm. Defining how metabolic inputs intersect with chromatin regulation during meiosis will be essential for understanding the molecular basis of paternal epigenetic inheritance and how environmental factors shape developmental trajectories across generations.

Methods and Protocols

Animals

Mice were maintained on a 12:12 light:dark cycle in a temperature- and humidity-controlled vivarium (22 ± 2˚C; 40-50% humidity) with *ad libitum* access to food and water in a pathogen-free animal care facility. All animal procedures were approved by the Institutional Animal Care and Use Committee (IACUC protocol no. 21931 and 23545) at the University of California, Davis. All mice were maintained on a C57BL/6J background (Jackson Laboratory, 000664). The study was conducted and reported in accordance with the ARRIVE guidelines.

Dietary treatments

Dietary folate concentrations were based on established paternal diet mouse models (Knock *et al*, 2008; Lismer *et al.*, 2021). The folate sufficient (FS) diet contained 2.0 mg/kg folic acid (TD.01369, Inotiv), whereas the folate deficient (FD) diet contained 0.3 mg/kg folic acid (TD.01546, Inotiv). All breeder mice were maintained on the FS diet. Male littermates were weaned at 3 weeks of age, and litters with at least two males were randomly assigned to either the FS or FD diet. Mice remained on their assigned diets for 11 weeks and were sacrificed at 14 weeks of age.

Preparation of meiotic chromosome spreads

Meiotic chromosome spreads were prepared as previously described (Alavattam *et al*, 2018). Testes were excised, detunicated, and seminiferous tubules were detangled in 1x phosphate-buffered saline (PBS). Tubules were sequentially washed in PBS and incubated in hypotonic extraction buffer (HEB) (30 mM Tris base, 17 mM trisodium citrate, 5 mM ethylenediaminetetraacetic acid (EDTA), 50 mM sucrose, 5 mM dithiothreitol (DTT), and 1x cOmplete Protease Inhibitor Cocktail (Sigma, 11836145001) on ice for 1 h. Tubules were mechanically dissociated in 100 mM sucrose, and cell suspensions were applied to positively charged slides (Probe On Plus, Thermo Fisher Scientific, 22-230-900) precoated with fixation solution (2% paraformaldehyde, 0.1% Triton X-100, and 0.02% sodium monododecyl sulfate, adjusted to pH 9.2 with sodium borate buffer). Slides were incubated in a humid chamber at room temperature for a minimum of 4 hours, air-dried, washed twice in 0.4% Photo-Flo (Kodak, 146-4510) and stored at -80˚C until use.

Histology and Immunostaining

Testes were fixed with 4% paraformaldehyde with 0.1% Triton X-100 in PBS at 4˚C overnight, dehydrated in 70% ethanol, and embedded in paraffin. Sections (4 μm) were deparaffinized and subjected to antigen retrieval in citrate buffer (pH 6.1, DAKO, S-1700) using an autoclave (121˚C, 15 psi, 10 minutes). Sections were blocked in Blocking One Histo (Nacalai USA, 06349-64) and then incubated in primary antibodies at 4˚C overnight. Alexa Fluor-conjugated secondary antibodies were applied for 1 h at room temperature. Slides were counterstained with DAPI and mounted in ProLong Gold. Images were obtained with a Nikon AX Confocal microscope system and were processed using NIS-Elements Advanced Research (Nikon), Photoshop (Adobe), and Illustrator (Adobe) software. Images were acquired using identical microscope settings (laser power, gain, and exposure time) across experimental conditions within each staining

experiment. Negative controls were performed in parallel by omitting the primary antibody while retaining all subsequent staining and imaging steps.

This study used the following primary antibodies at the following dilutions [format: host-protein (source or company with product/catalog number if applicable), dilution]: goat anti-ZBTB16/PLZF (R&D Systems, AF2944), 1/200; goat anti-cKIT (R&D Systems, AF1356), 1/500; mouse anti-H2AX-pS139 conjugated Alexa 647 (γH2AX) (Millipore, 05-636), 1/500; guinea pig anti-H1T (a gift from Dr. Mary Ann Handel (Inselman *et al*, 2003)), 1/500; rabbit anti-SOX9 (Millipore, AB5535), 1/500; rabbit anti-S-adenosylmethionine (MyBioSource, MBS2015171), 1/500.

FACS-isolation of male germ cells

PSs and RSs were isolated using Fluorescence-activated cell sorting (FACS) as described previously (Yeh *et al.*, 2021). In brief, single cell suspensions were generated from seminiferous tubules by enzymatic dissociation in DMEM containing 2mg/mL Type 1 collagenase (Worthington, CLS1), 0.25 mg/mL DNase I (Sigma, D5025), 1.5 mg/mL hyaluronidase (Sigma, H3506), and 700 U/mL recombinant collagenase (FUJIFILM Wako Pure Chemical Corporation, 036-23141) at 35˚C followed by several PBS washes. Cells were filtered through 70 μm strainers (Falcon, 352350) and washed in FACS buffer (PBS + 2% FBS). PSs and RSs were isolated using 2 μL/mL Vybrant DyeCycle Violet. Sorting was performed on a Cell Sorter SH800 (SONY) into collection buffer (50% FBS diluted in PBS). After sorting, cells were washed in PBS, resuspended in CELLBANKER 1 cryopreservation medium (Zenogen Pharma Co, 11910), and stored at -80˚C until use.

Bulk RNA-seq library generation and sequencing

FACS-isolated PSs (~50,000) and RSs (~100,000) were collected from three independent biological replicates. ERCC RNA Spike-In Mix 1 (Invitrogen, 4456653) diluted 1:10,000 was added prior to RNA extraction (5 μL for PS samples, 10 μL for RS samples). Total RNA was isolated using the RNeasy Plus Mini Kit (QIAGEN, 74134) according to the manufacturer's instructions. Libraries were prepared using the NEBNext® Single Cell/Low Input RNA Library Prep Kit for Illumina® (NEB, E6420S) sequenced on the Illumina NovaSeq X Plus platform (150 bp paired-end).

Bulk RNA-seq read processing, quantification, and differential expression analysis

Paired-end RNA-seq reads were adapter- and quality-trimmed using Trim Galore (v0.6.10) with parameters --paired --nextera --quality 25 --length 30 and FastQC (v0.12.1) reporting. Trimmed reads were aligned to mm10 (GRCm38) using HISAT2 (v2.2.1). Alignments were converted to BAM format using SAMtools (v1.16.1), and uniquely mapped reads were retained (MAPQ ≥30; flags -q 30 -F 4). Filtered BAM files were sorted and indexed.

Gene-level counts were generated using featureCounts (Subread v2.0.2) with the GENCODE vM25 annotation in paired-end mode (-p -B -C). Counts were generated separately for each biological replicate.

Differential expression analysis was performed using DESeq2 (v1.38.3). For each cell type (PS and RS), count matrices were constructed by merging replicate count files by gene identifier. The design formula was: ~ batch + condition where

batch corresponded to biological replicate. Differential expression was assessed using the Wald test. Differentially expressed genes (DEGs) were defined using nominal P value < 0.05 and |log2FoldChange| > 1.5.

For quality control, variance-stabilizing transformation (VST; blind = TRUE) was applied. Pearson correlation matrices were calculated from VST-transformed counts and visualized using pheatmap (v1.0.13). MA plots were generated using ggplot2 (v3.5.1).

ATAC-seq library preparation and sequencing

ATAC-seq libraries were prepared as previously described from FACS-isolated PSs (~50,000) and RSs (~100,000) collected from five independent biological replicates. Nuclei were isolated and subjected to Tn5-transposase (made in-house) at 37˚C for 30 min. After tagmentation, the transposed DNA was purified using the MinElute kit (Qiagen, 28004) following the manufacturer's instructions. Libraries were amplified using PCR, with cycle number determined by qPCR to reach 25% saturation. Libraries were purified using SPRIselect beads (Beckman Coulter, B23317) and sequenced on an Illumina NovaSeq X Plus (150-bp paired end).

ATAC-sequencing read processing, peak calling, and differential accessibility analysis

Raw paired-end ATAC-seq reads were adapter- and quality-trimmed using Trim Galore (v 0.6.10) with FastQC (v0.12.1) reporting. Trimmed reads were aligned to the mouse reference genome (mm10/GRCm38) in paired-end mode with parameters –end-to-end –no-mixed –no-discordant -I 10 -X 200. Alignments were converted to BAM format, sorted, and indexed using SAMtools (v 1.16.1).

To account for Tn5 insertion offsets, alignments were shifted using deepTools alignmentSieve (--ATACshift; v3.5.2). Uniquely mapped, properly paired reads were retained (SAMtools flags -f 2 -F 2048, MAPQ ≥30), and mitochondrial reads (chrM) were removed. ENCODE mm10 blacklisted regions (v2) were excluded using BEDTools (v2.31.0). Library complexity was assessed using csaw (readsDupFreq and estimateLibComplexity; v1.32.0). To normalize libraries to a common molecular complexity following the approach of Reske *et al*. (Reske *et al*, 2020), BAM files were downsampled using SAMtools to match the lowest number of unique fragments across the experiments per cell type. PCR duplicates were removed using Picard MarkDuplicates (v 3.0.0) with REMOVE_DUPLICATES=true, and final BAM files were sorted and indexed.

Peaks were called on each biological replicate using MACS3 (v3.0.0b3) with parameters –nomodel –nolambda -q 0.05 -g mm -B –SPMR –keep-dup all. Peak sets were filtered to remove blacklist region overlaps and non-standard contigs. Condition-level peak sets were obtained by pooling replicate BAMs within each condition and calling peaks with the same MACS3 parameters. A consensus peak file was defined as the union of the pooled peak sets from FS and FD samples.

Differential accessibility was assessed in R using csaw and edgeR (v3.40.2) using the consensus peak file as the working feature set ("peaks-only" analysis). Read counts over the consensus peaks were computed with csaw regionCounts using paired-end mode, restricting to standard chromosomes (chr1-19, X, Y), and discarding blacklisted regions. Low abundance peaks were filtered by average abundance (edgeR avgLogCPM threshold > -3). Library size normalization factors were computed using TMM normalization from binned genomic windows (csaw windowCounts with 10-kb bins) and applied to peak counts (csaw normFactors), following Reske *et al.* Differential accessibility was tested using edgeR quasi-likelihood negative binomial generalized linear models (estimateDisp; glmQLFit with robust=TRUE; glmQLFTest) comparing FD against FS samples.

To report region-level differential accessibility regions (DARs), nearby significant windows were merged (csaw mergeWindows; tolerance 500bp; maximum merged width 5kb), and each merged region was assigned statistical significance based on its most significant constituent window (csaw getBestTest). DARs were defined using P-value threshold of <0.05 and an absolute log2 fold-change threshold of ≥ 2. Normalized coverage tracks were generated using deepTools bamCoverage with BPM normalization.

CUT&Tag library preparation and sequencing

FACS-isolated PSs (~50,000) and RSs (~100,000) were collected from three independent biological replicates. CUT&Tag libraries of PSs and RSs were prepared as previously described (Kaya-Okur *et al*, 2020; Kaya-Okur *et al*, 2019) with some modifications (a step-by-step protocol https://www.protocols.io/view/bench-top-cut-amp-tag-kqdg34qdpl25/v3) using CUTANA™ pAG-Tn5 (Epicypher, 15-1017). To perform quantitative spike-in CUT&Tag, Drosophila S2 cells were added to mouse germ cells at a fixed ratio (1000 S2 cells to 5000 mouse germ cells) at the beginning of each reaction. The antibodies used were rabbit anti-H3K4me3 (1/50; Invitrogen; 703849, LOT 2920880), rabbit anti-H3K27ac (1/50; Cell Signaling Technology; 8173S), and rabbit anti-H3K27me3 (1/50; Cell Signaling Technology; 9733S). CUT&Tag libraries were sequenced on Illumina NovaSeq X Plus (150-bp paired end).

CUT&Tag data processing, spike-in normalization, and differential enrichment analysis

CUT&Tag paired-end reads were processed following the Henikoff Lab pipeline with modifications. Reads were adapter- and quality-trimmed using Trim Galore (v0.6.10) and aligned to mm10 (GRCm38) using Bowtie2 (v2.4.5) with parameters --end-to-end --very-sensitive --no-mixed --no-discordant --phred33 -I 10 -X 700. Spike-in Drosophila melanogaster DNA (S2-derived) was aligned separately to dm6 using Bowtie2 with additional parameters --no-overlap --no-dovetail to prevent cross-mapping.

Mouse-aligned BAM files were sorted and indexed using SAMtools (v1.16.1). ENCODE mm10 blacklist regions (v2) were removed using BEDTools (v2.31.0), and properly paired high-confidence reads were retained (SAM flags -f 2 -F 2048, MAPQ ≥30). Library complexity was estimated using ATACseqQC (readsDupFreq, estimateLibComplexity), and within each cell type × histone mark group, BAM files were downsampled to the minimum unique fragment count across replicates. PCR duplicates were removed using Picard MarkDuplicates (v3.0.0).

Spike-in normalization factors were calculated per replicate as: scale factor = 100,000 / (aligned dm6 reads)
Replicate-level spike-in–scaled coverage tracks were generated using deepTools bamCoverage (v3.5.5) with parameters --binSize 1 --extendReads --samFlagInclude 64 --normalizeUsing RPKM --scaleFactor <sample-specific factor>.
For visualization only, biological replicates were merged using SAMtools merge. Group-level scale factors were calculated as: scale factor = 100,000 / (sum of aligned dm6 reads across replicates). Merged spike-in–scaled BigWig tracks were generated for genome browser visualization (IGV v2.14.1).

Replicate concordance was assessed using deepTools multiBigwigSummary (bins mode). Log2-transformed signals were batch-corrected using limma (removeBatchEffect, v3.54.2), and Pearson correlation matrices were visualized using pheatmap (v1.0.13).

For differential enrichment analysis, replicate-level scaled BigWig files were summarized using multiBigwigSummary (bins mode). The resulting matrices were analyzed using DESeq2 (v1.38.3). Because coverage tracks were spike-in normalized prior to modeling, size factors were fixed to 1. Region values were scaled by a constant and rounded to integers prior to modeling. Differential enrichment was assessed using the design formula ~ batch + condition, comparing FD and FS samples using the Wald test. Differentially enriched regions (DERs) were defined using adjusted P value < 0.05 and |log2FoldChange| > 1.

Single-cell RNA-seq library preparation

Single cell suspensions were prepared from testes collected from two independent biological replicates as described above. Dead cells were excluded by 7-AAD Viability Stain (35 µL/mL), and viable cells were sorted prior to fixation. For each biological replicate, at least 1 x 10^6 viable testicular cells were collected. Cells were fixed for 22 h at 20 ˚C using the Chromium Next GEM Single Cell Fixed RNA Sample Preparation kit (10X Genomics, 1000414). Approximately 20,000 cells were loaded on the Chromium Controller (10X Genomics Inc.). Libraries were prepared using the Chromium GEM-X Flex Reagent kits (10X Genomics, CG000787 Rev A) and sequenced on the Element Biosciences AVITI system using a paired-end read configuration of 28 bp (Read 1) × 10 bp (i7 index) × 10 bp (i5 index) × 90 bp (Read 2).

Single-cell RNA-seq processing and analysis

Alignment and gene counting was performed using the cloud-based 10x Genomics Cell Ranger Multi pipeline (v9.0.0) against the mouse reference genome GRCm39 2024-A.
Downstream analysis was performed in R using Seurat (v5.3.0; SeuratObject v5.1.0). Feature-barcode matrices were loaded using Read10X_h5 and converted to Seurat objects with an initial filter of ≥200 detected genes per cell. The fraction of mitochondrial transcripts was calculated using PercentageFeatureSet (pattern “^mt-”), and low-quality cells were removed by filtering for 200 < nFeature_RNA ≤ 4,000 and mitochondrial content <10%. Each sample was normalized using SCTransform (SCTransform, default parameters), and datasets were integrated using SCT-based integration with default integration features (SelectIntegrationFeatures), anchor identification (FindIntegrationAnchors,

normalization.method = “SCT”), and data integration (IntegrateData). Principal component analysis was performed on the integrated assay (RunPCA), and clustering was carried out using a shared nearest-neighbor graph constructed from the first 10 principal components (FindNeighbors, dims = 1:10) followed by Louvain clustering (FindClusters, resolution = 0.4). UMAP embeddings were computed using the first 10 principal components (RunUMAP, dims = 1:10, min.dist = 0.3, spread = 1).

Doublets were identified using scDblFinder (v1.20.2) by converting the integrated Seurat object to a SingleCellExperiment and running scDblFinder. Cells classified as singlets were retained for downstream analyses. Clusters enriched for predicted doublets were identified by inspection of scDblFinder classifications and marker expression patterns and were excluded prior to re-running scaling, PCA, neighbor finding, clustering (resolution = 0.4), and UMAP on the curated dataset.

For higher-resolution analysis of meiotic spermatocytes, cells from spermatocyte clusters 3–8 were subset from the curated Seurat object and reclustered. The RNA assay was used for this analysis, RNA layers were joined using JoinLayers, and expression values were normalized using NormalizeData with the LogNormalize method. PCA, neighbor finding, clustering, and UMAP were repeated on the spermatocyte subset using the first 10 principal components, a clustering resolution of 0.4, and UMAP parameters of min.dist = 0.3 and spread = 1. Reclustering annotations were assigned based on expression of established stage-specific meiotic marker genes. Developmental trajectories within the reclustered spermatocyte population were inferred using Slingshot, and the proportions of FS and FD cells within each reclustered population were calculated.

For cluster-resolved differential expression testing between dietary conditions, the RNA assay was used. RNA layers were joined (JoinLayers) and normalized log-expression values were computed with NormalizeData (RNA assay). Within each cluster, cells were subset and identities were set to dietary group; differential expression between folate-deficient and folate-sufficient samples was tested using FindMarkers (Seurat default test) on the RNA assay using the normalized data layer (layer = “data”), with only.pos = FALSE. Genes were considered differentially expressed using thresholds of adjusted P value <0.05 and |log2 fold change| ≥ 1. The same differential expression workflow was applied to the reclustered spermatocyte populations for integration with bulk RNA-seq, ATAC-seq, and CUT&Tag datasets.

Identification of CGI genes and non-CGI genes

CpG islands (CGIs) were defined as published (Illingworth *et al*, 2010; Smallwood *et al*, 2011), and their coordinates of mouse genome GRCm38/mm10 assembly (n=17,017) were downloaded from UCSC genome browser. Genes were classified as CGI genes if a first base pair of any transcript TSSs ±100-bp overlapped a CGI. In this way, the total 67,340 genes from Gencode vM25 mouse gene annotations (after removing Chromosome M genes) were divided into CGI genes (n=25,775) and non-CGI genes (n=41,565).

Genome-wide multi-mark hotspot and CpG island density analysis

To identify genomic regions exhibiting coordinated molecular loss in FD pachytene spermatocytes, the mouse genome was divided into non-overlapping 5-Mb bins. Features showing decreased H3K27ac, decreased H3K4me3, or decreased RNA expression in FD PSs were assigned to genomic bins according to their genomic start position. For each molecular feature, the observed number of features within each bin was compared with the expected number based on the total number of features and the genomic fraction represented by the corresponding bin. A Poisson Z-score was calculated as Z = (observed − expected) / √expected, with zero-count bins retained in the analysis. Poisson Z-scores for H3K27ac, H3K4me3, and RNA were combined within each genomic bin using a Stouffer-style statistic, Z_combined = (Z_H3K4me3 + Z_H3K27ac + Z_RNA) / √n, where n = 3. Bins with a combined Z-score ≥2 were classified as multi-mark loss hotspots.

CpG island density was quantified across the same 5-Mb genomic bins using CpG island coordinates from the mm10 genome assembly. For CpG islands spanning bin boundaries, the number of base pairs overlapping each bin was calculated separately. Within each bin, total CpG island coverage was calculated as the sum of overlapping CpG island base pairs and normalized to bin length to obtain CpG island density as base pairs per Mb. Bins containing no CpG island overlap were retained with a density of zero.

The relationship between CpG island density and multi-mark loss was evaluated across all genomic bins using Spearman rank correlation. CpG island density between bins classified as multi-mark hotspots and non-hotspot bins was compared using a Wilcoxon rank-sum test. Genome-wide distributions of the combined multi-mark Z-score and CpG island density were visualized across 5-Mb genomic intervals.

Quantification and statistical analysis

All image quantifications were performed in a blinded manner. Images were exported as individual experimental units (e.g., individual seminiferous tubules for histological analysis) and file names were anonymized prior to analysis using the File Name Encrypter tool (Blind Analysis Tool plugin v1.0) for ImageJ (v1.53t). Investigators performing quantifications were unaware of dietary group assignments, and encrypted file names were decoded only after completion of analysis for statistical analysis. Signal intensity measurements were performed using NIS Elements Advanced Research (AR) software. Fluorescence intensity values were normalized to DAPI signal to control for variation in nuclear content and imaging conditions. For tubule-based quantifications, the number of positive cells per tubule was determined and normalized to tubule surface area, which was measured using manual region-of-interest tracing in NIS Elements AR.

Statistics

Statistical methods and P values for each plot are listed in the figure legends. Statistical significance for pairwise comparisons was assessed using two-tailed unpaired t-tests or Wilcoxon rank-sum tests, with the statistical test used for each comparison specified in the corresponding figure legend. Next-generation sequencing data were based on at least three independent replicates except for single-cell RNA sequencing, which was based on two biological replicates. No statistical methods were used to initially determine sample size in these experiments. Male littermates were randomly

assigned to FS or FD diets. After tissue collection, downstream sample processing was not randomized; instead, samples were processed as matched littermate pairs, with the corresponding FS and FD samples handled together. Investigators were aware of dietary group allocation during staining and other experimental procedures. However, quantitative analysis of images was performed with investigators blinded to dietary condition.

Data availability

Bulk RNA-seq data, ATAC-seq, CUT&Tag data, and scRNA-seq sets were deposited in the Gene Expression Omnibus under accession no. GSE324234.

The accession codes for the raw published data used in this study are as follows:

- THY1$^+$, PS, and RS RNA-seq (Fig. 1J): GSE55060 (Hasegawa *et al.*, 2015)
- KIT$^+$ RNA-seq (Fig. 1J): GSE89502 (Maezawa *et al.*, 2018a)
- MethylCap-seq (Fig. 3A) GSE262669 (Maezawa *et al.*, 2025)
- Sperm H3K4me3 (Fig. 6A-D) GSE135678 (Lismer *et al.*, 2021)

Sperm H3K4me3 data (GSE135678) (Lismer *et al.*, 2021) were reanalyzed, and differentially enriched regions (DERs) were identified using the following criteria: a p-value < 0.1 (quasi-likelihood F-test) and an average log2 CPM > 1.

Acknowledgments

We thank members of the Namekawa lab for discussions; AI Ikuyo for discussions and help with data analysis; and Mary Ann Handel for providing the H1T antibody. The sequencing was carried out at the DNA Technologies and Expression Analysis Core at the UC Davis Genome Center (RRID: SCR_017740), supported by NIH Shared Instrumentation Grant 1S10OD010786-01. We acknowledge the following funding sources: the NIGMS T32 predoctoral training program in Molecular and Cellular Biology (MCB) at UC Davis (T32GM007377) and a National Academies Ford Foundation Fellowship to J.M.E.; UC Davis Provost's Undergraduate Fellowship to R.V.K.; R35GM141085 to S.H.N.; and a supplement to R35GM141085 to J.M.E. and S.H.N.

Author contribution

J.M.E. and S.H.N. designed the study. J.M.E., R.V.K., and S.J. performed the experiments, with contributions from M.H. and Y.M. J.M.E. performed the computational analysis, with contributions from M.H., Y.M., A.S., and S.M. J.M.E., A.S., S.M., R.M.S., and S.H.N. interpreted the results. J.M.E. and S.H.N. wrote the manuscript with critical feedback from all authors. S.H.N. supervised the project.

Competing interests

The authors declare no competing interests.

References

Abe H, Yeh YH, Munakata Y, Ishiguro KI, Andreassen PR, Namekawa SH (2022) Active DNA damage response signaling initiates and maintains meiotic sex chromosome inactivation. *Nat Commun* 13: 7212

Alavattam KG, Abe H, Sakashita A, Namekawa SH (2018) Chromosome Spread Analyses of Meiotic Sex Chromosome Inactivation. *Methods Mol Biol* 1861: 113-129
Alavattam KG, Esparza JM, Hu M, Shimada R, Kohrs AR, Abe H, Munakata Y, Otsuka K, Yoshimura S, Kitamura Y *et al* (2024) ATF7IP2/MCAF2 directs H3K9 methylation and meiotic gene regulation in the male germline. *Genes Dev* 38: 115-130
Alavattam KG, Maezawa S, Andreassen PR, Namekawa SH (2021) Meiotic sex chromosome inactivation and the XY body: a phase separation hypothesis. *Cell Mol Life Sci* 79: 18
Berger F (2024) Meiosis as a mechanism for epigenetic reprogramming and cellular rejuvenation. *Development* 151
Berry RJ, Bailey L, Mulinare J, Bower C, Folic Acid Working G (2010) Fortification of flour with folic acid. *Food Nutr Bull* 31: S22-35
Bolcun-Filas E, Bannister LA, Barash A, Schimenti KJ, Hartford SA, Eppig JJ, Handel MA, Shen L, Schimenti JC (2011) A-MYB (MYBL1) transcription factor is a master regulator of male meiosis. *Development* 138: 3319-3330
Carone BR, Fauquier L, Habib N, Shea JM, Hart CE, Li R, Bock C, Li C, Gu H, Zamore PD *et al* (2010) Paternally induced transgenerational environmental reprogramming of metabolic gene expression in mammals. *Cell* 143: 1084-1096
Crider KS, Qi YP, Yeung LF, Mai CT, Head Zauche L, Wang A, Daniels K, Williams JL (2022) Folic acid and the prevention of birth defects: 30 years of opportunity and controversies. *Annu Rev Nutr* 42: 423-452
Deaton AM, Bird A (2011) CpG islands and the regulation of transcription. *Genes Dev* 25: 1010-1022
Eisenberg ML, Kim S, Chen Z, Sundaram R, Schisterman EF, Buck Louis GM (2014) The relationship between male BMI and waist circumference on semen quality: data from the LIFE study. *Hum Reprod* 29: 193-200
Eisenga BH, Collins TD, McMartin KE (1992) Incorporation of 3H-label from folic acid is tissue-dependent in folate-deficient rats. *J Nutr* 122: 977-985
Erkek S, Hisano M, Liang CY, Gill M, Murr R, Dieker J, Schübeler D, van der Vlag J, Stadler MB, Peters AH (2013) Molecular determinants of nucleosome retention at CpG-rich sequences in mouse spermatozoa. *Nat Struct Mol Biol* 20: 868-875
Ferramosca A, Zara V (2022) Diet and male fertility: The impact of nutrients and antioxidants on sperm energetic metabolism. *Int J Mol Sci* 23: 2542
Fice HE, Robaire B (2023) Aging affects gene expression in spermatids of Brown Norway rats. *Exp Gerontol* 173: 112086
Gaskins AJ, Colaci DS, Mendiola J, Swan SH, Chavarro JE (2012) Dietary patterns and semen quality in young men. *Hum Reprod* 27: 2899-2907
Giahi L, Mohammadmoradi S, Javidan A, Sadeghi MR (2016) Nutritional modifications in male infertility: a systematic review covering 2 decades. *Nutr Rev* 74: 118-130
Hammoud SS, Low DH, Yi C, Carrell DT, Guccione E, Cairns BR (2014) Chromatin and transcription transitions of mammalian adult germline stem cells and spermatogenesis. *Cell Stem Cell* 15: 239-253
Hasegawa K, Sin H-S, Maezawa S, Broering TJ, Kartashov AV, Alavattam KG, Ichijima Y, Zhang F, Bacon WC, Greis KD *et al* (2015) SCML2 Establishes the Male Germline Epigenome through Regulation of Histone H2A Ubiquitination. *Dev Cell* 32: 574-588
Hayashi K, Ogushi S, Kurimoto K, Shimamoto S, Ohta H, Saitou M (2012) Offspring from oocytes derived from in vitro primordial germ cell-like cells in mice. *Science* 338: 971-975
Hill PWS, Leitch HG, Requena CE, Sun Z, Amouroux R, Roman-Trufero M, Borkowska M, Terragni J, Vaisvila R, Linnett S *et al* (2018) Epigenetic reprogramming enables the transition from primordial germ cell to gonocyte. *Nature* 555: 392-396
Hinken M, Halwachs S, Kneuer C, Honscha W (2011) Subcellular localization and distribution of the reduced folate carrier in normal rat tissues. *Eur J Histochem* 55: e3
Hoek J, Steegers-Theunissen RPM, Willemsen SP, Schoenmakers S (2020) Paternal Folate Status and Sperm Quality, Pregnancy Outcomes, and Epigenetics: A Systematic Review and Meta-Analysis. *Mol Nutr Food Res* 64: e1900696
Holliday R (1984) The biological significance of meiosis. *Symp Soc Exp Biol* 38: 381-394
Hu M, Yeh YH, Maezawa S, Nakagawa T, Yoshida S, Namekawa SH (2024) PRC1 directs PRC2-H3K27me3 deposition to shield adult spermatogonial stem cells from differentiation. *Nucleic Acids Res* 52: 2306-2322
Illingworth RS, Gruenewald-Schneider U, Webb S, Kerr AR, James KD, Turner DJ, Smith C, Harrison DJ, Andrews R, Bird AP (2010) Orphan CpG islands identify numerous conserved promoters in the mammalian genome. *PLoS Genet* 6: e1001134
Inselman A, Eaker S, Handel MA (2003) Temporal expression of cell cycle-related proteins during spermatogenesis: establishing a timeline for onset of the meiotic divisions. *Cytogenet Genome Res* 103: 277-284

Jafari A, Gholizadeh E, Sadrmanesh O, Tajpour S, Yarizadeh H, Zamani B, Sohrabi Z (2023) The effect of folic acid supplementation on body weight and body mass index: A systematic review and meta-analysis of randomized controlled trials. *Clin Nutr ESPEN* 53: 206-213
Jankovic-Karasoulos T, Furness DL, Leemaqz SY, Dekker GA, Grzeskowiak LE, Grieger JA, Andraweera PH, McCullough D, McAninch D, McCowan LM *et al* (2021) Maternal folate, one-carbon metabolism and pregnancy outcomes. *Matern Child Nutr* 17: e13064
Kaya-Okur HS, Janssens DH, Henikoff JG, Ahmad K, Henikoff S (2020) Efficient low-cost chromatin profiling with CUT&Tag. *Nat Protoc* 15: 3264-3283
Kaya-Okur HS, Wu SJ, Codomo CA, Pledger ES, Bryson TD, Henikoff JG, Ahmad K, Henikoff S (2019) CUT&Tag for efficient epigenomic profiling of small samples and single cells. *Nat Commun* 10: 1930
Kimmins S, Sassone-Corsi P (2005) Chromatin remodelling and epigenetic features of germ cells. *Nature* 434: 583-589
Kitamura Y, Munakata Y, Abe H, Hu M, Oya S, Murugesan S, Rizwan M, Katz S, Picketts D, Schultz R *et al* (2025a) The SMARCA5-DMRT1 pioneer complex establishes epigenetic priming to direct male germline development. *Res Sq*
Kitamura Y, Namekawa SH (2024) Epigenetic priming in the male germline. *Curr Opin Genet Dev* 86: 102190
Kitamura Y, Namekawa SH (2025) The 3D genome during germline development and meiosis. *Trends Genet*
Kitamura Y, Takahashi K, Maezawa S, Munakata Y, Sakashita A, Katz SP, Kaplan N, Namekawa SH (2025b) CTCF-mediated 3D chromatin sets up the gene expression program in the male germline. *Nat Struct Mol Biol*: 1-14
Knock E, Deng L, Wu Q, Lawrance AK, Wang XL, Rozen R (2008) Strain differences in mice highlight the role of DNA damage in neoplasia induced by low dietary folate. *J Nutr* 138: 653-658
Lambrot R, Xu C, Saint-Phar S, Chountalos G, Cohen T, Paquet M, Suderman M, Hallett M, Kimmins S (2013) Low paternal dietary folate alters the mouse sperm epigenome and is associated with negative pregnancy outcomes. *Nat Commun* 4: 2889
Lesch BJ, Silber SJ, McCarrey JR, Page DC (2016) Parallel evolution of male germline epigenetic poising and somatic development in animals. *Nat Genet* 48: 888-894
Lin Z, Rong B, Lyu R, Zheng Y, Chen Y, Yan J, Wu M, Gao X, Tang F, Lan F *et al* (2025) SETD1B-mediated broad H3K4me3 controls proper temporal patterns of gene expression critical for spermatid development. *Cell Res* 35: 345-361
Lismer A, Dumeaux V, Lafleur C, Lambrot R, Brind'Amour J, Lorincz MC, Kimmins S (2021) Histone H3 lysine 4 trimethylation in sperm is transmitted to the embryo and associated with diet-induced phenotypes in the offspring. *Dev Cell* 56: 671-686.e676
Liu H-Y, Liu S-M, Zhang Y-Z (2020) Maternal Folic Acid Supplementation Mediates Offspring Health via DNA Methylation. *Reprod Sci* 27: 963-976
Ly L, Chan D, Aarabi M, Landry M, Behan NA, MacFarlane AJ, Trasler J (2017) Intergenerational impact of paternal lifetime exposures to both folic acid deficiency and supplementation on reproductive outcomes and imprinted gene methylation. *Mol Hum Reprod* 23: 461-477
Maezawa S, Hasegawa K, Yukawa M, Kubo N, Sakashita A, Alavattam KG, Sin HS, Kartashov AV, Sasaki H, Barski A *et al* (2018a) Polycomb protein SCML2 facilitates H3K27me3 to establish bivalent domains in the male germline. *Proc Natl Acad Sci U S A* 115: 4957-4962
Maezawa S, Sakashita A, Yukawa M, Chen X, Takahashi K, Alavattam KG, Nakata I, Weirauch MT, Barski A, Namekawa SH (2020) Super-enhancer switching drives a burst in gene expression at the mitosis-to-meiosis transition. *Nat Struct Mol Biol* 27: 978-988
Maezawa S, Yukawa M, Alavattam KG, Barski A, Namekawa SH (2018b) Dynamic reorganization of open chromatin underlies diverse transcriptomes during spermatogenesis. *Nucleic Acids Res* 46: 593-608
Maezawa S, Yukawa M, Hasegawa K, Sugiyama R, Iizuka M, Hu M, Sakashita A, Vidal M, Koseki H, Barski A *et al* (2023) PRC1 suppresses a female gene regulatory network to ensure testicular differentiation. *Cell Death Dis* 14: 501
Maezawa S, Yukawa M, Sakashita A, Barski A, Namekawa SH (2025) Site-specific DNA demethylation during spermatogenesis presets the sites of nucleosome retention in mouse sperm. *bioRxiv*
Mlodzik-Czyzewska MA, Malinowska AM, Chmurzynska A (2020) Low folate intake and serum levels are associated with higher body mass index and abdominal fat accumulation: a case control study. *Nutr J* 19: 53
Pereira GA, Bressan J, Oliveira FLP, Sant'Ana HMP, Pimenta AM, Lopes LL, Hermsdorff HHM (2019) Dietary Folate Intake Is Negatively Associated with Excess Body Weight in Brazilian Graduates and Postgraduates (CUME Project). *Nutrients* 11
Petrova B, Maynard AG, Wang P, Kanarek N (2023) Regulatory mechanisms of one-carbon metabolism enzymes. *J Biol Chem* 299: 105457
Rabbani M, Zheng X, Manske GL, Vargo A, Shami AN, Li JZ, Hammoud SS (2022) Decoding the spermatogenesis program: New insights from transcriptomic analyses. *Annu Rev Genet* 56: 339-368

Rando OJ, Simmons RA (2015) I'm eating for two: parental dietary effects on offspring metabolism. *Cell* 161: 93-105
Reske JJ, Wilson MR, Chandler RL (2020) ATAC-seq normalization method can significantly affect differential accessibility analysis and interpretation. *Epigenetics Chromatin* 13: 22
Rotimi DE, Iyobhebhe M, Oluwayemi ET, Olajide OP, Akinsanola BA, Evbuomwan IO, Asaleye RM, Ojo OA (2024) Energy metabolism and spermatogenesis. *Heliyon* 10: e38591
Rotimi DE, Singh SK (2024) Implications of lifestyle factors on male reproductive health. *JBRA Assist Reprod* 28: 320-330
Sakashita A, Ooga M, Otsuka K, Maezawa S, Takeuchi C, Wakayama S, Wakayama T, Namekawa SH (2023) Polycomb protein SCML2 mediates paternal epigenetic inheritance through sperm chromatin. *Nucleic Acids Res* 51: 6668-6683
Seisenberger S, Andrews S, Krueger F, Arand J, Walter J, Santos F, Popp C, Thienpont B, Dean W, Reik W (2012) The dynamics of genome-wide DNA methylation reprogramming in mouse primordial germ cells. *Mol Cell* 48: 849-862
Siklenka K, Erkek S, Godmann M, Lambrot R, McGraw S, Lafleur C, Cohen T, Xia J, Suderman M, Hallett M *et al* (2015) Disruption of histone methylation in developing sperm impairs offspring health transgenerationally. *Science* 350: aab2006
Sin HS, Kartashov AV, Hasegawa K, Barski A, Namekawa SH (2015) Poised chromatin and bivalent domains facilitate the mitosis-to-meiosis transition in the male germline. *BMC Biol* 13: 53
Smallwood SA, Tomizawa S, Krueger F, Ruf N, Carli N, Segonds-Pichon A, Sato S, Hata K, Andrews SR, Kelsey G (2011) Dynamic CpG island methylation landscape in oocytes and preimplantation embryos. *Nat Genet* 43: 811-814
Soumillon M, Necsulea A, Weier M, Brawand D, Zhang X, Gu H, Barthès P, Kokkinaki M, Nef S, Gnirke A *et al* (2013) Cellular source and mechanisms of high transcriptome complexity in the mammalian testis. *Cell Rep* 3: 2179-2190
Van den Veyver IB (2002) Genetic effects of methylation diets. *Annu Rev Nutr* 22: 255-282
van Uitert EM, Steegers-Theunissen RPM (2013) Influence of maternal folate status on human fetal growth parameters. *Mol Nutr Food Res* 57: 582-595
Watkins AJ, Dias I, Tsuro H, Allen D, Emes RD, Moreton J, Wilson R, Ingram RJM, Sinclair KD (2018) Paternal diet programs offspring health through sperm- and seminal plasma-specific pathways in mice. *Proc Natl Acad Sci U S A* 115: 10064-10069
Yang L, Wang W, Mao B, Qiu J, Guo H, Yi B, He X, Lin X, Lv L, Xu X *et al* (2022) Maternal folic acid supplementation, dietary folate intake, and low birth weight: A birth cohort study. *Front Public Health* 10: 844150
Yeh YH, Hu M, Nakagawa T, Sakashita A, Yoshida S, Maezawa S, Namekawa SH (2021) Isolation of Murine Spermatogenic Cells using a Violet-Excited Cell-Permeable DNA Binding Dye. *J Vis Exp*
Yeh YH, Hu M, Otsuka K, Alger BM, Nene SS, Wang H, Maezawa S, Namekawa SH (2026) DAXX Directs Dual Modes of H3.4-to-H3.3 Histone Replacement in the Male Germline. *Genes Dev* in press

[DATASET] Hasegawa K, Sin HS, Maezawa S, Kartashov AV, Alavattam KG, Bacon WC, Barski A, Namekawa SH (2015) SCML2 Establishes the Male Germline Epigenome. Gene Expression Omnibus, GSE55060.
https://www.ncbi.nlm.nih.gov/geo/query/acc.cgi?acc=GSE55060

[DATASET] Maezawa S, Hasegawa K, Kartashov A, Barski A, Namekawa S (2018) SCML2 establishes germline-specific bivalent domains. Gene Expression Omnibus, GSE89502.
https://www.ncbi.nlm.nih.gov/geo/query/acc.cgi?acc=GSE89502

[DATASET] Maezawa S, Otsuka K, Namekawa S (2025) DNA demethylation in spermatogenesis presets the sites of nucleosome retention in mouse sperm. Gene Expression Omnibus, GSE262669.
https://www.ncbi.nlm.nih.gov/geo/query/acc.cgi?acc=GSE262669

[DATASET] Lismer A, Kimmins S (2021) Histone H3 lysine 4 trimethylation in sperm is transmitted to the embryo and associated with diet-induced phenotypes in the offspring. Gene Expression Omnibus, GSE135678.
https://www.ncbi.nlm.nih.gov/geo/query/acc.cgi?acc=GSE135678

Figure legends

Figure 1. Folate deficiency affects spermatogenesis and alters the transcriptome in pachytene spermatocytes.

(A) Schematic of the folate-deficient (FD) dietary model. Breeder mice were maintained on a folate-sufficient (FS) diet.

(B) Dietary exposure timeline. Littermate males were maintained on an FS diet until weaning (3 weeks of age) and then randomly assigned to FS or FD diets until 14 weeks of age.

(C) Overview of spermatogenesis. Undifferentiated spermatogonia (Undiff) maintain the stem cell population and, upon differentiation cues, give rise to differentiating spermatogonia (Diff). Following meiotic entry, completion of autosomal synapsis marks pachytene spermatocytes (PSs), and subsequent reductional divisions generate haploid round spermatids (RSs), which ultimately differentiate into spermatozoa.

(D) Experimental design. Testes from adult FS or FD mice were collected for histological analysis or dissociated for fluorescence-activated cell sorting (FACS) of germ cell populations, followed by bulk RNA-seq, ATAC-seq, CUT&Tag, or single-cell RNA-seq.

(E) Representative testicular sections from FS (top) and FD (bottom) mice stained with DAPI (left) or immunostained for γH2AX (a marker of PS XY bodies) and H1T (a marker from mid-pachytene onward) (right). Scale bars, 50 μm.

(F) Box-and-whisker plots showing PS density per seminiferous tubule, quantified by γH2AX-positive XY bodies, in FS and FD testes (four biological replicates per condition). Points represent individual seminiferous tubules. Box plots show median and interquartile range; whiskers extend to 1.5× IQR. Statistical significance was determined using a two-sided Wilcoxon rank-sum (Mann–Whitney U) test.

(G) Box-and-whisker plots showing H1T-positive germ cell density per seminiferous tubule in FS and FD testes (three biological replicates per condition). Points represent individual seminiferous tubules. Box plots show median and interquartile range; whiskers extend to 1.5× IQR. Statistical significance was determined using a two-sided Wilcoxon rank-sum (Mann–Whitney U) test.

(H) Transcriptome comparison of FS and FD PSs (three biological replicates per condition). Differentially expressed genes (DEGs; $|\log2FoldChange| > 1.5$, $P < 0.05$) are highlighted (red, upregulated in FD; blue, downregulated in FD), with DEG counts indicated.

(I) Chromosomal distribution and proportion of CpG island (CGI) genes among PS DEGs.

(J) Heat maps showing Z-score–normalized expression of DEGs upregulated (left) or downregulated (right) in FD PSs.

$THY1^+$, undifferentiated spermatogonia; KIT^+, differentiating spermatogonia; PS, pachytene spermatocytes; RS, round spermatids.

Figure 2. Folate deficiency reshapes chromatin accessibility and histone modification landscapes in pachytene spermatocytes.

(A) Comparison of chromatin accessibility in FS and FD PSs (five biological replicates per condition). Differentially accessible regions (DARs; $|\log2 \text{ fold change}| \geq 2$, $P < 0.05$) are highlighted (red, gained in FD; blue, lost in FD), with counts indicated.

(B) Genomic annotation and chromosomal distribution of PS DARs.

(C) Comparison of H3K4me3 enrichment in FS and FD PSs (three biological replicates per condition). Differentially enriched regions (DERs; |log2FoldChange| > 1, adjusted $P < 0.05$) are highlighted (red, gained; blue, lost).
(D) Genomic annotation and chromosomal distribution of PS H3K4me3 DERs.
(E) Comparison of H3K27ac enrichment in FS and FD PSs (three biological replicates per condition). DERs (|log2FoldChange| > 1, adjusted $P < 0.05$) are highlighted.
(F) Genomic annotation and chromosomal distribution of PS H3K27ac DERs.
(G) Comparison of H3K27me3 enrichment in FS and FD PSs (three biological replicates per condition). DERs (|log2FoldChange| > 1, adjusted $P < 0.05$) are highlighted.
(H) Genomic annotation and chromosomal distribution of PS H3K27me3 DERs.

Figure 3. Folate deficiency shifts active and bivalent chromatin states at CpG island promoters in pachytene spermatocytes.

(A) CUT&Tag enrichment of H3K4me3, H3K27ac, and H3K27me3 at CGI genes and non-CGI-associated genes in FS and FD PSs. MethylCap-seq enrichment at CGI genes in wild-type PSs was reanalyzed from ref. (Maezawa *et al.*, 2025) and is shown for reference.
(B) Proportion of PS DARs and DERs (genic regions only) overlapping CGI genes. Counts are indicated.
(C) Proportion of CGI promoters (±100 bp from transcription start sites) classified as H3K4me3-only, H3K27me3-only, double-positive, or no modification. Promoter counts are indicated.

Figure 4. Folate deficiency alters transcriptomic and chromatin landscapes in round spermatids.

(A) Transcriptome comparison of FS and FD RSs (three biological replicates per condition). DEGs (|log2FoldChange| > 1.5, $P < 0.05$) are highlighted.
(B) Chromosomal distribution and proportion of CGI genes among RS DEGs.
(C) Comparison of chromatin accessibility in FS and FD RSs (five biological replicates per condition). DARs (|log2FoldChange| ≥ 2, $P < 0.05$) are highlighted.
(D) Genomic annotation and chromosomal distribution of RS DARs.
(E) Proportion of RS DARs and DERs (genic regions only) overlapping CGI genes.
(F) CUT&Tag enrichment of H3K4me3, H3K27ac, and H3K27me3 at CGI genes and non-CGI genes in FS and FD RSs.
(G) Comparison of H3K4me3 enrichment in FS and FD RSs (three biological replicates per condition). DERs (fold change ≥ 1, adjusted $P < 0.05$) are highlighted.
(H) Genomic annotation and chromosomal distribution of RS H3K4me3 DERs.
(I) Comparison of H3K27ac enrichment in FS and FD RSs (three biological replicates per condition). DERs (|log2FoldChange| > 1, adjusted $P < 0.05$) are highlighted.
(J) Genomic annotation and chromosomal distribution of RS H3K27ac DERs.
(K) Comparison of H3K27me3 enrichment in FS and FD RSs. No significant DERs were detected.

Figure 5. Single-cell transcriptomic profiling reveals altered germ cell composition and cluster-specific transcriptomic changes under folate deficiency.

(A–C) UMAP projections of germ cell scRNA-seq datasets from FS testes (A), FD testes (B), and integrated FS and FD datasets (C) (two biological replicates per condition).

(D) UMAP showing cluster identity of integrated germ cell datasets.

(E) Summary schematic of FD-associated phenotypes across spermatogenic subtypes. Subtype clusters are ordered by inferred developmental progression. Red arrows mark developmental stages where germ cell proportions are substantially reduced in FD mice.

(F) Proportion of FS and FD germ cells within each cluster ordered by inferred developmental progression.

(G) Number of DEGs per cluster ($|\log2FoldChange| \geq 1$, adjusted $P < 0.05$) (purple, upregulated in FD; teal, downregulated in FD),

(H) UMAP of reclustered spermatocyte populations showing ten subclusters spanning leptotene through the meiotic division transition. Cluster 9 represents leptotene/early zygotene cells (*Dmc1*, *Meiob*, *Spata22*, *Rad51*, and *Sycp3*); Cluster 6, zygotene/early pachytene cells (*Sycp1*, *Tex12*, *Piwil1*, *Tdrd1*, and *Adad2*); Cluster 5, early pachytene cells (*Piwil1*, *Tdrd1*, *Hspa2*, *Tcfl5*, and *H1f6*); Cluster 8, mid-pachytene cells (*Hspa2*, *Zfp541*, *Kctd19*, *Ccna1*, and *H1f6*); and Cluster 7, mid/late pachytene cells (*Nxf2*, *Scml2*, *Foxj1*, *Tsga8*, and *Cfap47*). Clusters 1 and 0 represent late pachytene cells, followed by Cluster 4 at the late pachytene/early diplotene transition, Cluster 2 at diplotene, and Cluster 3 at the late diplotene/meiotic division transition. Black and red lines indicate the interpreted main and alternative developmental trajectories, respectively.

(I) UMAP of the reclustered spermatocyte populations colored by folate group (FS or FD).

(J) Relative proportions of FS and FD cells within spermatocyte clusters along the main (top) and alternative (bottom) developmental trajectories. Percentages indicate the relative contribution of FS and FD cells to each cluster.

Figure 6. Chromatin regions altered in sperm originate from epigenomic perturbations during meiotic prophase I and are associated with CpG island-rich genomic regions

(A) CUT&Tag enrichment in FS and FD PSs at regions exhibiting increased H3K4me3 in sperm.

(B) CUT&Tag enrichment in FS and FD PSs at regions exhibiting decreased H3K4me3 in sperm.

(C) CUT&Tag enrichment in FS and FD RSs at regions exhibiting increased H3K4me3 in sperm.

(D) CUT&Tag enrichment in FS and FD RSs at regions exhibiting decreased H3K4me3 in sperm.

(E) Proportion of sperm H3K4me3 gain and loss regions overlapping CGI genes.

(F) Genome-wide distribution of multi-mark loss hotspots in FD PSs across 5-Mb genomic bins. Poisson Z-scores for regions exhibiting decreased H3K27ac, decreased H3K4me3, and decreased RNA expression were combined using a Stouffer-style Z-score. Bins with a combined Z-score ≥2 are shown.

(G) CpG island density across the same 5-Mb genomic bins, quantified as CpG island base-pair coverage per Mb.

(H) Correlation between CpG island density and the combined multi-mark loss Z-score across genomic bins. Spearman $\rho = 0.815$, $P = 1.18 \times 10^{-133}$.

(I) Proposed model of stage-specific chromatin remodeling in response to folate deficiency.

Fig. EV1. Folate deficiency reduces testicular SAM abundance and XY-body γH2AX without altering early germ cell populations or seminiferous tubule stage distribution.

(A) Representative testis sections from FS and FD mice immunostained for γH2AX and S-adenosylmethionine (SAM). Merged images and individual γH2AX and SAM channels are shown. Dashed outlines indicate representative seminiferous tubules used for fluorescence quantification. Box-and-whisker plots show SAM fluorescence intensity normalized to DAPI. Each point represents an individual seminiferous tubule from three biological replicates per condition (FS, n = 324; FD, n = 285). Scale bar, 25 μm.

(B–D) Box-and-whisker plots comparing testis-to-body weight ratio (B), body weight (C), and testis weight (D) between FS and FD mice (30 biological replicates per condition).

(E) Weekly food consumption per mouse in FS and FD groups throughout the dietary exposure period. Points represent individual mice from paired littermates, and lines indicate group means for each week. No significant differences were detected between diets at any time point after Benjamini–Hochberg correction for multiple testing.

(F) Representative testis sections immunostained for ZBTB16 (PLZF), marking undifferentiated spermatogonia, with quantification of $PLZF^+$ cell density. FS, four biological replicates, n = 87 tubules; FD, seven biological replicates, n = 152 tubules. Scale bar, 50 μm.

(G) Representative testis sections immunostained for KIT, marking differentiating spermatogonia, with quantification of KIT^+ cell density. Three biological replicates per condition (FS, n = 42 tubules; FD, n = 58 tubules). Scale bar, 50 μm.

(H) γH2AX immunostaining and quantification of γH2AX fluorescence intensity within XY bodies normalized to DAPI. FS, three biological replicates, n = 300 XY bodies; FD, five biological replicates, n = 500 XY bodies. Scale bar, 5 μm.

(I) Representative chromosome spreads from FS and FD spermatocytes at early, mid, and late pachytene and diplotene stages. SYCP3 is shown in green, γH2AX in red, and DAPI in blue. XY bodies are indicated by dashed boxes. Box-and-whisker plots show γH2AX fluorescence intensity within the XY body normalized to DAPI at each meiotic stage. Three biological replicates per condition; early pachytene, FS n = 36 and FD n = 59; mid pachytene, FS n = 64 and FD n = 110; late pachytene, FS n = 49 and FD n = 57; diplotene, FS n = 80 and FD n = 57. Scale bar, 5 μm.

(J) Representative testis sections immunostained for SOX9, marking Sertoli cells, with quantification of $SOX9^+$ cell density. FS, three biological replicates, n = 71 tubules; FD, five biological replicates, n = 126 tubules. Scale bar, 50 μm.

(K) Seminiferous tubule staging analysis in FS and FD testes. Schematics illustrate representative germ cell composition and the γH2AX- and H1T-based criteria used to classify tubules as stages I–V or IX–XI. Stacked bar plots show the relative proportions of tubules assigned to each stage group. FS, three biological replicates, n = 128 tubules; FD, five biological replicates, n = 331 tubules.

Box-and-whisker plots show the median and interquartile range; whiskers extend to 1.5× the interquartile range. P values for pairwise comparisons were determined using two-tailed unpaired t-tests. For panel E, P values were adjusted for multiple testing using the Benjamini–Hochberg method.

Fig. EV2. Reproducibility of transcriptomic and epigenomic datasets.

(A) Immunostaining of FACS-isolated PSs stained with DAPI (left) and RSs (right) stained with DAPI and H1T. Insets show higher magnification of PSs and RSs.
(B) Pearson correlation of RNA-seq datasets from FS and FD PSs (left) and RSs (right) (three biological replicates per condition).
(C) Pearson correlation of ATAC-seq datasets from FS and FD PSs (left) and RSs (right) (five biological replicates per condition).
(D) Pearson correlation of CUT&Tag datasets for H3K4me3, H3K27me3, and H3K27ac from FS and FD PSs (top) and RSs (bottom) (three biological replicates per condition).

Fig. EV3. Transcriptomic and epigenomic features of folate deficiency-responsive genes.
(A, B) Gene ontology (GO) analysis of genes upregulated (A; n = 625) and downregulated (B; n = 545) in FD pachytene spermatocytes (PSs). Selected enriched biological processes are shown. Bar length indicates −log10(FDR), and the number of genes associated with each pathway is indicated.
(C) MA plot showing differential gene expression between FD and FS PSs using a more stringent adjusted *P* value (*P-adj*) < 0.05 threshold. Seventy-five genes were upregulated and 40 were downregulated in FD PSs. Representative spermatid-associated and chromatin-regulatory genes are indicated.
(D) Developmental expression patterns of the 75 upregulated and 40 downregulated DEGs meeting the *P-adj* < 0.05 criterion across wild-type spermatogenesis. RNA-seq expression is shown for $THY1^+$ undifferentiated spermatogonia, KIT^+ differentiating spermatogonia, PSs, and round spermatids (RSs). Genes are annotated according to autosomal, X-chromosomal, or Y-chromosomal location.
(E) Genomic and promoter features of the 115 DEGs meeting the *P-adj* < 0.05 criterion. Left, proportions of upregulated and downregulated DEGs located on autosomes or sex chromosomes. Right, proportions of upregulated and downregulated DEGs associated with CpG island (CGI) or non-CGI promoters.
(F, G) Genome-browser tracks surrounding the *Ddx4* (F) and *Prdm2* (G) loci in FS and FD PSs and RSs. ATAC-seq, H3K4me3, H3K27ac, H3K27me3 CUT&Tag, and RNA-seq signals are shown. RefSeq gene annotations are displayed below each set of tracks.

Fig. EV4. Quality control, cluster validation, and functional annotation of spermatogenic cell populations.
(A) Summary of scRNA-seq quality control metrics.
(B) UMAP colored by number of detected genes per cell.
(C–F) UMAP feature plots of marker genes: *Kit*, *Pou5f2*, *Prm1*, and *Vim*.
(G) Heat map of the top five marker genes per cluster ordered by inferred developmental progression.
(H–K) Gene ontology analysis of DEGs in selected clusters.

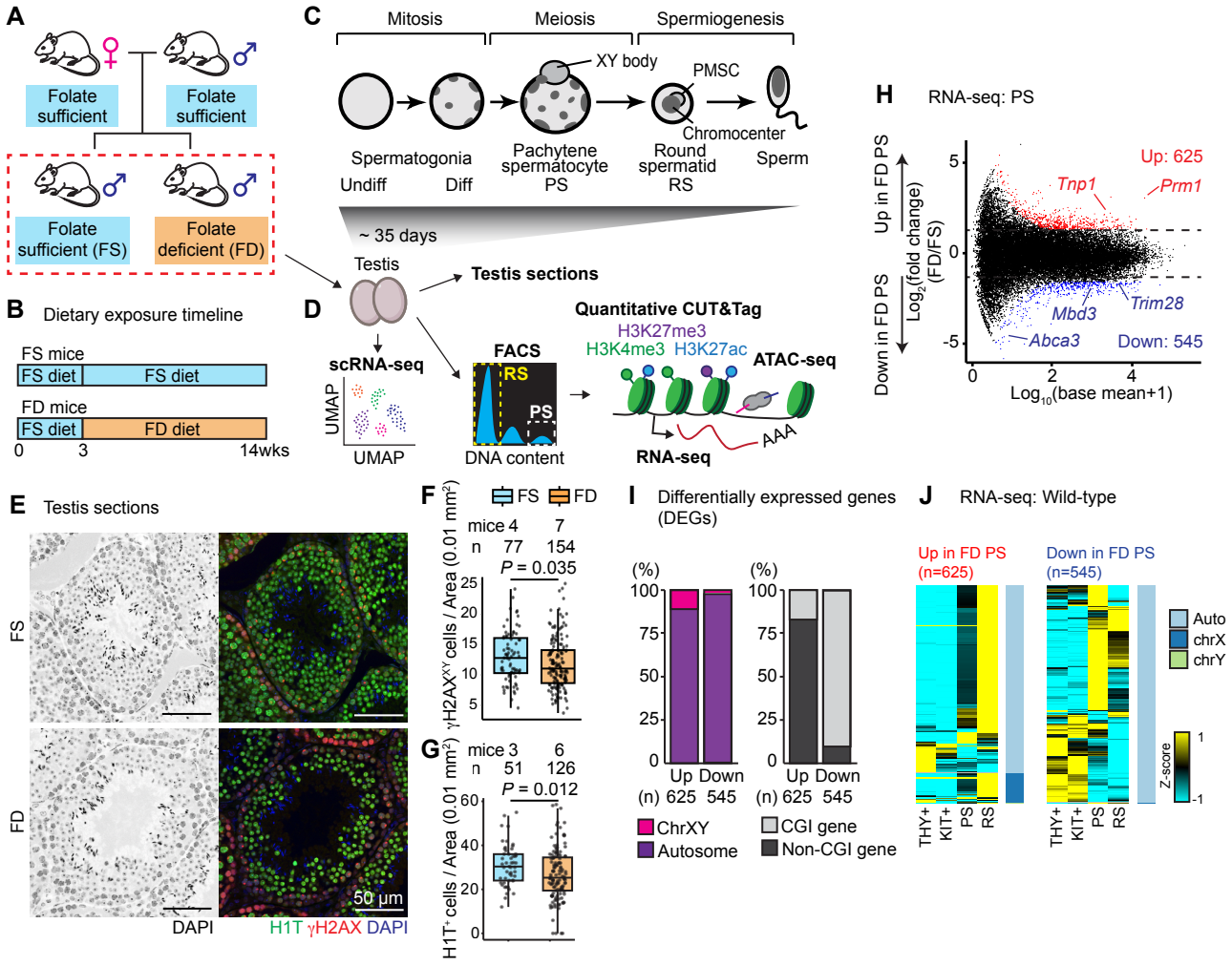
Fig. EV5. Stage-resolved single-cell analysis of spermatogenic responses to folate deficiency.
(A) UMAP feature plots showing expression of *Ddx4* in FS and FD datasets.

(B–F) Violin plots showing expression of *Ddx4* (B), *Adad1* (C), *Sycp1* (D), *Sycp2* (E), and *Tdrd1* (F) across spermatogenic cell clusters in FS and FD testes. Gray shading and asterisks indicate clusters in which the corresponding gene was identified as a differentially expressed gene (DEG) in the scRNA-seq analysis.
(G) Gene set enrichment analysis comparing spermatocyte Clusters 8 and 7. Pathways enriched in Cluster 8 relative to Cluster 7 are shown with normalized enrichment scores (NES).
(H) Stress-response module scores across reclustered spermatocyte populations.
(I) Proportion of upregulated and downregulated scRNA-seq DEGs associated with CpG island (CGI) promoters in each cluster. Percentages are indicated.

Appendix Figure Legends

Appendix Fig. S1. Integration of scRNA-seq differential expression with bulk transcriptomic and epigenomic profiles in pachytene spermatocytes.

Heatmaps show H3K4me3, H3K27ac, H3K27me3, ATAC-seq, and RNA-seq signals in folate-sufficient (FS) and folate-deficient (FD) pachytene spermatocytes across ±3 kb of transcription start sites (TSSs) for genes identified as differentially expressed in scRNA-seq clusters C0–C9. Genes are grouped according to their corresponding scRNA-seq cluster and direction of differential expression (Up or Down), with the number of genes in each group indicated on the left. Each row represents an individual gene. Signal intensity scales for each dataset are shown at the bottom.


A
Folate sufficient
Folate sufficient
Folate sufficient (FS)
Folate deficient (FD)
B
Dietary exposure timeline
FS mice
FS diet
FS diet
FD mice
FS diet
FD diet
0
3
14wks
C
Mitosis
Meiosis
Spermiogenesis
XY body
PMSC
Chromocenter
Spermatogonia
Undiff
Diff
Pachytene spermatocyte
PS
Round spermatid
RS
Sperm
~ 35 days
Testis
Testis sections
D
scRNA-seq
UMAP
UMAP
FACS
RS
PS
DNA content
Quantitative CUT&Tag
H3K27me3
H3K4me3 H3K27ac
ATAC-seq
AAA
RNA-seq
H
RNA-seq: PS
Up in FD PS
Down in FD PS
Log2(fold change) (FD/FS)
Up: 625
Down: 545
Tnp1
Prm1
Mbd3
Trim28
Abca3
Log10(base mean+1)
E
Testis sections
FS
FD
DAPI
H1T γH2AX DAPI
50 μm
F
FS
FD
mice 4 7
n 77 154
P = 0.035
γH2AXXY cells / Area (0.01 mm2)
G
mice 3 6
n 51 126
P = 0.012
H1T+ cells / Area (0.01 mm2)
I
Differentially expressed genes (DEGs)
(%)
Up Down
(n) 625 545
ChrXY
Autosome
CGI gene
Non-CGI gene
J
RNA-seq: Wild-type
Up in FD PS (n=625)
Down in FD PS (n=545)
THY+ KIT+
PS
RS
Auto
chrX
chrY
Z-score

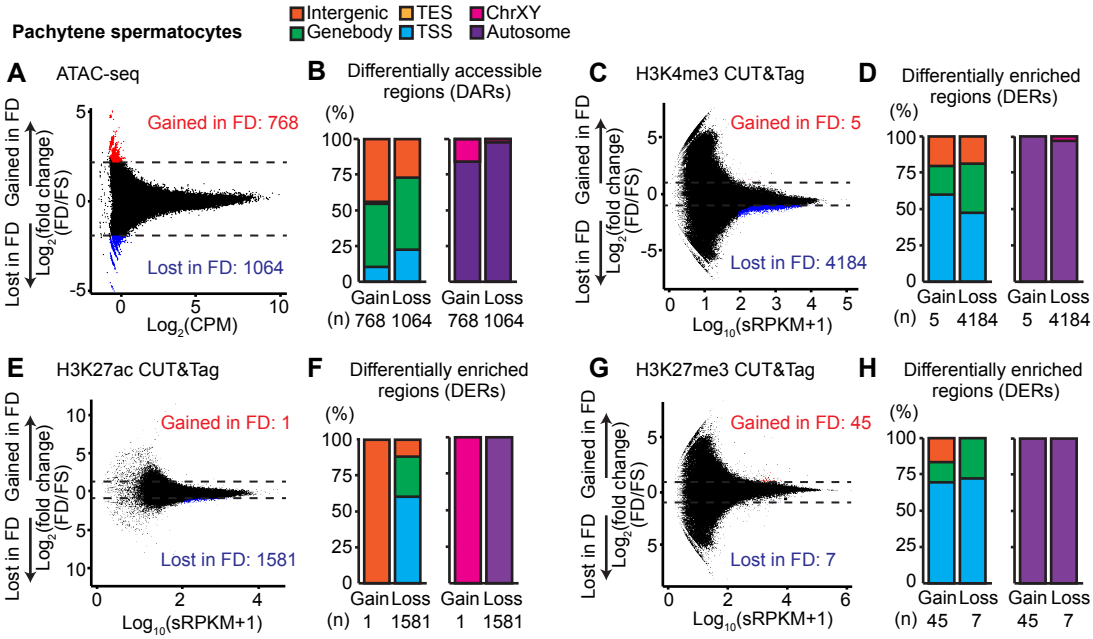
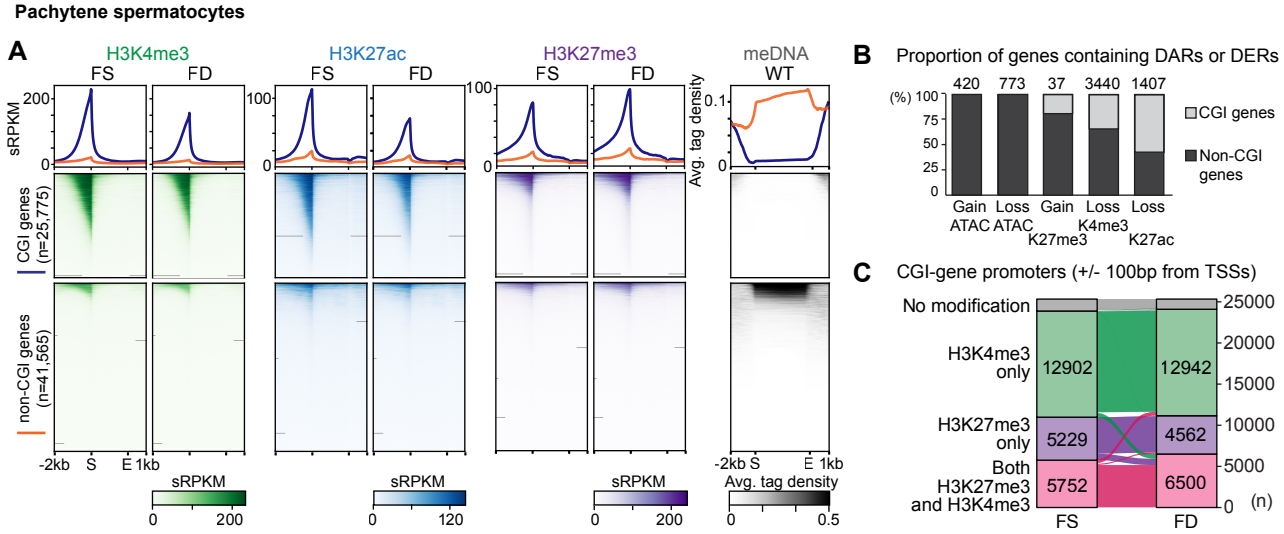

Pachytene spermatocytes
Intergenic
Genebody
TES
TSS
ChrXY
Autosome
A
ATAC-seq
Gained in FD: 768
Lost in FD: 1064
Log2(fold change) (FD/FS)
Log2(CPM)
B
Differentially accessible regions (DARs)
(%)
Gain Loss Gain Loss
(n) 768 1064 768 1064
C
H3K4me3 CUT&Tag
Gained in FD: 5
Lost in FD: 4184
Log10(sRPKM+1)
D
Differentially enriched regions (DERs)
(n) 5 4184 5 4184
E
H3K27ac CUT&Tag
Gained in FD: 1
Lost in FD: 1581
F
Differentially enriched regions (DERs)
(n) 1 1581 1 1581
G
H3K27me3 CUT&Tag
Gained in FD: 45
Lost in FD: 7
H
Differentially enriched regions (DERs)
(n) 45 7 45 7

Fig. 3 Esparza et al.



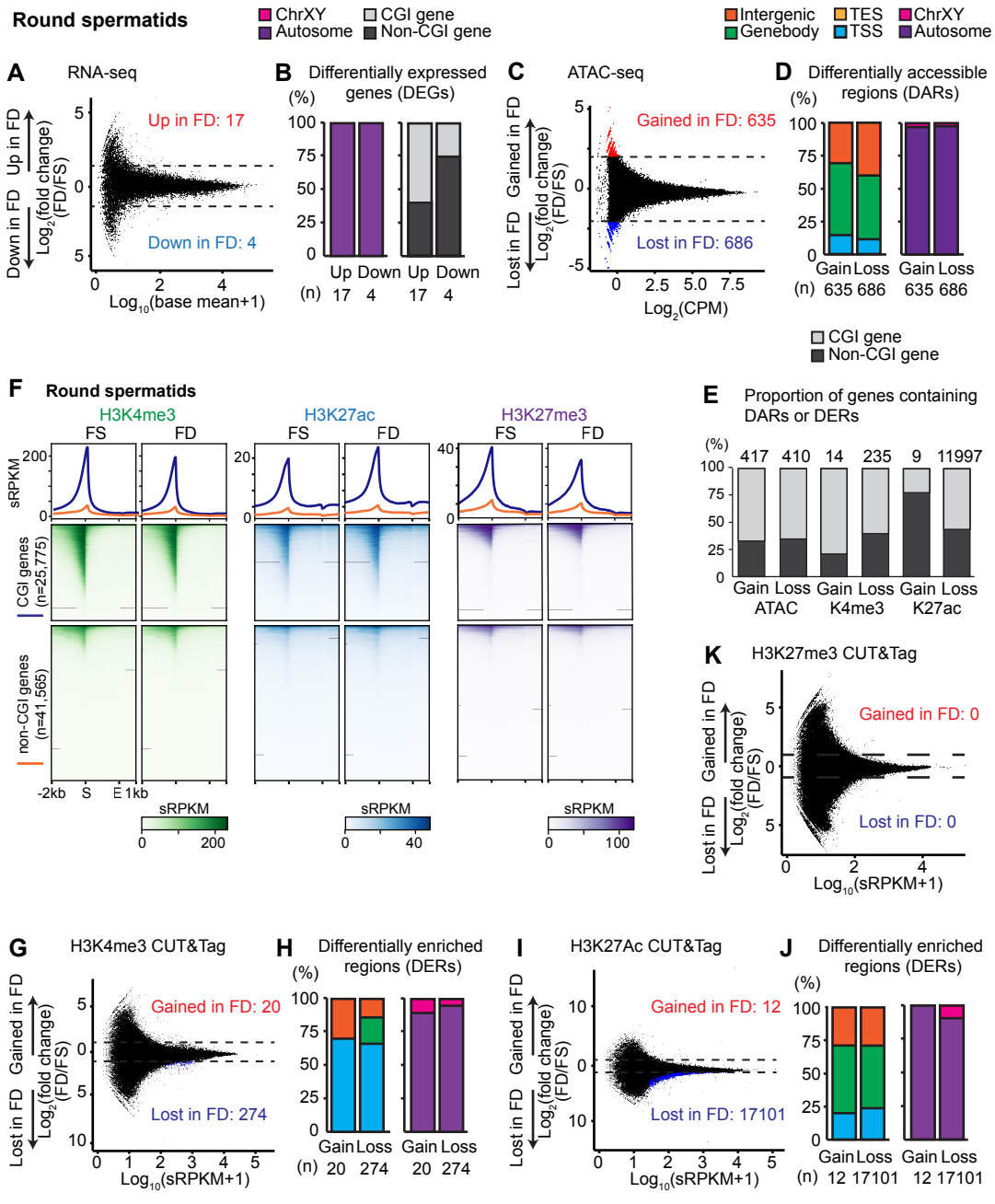
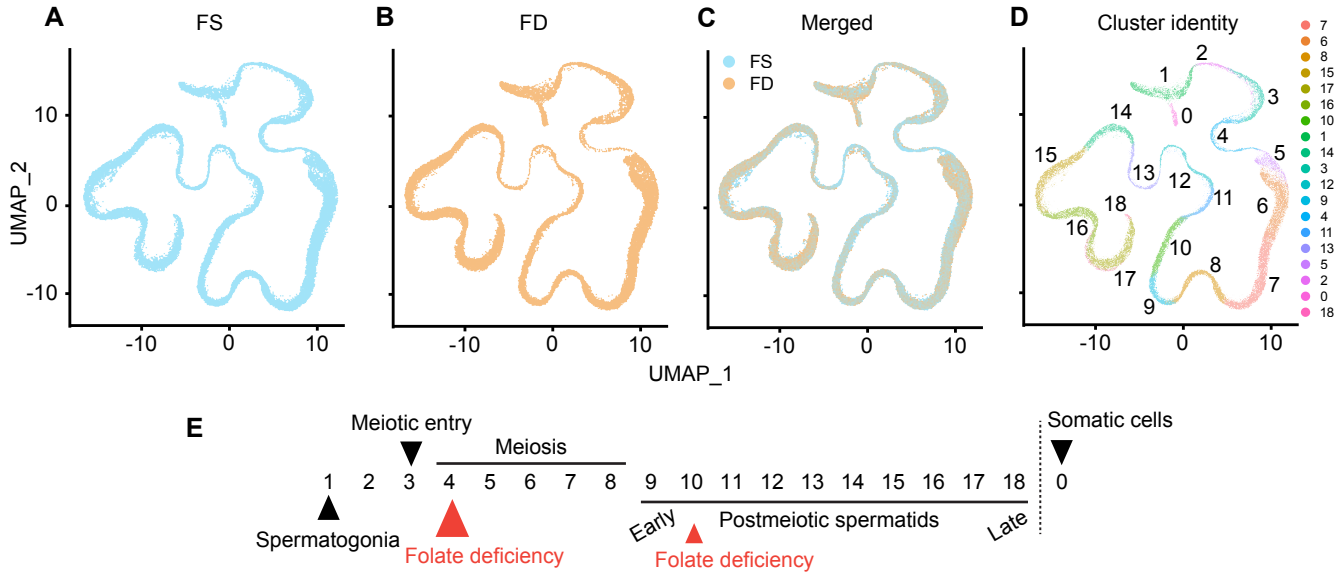
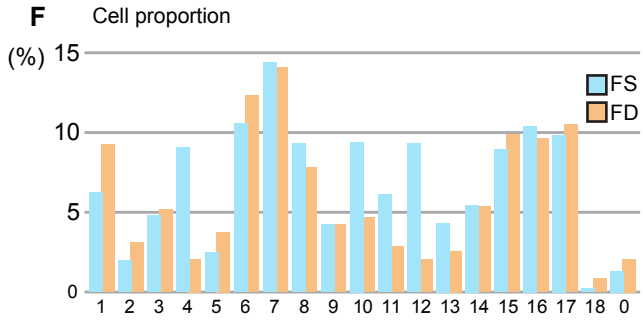
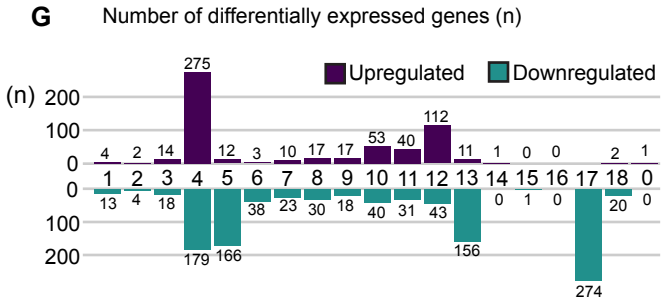
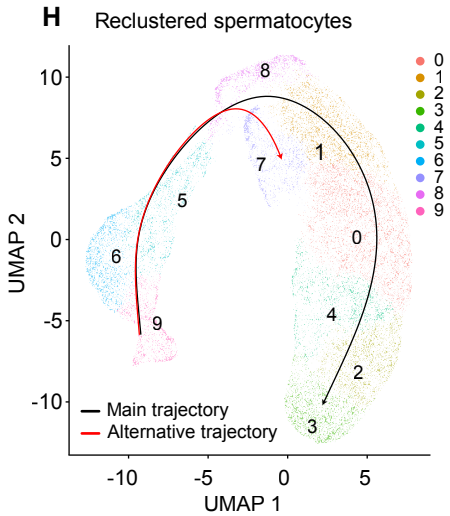

Round spermatids
ChrXY
Autosome
CGI gene
Non-CGI gene
Intergenic
Genebody
TES
TSS
ChrXY
Autosome
A
RNA-seq
Up in FD: 17
Down in FD: 4
Up in FD
Down in FD
Log2(fold change) (FD/FS)
Log10(base mean+1)
B
Differentially expressed genes (DEGs)
(%)
Up Down Up Down
(n) 17 4 17 4
C
ATAC-seq
Gained in FD: 635
Lost in FD: 686
Gained in FD
Lost in FD
Log2(CPM)
D
Differentially accessible regions (DARs)
Gain Loss Gain Loss
(n) 635 686 635 686
CGI gene
Non-CGI gene
F
Round spermatids
H3K4me3
H3K27ac
H3K27me3
FS
FD
sRPKM
CGI genes (n=25,775)
non-CGI genes (n=41,565)
-2kb S E 1kb
E
Proportion of genes containing DARs or DERs
417 410 14 235 9 11997
Gain Loss Gain Loss Gain Loss
ATAC K4me3 K27ac
K
H3K27me3 CUT&Tag
Gained in FD: 0
Lost in FD: 0
Log10(sRPKM+1)
G
H3K4me3 CUT&Tag
Gained in FD: 20
Lost in FD: 274
H
Differentially enriched regions (DERs)
(n) 20 274 20 274
I
H3K27Ac CUT&Tag
Gained in FD: 12
Lost in FD: 17101
J
Differentially enriched regions (DERs)
(n) 12 17101 12 17101

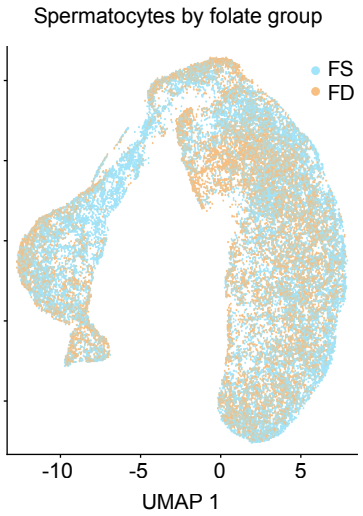
Fig. 5 Esparza et al.

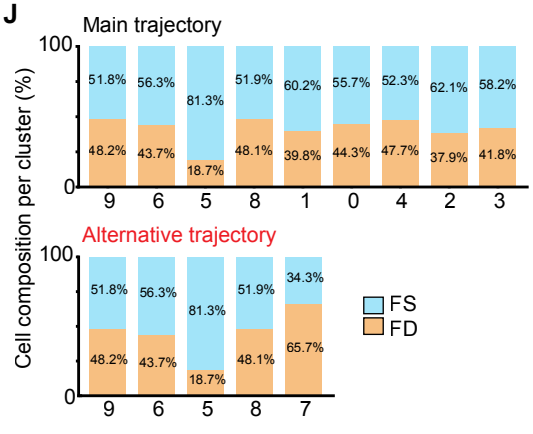


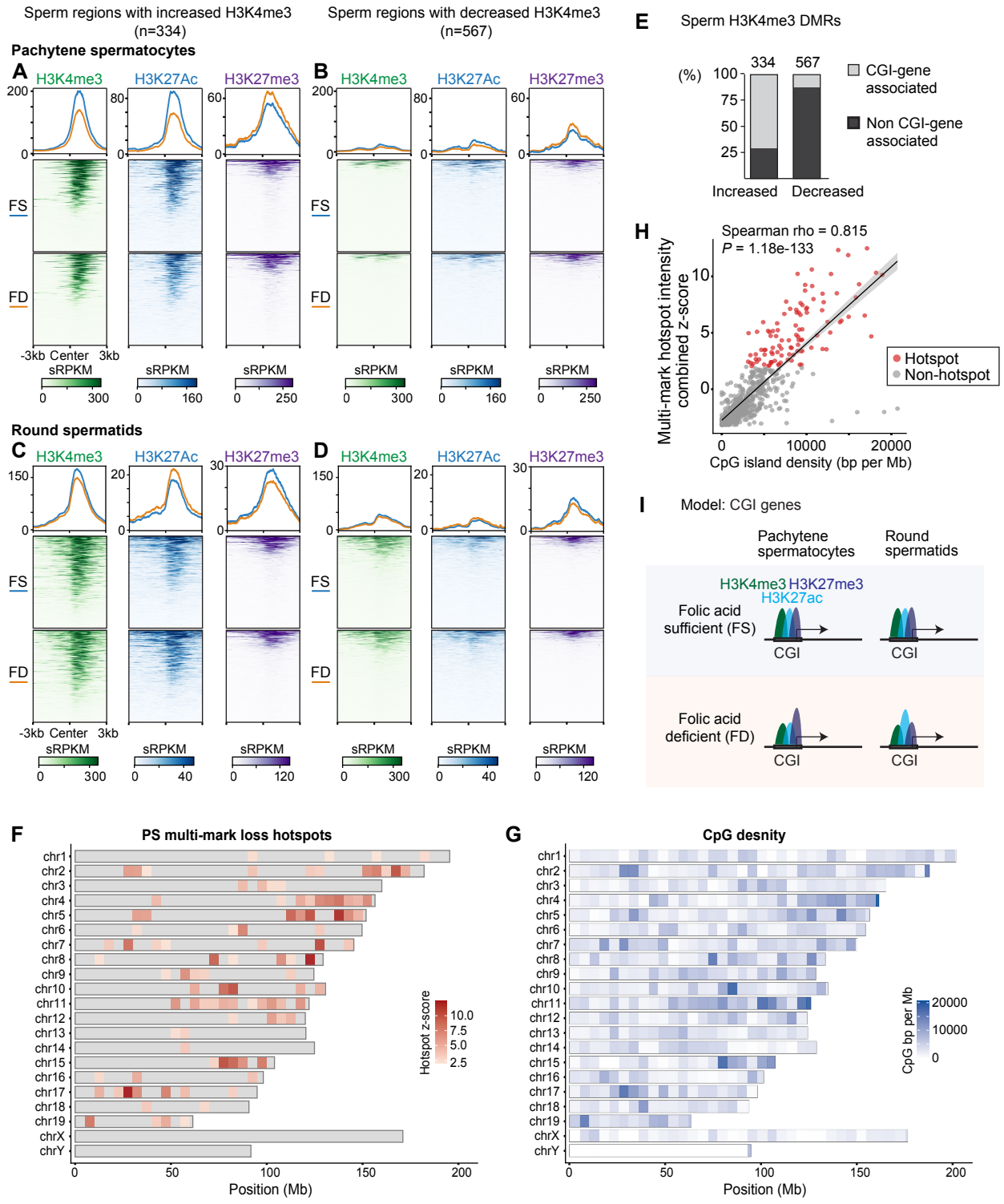


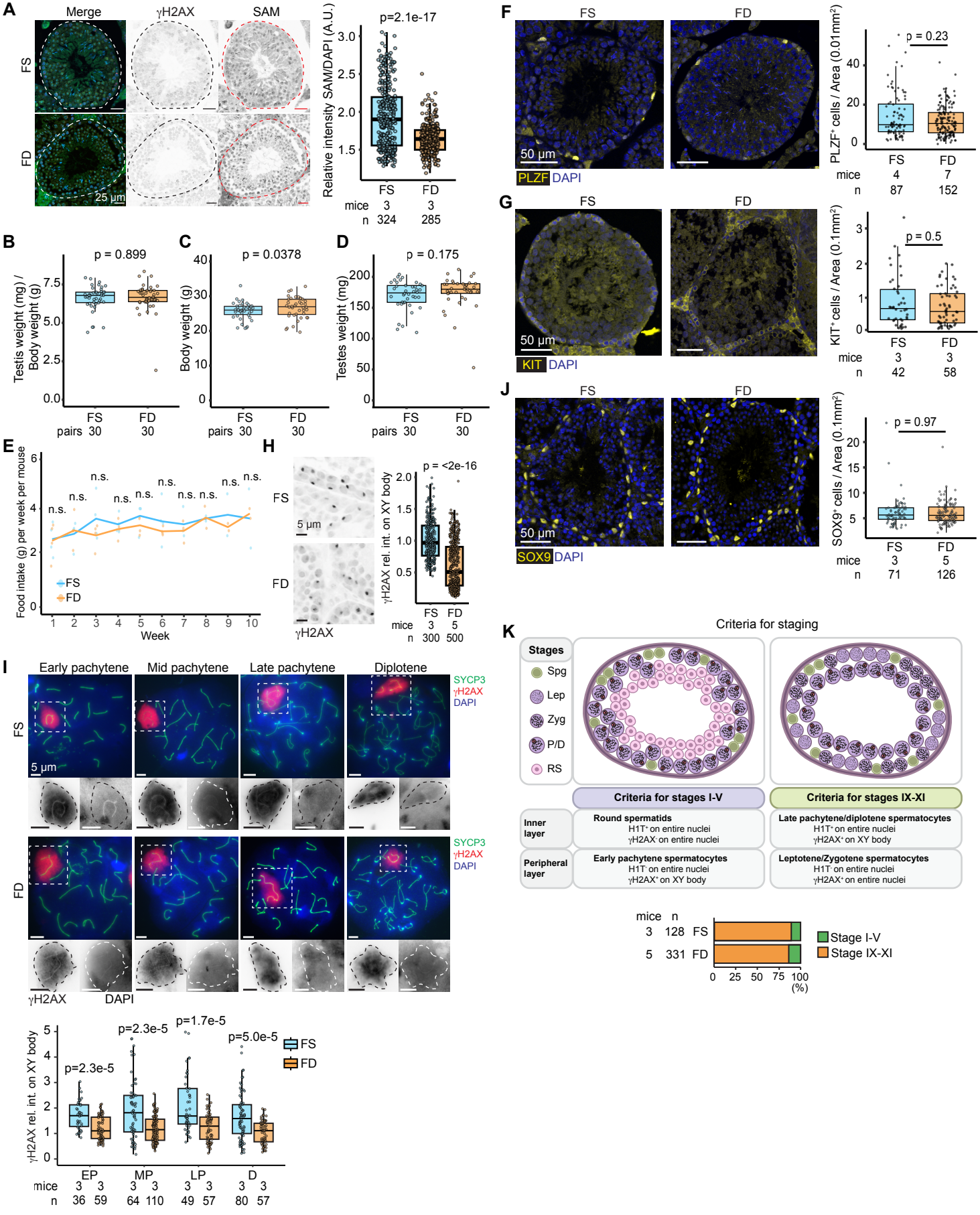


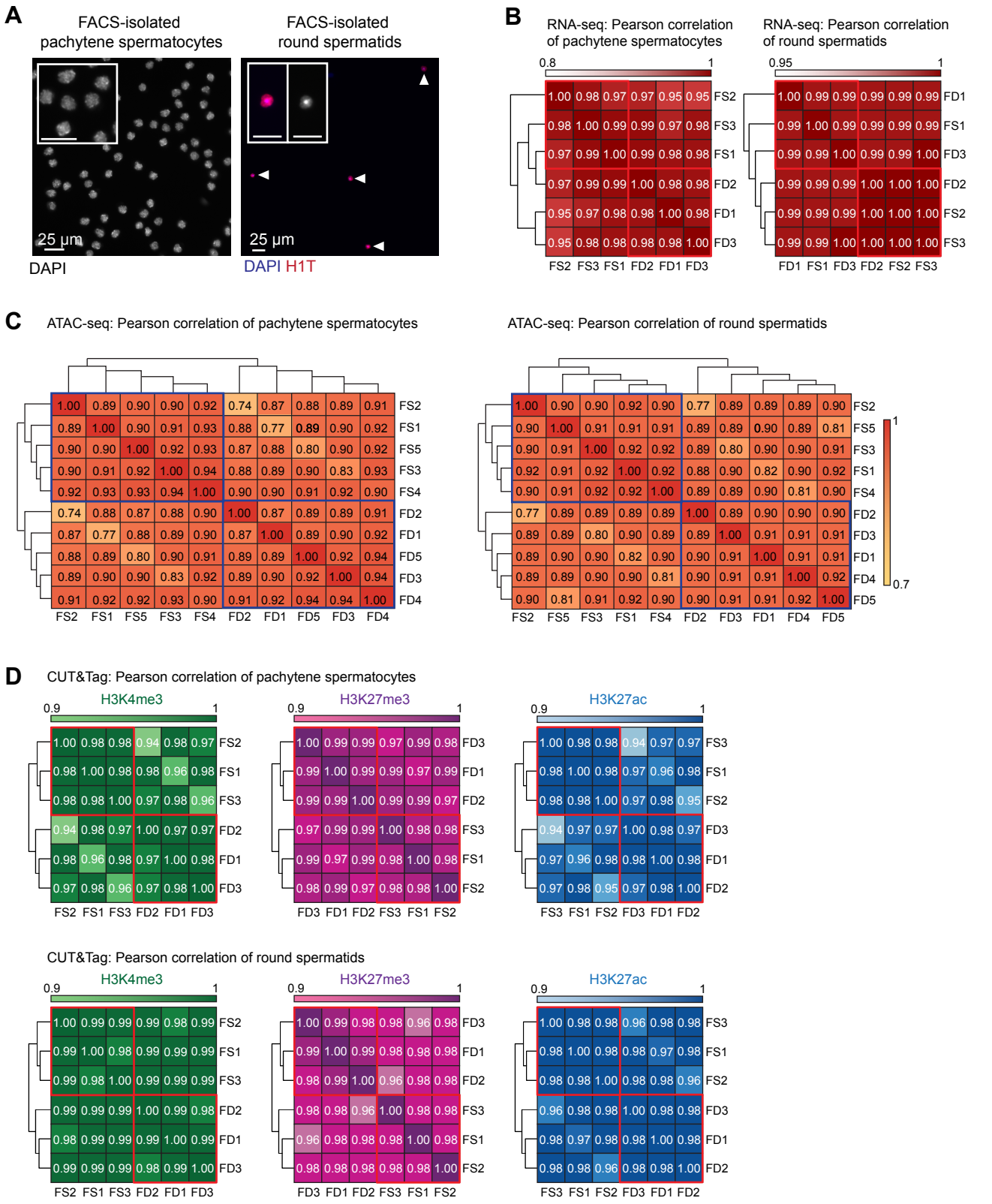


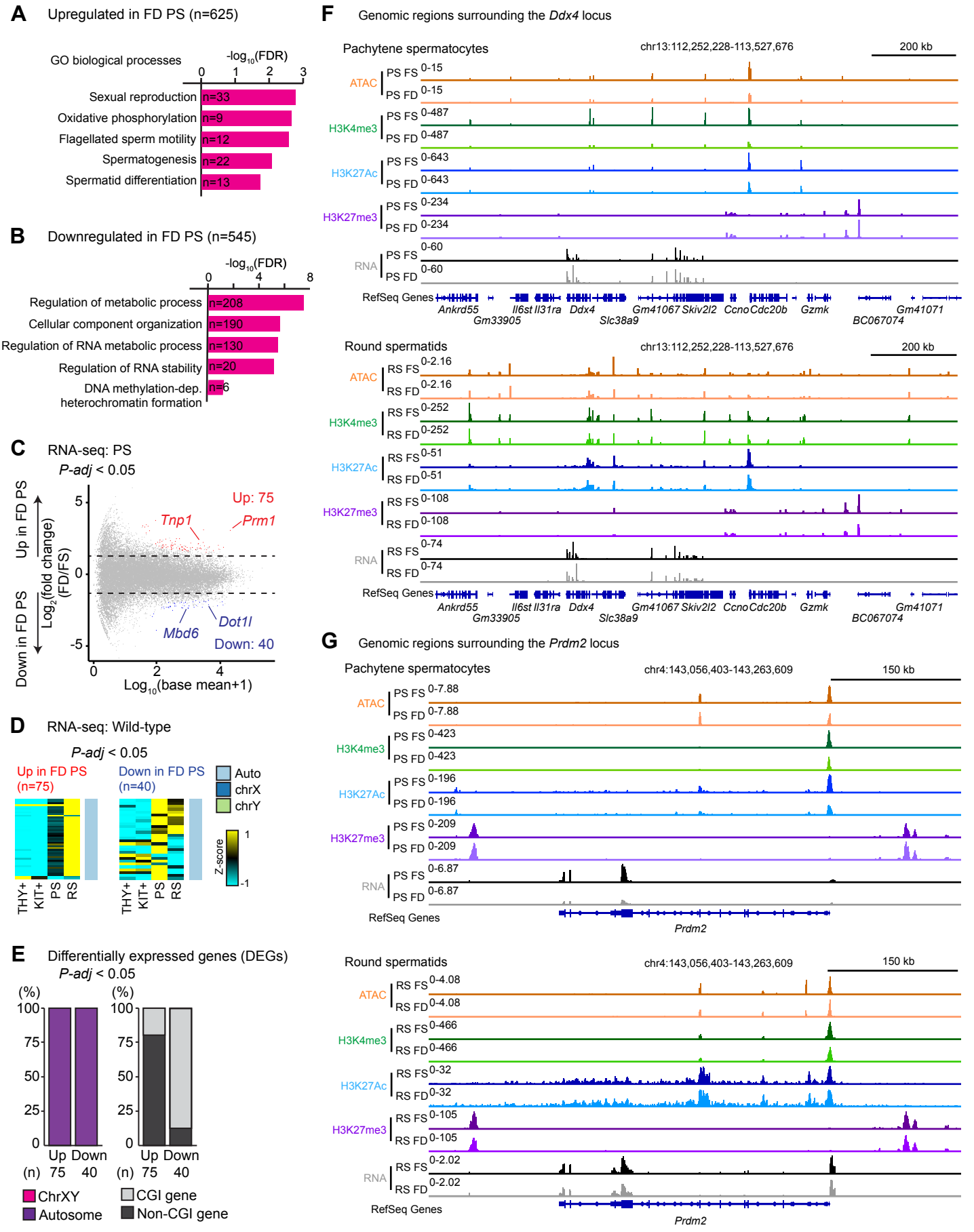





Sperm regions with increased H3K4me3 (n=334)
Sperm regions with decreased H3K4me3 (n=567)
Pachytene spermatocytes
A
B
H3K4me3
H3K27Ac
H3K27me3
FS
FD
-3kb Center 3kb
sRPKM
Round spermatids
C
D
E
Sperm H3K4me3 DMRs
(%)
334
567
CGI-gene associated
Non CGI-gene associated
Increased
Decreased
H
Spearman rho = 0.815
P = 1.18e-133
Multi-mark hotspot intensity combined z-score
CpG island density (bp per Mb)
Hotspot
Non-hotspot
I
Model: CGI genes
Pachytene spermatocytes
Round spermatids
H3K4me3 H3K27me3
H3K27ac
Folic acid sufficient (FS)
Folic acid deficient (FD)
CGI
F
PS multi-mark loss hotspots
Hotspot z-score
Position (Mb)
G
CpG desnity
CpG bp per Mb
Position (Mb)


A
Merge
γH2AX
SAM
FS
FD
25 μm
Relative intensity SAM/DAPI (A.U.)
p=2.1e-17
mice 3 3
n 324 285
B
p = 0.899
Testis weight (mg) / Body weight (g)
pairs 30 30
C
p = 0.0378
Body weight (g)
D
p = 0.175
Testes weight (mg)
E
Food intake (g) per week per mouse
n.s.
FS
FD
Week
H
γH2AX
5 μm
p = <2e-16
γH2AX rel. int. on XY body
mice 3 5
n 300 500
I
Early pachytene
Mid pachytene
Late pachytene
Diplotene
SYCP3
γH2AX
DAPI
5 μm
p=2.3e-5
p=2.3e-5
p=1.7e-5
p=5.0e-5
EP MP LP D
mice 3 3 3 3 3 3 3 3
n 36 59 64 110 49 57 80 57
F
PLZF DAPI
50 μm
p = 0.23
PLZF⁺ cells / Area (0.01mm²)
mice 4 7
n 87 152
G
KIT DAPI
p = 0.5
KIT⁺ cells / Area (0.1mm²)
mice 3 3
n 42 58
J
SOX9 DAPI
p = 0.97
SOX9⁺ cells / Area (0.1mm²)
mice 3 5
n 71 126
K
Criteria for staging
Stages
Spg
Lep
Zyg
P/D
RS
Criteria for stages I-V
Criteria for stages IX-XI
Inner layer
Round spermatids
H1T⁺ on entire nuclei
γH2AX⁻ on entire nuclei
Late pachytene/diplotene spermatocytes
H1T⁺ on entire nuclei
γH2AX⁺ on XY body
Peripheral layer
Early pachytene spermatocytes
H1T⁻ on entire nuclei
γH2AX⁺ on XY body
Leptotene/Zygotene spermatocytes
H1T⁻ on entire nuclei
γH2AX⁺ on entire nuclei
mice n
3 128 FS
5 331 FD
Stage I-V
Stage IX-XI
(%)


A
FACS-isolated pachytene spermatocytes
FACS-isolated round spermatids
25 µm
25 µm
DAPI
DAPI H1T
B
RNA-seq: Pearson correlation of pachytene spermatocytes
RNA-seq: Pearson correlation of round spermatids
C
ATAC-seq: Pearson correlation of pachytene spermatocytes
ATAC-seq: Pearson correlation of round spermatids
D
CUT&Tag: Pearson correlation of pachytene spermatocytes
H3K4me3
H3K27me3
H3K27ac
CUT&Tag: Pearson correlation of round spermatids

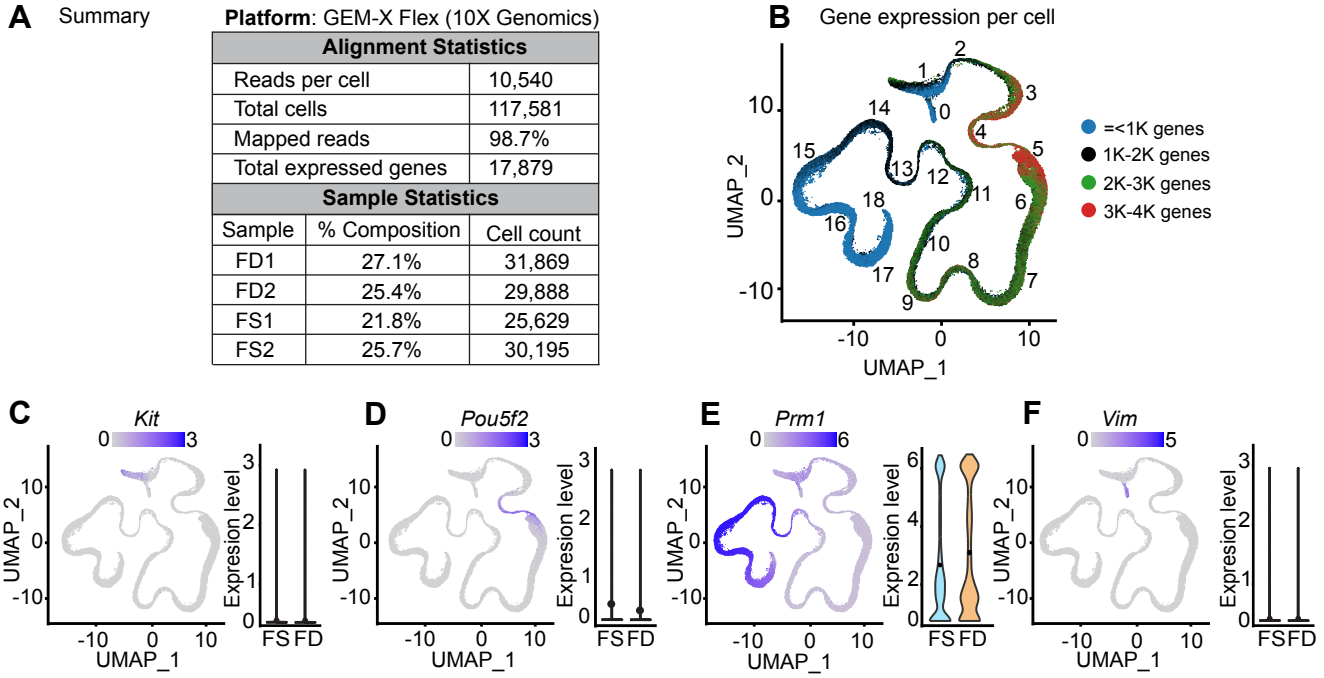

A
Upregulated in FD PS (n=625)
GO biological processes
-log10(FDR)
0
1
2
3
Sexual reproduction
n=33
Oxidative phosphorylation
n=9
Flagellated sperm motility
n=12
Spermatogenesis
n=22
Spermatid differentiation
n=13
B
Downregulated in FD PS (n=545)
-log10(FDR)
0
4
8
Regulation of metabolic process
n=208
Cellular component organization
n=190
Regulation of RNA metabolic process
n=130
Regulation of RNA stability
n=20
DNA methylation-dep. heterochromatin formation
n=6
C
RNA-seq: PS
P-adj < 0.05
Up in FD PS
Down in FD PS
Log2(fold change) (FD/FS)
Up: 75
Down: 40
Tnp1
Prm1
Mbd6
Dot1l
Log10(base mean+1)
D
RNA-seq: Wild-type
P-adj < 0.05
Up in FD PS (n=75)
Down in FD PS (n=40)
Auto
chrX
chrY
Z-score
THY+
KIT+
PS
RS
E
Differentially expressed genes (DEGs)
P-adj < 0.05
(%)
Up
Down
(n) 75 40
ChrXY
Autosome
CGI gene
Non-CGI gene
F
Genomic regions surrounding the Ddx4 locus
Pachytene spermatocytes
chr13:112,252,228-113,527,676
200 kb
ATAC
H3K4me3
H3K27Ac
H3K27me3
RNA
PS FS
PS FD
RefSeq Genes
Ankrd55
Gm33905
Il6st Il31ra
Ddx4
Slc38a9
Gm41067 Skiv2l2
Ccno Cdc20b
Gzmk
Gm41071
BC067074
Round spermatids
RS FS
RS FD
G
Genomic regions surrounding the Prdm2 locus
Pachytene spermatocytes
chr4:143,056,403-143,263,609
150 kb
Prdm2
Round spermatids

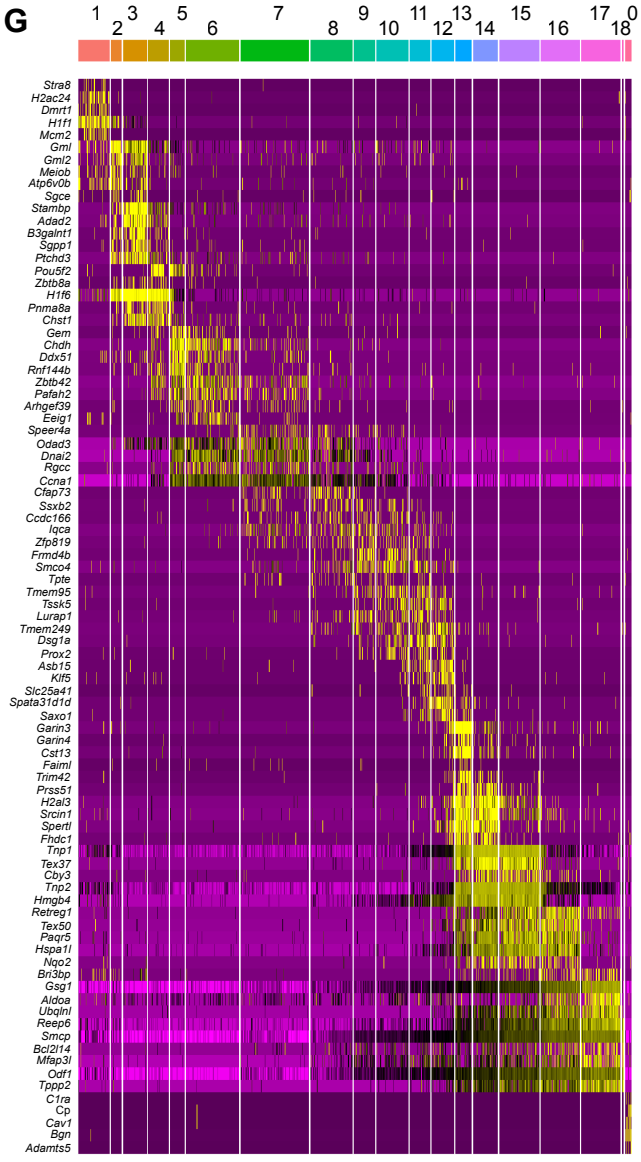
A Summary

Platform: GEM-X Flex (10X Genomics)

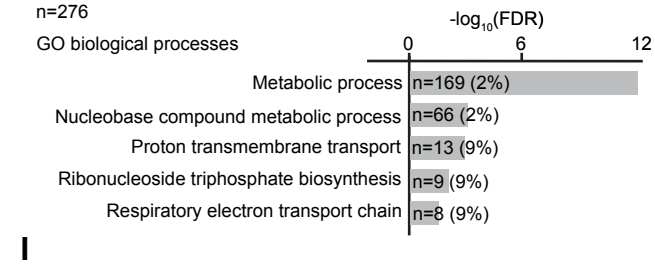
Alignment Statistics	
Reads per cell	10,540
Total cells	117,581
Mapped reads	98.7%
Total expressed genes	17,879

Sample Statistics		
Sample	% Composition	Cell count
FD1	27.1%	31,869
FD2	25.4%	29,888
FS1	21.8%	25,629
FS2	25.7%	30,195

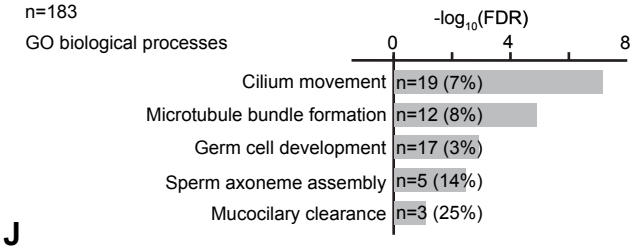




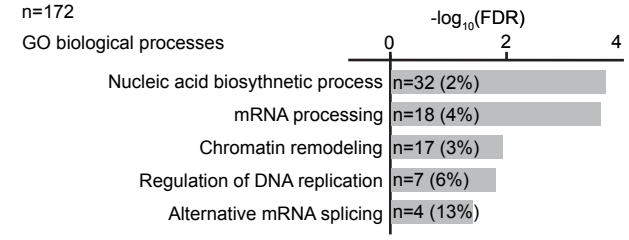
H
Increased transcription in Cluster 4
n=276
GO biological processes



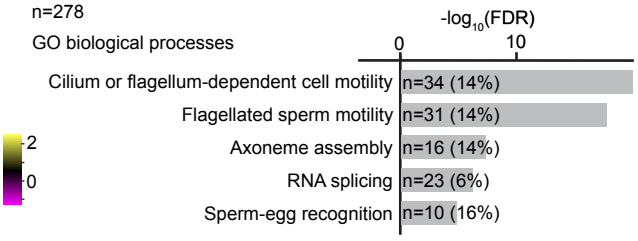
I
Decreased transcription in Cluster 4
n=183
GO biological processes

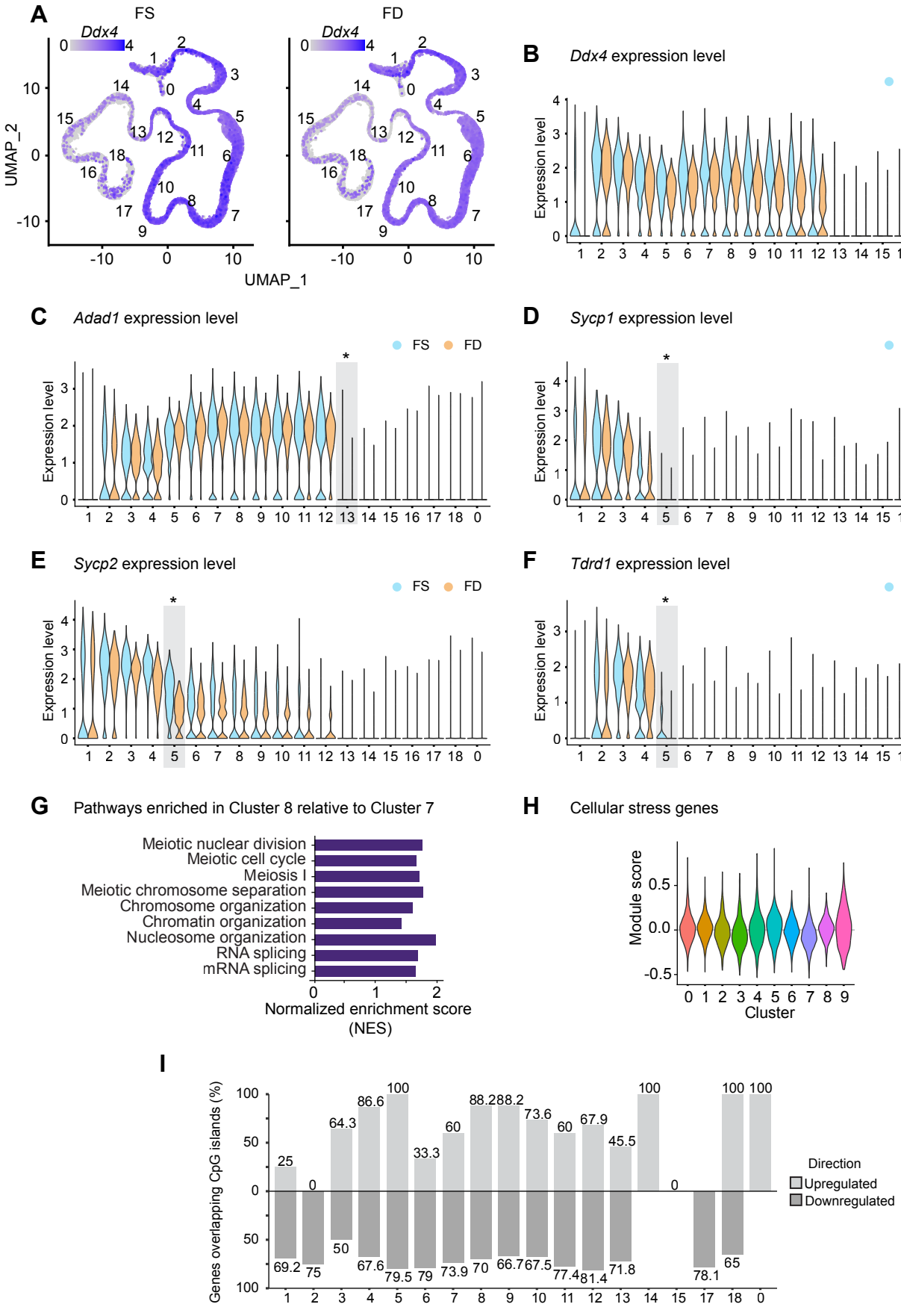


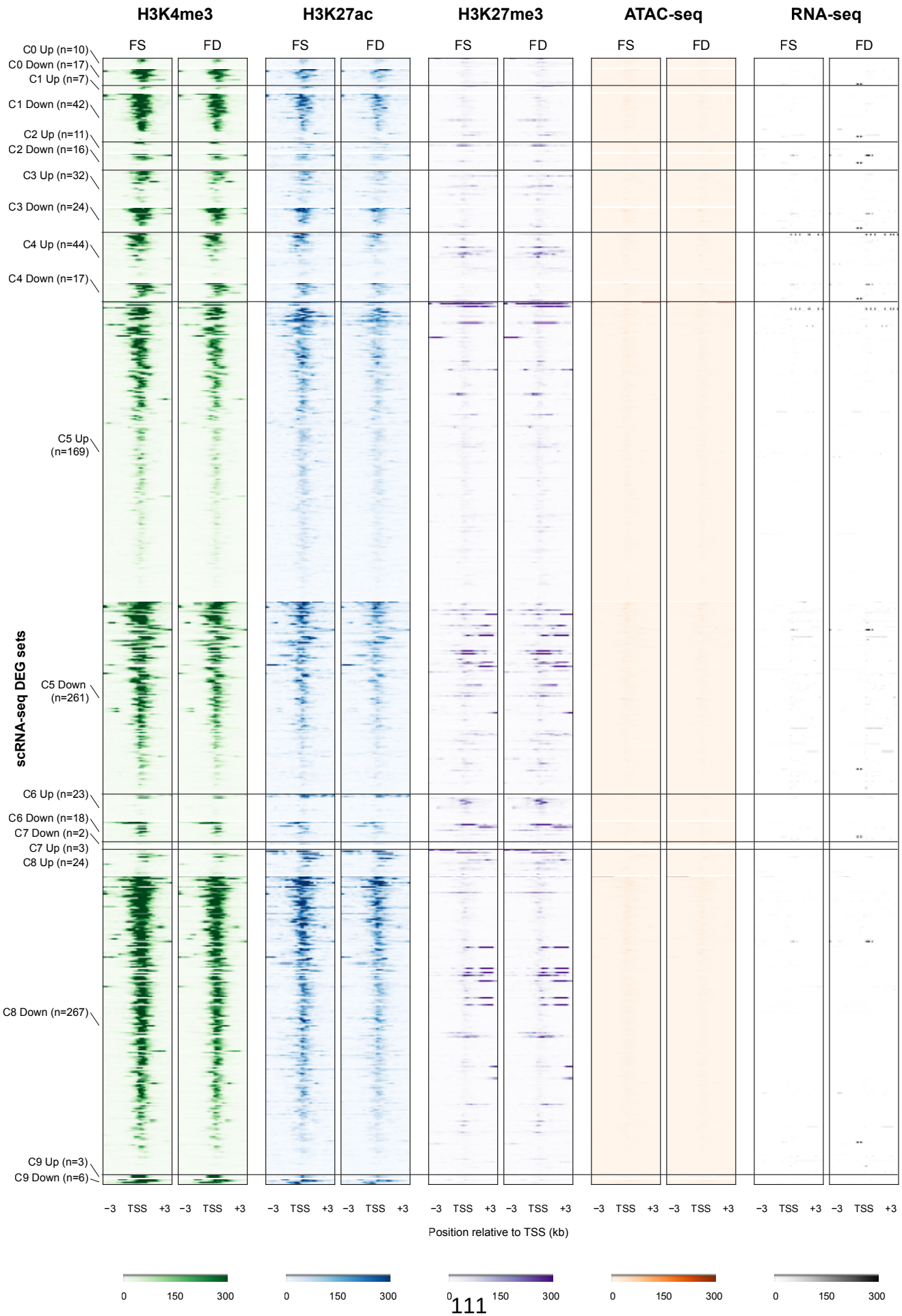
J
Decreased transcription in Cluster 5
n=172
GO biological processes



K
Decreased transcription in Cluster 17
n=278
GO biological processes




A
FS
FD
Ddx4
UMAP_1
UMAP_2
B
Ddx4 expression level
FS
FD
Expression level
C
Adad1 expression level
D
Sycp1 expression level
E
Sycp2 expression level
F
Tdrd1 expression level
G
Pathways enriched in Cluster 8 relative to Cluster 7
Meiotic nuclear division
Meiotic cell cycle
Meiosis I
Meiotic chromosome separation
Chromosome organization
Chromatin organization
Nucleosome organization
RNA splicing
mRNA splicing
Normalized enrichment score
(NES)
H
Cellular stress genes
Module score
Cluster
I
Genes overlapping CpG islands (%)
Direction
Upregulated
Downregulated


H3K4me3
H3K27ac
H3K27me3
ATAC-seq
RNA-seq
FS
FD
C0 Up (n=10)
C0 Down (n=17)
C1 Up (n=7)
C1 Down (n=42)
C2 Up (n=11)
C2 Down (n=16)
C3 Up (n=32)
C3 Down (n=24)
C4 Up (n=44)
C4 Down (n=17)
C5 Up (n=169)
C5 Down (n=261)
C6 Up (n=23)
C6 Down (n=18)
C7 Down (n=2)
C7 Up (n=3)
C8 Up (n=24)
C8 Down (n=267)
C9 Up (n=3)
C9 Down (n=6)
scRNA-seq DEG sets
−3
TSS
+3
Position relative to TSS (kb)
0
150
300

Structured Methods - Reagents and Tools Table

Instructions: Please complete the relevant fields below, adding rows as needed. The following page provides an example of a completed table and additional instruction for entering your data in the table.

Reagent/Resource	Reference or Source	Identifier or Catalog Number
Experimental Models		
C57/BL6 (M. Musculus)	Jackson Lab	
Diet		
Folate sufficient (2.0 mg/kg folic acid)	Inotiv	TD.01369
Folate deficient (0.3 mg/kg folic acid)	Inotiv	TD.01546
Antibodies		
Goat anti-ZBTB16/PLZF	R&D Systems	AF2944
Goat anti-CD117/cKIT	R&D Systems	AF1356
mouse anti-H2AX-pS139 conjugated Alexa 647 (γH2AX)	Millipore	05-636
guinea pig anti-H1T	a gift from Dr. Mary Ann Handel	
rabbit anti-SOX9	Millipore	AB5535
rabbit anti-H3K4me3	Invitrogen	703849, LOT 2920880
rabbit anti-H3K27ac	Cell Signaling Technology	8173S
rabbit anti-H3K27me3	Cell Signaling Technology	9733S
rabbit anti-S-adenosylmethionine	MyBioSource	MBS2015171
Chemicals, Enzymes and other reagents		
phosphate-buffered saline (PBS)	Fisher	BP399-20
Tris (CAS: 77-86-1)	Sigma	T1503-1KG
Sodium citrate tribasic dihydrate (CAS: 6132-04-3)	Sigma-Aldrich	C8532-1KG

ethylenediaminetetraacetic acid (EDTA) (CAS: 60-00-4)	Sigma-Aldrich	ED-500G
Sucrose (CAS: 57-50-1)	Sigma	50389-5KG
DL-Dithiothreitol (CAS: 3483-12-3)	Sigma-Aldrich	D0632-5G
cOmplete Protease Inhibitor Cocktail	Sigma	11836145001
Paraformaldehyde (CAS: 30525-89-4)	Sigma-Aldrich	158127-500G
Triton X-100 (CAS: 9002-93-1)	Sigma	T8787-100ML
Sodium dodecyl sulfate (SDS)	Sigma	L3771-1KG
Photo-Flo	Kodak	146-4510
Citrate buffer (pH 6.1)	DAKO	S-1700
Blocking One Histo	Nacalai USA	06349-64
ProLong Gold Antifade Mountant	Invitrogen	P36930
Collagenase	Worthington	CLS1
DNase I	Sigma	D5025
Hyaluronidase	Sigma	H3506
recombinant collagenase	FUJIFILM Wako Pure Chemical Corporation	036-23141
Vybrant DyeCycle Violet	Invitrogen	V35003
CELLBANKER 1 cryopreservation medium	Zenogen Pharma Co	11910
ERCC RNA Spike-In Mix 1	Invitrogen	4456653
RNeasy Plus Mini Kit	QIAGEN	74134
NEBNext® Single Cell/Low Input RNA Library Prep Kit for Illumina®	New England Biosciences	E6420S
Tn5 transposase enzyme	In-house	
MinElute PCR Purification Kit for PCR Cleanup	Qiagen	28004
SPRIselect beads	Beckman Coulter	B23317
CUTANA™ pAG-Tn5	Epicypher	15-1017
7-AAD Viability Stain	Thermo Fisher	00-6993-50
Chromium Next GEM Single Cell Fixed RNA Sample Preparation kit	10X Genomics	1000414

Chromium GEM-X Flex Reagent kits	10X Genomics	CG000787 Rev A
Software		
TrimGalore (v 0.6.10)	Felix Krueger	https://www.trimgalore.com/
HISAT2 (v2.2.1)	(Kim et al, 2019)	https://daehwankimlab.github.io/hisat2/
SAMtools (v1.16.1)	(Li et al, 2009)	https://www.htslib.org/doc/1.9/samtools.html
Subread (v2.0.2)	(Liao et al, 2013)	https://subread.sourceforge.net/
DESeq2 (v1.38.3)	(Love et al, 2014)	https://bioconductor.org/packages/devel/bioc/html/DESeq2.html
Pheatmap (v1.0.13)	https://cran.r-project.org/web/packages/pheatmap/index.html	https://cran.r-project.org/web/packages/pheatmap/index.html
ggplot2 (v3.5.1)	(Wickham, 2016)	https://cran.r-project.org/web/packages/ggplot2/index.html
FastQC (v0.12.1)	Babraham Bioinformatics	https://www.bioinformatics.babraham.ac.uk/projects/fastqc/
deepTools (v3.5.2)	(Ramirez et al, 2016)	https://deeptools.readthedocs.io/en/latest/source/deeptools.html
BEDTools (v2.31.0)	(Quinlan, 2014)	https://bedtools.readthedocs.io/en/latest/
Csaw (v1.32.0)	(Lun et al, 2016)	https://nbisweden.github.io/workshop-archive/workshop-ChIP-seq/2018-11-07/labs/lab-csaw.html
Picard (v3.0.0)	https://broadinstitute.github.io/picard/	https://broadinstitute.github.io/picard/
MACS3 (v3.0.0b3)	(Zhang et al, 2008)	https://macs3-project.github.io/MACS/

edgeR (v3.40.2)	(Robinson et al, 2009)	https://bioconductor.org/packages//release/bioc/html/edge.html
Integrative genomics viewer (v2.14.1)	(Thorvaldsdóttir et al, 2013)	https://igv.org/
Limma (v3.54.2)	(Ritche et al, 2015)	https://bioconductor.org/packages/release/bioc/html/limma.html
Cloud-based 10x Genomics Cell Ranger Multi pipeline (v9.0.0)	10X Genomics	https://www.10xgenomics.com/products/cloud-analysis
Seurat (v5.3.0)	Satija Lab	https://cran.r-project.org/package=Seurat
SeuratObject (v5.1.0).	Satija Lab	https://cran.r-project.org/package=SeuratObject
scDblFinder (v1.20.2)	(Germain et al, 2022)	https://bioconductor.org/packages/release/bioc/html/scDblFinder.html
Slingshot (v2.18.0)	(Street et al, 2018)	https://bioconductor.posit.co/packages/3.22/bioc/html/slingshot.html
ImageJ (v1.53t)	(Schneider et al, 2012)	https://imagej.net/downloads
Blind Analysis Tool (v1.0)	Astha Jaiswal 2019	https://imagej.net/Blind_Analysis_Tools
NIS Elements Advanced Research (AR)	Nikon	https://www.microscope.healthcare.nikon.com/en_AOM/products/software/nis-elements/nis-elements-advanced-research
CpG islands (mm10 assembly)	UCSC	https://genome.ucsc.edu/cgi-bin/hgTables?db=mm10&hgta_group=regulation&hgta_track=cpgIslandExt&hgta_table=cpgIslandExt&hgta_doSchema=d

		escribe+table+schema
Other		
Probe On Plus Microscope Slides	Thermo Fisher Scientific	22-230-900
70 µm strainers	Falcon	352350
Cell Sorter SH800	SONY	LE-SH800S
Sony SH800 and MA900 Sorting Chip-100µm (box of 40)	SONY	LE-C3210
Sony SH800 and MA900 Automatic Setup Beads	SONY	LE-B3001
NovaSeq X Plus Sequencer	Illumina	
AVITI Sequencer	Element Biosciences	

Concluding remarks

Conclusions

The development of male germ cells requires one of the most extensive chromatin transformations in mammalian biology. Throughout spermatogenesis, the epigenome is progressively reorganized to coordinate gene expression, chromosome architecture, genome defense, and the eventual packaging of the paternal genome into sperm. In Chapter 1, I described these coordinated and directional changes as an epigenetic trajectory. This framework emphasizes that each chromatin state both supports the immediate needs of a germ cell and establishes its competence to enter the next developmental stage. However, this trajectory is not executed in isolation. This dissertation demonstrates that its progression depends on both intrinsic chromatin regulators and the extracellular environment in which germ cells develop.

Chapter 2 identified ATF7IP2/MCAF2 as an intrinsic regulator of the meiotic epigenetic trajectory. MCAF2 is highly expressed during male meiosis and localizes to pericentric heterochromatin, the sex chromosomes, retrotransposon-derived loci, and thousands of autosomal promoters. On the sex chromosomes, MCAF2 acts downstream of the DNA damage response and facilitates the localization of SETDB1 and deposition of H3K9me3. Genetic deletion of *Mcaf2* disrupted meiotic sex chromosome inactivation, retrotransposon regulation, and broad autosomal gene expression, ultimately causing germ-cell arrest during meiotic prophase I (Alavattam et al., 2024). These findings expanded the known functions of H3K9me3 beyond constitutive heterochromatin and demonstrated that its spatial regulation contributes to both transcriptional repression and activation during meiosis.

The MCAF2 study also revealed that chromatin regulation during meiosis cannot always be explained by a simple relationship between one chromatin factor, one histone modification,

and one transcriptional outcome. Although SETDB1 is a known MCAF2-interacting protein, deletion of *Setdb1* in germ cells produces an earlier meiotic arrest than deletion of *Mcaf2*. MCAF2 also occupies a large proportion of promoters across the genome despite lacking a recognized DNA-binding domain. Together, these observations suggest that MCAF2 participates in multiple regulatory complexes and may use different interacting partners to perform its functions at promoters, retrotransposons, heterochromatin, and the sex chromosomes.

Whereas Chapter 2 examined the molecular machinery that directs the meiotic epigenome, Chapter 3 investigated its responsiveness to the nutritional environment. Paternal folic acid deficiency altered spermatogenic cell composition and produced extensive changes in gene expression, chromatin accessibility, and histone modifications. These effects were especially evident in pachytene spermatocytes, supporting meiosis as a period of heightened sensitivity to folate availability. CpG island-associated promoters were strongly represented among genes that lost active chromatin features and transcription, suggesting that promoter context influences the response to nutritional deficiency.

Single-cell analysis further showed that folate deficiency did not simply delay the entire spermatogenic program or induce a uniform cellular stress response. Instead, a subset of folate-deficient spermatocytes followed an alternative transcriptional trajectory that diverged from the expected path through pachytene. This population did not display strong enrichment for general stress pathways, suggesting that these cells occupied an altered developmental state rather than merely representing dying cells. In round spermatids, comparatively limited transcriptional changes were observed despite persistent and, in some cases, extensive chromatin alterations. Therefore, the postmeiotic findings do not indicate complete epigenetic recovery. Instead, they

suggest partial developmental compensation or a decoupling between the chromatin and transcriptional landscapes as germ cells progress beyond meiosis.

Together, these studies establish meiosis as a period of both epigenetic control and environmental responsiveness. Specialized factors such as MCAF2 help enforce the molecular organization required for meiotic progression, whereas folate availability influences the metabolic conditions under which this reprogramming occurs. Disrupting either layer alters the developmental trajectory, although the severity and nature of the resulting phenotypes differ. These findings support a model in which the male germline epigenome is highly programmed but not inflexible.

Future Directions

An important unanswered question from the MCAF2 study is how a protein without a known DNA-binding domain is recruited to such diverse genomic locations. Before completing this dissertation, I began developing an antibody to address this question. I generated and purified a 6×His-tagged fragment containing the MCAF2 SETDB1-binding region while selecting a sequence that was specific to MCAF2 and distinct from its homolog, MCAF1. This antigen was intended to produce an MCAF2-specific antibody that could be used to isolate endogenous MCAF2-containing protein complexes.

With additional time, I would use this antibody for co-immunoprecipitation followed by mass spectrometry (Co-IP MS) to define the MCAF2 interactome in meiotic germ cells. SETDB1 would provide a known positive control, while additional proteins could explain how MCAF2 is recruited to promoters and how it performs functions not shared with SETDB1. ATF7 is one candidate because MCAF2 was originally identified as an ATF7-interacting protein. However, the substantially milder phenotype of *Atf7* deletion (data not shown) suggests that ATF7, if confirmed as a partner, is unlikely to account for all MCAF2 functions. It may recruit MCAF2 to a subset of loci, or other transcription factors may compensate in its absence.

Proximity labeling using TurboID would provide a complementary approach. An endogenous MCAF2–TurboID fusion could capture transient or chromatin-associated proteins that may be lost during conventional purification. Candidate partners identified by either method could be tested through reciprocal co-immunoprecipitation, cellular colocalization, loss of function experiments, and genomic profiling. Separation of function MCAF2 mutants would also help distinguish SETDB1-dependent activities from other functions. Together, these experiments

could determine whether MCAF2 uses distinct protein complexes to regulate promoters, retrotransposons, pericentric heterochromatin, and the sex chromosomes.

For the folate study, a major next step would be to determine whether DNA methylation contributes to the strong relationship between CpG islands, loss of active histone modifications, and transcriptional repression. Enzymatic methyl-sequencing (EM-seq) of purified pachytene spermatocytes and round spermatids could be integrated with the existing RNA-seq, ATAC-seq, and CUT&Tag data. One possibility is that loss of H3K4me3 permits inappropriate DNA methylation at affected CpG island promoters, thereby stabilizing transcriptional repression. Alternatively, these promoters may remain hypomethylated despite losing active histone marks. Continued hypomethylation could preserve their regulatory competence and help explain why some transcriptional differences become less apparent after meiosis.

A dietary rescue experiment would determine whether the folate-deficient state is reversible. Following the 11-week deficient diet, mice could be returned to a folate-sufficient diet and evaluated across a time course. Single-cell RNA-seq could establish when the folate deficiency-enriched spermatocyte population disappears, while CUT&Tag and DNA methylation profiling could determine whether the chromatin landscape recovers at the same rate. Because newly generated germ cells would eventually replace those exposed during the deficient period, the timing of recovery would need to be interpreted relative to the spermatogenic cycle. Pulse-labeling or lineage-tracing strategies could distinguish true reversal within exposed cells from their replacement by newly developed cells.

Stable isotope tracing could connect dietary folate availability more directly to germ cell metabolism. Isotope-labeled folate could be used to trace folate-derived one-carbon units through methionine and S-adenosylmethionine metabolism and ultimately into methyl groups on DNA

and histones. LC–MS measurements of folate & folate derivatives, methionine, S-adenosylmethionine, and S-adenosylhomocysteine would help determine how rapidly the testis responds to folate restoration and whether metabolic recovery precedes or follows epigenetic recovery.

Finally, mating experiments are necessary to determine whether the chromatin alterations observed in folate-deficient fathers influence fertilization, embryonic development, or offspring health. These studies should begin by characterizing sperm from folate-sufficient and folate-deficient males and then examining which molecular differences remain detectable after fertilization. In vitro fertilization and embryo-transfer approaches could help isolate sperm-mediated effects from other parental or maternal influences. Profiling early embryos would be particularly important because similarity between fathers and adult offspring alone would not demonstrate direct inheritance of an epigenetic mark. Subsequent analysis of offspring development, fertility, and germ-cell chromatin could reveal whether paternal folate deficiency produces persistent biological consequences and whether returning fathers to a folate-sufficient diet before mating prevents them.

Final Perspective

This dissertation shows that the male germline epigenetic trajectory emerges from an interaction between intrinsic regulatory machinery and environmental conditions. MCAF2 helps organize meiotic chromatin and coordinate gene regulation, while folate availability influences the metabolic environment in which this extensive reprogramming occurs. These findings identify meiosis as a developmental window in which the germline must balance epigenetic stability with environmental responsiveness. Understanding how these regulatory layers intersect will be essential for explaining variation in male fertility and for determining when environmentally induced germline changes remain reversible, become fixed during sperm development, or influence the next generation.